Master's thesis

NTNU
Norwegian University of Science and Technology
Faculty of Engineering
Department of Geoscience and Petroleum

Kriti Panthi

Back calculation of in-situ stresses based on the performed secondary stress measurements by using numerical calculations - connected to the West Link Project

Master's thesis in Geotechnology
Supervisor: Roger Olsson
Co-supervisor: Øyvind Dammyr
February 2023

NTNU
Norwegian University of
Science and Technology

Kriti Panthi

Back calculation of in-situ stresses based on the performed secondary stress measurements by using numerical calculations - connected to the West Link Project

Master’s thesis in Geotechnology
Supervisor: Roger Olsson
Co-supervisor: Øyvind Dammyr
February 2023

Norwegian University of Science and Technology
Faculty of Engineering
Department of Geoscience and Petroleum

NTNU
Norwegian University of
Science and Technology

Abstract

The main objective of this thesis is to estimate and evaluate the undisturbed in-situ stress state that existed before excavating the pilot tunnels in a railway access cavern. The prediction of in-situ rock stresses is necessary since they are an important input for the stability assessments of underground openings. Thus, the design of a large underground cavern at a shallow depth requires reliable estimation of in-situ stress conditions. Geological conditions, topography, tectonic activity, and the geological history of glaciation and deglaciation have a significant influence on the magnitudes and orientations of the in-situ stresses. In-situ stress estimation can be based on various stress measurement methods, monitoring, elasticity theory and numerical modelling.

The access cavern, referred to as Mellanplan, presented in this study is a part of the West Link Project in Gothenburg, Sweden. The access cavern has a low overburden, where the average rock cover above the roof is estimated to be 11 m. Thus far, two pilot tunnels have been excavated at the top heading. SINTEF Community has conducted secondary stress measurements from the roof of the two pilot tunnels. The applied measurement technique was a 2D doorstopper method.

The estimation of in-situ stresses at a shallow depth in Mellanplan is achieved by validating the results from 3D numerical analyses with induced stresses obtained from doorstopper measurements. To generate the numerical models for stress analyses, geological conditions at Mellanplan are evaluated, and laboratory investigations are performed. The results from 2D doorstopper measurements are assessed, and an interpretation of the stress field at Mellanplan is carried out. The concepts from the final rock stress model (FRSM) suggested by ISRM (2012) are also applied to determine the in-situ stress state.

The 3D numerical modelling involves parametric stress analysis, where various stress inputs are evaluated. The stress parameters such as stress orientations, K-values (horizontal to vertical stress ratio) and locked-in stresses are the main input that induced change in the stress results from numerical analyses. After various numerical analyses, the numerical trials with varying horizontal stress orientations and K_H values led to the results that assisted the back-calculation of in-situ stresses. The back-calculated virgin stresses are further applied in a 2D numerical program for deformation analyses. The aim of the deformation analyses is to compare the measured vertical displacement with the numerical results.

The final rock stress model demonstrates the stress field at Mellanplan as $\sigma_H > \sigma_v > \sigma_h$. This stress state is considered viable at a shallow depth, from 0 masl. to 15.8 masl. The findings in the study imply that tectonic stress has a greater contribution to the major horizontal stress component. Residual stress is also predicted to have a significant influence on σ_H. Furthermore, σ_v and σ_h are suggested as gravitational stresses. However, geological structures may have an influence on the already low magnitude of σ_h. The orientation of σ_H is predicted at N150E, which slightly deviates from the previously estimated orientations at Gothenburg. This finding indicates the influence of geological structures that can result in some degree of stress rotation. Lastly, the displacement results from deformation analyses are different from the measured vertical deformation at the East pilot roof. Nonetheless, the results display an increase in the vertical displacements when the numerical model is generated with weathered joint conditions. The representation of joints in the 2D models is believed to be the factor affecting the displacement deviation.

Sammendrag

Hovedformålet med masteroppgaven er å estimere og evaluere in-situ spenningstilstanden som eksisterte før åpning av pilottunnelene i en berghall til et jernbaneprosjekt. Estimering av in-situ bergspenninger er nødvendige fordi de spiller en viktig rolle når det gjelder stabilitetsanalyser av undergrunnsanlegg. Dermed er det viktig med pålitelig in-situ spenningstilstand ved design av en stor berghall med lav overdekning. Geologiske forhold, topografi, tektonisk aktivitet, og den geologiske historien av nedising og isavsmelting har en betydelig innflytelse på størrelsen og orienteringen av in-situ spenningene. In-situ spenningstilstand kan bestemmes ved å utføre ulike spenningsmålinger, overvåkningsmetoder, elastisitetsteori og numerisk modellering.

Berghallen som er presentert i denne studien er en del av Västlänken prosjekt i Gøteborg, Sverige. Berghallen heter Mellanplan, og har lav overdekning. Den gjennomsnittlige bergoverdekningen over taket til hallen er estimert som 11 m. Per dags dato, er det kun to pilottunneler som har blitt konstruert i toppstollen. SINTEF Community har utført indusert spenningsmålinger fra taket til begge pilottunneler. 2D doorstopper metoden var brukt til bergspenningsmålinger.

Estimeringen av in-situ spenninger på et grunt dyp i Mellanplan oppnås ved å validere resultater fra 3D numeriske analyser med målte induserte spenninger fra 2D doorstopper. Utforming av numeriske modeller for spenningsanalyser er basert på vurderinger av det geologiske forholdet i Mellanplan og laboratorietester. I tillegg er resultater fra 2D doorstopper-målinger analysert, og det er gjennomført en vurdering av spenningstilstand i Mellanplan. Konseptene fra den endelige bergspenningsmodellen (the final rock stress model, FRSM) foreslått av ISRM (2012) er brukt for å bestemme den in-situ spenningstilstanden.

Den 3D numeriske modelleringen i studien innebærer parametriske spenningsanalyser, hvor ulike inngangsparametere relatert til bergspenninger er vurdert. Spenningsparametere som spenningsorienteringer, K-verdier (horisontal til vertikal spenningsforhold) og konstante spenninger (locked-in stresses) er de viktigste faktorer som førte til endring i spenningsresultatene fra numeriske analyser. Etter å ha utført ulike numeriske analyser, forsøk med varierende horisontale spenningsorienteringer og K_H verdier førte til resultater som kunne brukes til tilbakeberegning av in-situ spenninger. Den tilbakeberegnet bergspenninger er videre brukt som inngangsparametere i en 2D numerisk program for å gjennomføre deformasjonsanalyser. Formålet med deformasjonsanalysene er å sammenligne den målte vertikale deformasjonen med numeriske resultater.

Den endelige bergspenningsmodellen viser at spenningstilstanden i Mellanplan kan beskrives som $\sigma_H > \sigma_v > \sigma_h$. Denne spenningstilstanden regnes gyldig kun på grunt dyp, fra 0 moh. til 15,8 moh. Funnene i studien antyder at tektoniske spenninger har et større bidrag til den største horisontale spenningskomponenten. Residualspenninger er også estimert til å ha en betydelig bidrag til størrelsen av den største horisontalspenningen. Videre σ_v og σ_h er foreslått som gravitative spenninger. Likevel kan geologiske strukturer ha en innflytelse på den allerede lave σ_h verdier. Orientering av σ_H er estimert i retning N150E, som avviker litt fra de tidligere estimerte spenningsorientering i Gøteborg. Dette indikerer at geologiske strukturer har innflytelse på rotasjon av spenninger. Videre resultater fra deformasjonsanalyser avviker fra den målte vertikal deformasjonen på taket til den Østre piloten. Allikevel viser resultatene en økning i vertikal deformasjon når den numeriske modellen blir generert med forvitrende forhold av diskontinuiteter. Det antas at representasjon av diskontinuiteter i 2D modeller har påvirkning på deformasjonsavviket.

Acknowledgements

This thesis concludes my Master of Science in Geotechnology - Engineering Geology and Rock Mechanics. The thesis work is submitted to the Department of Geoscience and Petroleum at the Norwegian University of Science and Technology (NTNU) and comprises 30 ECTS credits.

I would like to express my gratitude to my supervisor Roger Olsson. His knowledge and expertise in engineering geology and rock mechanics have inspired me. During this final semester with the master's thesis, he has offered valuable guidance, insightful discussions and encouragement. I am thankful for the opportunity I have been given to gain knowledge and experiences related to this thesis work.

I also want to thank my co-supervisor, Øyvind Dammyr, for his valuable guidance and good discussions. I am grateful for his advice, especially towards the work related to numerical modelling. Further, Eric Hegardt is greatly appreciated for assisting me during the project site visitations at the West Link. Gunnar Vistnes and Jon Runar Drotninghaug from the Rock Mechanics Laboratory at NTNU are also thanked for the preparation work of rock specimens and their constant guidance during laboratory investigations.

Finally, I extend my gratitude to my family and friends for their support and encouragement during the completion of my master's thesis. In this context, my brother is especially acknowledged for reviewing my manuscripts.

Trondheim, 13th February 2023

Kriti Panthi

Contents

1 Introduction

1.1 Background of the study

Gothenburg is Sweden's second-largest city and one of the fastest-growing regions in Northern Europe. Seventy per cent of Scandinavia's total industrial capacity has been established within a 500-kilometre radius of the Gothenburg region. The increasing growth, in terms of population and economy, has resulted in capacity issues with the current railway traffic in and around Gothenburg. Therefore, The West Link Project (Västlänken) has been introduced as a solution for an improved and reliable railway system. West Link will increase the commute capacity, train frequency and accessibility to the city with a new railway system. The project started in 2018 and is estimated to commence in 2026. The Swedish Transport Administration, Trafikverket, is the owner of the project (Trafikverket, 2021).

The West Link Project includes the construction of railway track tunnels and three new stations underneath the city of Gothenburg. The project is divided into four main areas, Centralen, Kvarnberget, Haga and Korsvägen (Figure 1.1). Korsvägen section consists of train tunnels, an underground station and a connection to the railway line in the south (Trafikverket, 2022a). The excavation of the access cavern in Korsvägen, also referred to as Mellanplan, started in 2021. At the present, only two pilots of the top heading at Mellanplan are excavated. A rock pillar remains between the pilots.

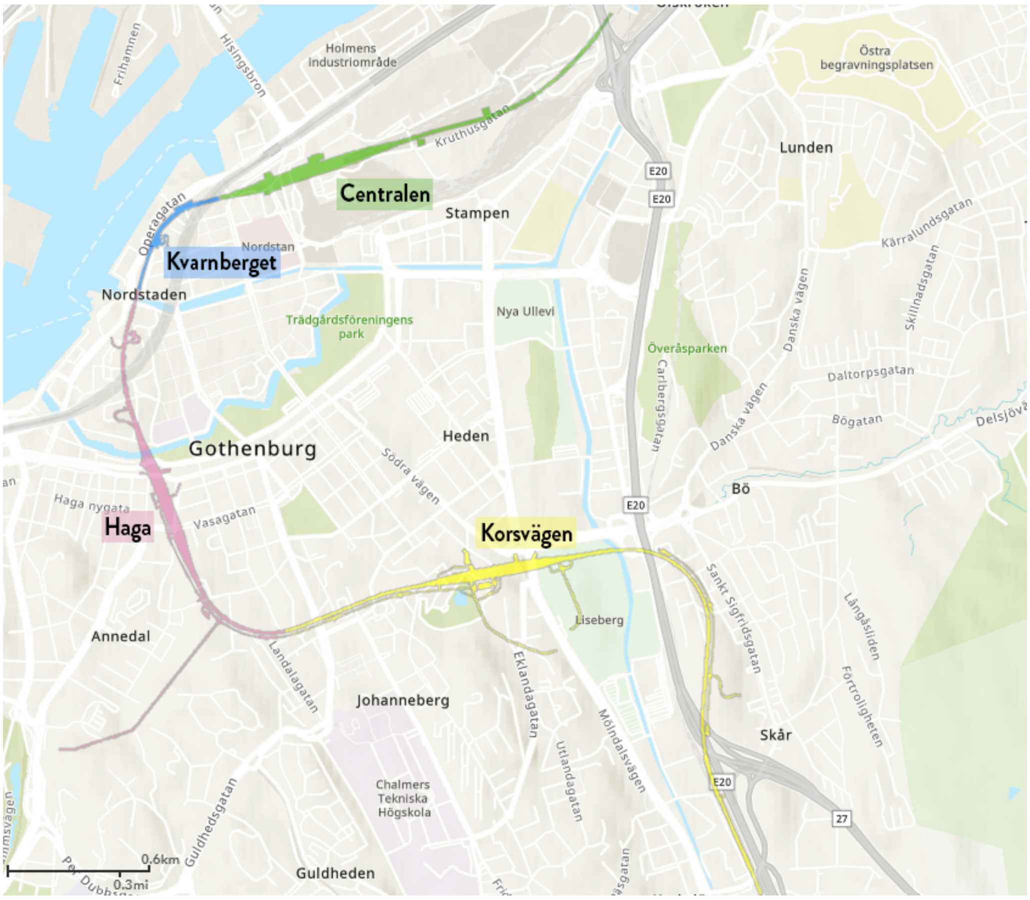

Figure 1.1: Overview of Centralen, Kvarnberget, Haga and Kosvägen in Västlänken. From: Trafikverket (2022e).

The access cavern in Korsvägen has a low overburden, which varies between 7 m to 15 m across excavated geometry. The span of the cavern is 28.8 m (Trafikverket, 2016c). High horizontal stresses can be advantageous when constructing an underground cavern with a large span at a shallow depth. Therefore, the knowledge of in-situ stress conditions is an important input for the stability analysis of underground openings. The stability issues also depend on other factors, e.g., geological conditions and geometry of the excavation (Martin et al., 2003).

In-situ stress state estimation can be based on elasticity theory, various stress measurement methods, monitoring and numerical modelling. Prior to West Link, few rock stress measurements were conducted in the Gothenburg region. The stress field in Fennoscandian Shield generally depicts higher horizontal stresses than vertical stress at shallow depths. The results from the stress measurements near the ground surface often have widespread data (Trafikverket, 2014). According to the International Society for Rock Mechanics and Rock Mechanics, ISRM (2012), the uncertainties of in-situ stress conditions can be reduced with a combination of stress measurements and numerical modelling.

In April 2022, SINTEF Community, department of Rock and Soil Engineering conducted secondary stress measurements at Mellanplan, Korsvägen. The stress measurements were carried out from the roof of the two pilots by using the 2D doorstopper method (SINTEF, 2022a). The measured secondary stresses can be applied to estimate the in-situ stresses before the excavation at the top heading of Mellanplan. In addition to stress measurements, displacements in the pilots are also monitored. A combination of in-situ stress back-calculation and an assessment of displacements are valuable for future stability analysis regarding the removal of the remaining rock pillar in Mellanplan. It should be noted that in-situ stresses are also referred to as virgin stresses/primary stresses in this thesis.

1.2 Scope of the study

The master's thesis focuses on the top heading section of the access cavern in Korsvägen. The access cavern, Mellanplan is located between the station tunnel in the east and track tunnels in the west (Figure 1.2). Thus far, two pilot tunnels have been excavated at each side of the cavern.

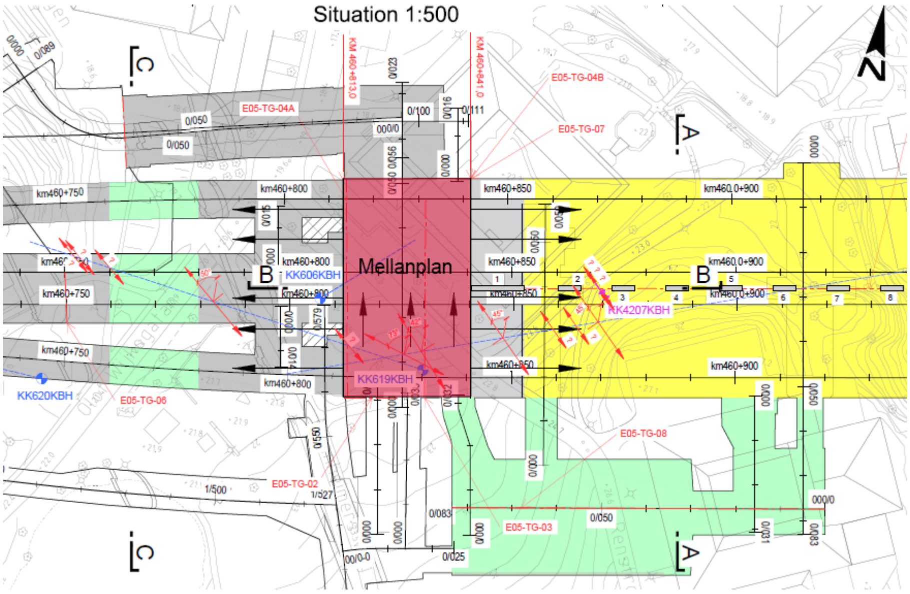

Figure 1.2: Mellanplan is highlighted with a red rectangle. From: Trafikverket (2018).

The aim of this master's thesis is to back-calculate the in-situ stresses at a shallow depth in Mellanplan. The main focus lies on the rock mass above the top heading of the access cavern. The measured secondary stresses have been utilised for the assessment of the local in-situ stress state. Furthermore, the estimated primary stresses have been applied to assess and compare the calculated displacements with the monitored displacements in the pilot tunnels.

The objectives of the thesis are the following:

1. Theoretical study on the design principles of rock caverns, mechanical and geological properties of rocks, and rock mass quality.
2. Review the existing theory on rock stresses and its measurement methods.
3. Interpretation of geological mapping and photogrammetry of the excavated pilots in Mellanplan.
4. Laboratory testing on rock samples collected during field investigations.
5. Interpretation of the stress field in Mellanplan before developing a final rock stress model (FRSM). This includes an evaluation of the stress results from 2D doorstopper measurements.
6. Evaluation and comparison between secondary stresses from the doorstopper measurements and the secondary stresses achieved from 3D numerical modelling. 3D numerical analyses are based on geological parameters obtained from objectives 3 and 4.
7. Back-calculation of in-situ stresses on the basis of the results from 3D numerical models.
8. Further application of the back-calculated in-situ stresses in a 2D numerical modelling program to compare the measured displacements with the numerically calculated displacements.
9. Discussion on the results from the numerical analyses.

1.3 Methodology

The following methodology has been applied during the thesis work:

1. Literature review:

   The literature review is the basis for the theory and methods presented in this thesis work. The majority of the review is based on scientific articles, conference and symposium proceedings, and relevant rock mechanics and rock engineering books. The collected literature is from the databases provided by the university library of the Norwegian University of Science and Technology (NTNU). Additionally, books and compendiums provided by NTNU courses are also utilised.

2. Background study on The West Link Project and Mellanplan:

   Reports, project descriptions and CAD drawings provided by Trafikverket are used as background materials to get an overview of the West Link Project and Mellanplan. Evaluation of the geological conditions at Mellanplan is based on the data available on executed geological mappings, project reports, photogrammetry and field investigations. Information on in-situ stress estimations at Gothenburg and deformation monitoring at Mellanplan are also valuable for this study. The author also visited the project site twice, to get a better overview and knowledge of Mellanplan, and to collect rock samples for laboratory investigation.

3. Illustrations:

   Some of the illustrations in this thesis work are made by the author. These illustrations are based on theoretical concepts or descriptions of the West Link project. The illustrations created by the author are carried out using Adobe programs: *Photoshop* and *Illustrator*. Moreover, for the evaluation of joint data, steoreonet is created by using a Rocscience program called *Dips*.

4. Estimation of rock mass properties:

   Rock mass properties are estimated by applying the following methods:

   - Interpretation of data from geological mapping, project reports and photogrammetry.
   - Laboratory investigations.
   - Classification systems and empirical relationships.

5. Secondary stress measurement data from Mellanplan:

   The data from the secondary stress measurements performed by SINTEF is one of the essential background studies utilised in this thesis work. The main objective of the thesis regarding the back-calculation of rock stresses is associated with the results from the secondary stress measurements. In addition to gaining knowledge from the stress report developed by SINTEF, the author has had direct correspondence with one of the research engineers that performed the stress measurements at Mellanplan.

6. Stress and displacement analyses:

   The stress analyses are performed in a 3D numerical program, *RS3*, to back-calculate the in-situ stress state at the top heading in Mellanplan. The back-calculated rock stress is further applied in a 2D numerical program, *RS2*, to compare the displacements achieved from numerical analyses to the measured displacements. Both *RS3* and *RS2* are finite element programs provided by Rocscience.

1.4 Limitations

One of the challenges for the master's study includes the limitation for the author to conduct geological mappings. During the site visitation of Korsvägen at the West Link Project, the excavated pilot tunnels at Mellanplan no longer had exposed rock mass. The pilots were sprayed with shotcrete, and rock bolts were implemented. Therefore, the author had to rely on handwritten geological mappings provided by Trafikverket to establish input parameters for numerical analysis. The author collected and translated the data from the geological mappings to make a digitalised version. Furthermore, other background materials are also applied to determine reliable input parameters for numerical models. The author had to evaluate and interpret the existing material to establish an understanding of the geological conditions at the access cavern in Korsvägen.

First-hand information on stress measurements conducted by SINTEF, deformation monitoring and previous in-situ stress measurements near Mellanplan is not available for the study. The author had to rely solely on the results reported. The detailed methodology and calculations applied in these field investigations are limited, and thus could not be counter-checked by the author.

The rock specimens collected for the laboratory investigations are limited to granodiorite gneiss. Due to practicality and time restrictions, only gneiss rock cores could be collected from the second project site visitation.

The final limitation of this study is related to numerical analysis. Numerical models consist solely of the top heading and do not include other excavated areas nearby the access cavern, e.g., the access tunnel to the top heading. Simplifications and assumptions regarding geological conditions and rock stresses are made. Therefore, the input parameters in the analyses may carry a few uncertainties.

2 Design principles of rock caverns

Underground caverns are used for a variety of purposes in civil engineering, e.g., caverns for the installation of turbines, generators and transformers in hydropower projects, rock caverns for storage, underground sports facilities and caverns for underground train stations. Due to high capital costs and risks related to public access to these underground facilities, the design of underground caverns has to ensure absolute minimum risks. In addition, the design should provide cost-effective and practical engineering solutions (Hoek, 2007). During the design procedure, results from the engineering geological investigations should be prioritised. The aim of the design is to avoid instability issues or to reduce risks associated with them (Nilsen and Thidemann, 1993). Due to the small overburden in the access cavern in Korsvägen, this chapter focuses on the design principles of shallow seated caverns.

2.1 Location and orientation

The decisions concerning the location of an underground cavern are among the most important stages during the design and construction process. The site selection determines the rock mass quality in which the cavern complex will be excavated. For a rock cavern in a shallow depth, minimum rock cover should be determined in the early stages of design. Generally, the opening is favoured to be located deep enough to have a reasonable layer of unweathered rock above the roof. Due to several glaciations, the weathered zone in Scandinavia often only exists a few meters below ground water-level. Furthermore, the rock cover should also be thick enough to develop normal stresses on joints for a self-supporting roof (Nilsen and Thidemann, 1993). As shown in Figure 2.1 regarding hard rocks, approximately 5 metres of rock mass layer is considered reasonable for spans of 20 metres, given that the layer is measured from maximum overbreak above the roof line.

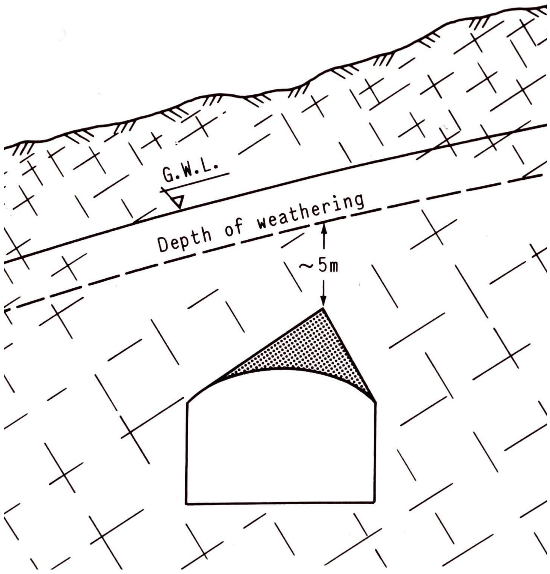

Figure 2.1: Minimum rock cover for an underground opening in shallow depth. From: Selmer-Olsen and Broch (1977).

Underground projects are considered unique, as geological conditions and demands vary from one project to another. Factors other than engineering geology can constrain the decisions on location, where a favourable site may be reduced to a limited area. The limitations experienced in cavern locations are often related to the location of the access tunnels, external traffic, and the operation and size of the cavern complex. Due to such constraints, the installation of a cavern should be optimised regarding geology and topography. The predominant factors in optimisation are adequate overburden, avoidance of weakness zones or acceptance of the shortest possible distance while crossing them, and favourable rock stresses. Both extremely low and high rock stresses are considered unfavourable. Low stresses in a rock mass can result in reduced confinement and arching effects, while very high rock stresses can give rise to spalling and rock burst (Broch et al., 2016).

The optimisation also includes the prevention of adverse cavern orientation relative to the orientation of weakness zones, major discontinuities and major rock stresses. For rock caverns with low overburden, it is preferred to orient the length axis along the bisection line of the maximum angle between two major joint directions, as shown in Figure 2.2. However, the orientation of the cavern should not be parallel with the direction of other joints (Nilsen and Thidemann, 1993).

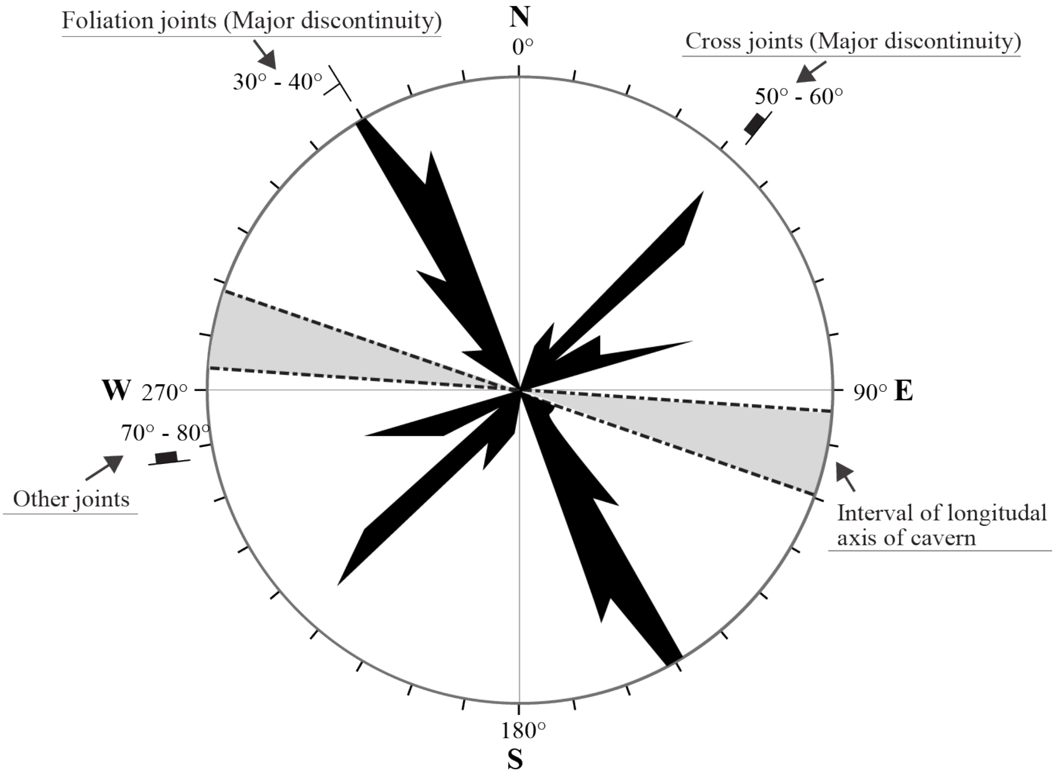

Figure 2.2: *Rosette plot illustrating the favourable orientation of shallow seated caverns with respect to joint directions. Based on: Nilsen and Thidemann (1993).*

2.2 Span width

Generally, stability issues in caverns increase with an increasing span. Large cavern spans are often more challenging than narrow caverns due to confinement issues and the necessity of securing an arching effect. Reduction in confinement can result in wedges sliding and instabilities during excavation (Broch et al., 2016). The arching effect is a natural pressure arch that occurs during excavation and bears the ground pressure. The natural arch pressure is obtained as a function of rock mass quality, rock stresses and shape of the roof and acts as a protection shield over the excavation (Li, 2017).

Formation of the natural arch is challenging when a large span is combined with a small overburden. Instead, underground excavations near the surface tend to have arching deformations directed towards the free ground. In such situations, it is favourable to have high horizontal stresses. The horizontal stresses that are at least equal to or greater than the vertical stress are beneficial for the stability of shallow seated caverns with large spans (Barton and Hansteen, 1978).

2.3 Cavern shape

The basic goal for a cavern design is to achieve an even distribution of compressive stresses in the rock mass surrounding the underground opening. Such stress distribution is obtained by giving the excavated opening a simple form with an arched roof. Moreover, corners and edges should be avoided if possible while designing a cavern shape. The rock mass in sharp areas can be destressed and often result in overbreak during blasting or instability issues after blasting (Nilsen and Thidemann, 1993).

The purpose of the cavern generally dictates the shape and size of the excavation. Although the stability of an underground opening increases with a circular shape, rounded caverns are more complicated to excavate. The excavation method called benching is preferred for large caverns. Hence, cavern walls are generally vertical. The cross-section of a rock cavern also depends on the magnitude and the orientation of the major rock stresses, as illustrated in Figure 2.3.

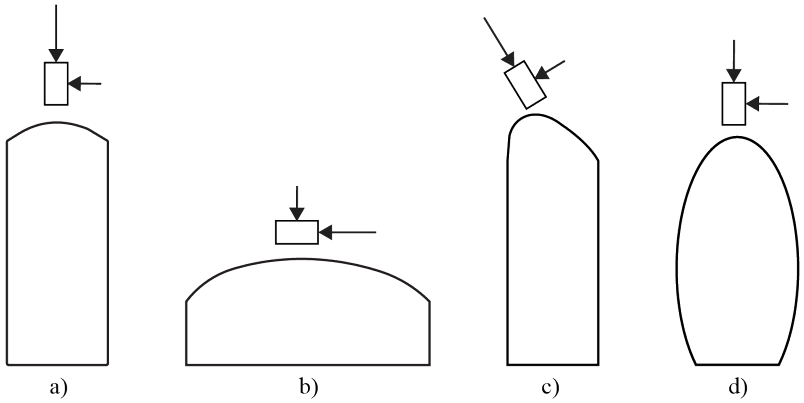

Figure 2.3: *Optimised cavern cross-section relative to the magnitude and the orientation of major rock stresses. a) vertical σ_1 > horizontal σ_3, b) vertical σ_3 < horizontal σ_1, c) sloping anisotropy and d) approximately hydrostatic conditions with vertical σ_1 = horizontal σ_3. Modified after: Broch et al. (2016).*

2.4 Rock support

In general, rock support refers to any measure aiming to improve the stability of rock masses by applying support elements. Support elements can be rock bolts, cables, shotcrete, concrete lining, meshes and rebars. The main goal for stability improvement is to design rock support in accordance with the underground conditions in a cavern. Flexible support methods are preferred in order to quickly adjust the support while encountering variation in rock mass quality (Nilsen and Palmström, 2000).

A rock support system provides three main functions: reinforcement, holding and retention. Reinforcement indicates the strengthening of the rock mass, holding refers to the suspension of loosened rock blocks, and retention involves confinement of the exposed rock surfaces. Rock bolts installed systematically provide reinforcement and holding functions for the loosened blocks. Retention is achieved by applying shotcrete, mesh or other thin liners on the rock surface (Kaiser et al., 1996).

An underground opening in shallow depth is exposed to low in-situ rock stresses, where rock failure in the surrounding rock is limited to a small depth. The main aim of the support system, in this case, is to avert the potentially loosened or failed blocks in the failure zone from falling. Therefore, spot bolting or systematic bolting can be enough to achieve rock mass stability. The rock bolts should be installed beyond the failure zone, and into the natural pressure arch as shown in Figure 2.4a. Due to large spans, the failure zone can extend beyond the length of the bolts. Figure 2.4b illustrates that in such conditions, both rock bolts and shotcrete are applied. Rock bolts are tightly installed to develop an artificial pressure arch in the failure zone (Li, 2017).

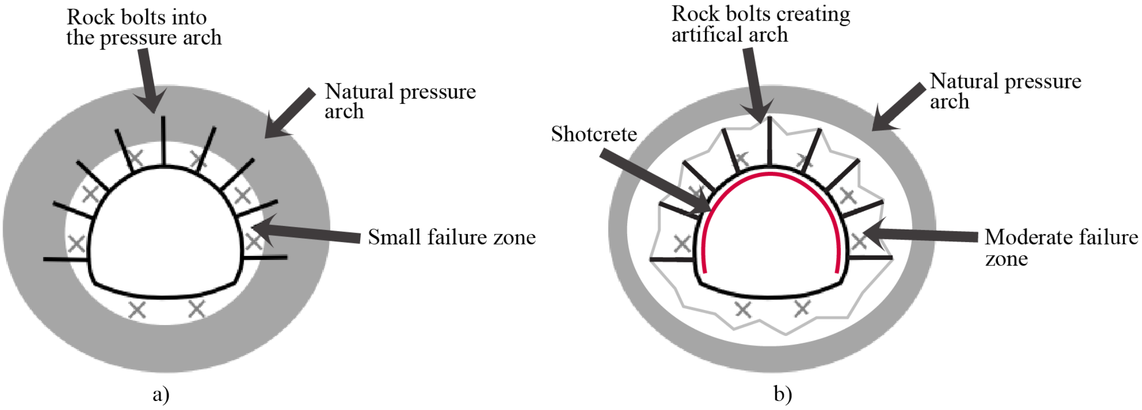

Figure 2.4: *a) Rock bolts installed into the natural pressure arch. b) Rock bolts and shotcrete installed to create artificial pressure arch. Illustrations are modified after: Li (2017).*

2.5 Numerical modelling

Numerical modelling is an essential tool for analysing the fundamental processes that occur in a rock mass. In order to analyse rock mass conditions and stability issues, a numerical model should include the geometry of the problem, rock mass strength and deformability, relevant material parameters, fracture mechanism and boundary conditions. Since rock mass is a complex material, it is challenging to create a model that accurately represents the situation mathematically.

Various numerical modelling techniques have been developed throughout the years. In rock engineering, continuum and discrete methods are the most frequently applied numerical methods. In continuum models, the rock mass behaves as a continuum medium, and there is a continuity between the elements. On the other hand, discrete methods involve discontinuous models where separate elements are considered discontinuous. However, the elements in discrete models are individually continuous and interact with one another (Nikolic et al., 2016).

The choice of application between continuous and discontinuous models depends on various factors, but predominantly on the problem scale and fracture systems. Usually, the continuum method, such as the finite element method (FEM), is utilised for rock masses with no fractures or with many fractures (Figure 2.5a and d). In cases with few discontinuities, the continuous models can be applied if there are no fracture openings (Figure 2.5b). When the rock mass is moderately fractured, the discrete element method (DEM) tends to be more suitable (Figure 2.5c).

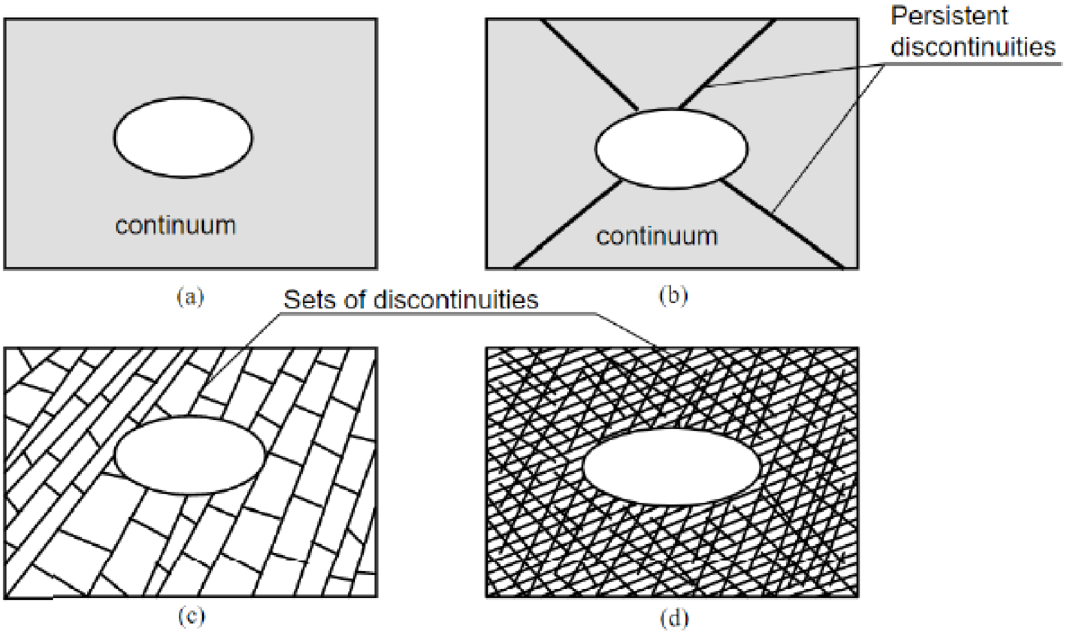

Figure 2.5: *Numerical methods for excavation in a rock mass. a) Continuum method, b) Continuum with fractures or discrete method, c) Discrete method and d) Continuum method. From: Jing (2003).*

Further development of finite element methods includes the extended finite element method (XFEM). XFEM has been developed to overcome challenges with fractures in a continuous model. The joints and cracks can be modelled in the XFEM domain without conforming to the mesh. Additionally, XFEM also has the capacity to interact with the support elements, such as bolts, liners and structural interface (Rocscience, 2022f).

According to Broch et al. (2016), it is common to perform numerical analyses for large span caverns, caverns in challenging ground conditions and multi-cavern schemes. Such analyses are carried out to study the stress distribution and stability issues governing the design and support. It is also emphasised that numerical analyses should under no circumstance completely substitute the experiences and observations made during construction.

3 Properties of rocks and rock mass

3.1 Introduction

Rocks are defined as naturally occurring solid aggregates with one or various minerals. These minerals differ from one another due to their different physical properties. Therefore, the physical and mechanical properties of rocks are influenced by the type and amount of minerals they contain. Other factors influencing rock properties are mineral size, shape, orientation and binding forces between them. Intact rock properties are not sufficient to define the actual behaviour of a rock mass underground. A rock mass is defined as an in-situ material containing intact rock, discontinuities and structural features (Nilsen and Thidemann, 1993).

According to Panthi (2006) rock mass is a heterogeneous material, characterised by two main features: rock mass quality and the mechanical processes acting on the rock mass (Figure 3.1). These two features are significantly dependent on each other and are influencing factors to the stability of underground excavation.

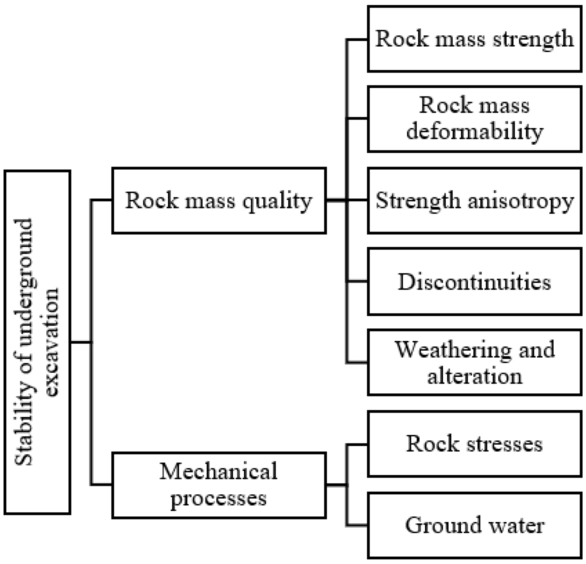

Figure 3.1: *Influencing factors on the stability of an underground excavation. Modified after: Panthi (2006).*

This chapter will not present any theory on groundwater since the numerical analyses performed in this study do not include its effects. Furthermore, the West Link has predicted dry conditions regarding groundwater throughout the entire project.

3.2 Physical properties of intact rocks

The physical properties of intact rocks have a direct influence on the behaviour of underground openings. The main physical properties of rocks consist of density, porosity, wave velocity and heat transfer and expansion. The scope of this study includes laboratory tests, where the density and wave velocity of intact rocks are determined. Due to their relevance to the thesis, they are discussed in the sections below.

3.2.1 Density

In general, intact rocks have a density in the range of 2.5-3.2 g/cm^3. Sandstones with higher porosity are in the lower range, while gabbro and basalts are in the upper range. Metamorphic rocks, such as granites, often have a density of 2.65-2.7 g/cm^3. Density is a valuable parameter for rock stress evaluations and stability analyses. In the case of coherent rock specimens, e.g., core specimens from boreholes, the density of rock materials are determined by calculating volumes and weighing the specimens (Nilsen and Thidemann, 1993).

3.2.2 Wave velocity

Wave velocities are measured in rock specimens, often core bits, to obtain general information about rock type and quality. One of the suggested methods for determining sound velocity by ISRM (1978b) involves a non-destructive test where a high-frequency ultrasonic pulse is transferred through a rock specimen. The equipment consists of a pulse generator unit and transducers that are placed between a specimen. From the equipment, the travel time of P-waves (primary waves) can be determined. Sound velocity is then calculated as a ratio between specimen length and P-wave travel time (Nilsen and Thidemann, 1993). Table 3.1 presents typical P-wave velocities for some rock types.

Table 3.1: *Examples of P-wave velocities. Based on: Reynolds (2011).*

Rock type	$V_p [m/s]$
Sandstone	1400 - 4500
Limestone (hard)	2800 - 7000
Shales	2000 - 4100
Granites	4600 - 6200
Basalt	5500 - 6500
Grabbro	6400 - 7000
Gneiss	3500 - 7600

3.3 Geological features of rock mass

Discontinuities are structural or geological features that alter the homogeneity of a rock mass. In general, discontinuities are formed as a result of movements in rock mass from various tectonic activities. Discontinuity, as a general term, can be described as any mechanical discontinuity in the rock mass having zero or close to zero tensile strength. The term includes various geological features such as joints, bedding planes, foliation planes and weakness zones (Nilsen and Palmström, 2000). The properties of discontinuities highly influence the properties of the in-situ rock mass. In strong and hard rocks, including Scandinavian crystalline rocks, the importance of discontinuities often governs over other rock properties (Nilsen and Thidemann, 1993).

3.3.1 Rock mass jointing

According to Nilsen and Palmström (2000), joints are three-dimensional discontinuities composed of two matching surfaces called joint walls. Joints are the most common structural features to appear in a rock mass. A group of parallel joints form a joint set, and various joint sets intersect to form a joint system. Joints have several characteristics, they can be open, filled or healed. Joints are frequently formed parallel to bedding planes, foliations or slaty cleavage, and thus they can be termed *bedding joints*, *foliations joints* or *cleavage joints*. Joints that cross such planes are generally termed as *cross joints* (Brady and Brown, 2006).

The mechanical properties of joints are governed by frictional conditions or the shear strength along joint walls. The distance between matching joint walls controls the interlocking between them. When interlocking is absent, the properties of joint filling determine the shear strength of the joint. As separation decreases, the roughness of the joint walls is the main contributor to the shear strength (Nilsen and Palmström, 2000). The shear strength of joints is defined by the Coulomb law, presented in Equation 3.1.

$$\tau = \sigma_n \tan \phi \tag{3.1}$$

σ_n and ϕ represent normal stress and active friction angle of the joint surface, respectively (Li, 2021). The active friction angle is expressed with two factors: basic friction angle (ϕ_b) and dilation angle (i). The basic friction angle is determined from tilt tests, while the dilation angle is a joint parameter that describes roughness (Patton, 1966). The active friction angle of the joints can be defined as:

$$\phi = \phi_b + i \tag{3.2}$$

There are two types of active friction angles: peak active friction angle (ϕ_p) and residual friction angle (ϕ_r). The peak active friction angle is related to peak shear strength, and the residual active friction angle is related to residual shear strength. The summation of residual friction angle and dilation angle gives peak friction angle, $\phi_p = \phi_r + i$. According to Barton (1976) the dilation angle can be expressed with Equation 3.3.

$$i = JRClog_{10}\left(\frac{JCS}{\sigma_n}\right) \tag{3.3}$$

where JRC is Joint Roughness Coefficient, and JCS is Joint Compressive Strength.

3.3.2 Weakness zones and faults

A weakness zone is described as a part of the rock mass where mechanical properties are significantly lower than the surrounding rock mass. Weakness zone is a collective term for faults, shear zones, thrust zones and weak mineral layers. Faults can be identified as minor to major structures in a rock mass due to tectonic activities. The typical thickness of minor faults varies from a decimetre to a metre, while the width of major faults ranges from several metres to hundreds of metres. The surface walls of faults are generally slickenside as a result of shear displacement. Faults can differ in composition, from crushed rock material to highly weathered or altered rock mass. Weathering and alteration often result in the formation of filling materials referred to as gouge (Figure 3.2). Filling materials normally consists of clay fillings or clay-like materials (Nilsen and Palmström, 2000).

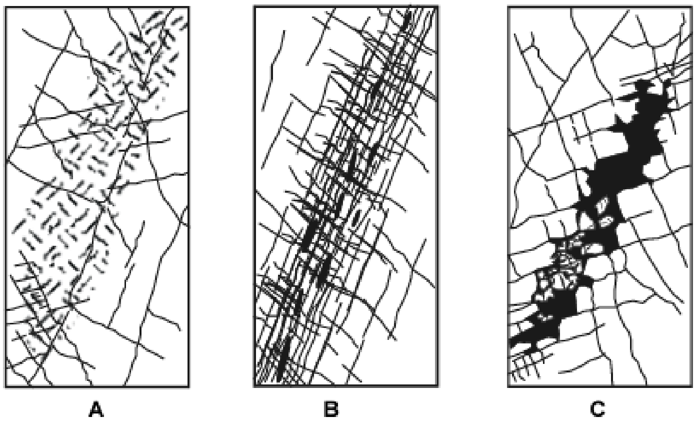

Figure 3.2: *Development of faults. Black colour indicates filling material. From: Nilsen and Palmström (2000).*

3.4 Rock mass strength and deformability

Rock mass strength is defined as the ability to withstand stress and deformation. The presence of discontinuities and foliation or schistosity planes affect the strength of the rocks, as well as the orientation of the structures relative to the direction in which the strength is assessed (Panthi, 2006). Rock mass strength and deformation vary from the strength and deformation of an intact rock. In general, intact rock specimens are homogeneous with few discontinuities and are stronger than the rock mass. Therefore, a small rock specimen may not represent the actual rock mass strength and deformation (Bieniawski and Van Heerdan, 1975).

3.4.1 Factors influencing rock mass strength

The strength of an intact rock can be determined by various laboratory test methods, such as the uniaxial compressive strength test, triaxial test and point load strength test (Nilsen and Palmström, 2000). Although intact rock specimens are commonly homogeneous with few discontinuities, other factors influence their strength. Thus, these influencing factors should be assessed while conducting rock strength tests, as they are also important for the estimation of rock mass strength. Weathering and anisotropy are relevant influencing factors for the thesis study and hence are discussed below.

Weathering and alteration

Rocks formed beneath the surface can be exposed to the atmosphere as a result of erosion by glaciers, water, waves and wind. Due to forces and reagents, these rocks can break apart and transform into finer material. The process of disintegration and decomposition of rock material is known as rock weathering. The rock material loses its coherence by breakdown or mechanical disintegration, resulting in the opening or formation of new joints, fracturing of mineral grains and opening of grain boundaries. While chemical decomposition involves rock decay accompanied by changes in chemical and mineralogical composition. The main results of decomposition include discolouration of rock, decomposition of silicate minerals eventually transforming to clay minerals, and leaching of calcite and salt minerals (Nilsen and Palmström, 2000).

Weathering and alteration reduce rock properties, such as strength, deformability, slaking durability and frictional resistance. Permeability in rocks can also increase significantly due to weathering. Therefore, from an engineering perspective, weathering should be addressed during the classification of rock mass quality (Panthi, 2006).

Anisotropy

Anisotropy in rock materials is a result of foliation, schistosity, layering or bedding. The orientation of foliations in sedimentary and metamorphic rocks determines the degree of strength anisotropy. While in rock mass systems, major discontinuities and weakness zones will also have an impact on the strength anisotropy. Another influencing factor on the degree of anisotropy is the amount and arrangement of elastic and anisotropic minerals, e.g., mica, amphiboles, chlorite and some pyroxenes. The parallel orientations of these sheet minerals are common in metamorphic rocks in which the weakness planes can appear along their layers (Nilsen and Palmström, 2000). Layers of weakness planes and schistose rocks lack sufficient bonding and friction and may result in a strength reduction. Additionally, these planes and rocks will have a reduced self-supporting capacity. These behaviours in a rock mass can lead to stability problems during excavation.

Figure 3.3 illustrates the effect of anisotropy on the uniaxial compressive strength of intact rocks. According to the data in the figure, the strength of intact rocks is lowest when the schistosity or foliation plane is inclined at approximately 30° from the direction of loading. The highest strength appears to occur when the plane is perpendicular to the loading direction. Figure 3.3 depicts that rocks containing sheet minerals like mica, chlorite, graphite and talc have considerable anisotropy (Panthi, 2006).

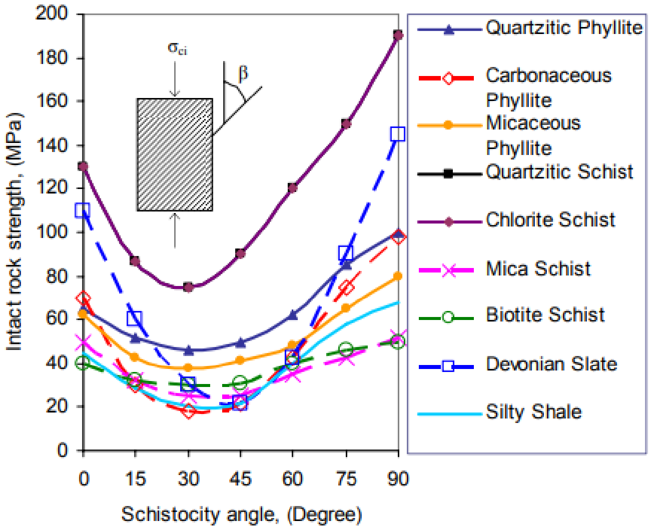

Figure 3.3: *Variation of uniaxial compressive strength at different angles of the schistosity plane. From: Panthi (2006).*

One of the methods to determine the degree of anisotropy is point load testing. According to ISRM (1985) Strength Anisotropy Index ($I_{a(50)}$) is calculated from point load tests. The Strength Anisotropy is defined as the ratio of the greatest to least Point Load Strength Indices

($I_{s(50)}$). Values of $I_{a(50)}$ close to 1.0 are assumed to be quasi-isotropic, while higher values describe anisotropic rocks. Table 3.2 presents the classification of point load strength anisotropy proposed by Tsidzi (1990).

Table 3.2: *Classification of point load strength anisotropy proposed by Tsidzi (1990).*

Nature of rock	Strength anisotropy index (I$_a$)	Descriptive term
Very strongly foliated	>3.5	Very highly anisotropic
Strongly foliated	3.5-2.5	Highly anisotropic
Moderately foliated	2.5-1.5	Moderately anisotropic
Weakly foliated	1.5-1.1	Fairly anisotropic
Very weakly foliated or non-foliated	<1.1	Quasi-isotropic

3.4.2 Rock mass strength

The uniaxial compressive strength test (UCS test) is the most common laboratory testing method to determine the strength of an intact rock. The compressive strength (UCS) of an intact rock is generally denoted as σ_c or σ_{ci}. As discussed by ISRM (1979), σ_{ci} is defined as:

$$\sigma_{ci} = \frac{P}{A_o} \tag{3.4}$$

where P is the compressive load and A_o is the cross-sectional area of the rock specimen. Furthermore, Young's modulus (E_i) and Poisson's ratio (ν) can be calculated from the stress and strain curve derived from the UCS tests. Young's modulus is expressed in Equation 3.5 as a ratio between stress (σ) and strain (ϵ). Compressive stresses and strains are considered positive components in rock engineering. Moreover, Poisson's ratio is defined in Equation 3.6 as a ratio between radial strain (ϵ_r) and axial strain (ϵ_a) (Nilsen and Thidemann, 1993).

$$E_i = \frac{\Delta\sigma}{\Delta\epsilon} \tag{3.5}$$

$$\nu = -\frac{\epsilon_r}{\epsilon_a} \tag{3.6}$$

The compressive strength of an intact rock can be divided into different strength classifications as shown in Table 3.3.

Table 3.3: *Classification of the uniaxial compressive strength or rocks (ISRM, 1981).*

Classification	Uniaxial compressive strength [MPa]
Extremely low strength	0.25-1
Very low strength	1-5
Low strength	5-25
Medium strength	25-50
High strength	50-100
Very high strength	100-250
Extremely high strength	>250

Unlike intact rock, the strength of rock mass is challenging to determine by laboratory tests or direct measurements in the field. Various empirical formulae have been postulated to estimate the rock mass strength, with some examples given in Table 3.4. According to authors in Table 3.4, rock mass strength (σ_{cm}) is a function of intact rock strength (σ_{ci}). Some of the equations also include rock mass classifications such as Rock Mass Rating (RMR), Rock Mass index (RMi) or Q-system.

Table 3.4: *Estimation of rock mass strength.*

Suggested by	Rock mass strength (σ_{cm})
Bieniawski (1993)	$\sigma_{cm} = \sigma_{ci} \times \left[\frac{RMR-100}{24}\right]$
Palmstrøm (1995)	$\sigma_{cm} = RMi = \sigma_{ci} \times JP$
Barton (2002)	$\sigma_{cm} = 5\gamma \times \left[\frac{\sigma_{ci}}{100} \times Q\right]^{\frac{1}{3}}$
Hoek et al. (2002)	$\sigma_{cm} = \sigma_{ci} \times s^a$
Panthi (2006) and Panthi (2017)	For schistose and deformable rock mass: $\sigma_{cm} = \frac{\sigma_{ci}^{1.5}}{60}$ For massive, homogeneous, and brittle rock mass: $\sigma_{cm} = \frac{\sigma_{ci}^{1.6}}{60}$

3.4.3 Rock mass deformability

Deformation of rock mass occurs when it experiences load. In elastic deformation, various constants can define the relationship between the applied stress and the strain response (Nilsen and Palmström, 2000). Young's modulus or E-modulus (E_i) is among these constants. Bieniawski (1978) suggested that the modulus of elasticity is not applicable for jointed rock mass due to its inelastic behaviour. Rock mass deformation is dependent on both the deformation of intact rock and discontinuities. Thus, the term modulus of deformation (E_{rm}) is preferred for jointed rock mass. According to ISRM (1975) the definition of modulus of deformation is given as "the ratio of stress to corresponding strain during loading of rock mass including elastic and inelastic behaviour".

The modulus of deformation can be measured directly in the field by utilising e.g., plate loading test, dilatometer test, flat jack test, hydraulic chamber etc. These test methods often provide values that differ significantly from one another. Additionally, they are also considered time-consuming and costly. As a result of such difficulties, many authors have postulated empirical formulae for the estimation of rock mass deformation modulus. Some of them are presented in Table 3.5.

Table 3.5: *Estimation of rock mass deformation modulus.*

Suggested by	Rock mass deformation modulus (E_{rm})
Bieniawski (1978)	$E_{rm} = 2RMR - 100$
Palmstrøm (1995)	$E_{rm} = 5.6 \times RMi^{0.375}$
Barton (2002)	$E_{rm} = 10 \times Q_c^{\frac{1}{3}}$
Hoek and Diederichs (2006)	$E_{rm} = E_i\big[0.02 + \frac{1-D/2}{1+exp((60+15D-GSI)/11)}\big]$
Panthi (2006) and Panthi (2017)	For schistose and deformable rock mass: $E_{rm} = E_i\frac{\sigma_{ci}^{0.5}}{60}$ For massive, homogeneous, and brittle rock mass: $E_{rm} = E_i\frac{\sigma_{ci}^{0.6}}{60}$

3.5 Failure criteria

In engineering geology, the term failure can be described as a loss in load carrying capacity of a material. Various theories and criteria have been developed to explain and estimate when and where failure will occur in a rock mass. These theories make assumptions that a failure will occur as a result of a specific mechanism when a specific mechanical property is exceeded. In addition, it is often assessed upon which principal stress condition will result in such a failure (Myrvang, 2001). The theoretical criteria rarely reflect the actual nature of the failure mechanism in a rock mass. Despite this limitation, out of many empirical relationships, the Mohr-Coulomb criterion and the Generalized Hoek-Brown criterion are widely applied in rock engineering (Li, 2021). This thesis only includes the application of the Generalized Hoek-Brown criterion for numerical modelling. Hence, this criterion alone is further described.

3.5.1 Generalized Hoek-Brown critertion

The Generalized Hoek-Brown criterion is an empirically derived, non-linear failure criterion which agrees with experimental data over a range of confining stresses. The criterion has been established through an extensive evaluation of data from laboratory tests covering a vast range of intact rock types (Eberhardt, 2012). The Generalized Hoek-Brown introduced by Hoek et al. (1995) is expressed as:

$$\sigma_1 = \sigma_3 + \sigma_{ci}\left(m_b\frac{\sigma_3}{\sigma_{ci}} + s\right)^a \tag{3.7}$$

where σ_1 and σ_3 are major and minor principal stresses, respectively at failure. Moreover, σ_{ci} is the uniaxial compressive strength of the intact rock, and m_b, s and a are material constants defined by Hoek et al. (2002) as:

$$m_b = m_i exp\left(\frac{GSI - 100}{28 - 14D}\right) \tag{3.8}$$

$$s = exp\left(\frac{GSI - 100}{9 - 3D}\right) \tag{3.9}$$

$$a = \frac{1}{2} + \frac{1}{6}\left(e^{-GSI/15} - e^{-20/3}\right) \tag{3.10}$$

In Equation 3.8, m_i is a material constant for intact rock, while in Equations 3.8-3.10 GSI is the Geological Strength Index. D is the disturbance factor that depends on the degree of disturbance of rock mass due to blasting and stress relaxation. The factor varies from 0 for undisturbed rock mass to 1 for very disturbed rock mass.

3.5.2 Practical application of Hoek-Brown

The application of a failure criterion should be based on the type of rock mass being investigated. Mohr-Coulomb criterion can be considered best fitted in situations where rock mass is dominated by single- or two joint sets. In addition, it can also be used when one of the joint sets is significantly weaker than the others. Generalized Hoek-Brown is applicable for intact rock or heavily jointed rock masses. In the case of two joint sets, the Hoek-Brown failure criterion can be utilised with care, provided that neither of the joint set has a dominant influence on the material behaviour. In conditions where a single set of discontinuities controls rock mass stability, the Hoek-Brown criterion is only applicable to the intact rock components (Hoek et al., 1995).

Hoek (2007) and Eberhardt (2012) have suggested that Hoek-Brown can be applied indirectly in numerical calculations performed in terms of Mohr-Coulomb failure criterion. Equivalent Mohr-Coulomb parameters, friction angle (ϕ) and rock mass cohesion (c) can be achieved from Hoek-Brown parameters by fitting an average linear relationship to the non-linear Hoek-Brown envelop for a range of minor principal stress (Figure 3.4). The range can be defined as T_o < σ_3 < σ_{3max}, where T_o is tensile stress, and σ_{3max} is the upper limit of confining stress. The upper limit of σ_{3max} is often unique for each individual case. Therefore, the relationship between Hoek-Brown and Mohr-Coulomb may vary between different projects. It is recommended to clearly evaluate the values of the minor principal stress before applying programs to calculate equivalent Mohr-Coulomb. In case of high σ_{3max} values, equivalent cohesion may be too high and friction angle too low.

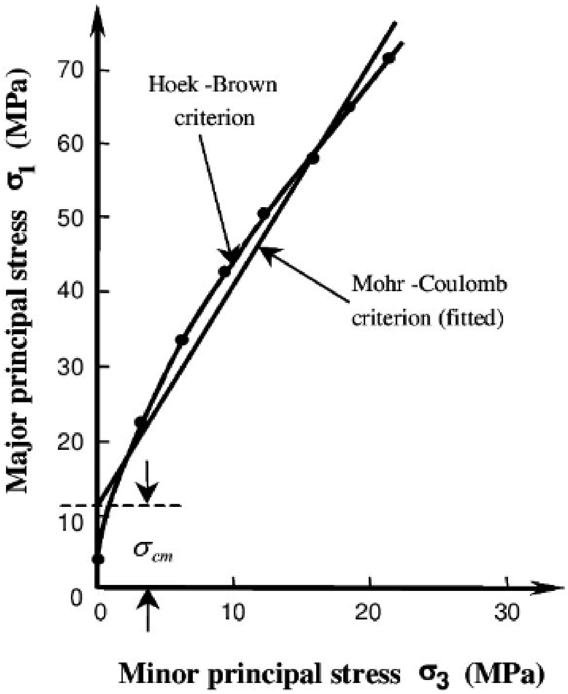

Figure 3.4: *Example of a relationship between major and minor principal stresses for Hoek-Brown criterion and equivalent linear Mohr-Coulomb criterion. Modified after: Hoek and Brown (1997).*

3.5.3 Barton-Bandis criterion

Knowledge about joint characteristics and their mechanical properties is valuable to understand rock failure controlled by discontinuities. Thus, several joint criteria have been developed to provide an estimation of failure along a joint surface. The Barton-Bandis criterion is one of the most recognised and applied joint failure criteria. The main aspect of the criterion is the quantitative characterisation of the investigated joints or joint sets, in order to provide three input joint parameters. These parameters concern JRC, JCS and an empirically-derived residual friction angle, ϕ_r (Barton and Bandis, 1990). Based on the joint relations presented in Section 3.3.1, the Barton-Bandis criterion includes the following equation introduced by Barton and Choubey (1977).

$$\tau = \sigma_n \tan\left[JRClog_{10}\frac{JCS}{\sigma_n} + \phi_r\right] \tag{3.11}$$

Equation 3.11 is an estimation for the shear strength of weathered and unweathered joints. JRC values are determined in the field by using a profile gauge and comparing the joint surface profiles to standard roughness profiles illustrated in Figure 3.5

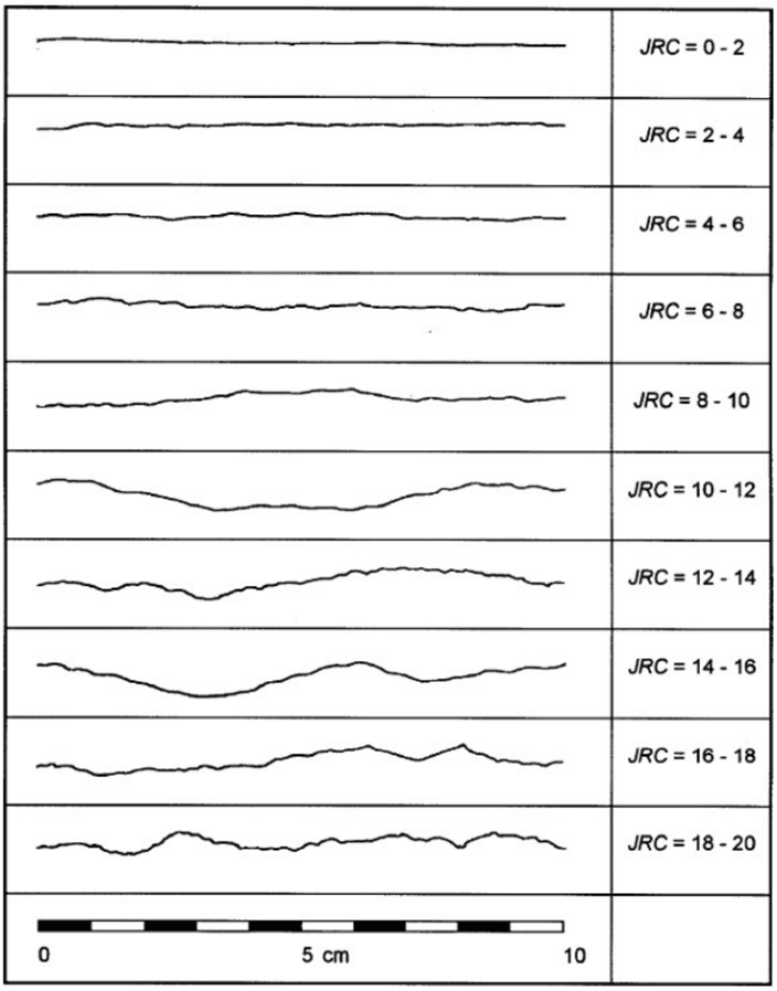

Figure 3.5: *Rock joint roughness profiles showing the typical range of JRC. From: Barton and Choubey (1977).*

JCS is determined by performing Schmidt hammer measurements on rock and joint surfaces. A combination of rebound number (Schmidt hardness) obtained from the hammer and unit weight of the rock provides an estimation for uniaxial compressive strength, as shown in Figure 3.6. The UCS values derived from the Deere-Miller graph are considered JCS values. Nonetheless, the effect of weathering and water on joint surfaces should be considered as they reduce JCS values. Furthermore, jointed rock mass can be affected by blasting, and contain small asperities on the joint surfaces, which can influence the rebound values obtained by Schmidt hammer (ISRM, 2009).

Barton-Bandis criterion also include the residual friction angle, ϕ_r, which is obtained by performing tilt test and applying following Equation 3.12 suggested by Barton and Choubey (1977). As mentioned in Section 3.3.1, values of basic friction angle (ϕ_b) are obtained from tilt tests.

$$\phi_r = (\phi_b - 20^\circ) + 20\left(\frac{r}{R}\right) \tag{3.12}$$

In Equation 3.12 R is the Schmidt rebound on unweathered smooth surface of a rock, and r is the rebound number for a weathered joint surface. In the case of unweathered joint conditions, the residual friction angle can be estimated as basic friction angle, ϕ_r=ϕ_b.

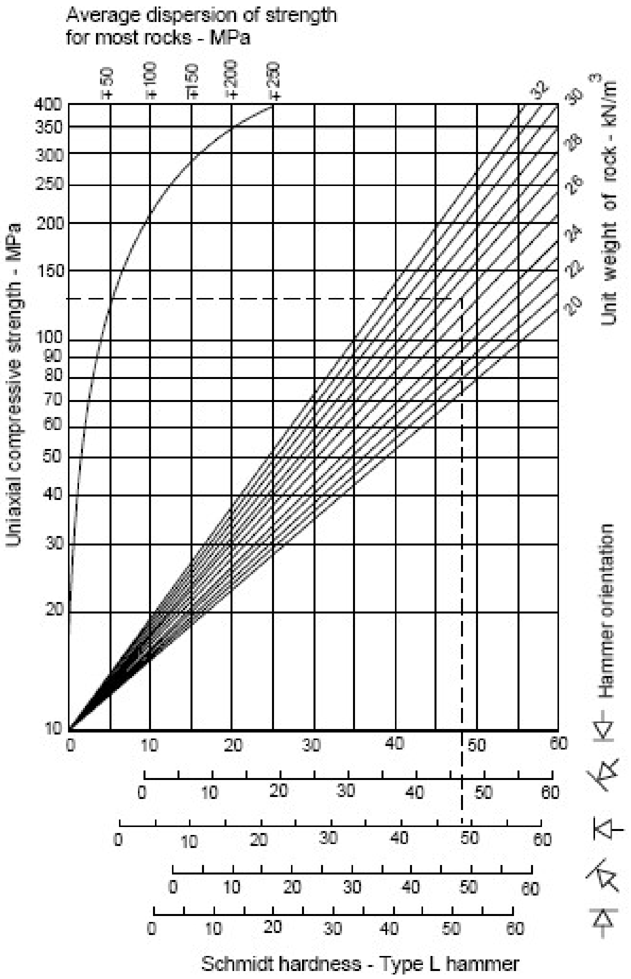

Figure 3.6: *Determination of UCS values from Schmidt hammer measurements and unit weight of the rock. From: Deere and Miller (1966).*

4 Rock mass classification

4.1 Introduction

The purpose of a rock mass classification system is to obtain a general rating of rock mass quality and to evaluate rock support and support design. Frequently applied classification systems in Scandinavia are the Q-system and the Rock Mass Rating system (RMR). Other systems, such as Geological Strength Index (GSI), are also utilised for the evaluation of rock mass quality. The referred classification systems consist of geological and material parameters, where each parameter is classified into given values or ratings to express rock mass quality with respect to stability. Based on the values or ratings, the rock mass is allocated into different rock mass groups or classes. Such characterisation of rock mass quality provides a good reference basis regarding communication between the users of the systems (engineering geologists and geologists) and the other actors in the project, e.g., owner, contractors and consultants (Stille and Palmström, 2003).

Despite the inclusion of various rock mass parameters, none of the mentioned systems consider every geological condition that has an influence on rock mass stability (Nilsen, 2016). Moreover, the parameters in classification systems are often challenging to quantify. Thus, the evaluation of rock mass quality and rock support can be more or less based on experience and practical judgement (Nilsen and Thidemann, 1993).

4.2 Q-system

The Q-system, also referred to as the Rock Mass Quality-system is based on a large database of tunnel projects. The classification system was presented by Barton et al. (1974) and developed in Norwegian Geotechnical Institute (NGI), and has been updated several times. The Q-value is defined by a combination of six parameters, presented in Equation 4.1 (NGI, 2022).

$$Q = \frac{RQD}{J_n} \times \frac{J_r}{J_a} \times \frac{J_w}{SRF} \tag{4.1}$$

where

RDQ = Rock Quality Designation,

J_n = Joint set number,

J_r = Joint roughness number,

J_a = Joint alteration number,

J_w = Joint water reduction factor, and

SRF = Stress reduction factor

Each fraction in Equation 4.1 describes three main stability factors regarding the underground openings. RQD/J_n is an expression for the degree of jointing, J_r/J_a defines joint friction and J_w/SRF describes active stress. The description for the quantification of Q-parameters is presented in Figure 4.1.

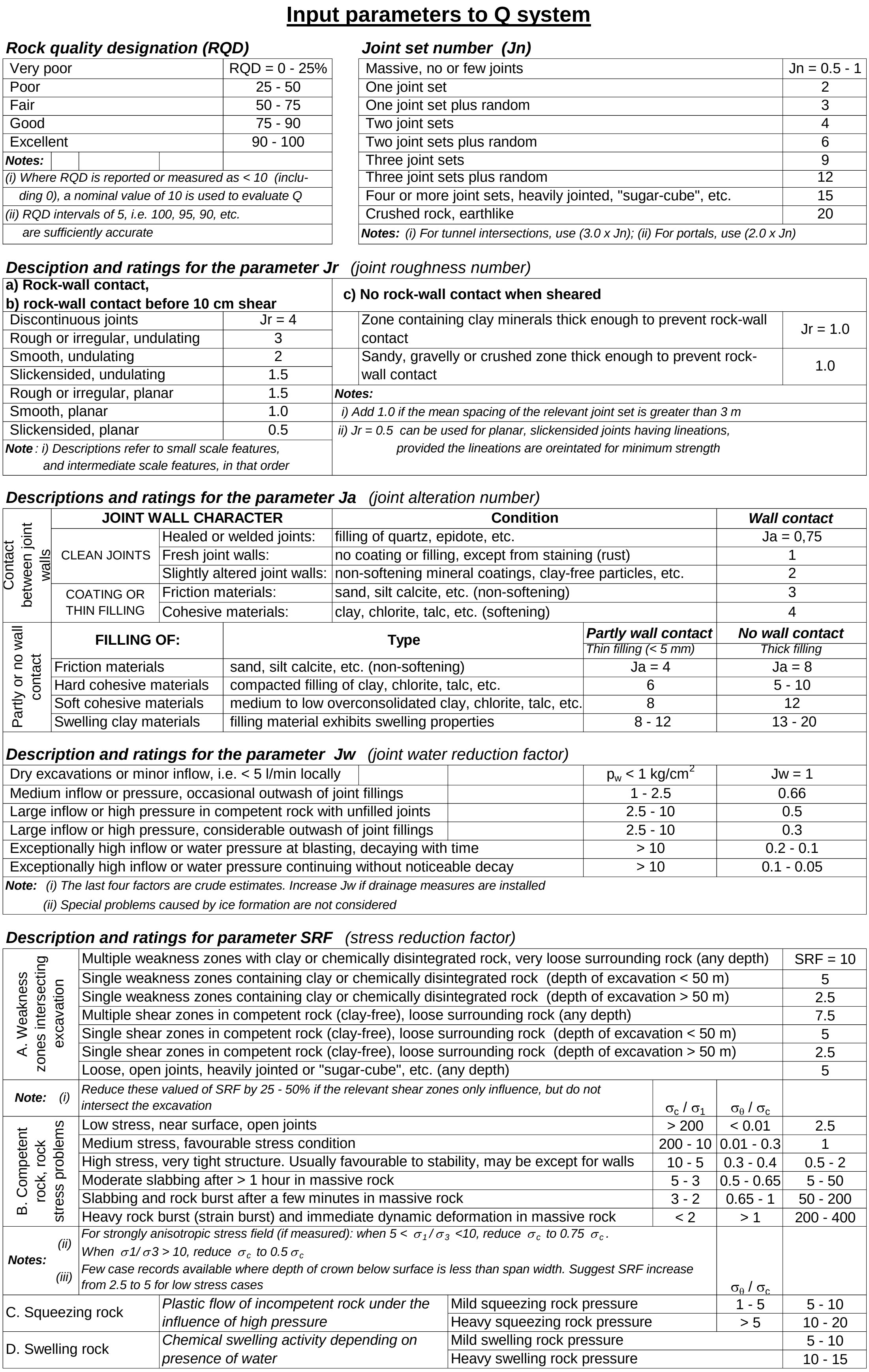

Input parameters to Q system

Rock quality designation (RQD)

Very poor	RQD = 0 - 25%
Poor	25 - 50
Fair	50 - 75
Good	75 - 90
Excellent	90 - 100

Notes:
(i) Where RQD is reported or measured as < 10 (including 0), a nominal value of 10 is used to evaluate Q
(ii) RQD intervals of 5, i.e. 100, 95, 90, etc. are sufficiently accurate

Joint set number (Jn)

Massive, no or few joints	Jn = 0.5 - 1
One joint set	2
One joint set plus random	3
Two joint sets	4
Two joint sets plus random	6
Three joint sets	9
Three joint sets plus random	12
Four or more joint sets, heavily jointed, "sugar-cube", etc.	15
Crushed rock, earthlike	20

Notes: *(i) For tunnel intersections, use (3.0 x Jn); (ii) For portals, use (2.0 x Jn)*

Desciption and ratings for the parameter Jr *(joint roughness number)*

a) Rock-wall contact, b) rock-wall contact before 10 cm shear		**c) No rock-wall contact when sheared**	
Discontinuous joints	Jr = 4	Zone containing clay minerals thick enough to prevent rock-wall contact	Jr = 1.0
Rough or irregular, undulating	3		
Smooth, undulating	2	Sandy, gravelly or crushed zone thick enough to prevent rock-wall contact	1.0
Slickensided, undulating	1.5		
Rough or irregular, planar	1.5	***Notes:***	
Smooth, planar	1.0	*i) Add 1.0 if the mean spacing of the relevant joint set is greater than 3 m*	
Slickensided, planar	0.5	*ii) Jr = 0.5 can be used for planar, slickensided joints having lineations, provided the lineations are oreintated for minimum strength*	

Note *: i) Descriptions refer to small scale features, and intermediate scale features, in that order*

Descriptions and ratings for the parameter Ja *(joint alteration number)*

	JOINT WALL CHARACTER		Condition	***Wall contact***
Contact between joint walls	CLEAN JOINTS	Healed or welded joints:	filling of quartz, epidote, etc.	Ja = 0,75
		Fresh joint walls:	no coating or filling, except from staining (rust)	1
		Slightly altered joint walls:	non-softening mineral coatings, clay-free particles, etc.	2
	COATING OR THIN FILLING	Friction materials:	sand, silt calcite, etc. (non-softening)	3
		Cohesive materials:	clay, chlorite, talc, etc. (softening)	4

	FILLING OF:	Type	***Partly wall contact*** *Thin filling (< 5 mm)*	***No wall contact*** *Thick filling*
Partly or no wall contact	Friction materials	sand, silt calcite, etc. (non-softening)	Ja = 4	Ja = 8
	Hard cohesive materials	compacted filling of clay, chlorite, talc, etc.	6	5 - 10
	Soft cohesive materials	medium to low overconsolidated clay, chlorite, talc, etc.	8	12
	Swelling clay materials	filling material exhibits swelling properties	8 - 12	13 - 20

Description and ratings for the parameter Jw *(joint water reduction factor)*

Dry excavations or minor inflow, i.e. < 5 l/min locally	p_w < 1 kg/cm^2	Jw = 1
Medium inflow or pressure, occasional outwash of joint fillings	1 - 2.5	0.66
Large inflow or high pressure in competent rock with unfilled joints	2.5 - 10	0.5
Large inflow or high pressure, considerable outwash of joint fillings	2.5 - 10	0.3
Exceptionally high inflow or water pressure at blasting, decaying with time	> 10	0.2 - 0.1
Exceptionally high inflow or water pressure continuing without noticeable decay	> 10	0.1 - 0.05

Note: *(i) The last four factors are crude estimates. Increase Jw if drainage measures are installed*
(ii) Special problems caused by ice formation are not considered

Description and ratings for parameter SRF *(stress reduction factor)*

A. Weakness zones intersecting excavation	Multiple weakness zones with clay or chemically disintegrated rock, very loose surrounding rock (any depth)			SRF = 10
	Single weakness zones containing clay or chemically disintegrated rock (depth of excavation < 50 m)			5
	Single weakness zones containing clay or chemically disintegrated rock (depth of excavation > 50 m)			2.5
	Multiple shear zones in competent rock (clay-free), loose surrounding rock (any depth)			7.5
	Single shear zones in competent rock (clay-free), loose surrounding rock (depth of excavation < 50 m)			5
	Single shear zones in competent rock (clay-free), loose surrounding rock (depth of excavation > 50 m)			2.5
	Loose, open joints, heavily jointed or "sugar-cube", etc. (any depth)			5
Note: *(i)*	*Reduce these valued of SRF by 25 - 50% if the relevant shear zones only influence, but do not intersect the excavation*	σ_c / σ_1	σ_θ / σ_c	
B. Competent rock, rock stress problems	Low stress, near surface, open joints	> 200	< 0.01	2.5
	Medium stress, favourable stress condition	200 - 10	0.01 - 0.3	1
	High stress, very tight structure. Usually favourable to stability, may be except for walls	10 - 5	0.3 - 0.4	0.5 - 2
	Moderate slabbing after > 1 hour in massive rock	5 - 3	0.5 - 0.65	5 - 50
	Slabbing and rock burst after a few minutes in massive rock	3 - 2	0.65 - 1	50 - 200
	Heavy rock burst (strain burst) and immediate dynamic deformation in massive rock	< 2	> 1	200 - 400
Notes: *(ii)* *(iii)*	*For strongly anisotropic stress field (if measured): when 5 < σ_1/σ_3 <10, reduce σ_c to 0.75 σ_c. When $\sigma 1/\sigma 3$ > 10, reduce σ_c to 0.5 σ_c* *Few case records available where depth of crown below surface is less than span width. Suggest SRF increase from 2.5 to 5 for low stress cases*		σ_θ / σ_c	
C. Squeezing rock	*Plastic flow of incompetent rock under the influence of high pressure*	Mild squeezing rock pressure	1 - 5	5 - 10
		Heavy squeezing rock pressure	> 5	10 - 20
D. Swelling rock	*Chemical swelling activity depending on presence of water*	Mild swelling rock pressure		5 - 10
		Heavy swelling rock pressure		10 - 15

Figure 4.1: *Description of Q-parameters as provided in (NGI, 2022).*

The Q-system divides rock mass into nine different categories, as shown in Figure 4.2. When rock mass quality is assessed, the Q-system is further applicable to estimate rock support provided that the span or height of the excavation and the stability requirements to use the underground opening (excavation support ratio, ESR) are known.

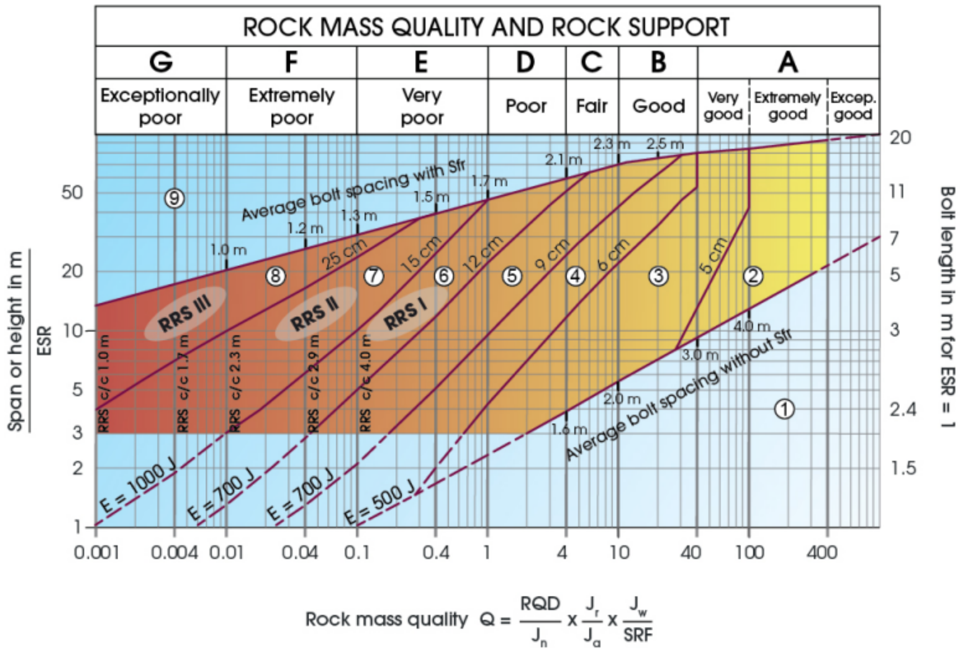

Figure 4.2: Rock mass quality and rock support chart from Q-system. From: NGI (2022).

Palmström and Broch (2006) presented some limitations with Q-system, as its applicability is best suited when Q-values are between 0.1 and 40 for tunnels with a span between 2.5 m and 30 m. Although there are parameters for overstressing, it is suggested that Q-system should be applied with care in rock bursting conditions and squeezing ground. Similarly, the use of the Q-system should be evaluated thoroughly considering weakness zones, where swelling ground occurs.

4.3 RMR

Bieniawski (1976) developed and published details regarding a rock mass classification called the Geomechanics Classification, now widely known as the Rock Mass Rating system (RMR). Similar to the Q-system, this system has been successively refined over many years. The RMR-system utilises the following six rock mass parameters (Bieniawski, 1989):

1. Uniaxial compressive strength of intact rock material ($A1$)
2. Rock quality designation, RQD ($A2$)
3. Spacing of discontinuities ($A3$)
4. Condition of discontinuities ($A4$)
5. Groundwater conditions ($A5$), and
6. Orientation of discontinuities (B)

The users of RMR-system, utilise the following Figure 4.3 to determine the parameter ratings.

A. CLASSIFICATION PARAMETERS AND THEIR RATINGS

PARAMETER			**Range of values // ratings**						
1	Strength of intact rock material	Point-load strength index	> 10 MPa	4 - 10 MPa	2 - 4 MPa	1 - 2 MPa	For this low range uniaxial compr. strength is preferred		
		Uniaxial compressive strength	> 250 MPa	100 - 250 MPa	50 - 100 MPa	25 - 50 MPa	5 - 25 MPa	1 - 5 MPa	< 1 MPa
	RATING		**15**	**12**	**7**	**4**	**2**	**1**	**0**
2	Drill core quality RQD		90 - 100%	75 - 90%	50 - 75%	25 - 50%	< 25%		
	RATING		**20**	**17**	**13**	**8**	**5**		
3	Spacing of discontinuities		> 2 m	0.6 - 2 m	200 - 600 mm	60 - 200 mm	< 60 mm		
	RATING		**20**	**15**	**10**	**8**	**5**		
4	Condition of discontinuities	Length, persistence	< 1 m	1 - 3 m	3 - 10 m	10 - 20 m	> 20 m		
		Rating	**6**	**4**	**2**	**1**	**0**		
		Separation	none	< 0.1 mm	0.1 - 1 mm	1 - 5 mm	> 5 mm		
		Rating	**6**	**5**	**4**	**1**	**0**		
		Roughness	very rough	rough	slightly rough	smooth	slickensided		
		Rating	**6**	**5**	**3**	**1**	**0**		
		Infilling (gouge)	none	Hard filling		Soft filling			
			-	< 5 mm	> 5 mm	< 5 mm	> 5 mm		
		Rating	**6**	**4**	**2**	**2**	**0**		
		Weathering	unweathered	slightly w.	moderately w.	highly w.	decomposed		
		Rating	**6**	**5**	**3**	**1**	**0**		
5	Ground water	Inflow per 10 m tunnel length	none	< 10 litres/min	10 - 25 litres/min	25 - 125 litres/min	> 125 litres /min		
		$p_w / \sigma 1$	0	0 - 0.1	0.1 - 0.2	0.2 - 0.5	> 0.5		
		General conditions	completely dry	damp	wet	dripping	flowing		
	RATING		**15**	**10**	**7**	**4**	**0**		

p_w = joint water pressure; $\sigma 1$ = major principal stress

B. RATING ADJUSTMENT FOR DISCONTINUITY ORIENTATIONS

		Very favourable	Favourable	Fair	Unfavourable	Very unfavourable
RATINGS	Tunnels	**0**	**-2**	**-5**	**-10**	**-12**
	Foundations	**0**	**-2**	**-7**	**-15**	**-25**
	Slopes	**0**	**-5**	**-25**	**-50**	**-60**

C. ROCK MASS CLASSES DETERMINED FROM TOTAL RATINGS

Rating	100 - 81	80 - 61	60 - 41	40 - 21	< 20
Class No.	I	II	III	IV	V
Description	VERY GOOD	GOOD	FAIR	POOR	VERY POOR

D. MEANING OF ROCK MASS CLASSES

Class No.	I	II	III	IV	V
Average stand-up time	10 years for 15 m span	6 months for 8 m span	1 week for 5 m span	10 hours for 2.5 m span	30 minutes for 1 m span
Cohesion of the rock mass	> 400 kPa	300 - 400 kPa	200 - 300 kPa	100 - 200 kPa	< 100 kPa
Friction angle of the rock mass	< 45°	35 - 45°	25 - 35°	15 - 25°	< 15°

Figure 4.3: *Description of RMR-parameters. From: Bieniawski (1989).*

The ratings in Figure 4.3 are summed to obtain a RMR-value. Thus, the value of RMR is expressed as given in Equation 4.2.

$$RMR = A1 + A2 + A3 + A4 + A5 + B \tag{4.2}$$

The RMR-system allocates rock mass into five different classes as shown in Figure 4.4. Based on the rock mass class, the excavation method and rock support are estimated. Figure 4.4 presents excavation and support for a horseshoe-shaped tunnel with a span of $10m$.

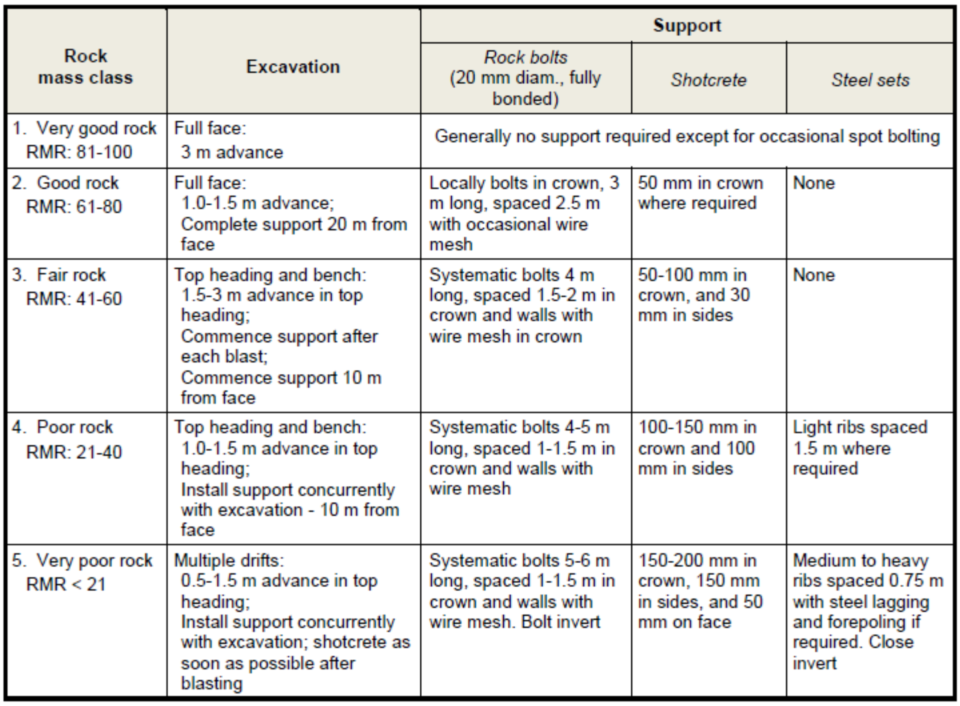

Rock mass class	Excavation	Support		
		Rock bolts (20 mm diam., fully bonded)	*Shotcrete*	*Steel sets*
1. Very good rock RMR: 81-100	Full face: 3 m advance	Generally no support required except for occasional spot bolting		
2. Good rock RMR: 61-80	Full face: 1.0-1.5 m advance; Complete support 20 m from face	Locally bolts in crown, 3 m long, spaced 2.5 m with occasional wire mesh	50 mm in crown where required	None
3. Fair rock RMR: 41-60	Top heading and bench: 1.5-3 m advance in top heading; Commence support after each blast; Commence support 10 m from face	Systematic bolts 4 m long, spaced 1.5-2 m in crown and walls with wire mesh in crown	50-100 mm in crown, and 30 mm in sides	None
4. Poor rock RMR: 21-40	Top heading and bench: 1.0-1.5 m advance in top heading; Install support concurrently with excavation - 10 m from face	Systematic bolts 4-5 m long, spaced 1-1.5 m in crown and walls with wire mesh	100-150 mm in crown and 100 mm in sides	Light ribs spaced 1.5 m where required
5. Very poor rock RMR < 21	Multiple drifts: 0.5-1.5 m advance in top heading; Install support concurrently with excavation; shotcrete as soon as possible after blasting	Systematic bolts 5-6 m long, spaced 1-1.5 m in crown and walls with wire mesh. Bolt invert	150-200 mm in crown, 150 mm in sides, and 50 mm on face	Medium to heavy ribs spaced 0.75 m with steel lagging and forepoling if required. Close invert

Figure 4.4: *Rock mass class and recommended excavation and rock support from RMR-system. The suggestions are best suited for horseshoe-shaped tunnel with a width of 10* m. *From: Bieniawski (1989).*

Although stresses up to 25 MPa are included in the estimation of RMR values, the classification system does not include parameters that describe rock stresses. Therefore, rock bursting and squeezing due to overstressing are not included in the RMR-system. Furthermore, the inclusion of faults and weakness zones is ambiguous. Such limitations should be evaluated before utilising the Rock Mass Rating system (Palmström, 2009).

4.4 GSI

The Geological Strength Index (GSI) was first introduced by Hoek (1994) as a complement to the Generalized Hoek-Brown failure criterion. In addition, to evaluate the failure of an intact rock, the inclusion of the GSI value extended the use of the criterion to evaluate rock mass failure as well. GSI has been subsequently modified and expanded throughout the years as experiences were gained on its application to rock engineering. The GSI classification system is incorporated in the material parameters m_b, s and a, formerly introduced in Section 3.5.1. The user of the classification system generally utilises a GSI chart, illustrated in Figure 4.5. There are also quantified versions of GSI charts, e.g., the version produced by Cai et al. (2007), which consists of joint spacings.

The key aspect of the GSI classification system is that rock masses are influenced by the discontinuities of the rock mass and the joint surface conditions. These two influencing factors are evaluated by applying a GSI chart. The ratings in GSI-system vary between 0 to 100 as shown in Figure 4.5. Poor rock mass conditions have low GSI values, while high GSI-values indicate good rock mass conditions (Hoek, 2007).

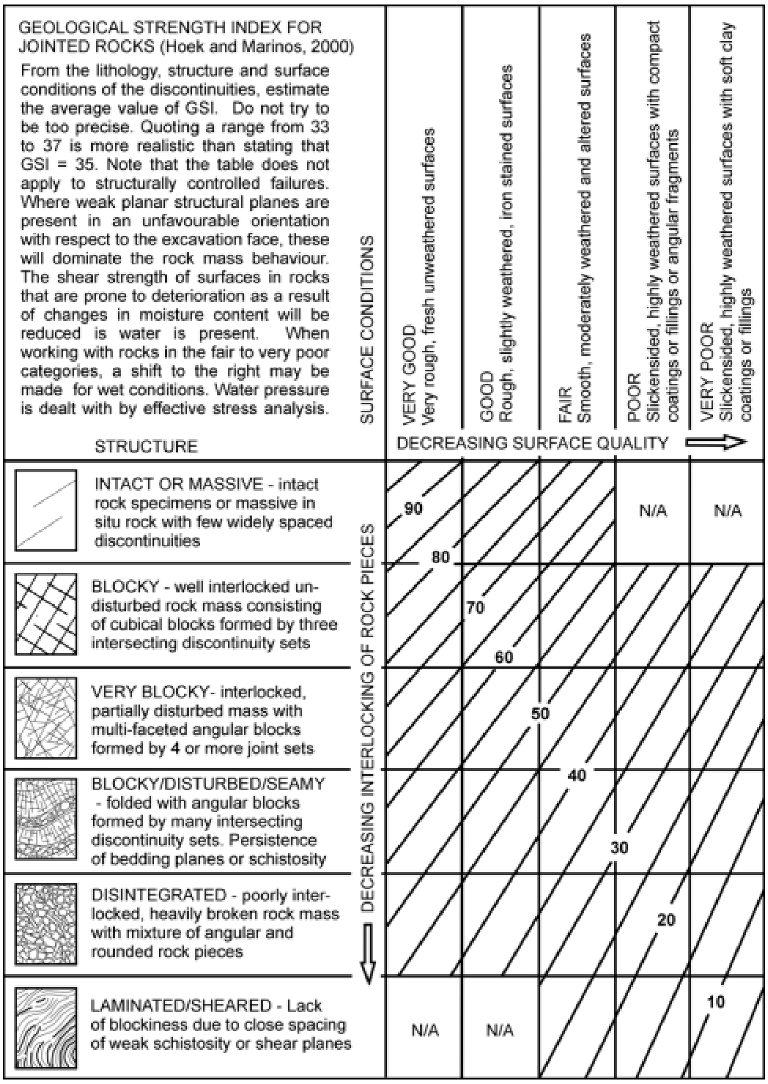

GEOLOGICAL STRENGTH INDEX FOR JOINTED ROCKS (Hoek and Marinos, 2000)

From the lithology, structure and surface conditions of the discontinuities, estimate the average value of GSI. Do not try to be too precise. Quoting a range from 33 to 37 is more realistic than stating that GSI = 35. Note that the table does not apply to structurally controlled failures. Where weak planar structural planes are present in an unfavourable orientation with respect to the excavation face, these will dominate the rock mass behaviour. The shear strength of surfaces in rocks that are prone to deterioration as a result of changes in moisture content will be reduced is water is present. When working with rocks in the fair to very poor categories, a shift to the right may be made for wet conditions. Water pressure is dealt with by effective stress analysis.

INTACT OR MASSIVE - intact rock specimens or massive in situ rock with few widely spaced discontinuities

BLOCKY - well interlocked un-disturbed rock mass consisting of cubical blocks formed by three intersecting discontinuity sets

VERY BLOCKY- interlocked, partially disturbed mass with multi-faceted angular blocks formed by 4 or more joint sets

BLOCKY/DISTURBED/SEAMY - folded with angular blocks formed by many intersecting discontinuity sets. Persistence of bedding planes or schistosity

DISINTEGRATED - poorly inter-locked, heavily broken rock mass with mixture of angular and rounded rock pieces

LAMINATED/SHEARED - Lack of blockiness due to close spacing of weak schistosity or shear planes

__Figure 4.5:__ Basic GSI chart for blocky rock masses. From: Hoek (2007).

In comparison with the Q-system and RMR-system, the GSI-system does not consist of recommendations regarding rock support based on the rock mass quality. The GSI classification system is mainly used to describe rock masses. Nilsen (2016) suggested that the values of GSI can be divided into various rock mass classes, as shown in Table 4.1.

__Table 4.1:__ GSI classes suggested by Nilsen (2016).

GSI - rock mass classes				
Very good	Good	Medium	Poor	Very poor
>75	56-75	36-55	21-35	≤ 20

According to Marinos et al. (2005), the GSI-system is not recommended for rock masses with a clear and defined dominant structural orientation. For example, an undisturbed slate with a highly anisotropic behaviour should not be assigned GSI values from charts. Another inappropriate application of GSI is on strong hard rocks with few discontinuities spaced at large distances, e.g., distances similar to the span of an underground opening.

4.5 Interlink between classification systems

Various authors have suggested proposals for conversions between different classification systems. Interlinks between classifications provide the opportunity to evaluate rock mass through different systems. The frequently applied conversions between GSI, RMR, and Q are presented in Equations 4.3, 4.5 and 4.7.

According to Hoek et al. (1995), the 1989 RMR classification by Bieniawski can be correlated to GSI by applying Equation 4.3. This conversion is only applicable under dry conditions regarding water inflow, favourable orientations of discontinuities, and RMR > 23.

$$GSI = RMR_{89} - 5 \tag{4.3}$$

Hoek et al. (1995) also presented a modified version of the Q-system, referred to as the modified Tunneling Quality Index (Q'). Q' is defined by Rock Quality Designation (RQD), joint set number (J_n), joint roughness number (J_r) and joint alteration number (J_a), as presented Equation 4.4. The modified Q-system assumes dry rock mass conditions and medium stress conditions. The value of Q' can be used to estimate the value of GSI, as expressed in Equation 4.5.

$$Q' = \frac{RQD}{J_n} \times \frac{J_r}{J_a} \tag{4.4}$$

$$GSI = 9 \times Log_e Q' + 44 \tag{4.5}$$

Relationships between RMR and Q have been published by both Bieniawski (1989) and Barton (1995) as presented in Equations 4.6 and 4.7, respectively.

$$RMR \approx 9 \times Log_e Q + 44 \tag{4.6}$$

$$RMR = 15 \times log Q + 50 \tag{4.7}$$

Correlations between GSI and the adjusted RMR and Q values are necessary when the estimations of GSI values are needed, given that they cannot be determined directly. For example, GSI values are required as input for the Generalized Hoek-Brown criterion. However, as discussed by Marinos et al. (2005), these correlations are not recommended for weak rock masses (e.g. GSI < 35).

5 Rock stresses

5.1 In-situ stresses

The stresses in a rock mass exist as a result of the overburden weight and due to the events from its geological history. The stress condition that exists in the rock mass prior to any construction disturbance is called the in-situ stress state. Knowledge of the in-situ stress condition in a rock mass is important when dealing with stability challenges related to rocks in civil and mining engineering. In general, stress magnitudes increase with depth. Consequently, stress-related stability issues due to high stresses also increase with increased depth. For shallow seated underground openings, stability issues can occur due to insufficient horizontal and vertical stresses or because of high stress anisotropy caused by high horizontal stresses (Amadei and Stephansson, 1997).

In civil and mining engineering, in-situ stresses influence the distribution and magnitude of the stresses around the underground excavations, e.g, caverns, tunnels or shafts (Hoek, 2007). These secondary stresses are referred to as induced stresses and are created by artificial disturbances such as underground excavations and drillings. As discussed by Amadei and Stephansson (1997) rock stresses can be divided into in-situ (virgin/primary) stresses and induced stresses, where in-situ stresses consist of various stress classifications. The authors proposed that the virgin stress state is composed of gravitational stresses, tectonic stresses, residual stresses, and terrestrial stresses, as illustrated in Figure 5.1.

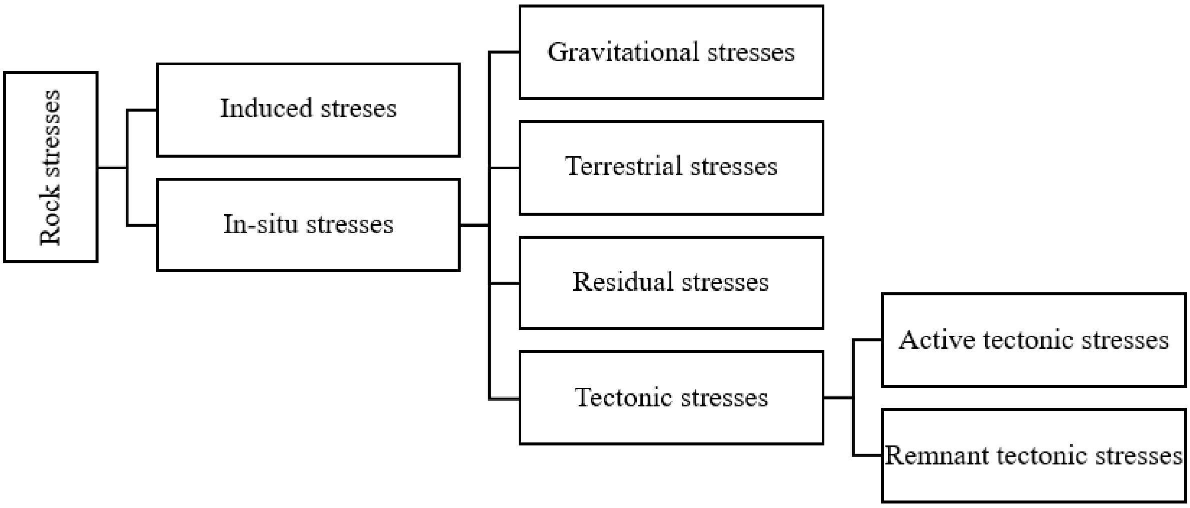

Figure 5.1: *Proposed stress terminology. Modified after: Amadei and Stephansson (1997).*

Gravitational stresses exist due to rock mass overburden, where flat ground and topography have various effects on the stress state. Terrestrial stresses are related to, for example, seasonal temperature variations and tidal stresses due to Moon's pull. Furthermore, tectonic stresses are a result of tectonic activities, while residual stresses are stress components that remain in the rock mass even after the external forces and moments are removed. Tectonic stresses can be divided into active and remnant tectonic stresses. Active tectonic stresses describe the present day straining of the Earth's crust, e.g., volcanic activity, slab pull and ridge push. While remnant tectonic stress is similar to residual stress, but includes tectonic activity, such as faulting, folding and jointing (Amadei and Stephansson, 1997).

An infinitesimal cube within a rock mass consists of three normal stress components (σ_{xx}, σ_{yy}, σ_{zz}) and three shear stress components (τ_{xy}, τ_{yz}, τ_{xz}), illustrated in Figure 5.2. In this case, τ_{xy}=τ_{yx}, $\tau_{yz} = \tau_{zy}$ and $\tau_{xz} = \tau_{zx}$.

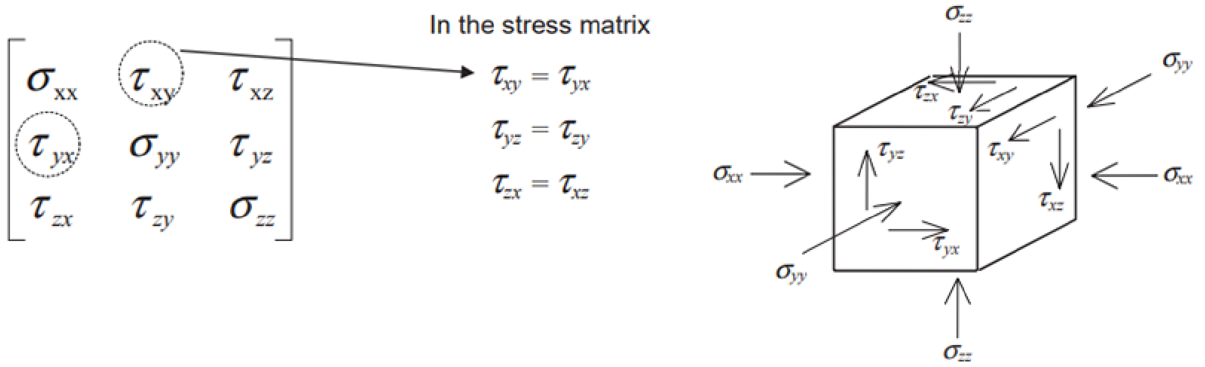

Figure 5.2: Normal and shear stress components on an infinitesimal cube in a rock mass. From: ISRM (2003).

The stress state at a certain point in a rock mass is often presented in terms of orientation and magnitude of the principal stresses. Principal stress planes occur when three mutually perpendicular planes have shear stress components with zero magnitudes. The normal stresses across these stress planes are defined as principal stresses. It is convenient to describe the stress condition using principal stresses as they provide direct information on the maximum and minimum values of the normal stresses. Moreover, it is always achievable to find an orientation of the cube where all the shear stresses disappear, resulting in only normal stresses acting. The conventional notation of the principal stresses is σ_1 (major stress), σ_2 (intermediate stress) and σ_3 (minor stress), as shown in Figure 5.3. However, often in-situ stresses are described as horizontal and vertical stresses. The notations applied are σ_H for major horizontal stress, σ_h for minor horizontal stress and σ_v for vertical stress.

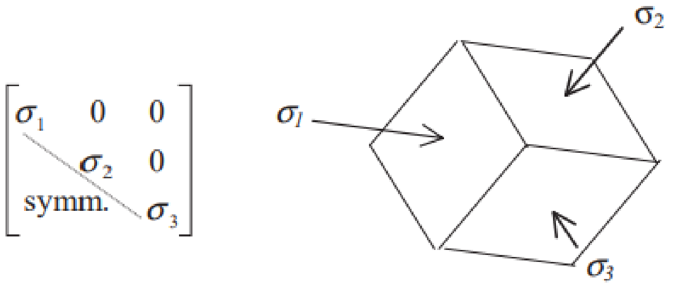

Figure 5.3: Principal stresses are normal stresses acting on planes with no shear stresses. From: ISRM (2003).

5.2 Estimation of in-situ stresses

In the early stages of engineering design, an attempt to estimate the in-situ stress field often takes place prior to the measuring of virgin stresses with various stress measurement methods. Such estimations are based on various factors that have an influence on the in-situ stress state. However, the process of predicting in-situ stresses should not be considered a replacement for stress measurements. To date, there are no methods available to make an exact prediction of virgin stresses in a rock mass. Therefore, ISRM (2012) published “Suggested methods for rock stress estimation” to develop a final rock stress model (FRSM) of a site or an area. According to ISRM (2012) prediction of in-situ stresses requires the best estimate stress model (BESM) before stress measurements, followed by integrated stress determination (ISD) and verification of measurement results in a 2D/3D numerical model. This is discussed more in Chapter 8 in relation to the thesis work. The following sections below will present factors influencing in-situ stresses that are relevant regarding the estimation and assessment of rock stresses in this study.

5.2.1 Gravitational stresses

When predicting an in-situ stress state, it is common practice to assume that three components can describe it: a vertical stress component (σ_v) and two horizontal stress components (σ_H and σ_h). The vertical component is generally a result of the weight of the overlying rock at a specific depth and is defined as:

$$\sigma_v = \rho g z \tag{5.1}$$

where ρ is the density of the rock mass, g is the gravity acceleration and z is the depth below ground. The horizontal stress components are assumed to be uniform ($\sigma_H = \sigma_h$) when only gravitational stresses influence the stress field. In general, σ_H represents maximum horizontal stress, while σ_h is minimum horizontal stress. The horizontal components due to gravitational loads depend on the Poisson’s ratio (v), as expressed in Equation 5.2.

$$\sigma_H = \sigma_h = \frac{v}{1-v}\sigma_v \tag{5.2}$$

5.2.2 Residual stresses

Residual stresses can be described as the stress state remaining in the rock mass, although the originating mechanism has come to an end. These stresses are often related to heterogeneous physical or chemical processes in a limited area of a rock mass volume. In rock engineering, they are often referred to as internal or locked-in stresses. Residual stresses can remain in the rock mass that has been subjected to higher stresses in the past compared to the present conditions. When those rocks relax as a result of load reduction, for instance, due to erosion, or temperature changes because of cooling, restraints are developed by the interlocking fabric of the rock. The rock then reaches a new equilibrium where internal tensile and compressive forces are balanced (Li, 2021).

5.2.3 Tectonic stresses

The interaction of tectonic plates with each other and with the Earth’s mantle results in tectonic stresses. The two main groups of forces that are known to be responsible for the tectonic stresses are broad-scale tectonic forces and local tectonic forces, as presented in Figure 5.4. Tectonic stresses behave as constant stresses in areas where the width and length are significantly thicker than the elastic part of the lithosphere (Zoback et al., 1989).

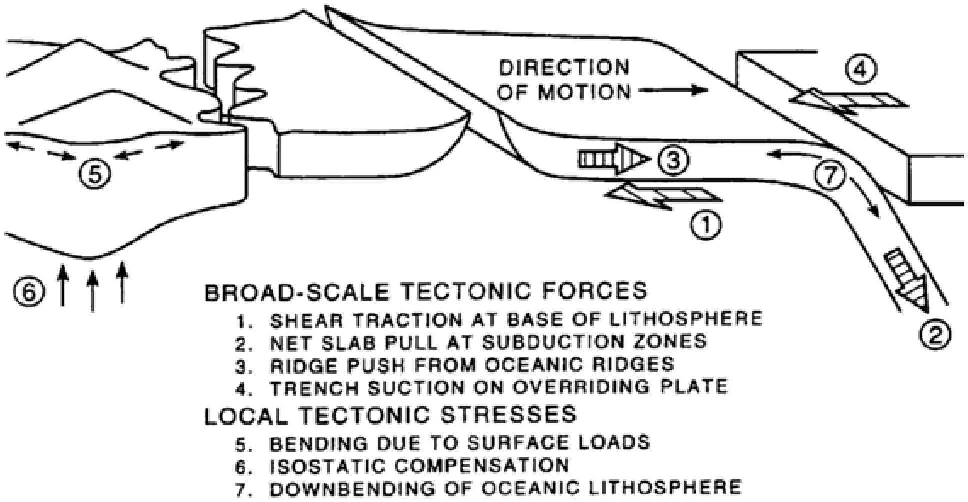

Figure 5.4: *Boundary forces responsible for the development of tectonic stresses. From: Zoback et al. (1989).*

In Scandinavia, tectonic stresses contribute to horizontal stresses with the driving forces principally from the Mid-Atlantic ridge. Compared to gravitational stresses, tectonic stresses at shallow depths represent a larger part of the total stress state. Thus, horizontal stresses influenced by tectonic stresses can have relatively higher magnitudes than vertical stress. Often the total horizontal stresses contributed by tectonic stresses are expressed with Equations 5.3 and 5.4, where $\sigma_{tec_{max}}$ is the maximum tectonic stress and $\sigma_{tec_{min}}$ is the minimum tectonic stress (Amadei and Stephansson, 1997).

$$\sigma_H = \frac{v}{1-v}\sigma_v + \sigma_{tec_{max}} \tag{5.3}$$

$$\sigma_h = \frac{v}{1-v}\sigma_v + \sigma_{tec_{min}} \tag{5.4}$$

5.2.4 Influence of topography

The topography can have a considerable effect on the magnitude and direction of in-situ stresses. When the ground surface is irregular, the assumptions on the principal stresses appearing vertical and horizontal with depth breaks down. For instance, Figure 5.5 illustrates the behaviour of rock stresses in a topography consisting of hills and valleys with no surface loads. Assuming traction-free boundary conditions in Figure 5.5, the principal stresses are either parallel or normal to the ground surface of the slope (Amadei and Stephansson, 1997).

The horizontal stresses in hilltops are often low due to destressing caused by the lack of confinement in the rock mass. Whereas, near the ground surface in a valley, high horizontal stresses are registered. As illustrated in Figure 5.5, the influence of the topography is considerable near the ground surface. With increasing depth, the principal stresses reach the same directions as when the ground surface is horizontal with no topography effects from the surroundings (Li, 2021).

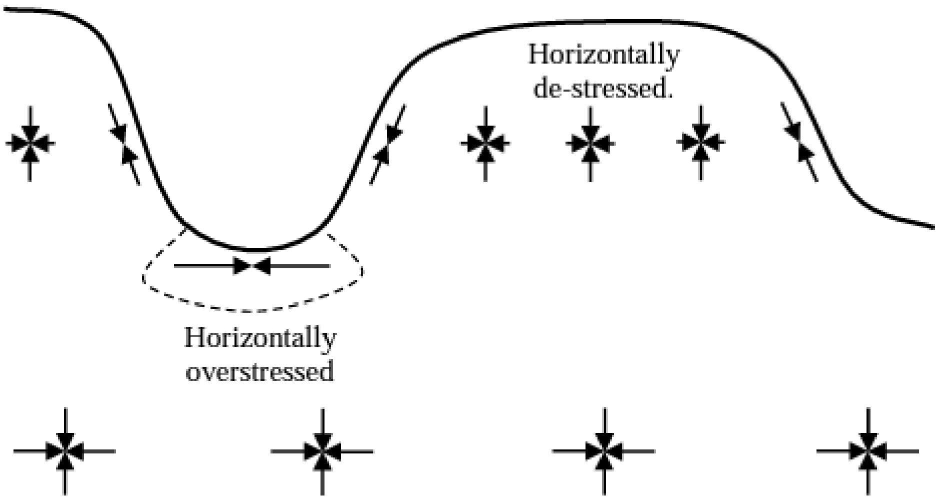

Figure 5.5: *Rock stress orientations and relative magnitudes in an irregular topography. From: Li (2021).*

5.2.5 Effect of weathering and geological structures

Weathered rock mass will have a decreased strength and stiffness, which reduces its capability to hold the same magnitude of rock stresses as an unaltered rock mass. The in-situ stresses will most likely be redistributed from the ground surface and downwards until they reach unweathered rock mass (Nilsen and Thidemann, 1993). Weathering often occurs at shallow depths, and therefore the stress state near ground surfaces can be destressed or close to being destressed.

In general, rock masses are inhomogeneous, and the existence of geological structures and heterogeneities will have an influence on the magnitude and distribution of in-situ stresses. Geological structures can make the local stress state vary from the regional stress field, and often contribute to the scatter observed in stress measurements (Fairhurst, 1986). When a stress field is approaching a major discontinuity, the behaviour of the stress distribution is dependent on the material property of the discontinuity. Figure 5.6a illustrates an open discontinuity, where stresses cannot transect it, and the major principal stress is diverted parallel to the structure. If the material in discontinuity has similar material properties as the surrounding rock mass, the principal stresses are unaffected, as shown in Figure 5.6b. Figure 5.6c depicts a situation where the material in the discontinuity is more rigid than the surrounding rock mass, resulting in major principal stress diverting perpendicular to the discontinuity surface (ISRM, 2012).

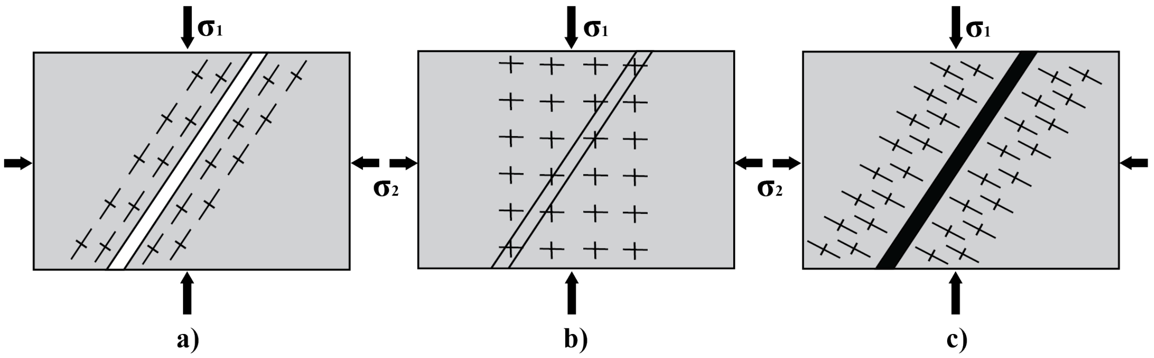

Figure 5.6: *Stress distribution relative to the material property of discontinuity. Only 2D principal stresses close to the discontinuity are shown in the figures. a) Open discontinuity, b) Discontinuity with similar material properties as surrounding rock, and c) Discontinuity with rigid material than surrounding rock. Based on: ISRM (2012).*

Geological structures, such as faults, dikes, veins and dikes etc., have been used by structural geologists as indicators of paleo-stresses. Paleo-stresses are stresses prevailing at the time of the genesis of the geological structure. The stresses created during the geological activity may be modified due to later tectonic events, uplift, glaciation and erosion. Hence, orientations of the principal stresses can be different in the current stress field than during the development of the geological structure (ISRM, 2012). Li (2006) suggested that unloading in the direction of compression in the post-failure stage may change the order of principal stresses, σ_1 and σ_2 in the present stress field, as depicted in Figure 5.7. Therefore, in order to estimate stress orientations, knowledge surrounding recent and local geological structures is important.

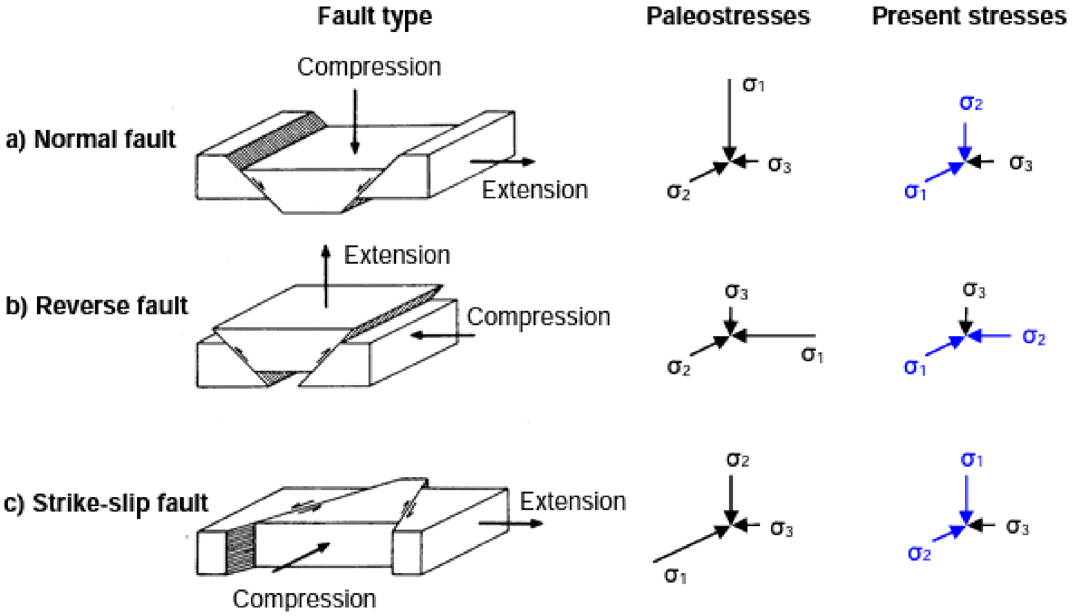

Figure 5.7: *Estimation of stress orientations based on fault type. From: Anderson (1951) and modified by Li (2021).*

5.2.6 Effect of anisotropy

Rocks of sedimentary and metamorphic origin are generally anisotropic, meaning their properties change in different directions. There are usually three main types of isotropies considered in rock mechanics: complete isotropy, transverse isotropy and orthotropy (Figure 5.8).

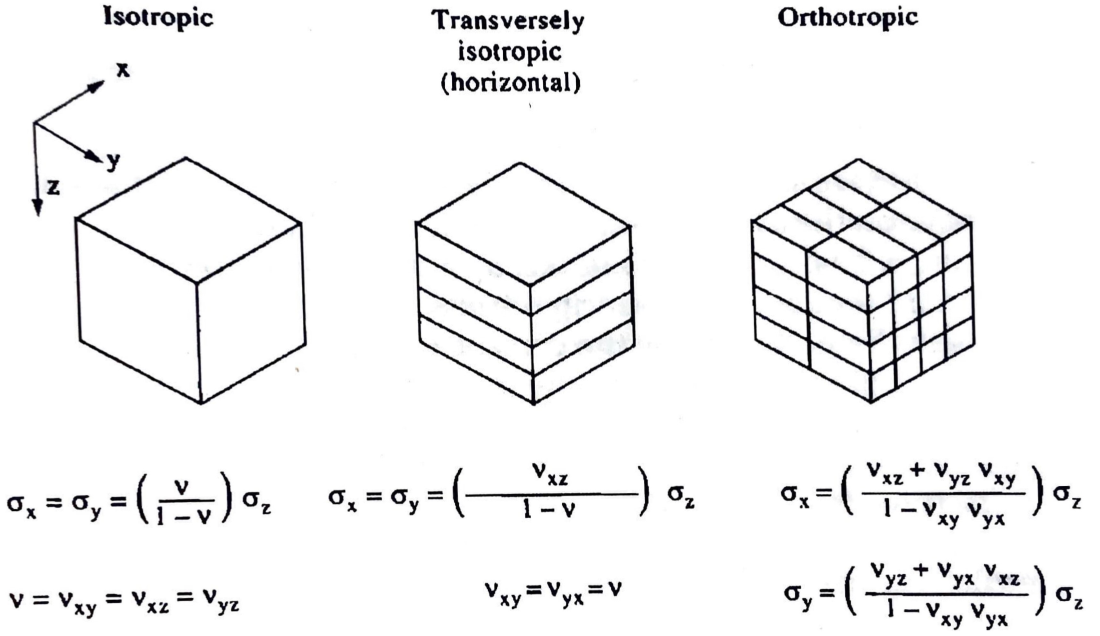

Figure 5.8: *Correlation between vertical and elastically induced horizontal stresses for various types of isotropies. From: Hudson and Harrison (1997).*

Complete isotropic rock mass under gravitational loading has the same properties in all directions. Furthermore, the horizontal stresses are uniform gravitational stresses. A transversely isotropic rock mass has different properties in two directions, e.g., vertical and horizontal directions. The horizontal stresses in transverse isotropic material are equal given that Poisson's ratio in the vertical direction (ν_{xz}) is applied. In an orthotropic case, rock mass consists of different properties in three perpendicular directions. When an orthotropic rock mass is subjected to gravitational loading, it induces different horizontal stresses. Unlike isotropic conditions, in some ranges of anisotropic rock mass, the horizontal stresses are higher than the vertical stresses. Moreover, in the orthotropic case, it is also possible for one horizontal stress component to be higher than the other. The frequent inconsistency in estimating in-situ stresses lies in the oversimplification of a rock mass as a complete isotropic material (Hudson and Harrison, 1997).

5.2.7 Effect of erosion and glaciation

Earth's crust has been subjected to loading due to inland ice, layers of sediments and sedimentary rocks, which are several kilometres thick. Erosion and glaciation effects are mechanisms considered to be responsible for high horizontal stresses at shallow depths (Amadei and Stephansson, 1997). Goodman (1989) summarised the effect of erosion by presenting Equation 5.5. K_0 is the initial horizontal to vertical stress ratio at a certain point located at a depth, z_0. The rock mass is subjected to unloading when a thickness (Δz) of a layer is removed. Based on the theory of elasticity, the new stress ratio (K) between horizontal and vertical stresses at a depth $z = z - \Delta z$ provides the equation below.

$$K = K_0 + \left[K_0 - \frac{\nu}{1-\nu} \right] \times \frac{\Delta z}{z_0 - \Delta z} \tag{5.5}$$

Equation 5.5 does not apply to melting of the ice in land since the ice and the bedrock have various densities. However, it has been suggested that high in-situ stresses can also result from glacier loading, isostatic movements and post-glacial uplift. Scandinavia and Canada are examples of bedrocks subjected to such glacial effects. As a result of the melting of the ice and gradual rebound, locked-in stresses remain due to incomplete isostatic recovery (Amadei and Stephansson, 1997). In Scandinavia, the stress field often involves high horizontal stresses relative to the vertical stress in the uppermost few hundred metres of bedrock (ISRM, 2012). This gives relatively high values of the ratio between the horizontal and vertical stress components, i.e. high K-values.

5.2.8 Variation of in-situ stresses with depth

The magnitudes of horizontal and vertical in-situ stresses vary with depth at different sites and parts of the world. Various authors have proposed relations to describe such variations. The majority of the data available involve depths of less than 3000 m. Stress data are collected from various measurements conducted in different regions of the world (Amadei and Stephansson, 1997). The ratio between horizontal and vertical stresses against depth is frequently used to express the variation of in-situ stresses. Figure 5.9 shows an example of the mentioned stress relation, proposed by Brown and Hoek (1978).

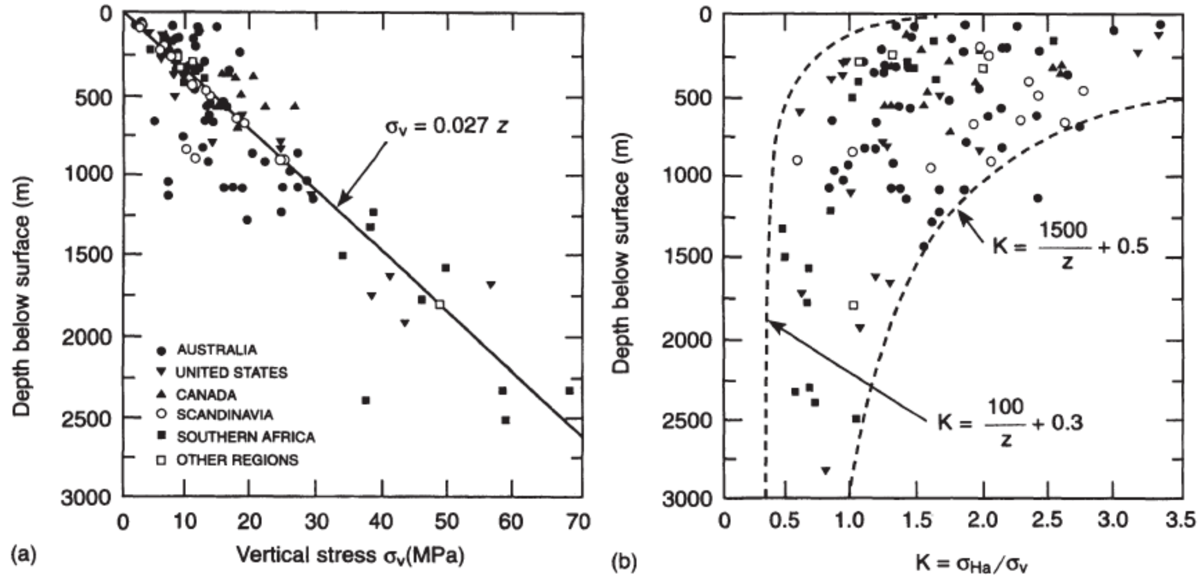

Figure 5.9: *a) Plot of measured vertical stress against depth below surface, z. b) Variation of measured average horizontal to vertical stress ration with depth below surface, z. From: Brown and Hoek (1978).*

Commonly used notations for horizontal to vertical stress ratios are, K_H and K_h. The Equations 5.6 and 5.7 define the K-values based on the continuous and linear elastic model.

$$K_H = \frac{\sigma_H}{\sigma_v} \tag{5.6}$$

$$K_h = \frac{\sigma_h}{\sigma_v} \tag{5.7}$$

Vertical stress is often estimated from the simple relationship of the vertical gravitational stress, as indicated in Equation 5.1. The specific unit weight ($\gamma = \rho g$) of intact rocks varies between 0.025 and 0.032 MN/m^3. Thus, the vertical gravitational stress increases linearly with depth below the surface, z (Martin et al., 2003). Unlike vertical stress, horizontal stresses in Scandinavia are influenced by other factors as well as gravitational loading. According to Hudson and Harrison (1997) and Amadei and Stephansson (1997), high horizontal stresses are caused by tectonics, rock anisotropy, local effects by discontinuities, erosion and gradual post-glacial rebound. Therefore, in regions with stated stress conditions, horizontal stresses may not have a linear relationship with a depth ranging from the ground surface to e.g., 3000 m.

On the other hand, the in-situ stress state at a shallow depth is often complex and relatively less measured and reported. Thus, the variation of horizontal stresses with the vertical stress component can differ near the ground surfaces. Challenges also arise, when measured stress data are often widely spread at shallow depths (Martin et al., 2003).

5.3 Stress measurements

ISRM (2012) recommends rock stress measurements after the best estimation of in-situ stresses is established. Data and knowledge gained from the best estimated stress model (BESM) can be utilised in selecting the most suitable method for in-situ stress measurements. As pointed out by Hudson and Harrison (1997), there are two main stress measurement methods: direct stress measurement and indirect stress measurement. There are also a few measurement methods that dominate the others as they have been practiced for several years, and have been both developed and improved with the purpose of determining 2D or 3D stress states. This Sub-chapter will concentrate on direct and dominating stress measurement methods. In addition, it will also present a brief theory on the analysis of Doorstopper measurements.

5.3.1 Direct stress measurement methods

Hydraulic fracturing

As discussed by Ljunggren et al. (2003), hydraulic fracturing (HF) is a stress measurement method that determines the stress field by applying hydraulic pressures to stimulate the rock mass surrounding a borehole. Normally, a section less than a metre in a borehole is sealed off with a straddle packer. The sealed section is then gradually pressurised with a fluid, often water. The pressure from the fluid generates tensile stresses at the borehole sidewall. Pressurisation continues until a hydraulic fracture is initiated through tensile failure.

The fracture plane is usually parallel to the borehole axis, where two fractures occur in opposite positions on the borehole periphery. The orientation of minimum principal stress is perpendicular to the fracture plane. Furthermore, the direction of initiated fractures corresponds with the orientation of the maximum horizontal stress, provided that one principal stress is parallel to the vertical or sub-vertical borehole. The fracture orientation can be determined either by an impression packer and a compass or by utilising a borehole televiewer. Figure 5.10 presents a schematic layout of hydraulic fracturing.

Conventional hydraulic fracturing is a 2D stress measurement method. Therefore, in a vertical borehole, minimum and maximum horizontal stresses can be determined.

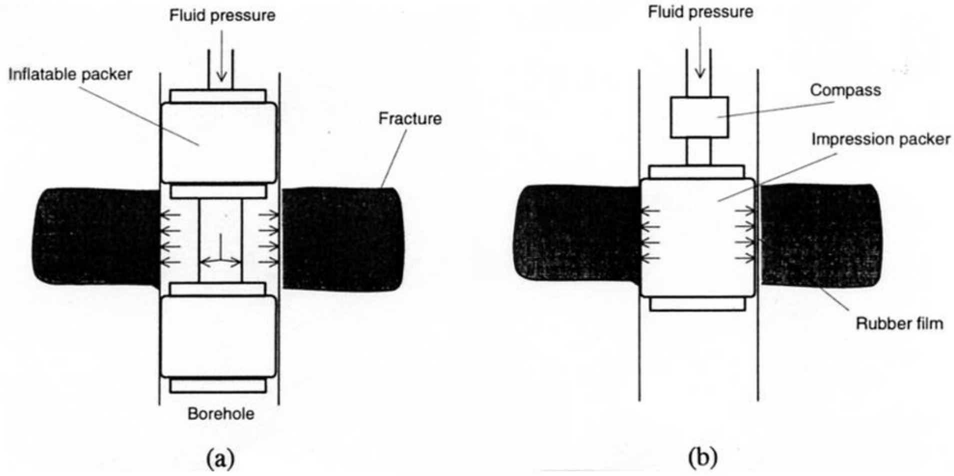

Figure 5.10: *a) The pressurisation of borehole until fracture plane is established in the borehole sidewall. b) Obtaining fracture orientation with impression packer and compass. From: Amadei and Stephansson (1997).*

Hydraulic test on pre-existing fractures

Hydraulic test on pre-existing fractures (HTPF) is a modified version of the hydraulic fracturing method. In addition to utilising the same equipment as the HF method, the HTPF method is also based on the measurements of the same parameters as hydraulic fracturing. The modified hydraulic test involves the re-opening of an existing fracture of known orientation in the borehole wall, and thereby measuring the normal stress across the fracture plane (Amadei and Stephansson, 1997).Figure 5.11 illustrates a simple sketch of both the HF and HTPF test methods.

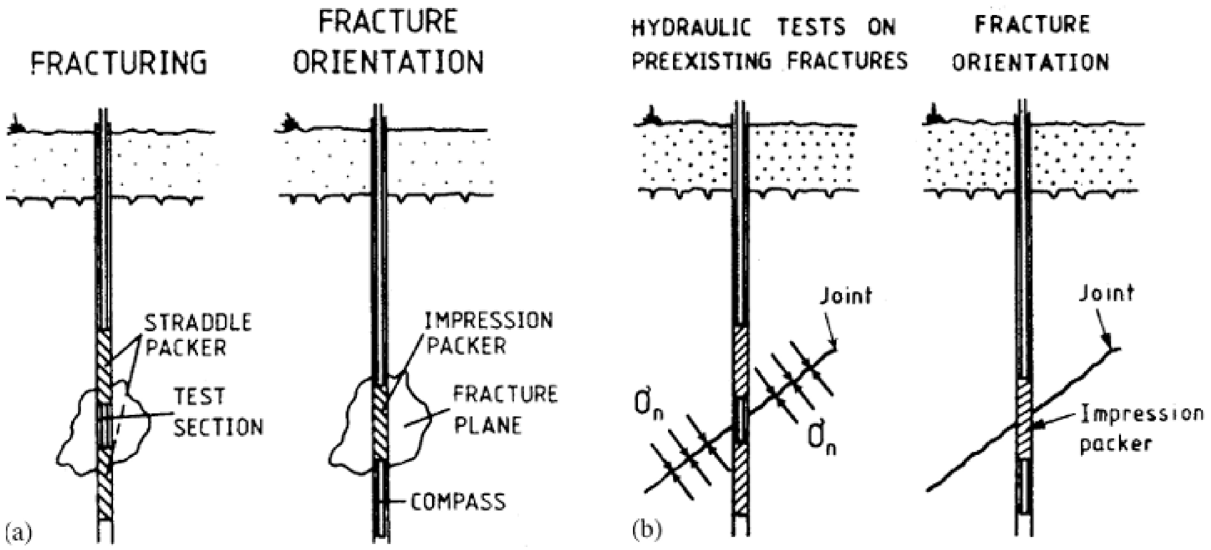

Figure 5.11: *a) Hydraulic fraturing (HF) b) Hydraulic test on pre-existing fractures (HTPF). From: Ljunggren et al. (2003).*

The HTPF method can be applied to determine both 2D and 3D stress states. When performing the HTPF tests, the tested fracture must be planar, and of a size where uniform normal stress can be assumed. This stress measurement method is dependent on four field parameters: test depth, dip and strike of the tested fracture and shut-in pressure. The shut-in pressure is equal to the normal stress across the fracture plane. When a large number of fractures with various dips and strikes are tested, either 2D or 3D stress conditions can be estimated.

In order to determine the 2D stress state, at least six different fractures are required. Although, it is suggested to conduct tests on 10-12 isolated, pre-existing fractures with various dips and strikes in the borehole wall within a certain depth interval of interest. For the 3D stress field, it is recommended to perform at least 18-20 successful tests. The 3D alternative does not require the assumption where the vertical stress has to be a principal stress (Ljunggren et al., 2003).

Overcoring of measuring cells in pilot holes

There are two main overcoring methods: overcoring of cells in pilot holes and overcoring of borehole-bottom cells. Overcoring based on measuring cells installed in the pilot holes involves the use of soft inclusion cells. Ljunggren et al. (2003) pointed out that the principle of soft inclusion cell is based on the theory of linear elasticity for continuous, isotropic and homogeneous rock mass. The most frequently used instruments based on the principle above are the CSIR cell, CSIRO cell and Borre Probe cell. All three instruments measure at least six strain components in various directions of the borehole wall to determine the complete stress tensor at the test depth. The strain components are measured by the triaxial cells with strain gauges in the pilot hole. An example of nine strain gauges in a CSIRO cell is depicted in Figure 5.12

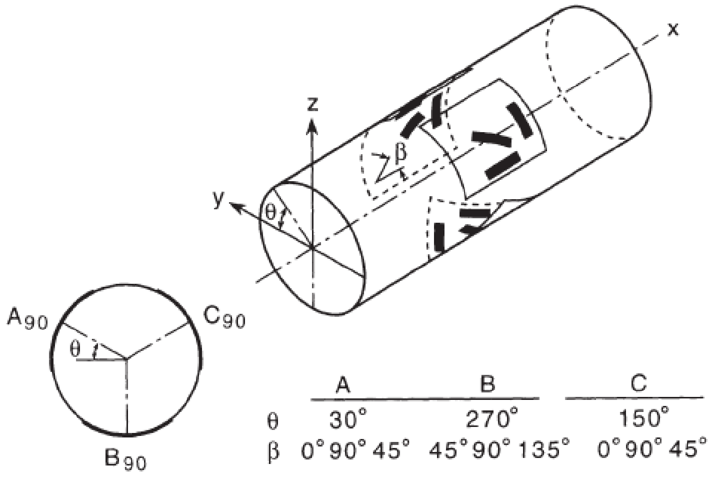

Figure 5.12: *Strain gauges and their orientations in a CSIRO cell. From: Worotnick and Walton (1976).*

This overcoring method allows the 3D state field to be determined from a single measurement point. The 3D overcoring method is recognised to be a reliable stress measurement approach, provided acceptable field conditions, e.g., homogeneous rock mass and low to medium rock stresses. CSIR and CSIRO cells are best suited for dry conditions. However modified versions of CSIR and the Borre probe cells accept water-filled holes. Moreover, the Borre Probe cell has a built-in datalogger, which allows continuous logging of strain gauges and thus enhances the stress evaluation process.

Doorstopper

Doorstopper is one of the methods for overcoring of borehole-bottom cells. Doorstopper is a 2D overcoring stress measurement method. Similar to previously discussed 3D overcoring methods, the doorstopper instrument is based on the theory of linear elasticity for continuous and isotropic rocks. The principle behind the doorstopper method is the use of glued strain gauges on the flattened bottom-end of a borehole. Thus, a pilot hole is not required during doorstopper measurements. Following glued strain gauges, the borehole is extended by applying a coring crown to drill the borehole to the depth of interest. The effect of overcoring relieves the stresses at the flattened end of the borehole resulting in strain changes, which are then measured by the strain gauges (Amadei and Stephansson, 1997).

Doorstopper was first invented in South Africa in the 1960s, and since has been modified and further developed around the world. The Norwegian University of Science and Technology (NTNU) and the Foundation for Industrial and Technical Research (SINTEF) in Trondheim, Norway, have developed their own version of the doorstopper equipment since the late 1960s (Trinh et al., 2016). The procedure for NTNU/SINTEF Doorstopper is presented in Figure 5.13.

Since the NTNU/SINTEF Doorstopper measures the two-dimensional stress state, this method can only determine the stresses in the plane perpendicular to the borehole. Therefore, when the borehole is vertical, horizontal stresses can be obtained. SINTEF also conducts 2D biaxial tests on the core pieces with the doorstopper cells fixed to the core in order to measure E-modulus in the plane. The E-modulus determined from the biaxial tests are then used to obtain stress values (SINTEF, 2022a).

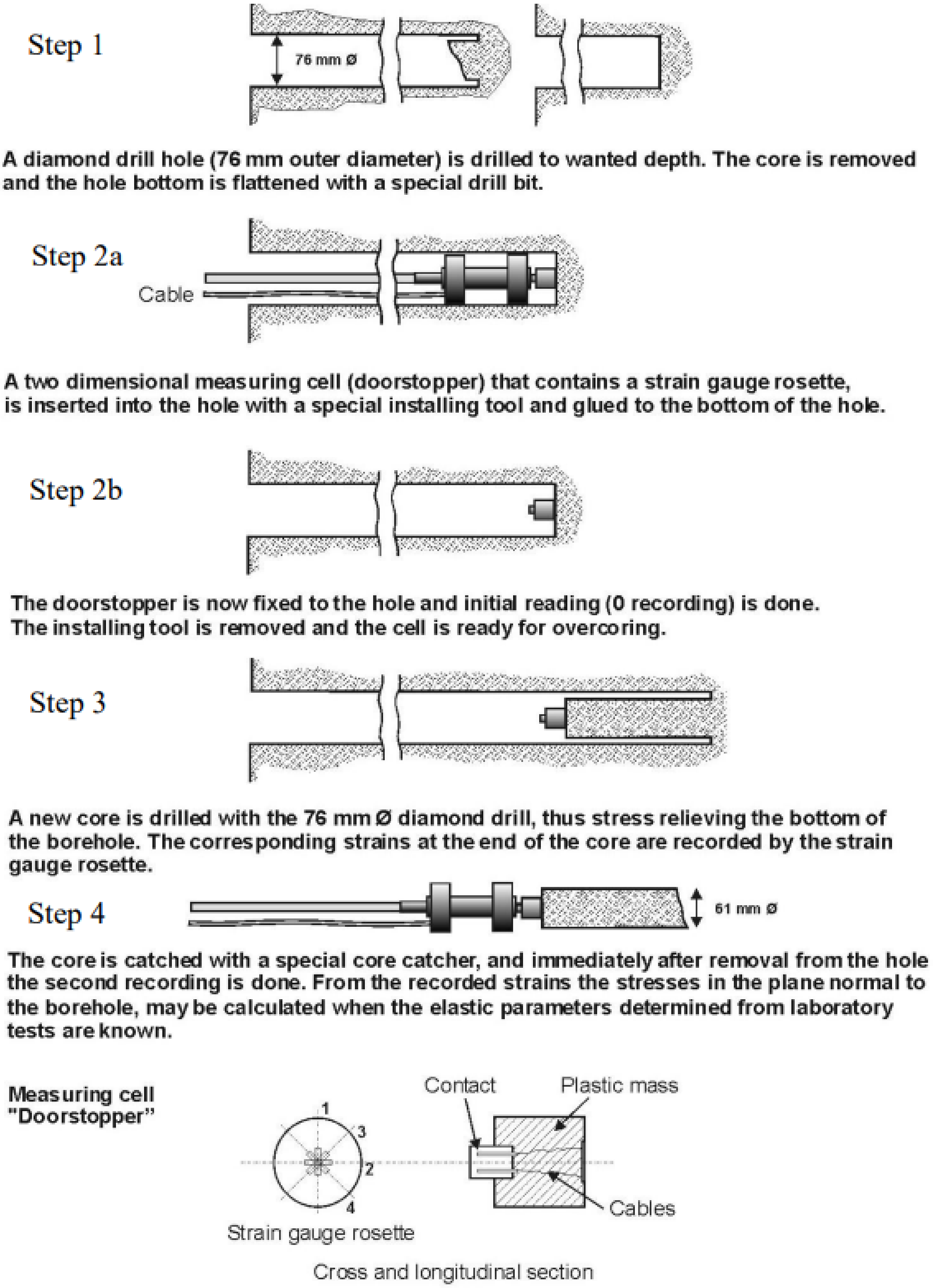

A diamond drill hole (76 mm outer diameter) is drilled to wanted depth. The core is removed and the hole bottom is flattened with a special drill bit.

A two dimensional measuring cell (doorstopper) that contains a strain gauge rosette, is inserted into the hole with a special installing tool and glued to the bottom of the hole.

The doorstopper is now fixed to the hole and initial reading (0 recording) is done. The installing tool is removed and the cell is ready for overcoring.

A new core is drilled with the 76 mm Ø diamond drill, thus stress relieving the bottom of the borehole. The corresponding strains at the end of the core are recorded by the strain gauge rosette.

The core is catched with a special core catcher, and immediately after removal from the hole the second recording is done. From the recorded strains the stresses in the plane normal to the borehole, may be calculated when the elastic parameters determined from laboratory tests are known.

Figure 5.13: *Procedure for 2D stress measurement with NTNU/SINTEF Doorstopper. From SINTEF and reproduced by: Li (2021).*

Overview of measurement methods

Table 5.1 shows the advantages and limitations of the stress measurement methods presented above. The overview is based on the discussion presented by Ljunggren et al. (2003), Amadei and Stephansson (1997) and Li (2021).

Table 5.1: *Advantages and limitations of selected stress measurement methods.*

Method	Advantages	Limitations
Hydraulic fracturing (2D measurement)	Efficient method to determine 2D stress state in the horizontal plane.	Large equipment, thus requires space.
	Advantageous for measurements at greater depth, due to its efficiency.	Theoretical limitations imply measurements should be performed in vertical or sub-vertical holes.
	Low scattering in results.	Challenges with core discing occur during when stresses are high.
	Includes measurements on a fairly large rock volume.	Difficult to determine stresses due to geological structures, e.g., foliation planes in gneissic rocks.
HTPF (2D/3D measurement)	With sufficient variation in strikes and dips of existing fractures, neither geological structures or high stresses cause obstacles to obtaining successful measurements.	Preliminary results cannot be obtained until all field testing is completed and the field results are processed.
	Unlike HF, does not require tensile strength and is independent from pore pressure effects.	More time consuming than HF because the borehole must be positioned at the locations of existing fractures with varying orientations.
Overcoring (2D/3D measurement)	Most developed stress measurement technique in both theory and practice.	Scattering results due to measurement cells are sensitive to isotropy, homogeneity and grain size of the rock.
		Challenges can be faced due to high stresses resulting in core discing.
Doorstopper (2D measurement)	Absence of pilot hole gives possibility for better measurements for jointed rocks, as well as rocks under high stress state.	Can only obtain stresses that are plane perpendicular to the borehole.
	Requires less time, compared with 3D overcoring. 2-3 tests can be carried out per day.	Normally, solutions for isotropic rocks. Although, solutions for anisotropic rocks have also been developed.

5.3.2 Analysis of the doorstopper measurements

Analysis of the doorstopper measurements involves strain measured with three or four strain gauges. As depicted previously in Figure 5.13, SINTEF utilises four strain gauges during the measurement procedure. In a four-element gauge system, the strains are measured in 0°, 45°, 90° and 135° directions. By applying an isotropic solution, according to Amadei and Stephansson (1997), Equations 5.8, 5.9 and 5.10 can be used to determine σ'_x, σ'_y and τ'_{xy}.

$$\sigma'_x = \frac{E}{2}\left[\frac{\epsilon_0 + \epsilon_{45}}{1-\nu} + \frac{\epsilon_0 - \epsilon_{45}}{1+\nu}\right] \tag{5.8}$$

$$\sigma'_x = \frac{E}{2}\left[\frac{\epsilon_0 + \epsilon_{45}}{1-\nu} - \frac{\epsilon_0 - \epsilon_{45}}{1+\nu}\right] \tag{5.9}$$

$$\tau'_{xy} = \frac{E}{2}\frac{\left(\epsilon_{90} - \epsilon_{135}\right)}{1+\nu} \tag{5.10}$$

These stresses σ'_x, σ'_y and τ'_{xy} are correlated with in-situ stress components σ_{xo}, σ_{yo}, $\sigma_{zo}$and τ'_{xyo}, as shown in Equations 5.11, 5.12 and 5.13. Where a, b, c and d are coefficients that can be determined by photoelasticity, experimental methods or numerical methods.

$$\sigma'_x = a\sigma_{xo} + b\sigma_{yo} + c\sigma_{zo} \tag{5.11}$$

$$\sigma'_y = a\sigma_{yo} + b\sigma_{xo} + c\sigma_{zo} \tag{5.12}$$

$$\tau'_{xy} = d\tau_{xyo} \tag{5.13}$$

Calculations conducted by SINTEF also include conversion of stress components from XY-plane to principal stresses in the plane perpendicular to the borehole (SINTEF, 2022b). Due to restrictions, the exact formula applied by SINTEF to determine principal stresses cannot be provided. For the doorstopper measurements, solutions for anisotropic rocks also have been developed, e.g., Corthesy et al. (1990) introduced a mathematical model that takes account of both non-linearity and transverse isotropy.

In solid and homogeneous rock mass, reliable results are achievable from the doorstopper measurements. Local heterogeneity has an influence on the doorstopper stress measurements. Thus, the summation of two orthogonal-oriented strains and their differences can be used to assess the homogeneity of the strain field (Yaméogo et al., 2013). This evaluation is also applied by SINTEF (2022a), where $\epsilon_0 + \epsilon_{90} = \epsilon_{45} + \epsilon_{135}$ indicates that the doorstopper measurement is of good quality.

5.4 Stress distribution

Any excavation of an underground opening will disturb the primary stresses in a rock mass. Stresses are redistributed around the periphery of the opening. The redistributed stresses are called secondary or induced stresses. Principal stress trajectories can be applied to demonstrate a new stress field (Hoek and Brown, 1980). As presented in Figure 5.14a such trajectories are imaginary lines in a stressed elastic body where the principal stresses act. The induced stresses in the figure are presented as tangential stresses (σ_θ). Figure 5.14b illustrates that the induced or secondary stresses near the tunnel periphery are higher before reaching the in-situ stress state at a distance away from the opening. Such stress behaviour occurs in an elastic condition when the horizontal stresses are equal to the vertical stress.

Induced stresses behave differently in non-circular openings than presented in the figure below. Non-symmetrical geometries and sharp corners have a significant influence on the magnitude of the secondary stresses. When the radius of curvature decreases in an excavation geometry, the magnitude of the induced stress will increase. A sharp corner can also result in a high stress concentration around the area. Such high stress concentrations are expected to occur in transitions between wall-roof and wall-floor in e.g., tunnels (Li, 2021).

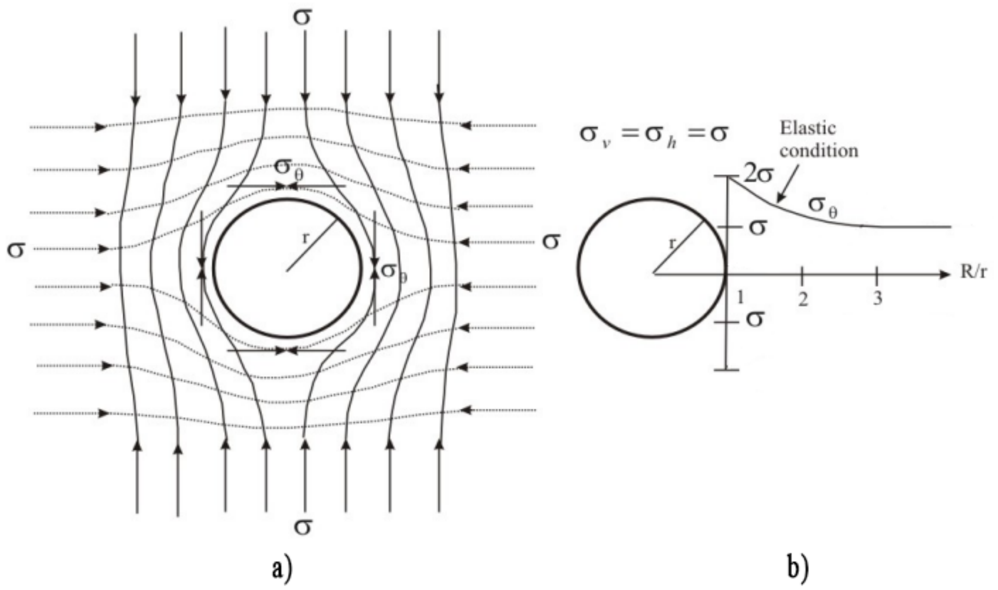

Figure 5.14: *a) Stress trajectories in a rock mass surrounding a circular opening. b) Secondary stress (tangential stress) distribution in an elastic stress condition. Modified after: Panthi (2006).*

When the horizontal stresses are greater than the vertical stresses at a shallow depth, the secondary stresses form major principal stress trajectories as shown in Figure 5.15. Low stresses at shallow depths can be crucial if the tunnel shape is not designed well, and can result in unnecessary low stress levels, such as tensional stresses, in the tunnel roof. The in-situ horizontal stress is generally greater than the in-situ vertical stress at low overburdens. This can result in destressed tunnel walls, and thus a rounded tunnel roof will minimise the risk of destressed tunnel walls, as illustrated in Figure 5.15a.

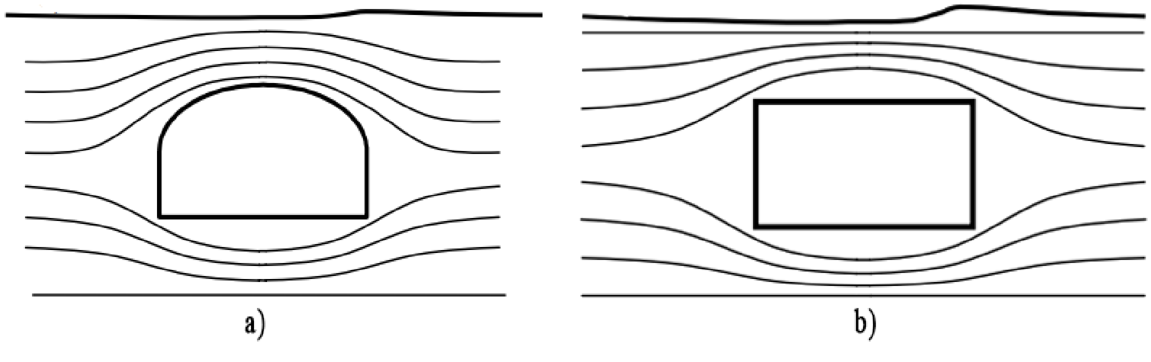

Figure 5.15: *Stress trajectories around a) a rounded tunnel crown and b) a flat roof. From: Töyrä (2004).*

In many situations, a lower overburden means lower stresses around the tunnel and the risk of block slip along pre-existing discontinuities increases. However, underground openings at a low overburden can also form concentrations of horizontal stresses above the excavation, resulting in stress-induced failure (Töyrä, 2004).

5.5 Stress induced instabilities

Two instability issues are often observed around an underground opening: 1) structurally controlled failure and 2) stress-induced failure. Structurally controlled failure involves gravity-driven processes leading to block fall (wedge failure). This form of instability issue is common in low confining-stress conditions at shallow depths. In the case of rock wedges falling, driven by gravity loading conditions, the rock blocks can fall or slide from the roofs and sidewalls of tunnels. Therefore, pre-existing geological structures have an important influence on the block falls, and hence affect the stability of an underground opening. The shear strength of discontinuities, as expressed in Equation 3.11, bounding the wedges is influenced by the confining stress, σ_n.

When stress magnitudes reach the rock mass strength or are greater, stress-induced failure occurs. In weak and soft rock mass, the failure or yielding can result in large displacements, where the deformation is a function of the size of the plastic zone relative to the tunnel diameter. In hard and strong rock mass, the yielding can lead to small displacements, given that the depth of failure is limited. Moreover, rock failure in hard rocks may occur in a violent manner by spalling or bursting (Martin et al., 2003).

The main approach to predicting the failure process is estimating the stress level and the rock mass strength. Such predictions are helpful for tunnel and support design. However, both during and after the construction of underground openings, the stability of the surrounding rock mass can be assessed on the basis of displacement measurements. Convergence measurement and extensometer monitoring are the most frequently used methods for rock deformation measurement. Convergence measurement is a technique that measures the relative displacement between two fixed points, e.g., wall-to-wall or wall-to-roof. On the other hand, the multipoint extensometer measures displacements within the rock mass.

6 The West Link Project

6.1 Project description

The West Link Project (Västlänken) is located in Gothenburg, Sweden. The owner of the project is the Swedish Transport Administration (Trafikverket). The project is established to achieve efficiency in both local and regional public transportation. West Link will improve travel in Gothenburg and West Sweden by increasing the railway capacity. The project includes an eight-kilometre long double-track railway infrastructure with a six-kilometre underground tunnel. In addition to the new railway tunnel, the West Link involves the construction of three new underground stations: Gothenburg Central Station, Haga and Korsvägen. The project area passes through the city from Olskroken in the north to Krokslätt in the south (Trafikverket, 2022f). The location map of the project is presented in Figure 6.1.

Figure 6.1: Location map of the West Link Project. From: Trafikverket (2022e).

The construction work in the West Link consists of both drill-and-blast excavation method and cut-and-cover. The drill-and-blast method is applied in the areas with rock mass, whereas the cut-and-cover is used when constructing through clay (Trafikverket, 2022f). In the Korsvägen section, both excavation methods will be utilised. However, the majority of the route in Korsvägen involves drill-and-blast advance, including the access cavern (Trafikverket, 2022a).

The construction of the access cavern (Mellanplan) in Korsvägen station started in 2021. Thus far, two pilot tunnels in the top heading are excavated (Figure 6.2). The next step in the excavation sequence of Mellanplan is the removal of the rock pillar between the pilots. The benching under the top heading will be conducted in accordance with the excavation of track- and station tunnels (Trafikverket, 2016c).

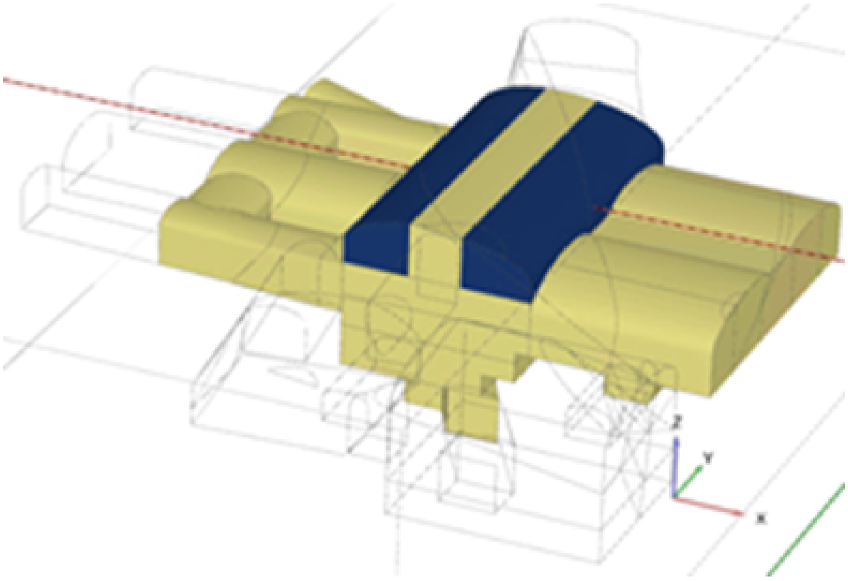

Figure 6.2: *Blue volumes represent the excavated pilot tunnels in the top heading. Illustration provided by: Olsson (2022d).*

Due to the scope of the thesis, this chapter will focus on the top heading of Mellanplan at the West Link Project. The top heading will often be referred to as Mellanplan, even though the entire access cavern is yet to be constructed.

6.2 Geometry and excavation sequence

Figure 6.3 presents the cross-section of the entire access cavern. The hatched area in the figure below illustrates the geometry of the top heading. Both pilot tunnels have a width of 10 m, whereas the rock pillar has a width of 8.8 m. Hence, the total span of Mellanplan is 28.8 m. The vertical walls in the top heading have different heights. The right wall has a height of 2.7 m, and the left has a height of 4.8 m. Likewise, the rock pillar has different wall heights of 8.4 m and 8.9 m. The total length of the access cavern is 50 m. The profile number at the start (south) of the top heading is 0/002, while the end (north) is 0/052. Moving forward in the thesis, the pilot on the right side in Figure 6.3 is termed East pilot, and the pilot on the left is West Pilot.

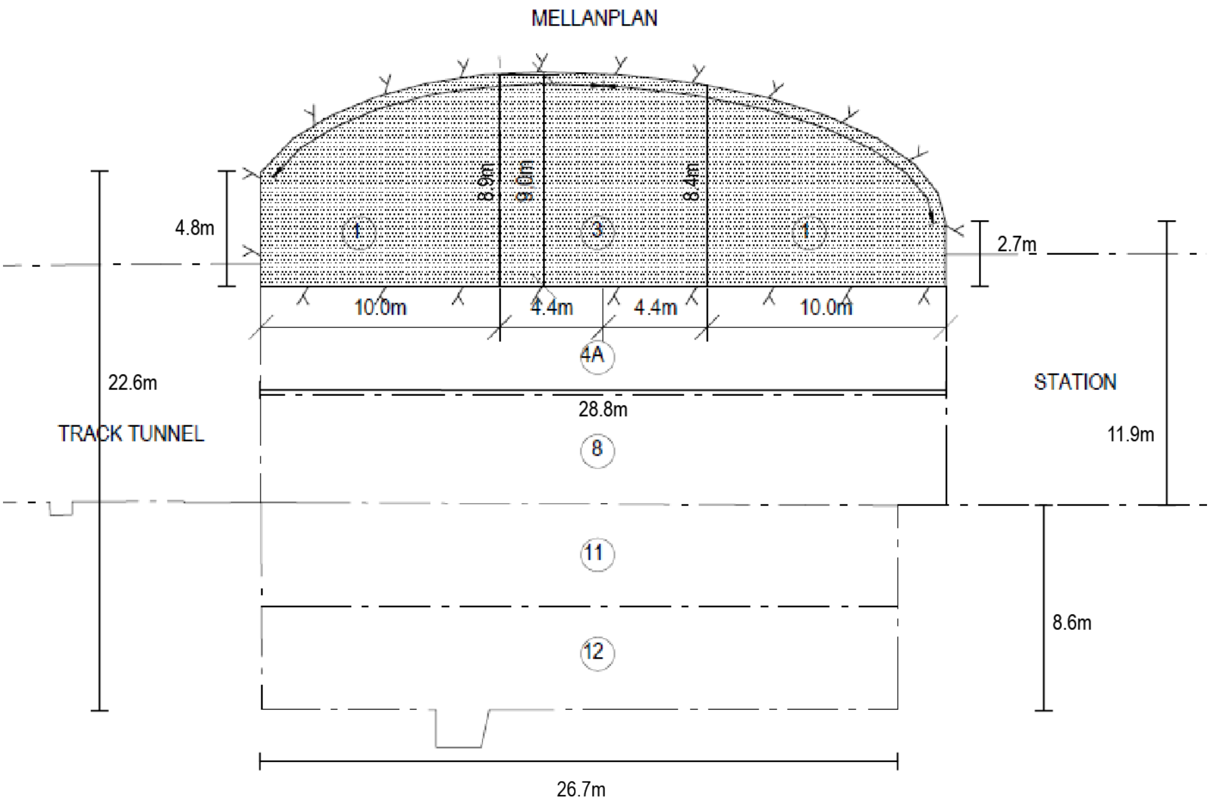

Figure 6.3: *Cross-section of the entire access cavern in Korsvägen. The hatched area depicts the top heading. From: Trafikverket (2022d).*

As mentioned in Sub-chapter 6.1, the first step in the excavation sequence of the top heading is the removal of the two pilots. The initial design for excavation is presented in Figure 6.4a, where the numbers indicate the order of steps to be followed. During the first project visit to Mellanplan, an observation was made regarding the actual excavated geometry. Based on the observation and overview map at the project site, Figure 6.4b illustrates the area of the top heading that has been excavated in reality. The grey-hatched sections are the remaining rock mass left. Figure 6.4 also illustrates the orientation of Mellanplan's length axis towards the north-south direction. The orientation of the access cavern is N11°W.

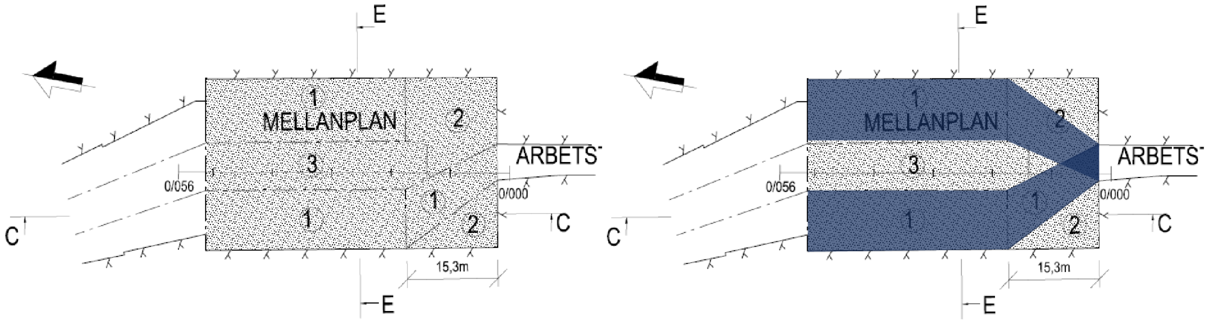

a)

b)

Figure 6.4: *Plan view of Mellanplan from above. a) Initial excavation sequence design. b) Blue overlay illustrates current shape of the excavated pilot tunnels. Modified after: Trafikverket (2022d).*

6.3 Executed field work

In addition to the background material provided by Trafikverket, formerly executed field investigations are utilised to evaluate the geological conditions in Mellanplan. These investigations also include stress measurements and deformation monitoring in Mellanplan. This sub-chapter will briefly describe the previously conducted field works, that are relevant to the study. The results from the field investigations are presented in the following sub-chapters and assessed by the author. It should be noted that the rock stresses are evaluated in Chapter 8.

6.3.1 Geological mapping at pilot tunnels

Following the excavations of pilot tunnels, geological mapping has been carried out by the contractors of the West Link Project. The contractors at the Korsvägen section are NCC and Wayss Freytag Ingenieurbau AG. The mapping of the West Pilot was conducted between June and October 2021. Meanwhile, the mapping of the East Pilot was between February and April 2022. Both pilot tunnels have a length of 50 m, which the contractors continuously mapped. In total, a length of 100 m of mapping is taken into account for the assessment of geological conditions at the top heading. The geological mapping comprises general information on the rock mass relevant for rock mass classification systems, and mapping of geological structures.

The author has collected the information from the geological mapping and divided the data into four sections: Q_{bas}, *Joints and* RMR_{bas}, *Structural mapping - West Pilot* and *Structural mapping - East Pilot*. The data are presented in Appendix A, B, C and D, respectively. In Appendix A and B, relevant data for rock mass quality and joints are presented. In Appendix C and D, the mappings of geological structures of the pilot tunnels are presented.

6.3.2 Photogrammetry and determination of JCS and JRC

The Swedish engineering consultancy, Tyréns AB, has conducted photogrammetry and determined the values for Joint Compressive Strength and Joint Roughness Coefficient.

Photogrammetry is a supplement for visually inspecting the rock mass conditions. Through photogrammetry, 3D images of rock mass in tunnels can be generated. The work for photogrammetry in Mellanplan was carried out continuously after the excavations and before the application of rock support in the pilots. The author is only provided with images and does not have access to 3D models retrieved from photogrammetry. Thus, the pictures from photogrammetry are solely applied for the GSI evaluation.

The Joint Compressive Strength (JCS) of the joint surfaces in pilot tunnels were conducted by Tyréns using an N-type Schmidt hammer. A test with a Schmidt hammer involves the plunger of the hammer pressed against the rock surface until energy is released. The hardness of the material influences the reflected energy. A rebound value is obtained from the reflected energy. For each test, the rebound value and the joint orientation have been registered (Tyréns and Olsson, 2022). JCS values are based on the mean rebound values (at least 10 impacts), rock density and the orientation of the hammer axis. For the detailed procedure, the reader is recommended to read the description given by ISRM (2009).

It should be noted that the rebound numbers from N-hammer are converted to L-type Schmidt hammer rebound values (Olsson, 2022d). According to ISRM (2009), the correlation between rebound numbers obtained by L-and N-type Schmidt hammer can be defined by Equation 6.1.

$$R_N = 1.0646R_L + 6.3673 \tag{6.1}$$

The Joint Roughness (JRC) values were determined using a profile gauge and comparing the joint profiles with roughness profiles by Barton and Choubey (1977). JRC values have been registered on a scale of 100 mm.

6.3.3 Stress measurements

In-situ stress measurements have been conducted in two measurement areas near Mellanplan, as shown in Figure 6.5. FracSinus RSM AB performed the measurements on behalf of Enviro-Planning AB. According to the Swedish Rock Engineering Research Foundation, called BeFo, a 3D overcoring method (Borre Probe cell) was applied at both Landeriet and Liseberget. Measurements at Landeriet and Liserberget were conducted in 2017 and 2018, respectively. The in-situ stress measurements were performed in a sub-vertical borehole in both locations. The borehole in Landeriet is referred to as KK4207KBH, whereas in Liseberget, the name of the borehole is given as KK4222KBH BeFo (2022). The terrain elevation at Landeriet was registered at +23 metres above sea level (masl.), while the end of the borehole reached -13 masl. The terrain level at Liseberget was documented at +17 masl., and the borehole end at -17 masl. (Olsson, 2020).

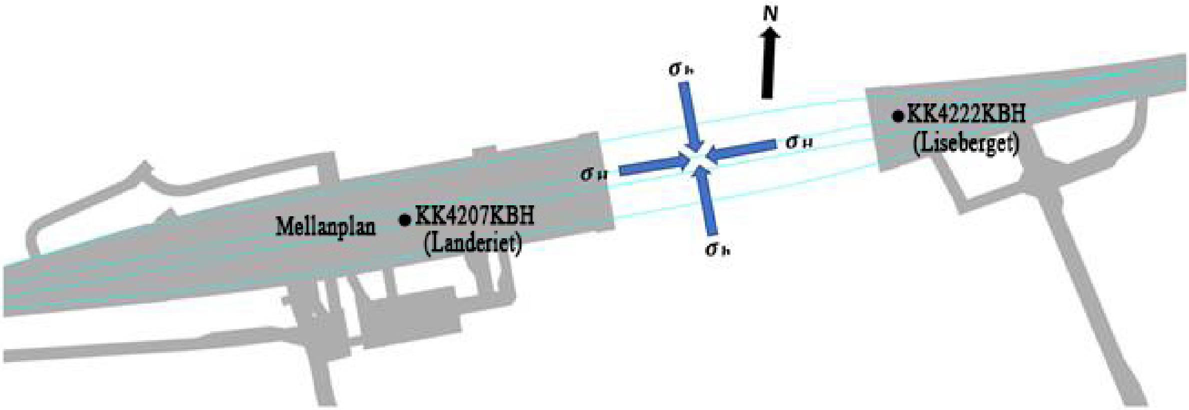

Figure 6.5: *Overcoring in-situ stress measurements in Landeriet (KK4207KBH) and Liseberget (KK4222KBH). From: Olsson (2022d).*

In addition to in-situ stress measurements, secondary stress measurements have been carried out by SINTEF Community, department of Rock and Soil Engineering, on behalf of Tyréns. The secondary stress measurements were conducted on the roof of both East and West pilots in Mellanplan at profile 0/028. The measurements were carried out in April 2022, where 2D Doorstopper method was utilised. Stress measurements were performed on vertical boreholes from the pilot roofs, and are referred to as DS1 (West pilot) and DS2 (East pilot). The 2D stress measurement in DS1 was performed in a 3.5 m long vertical hole above the roof, and in DS2 the vertical hole length was 4.5 m, as illustrated in Figure 6.6. In DS1, measurements were performed between 0.6 m and 3.5 m hole depth. While in DS2, measurements were performed between 1.3 m and 4.1 m.

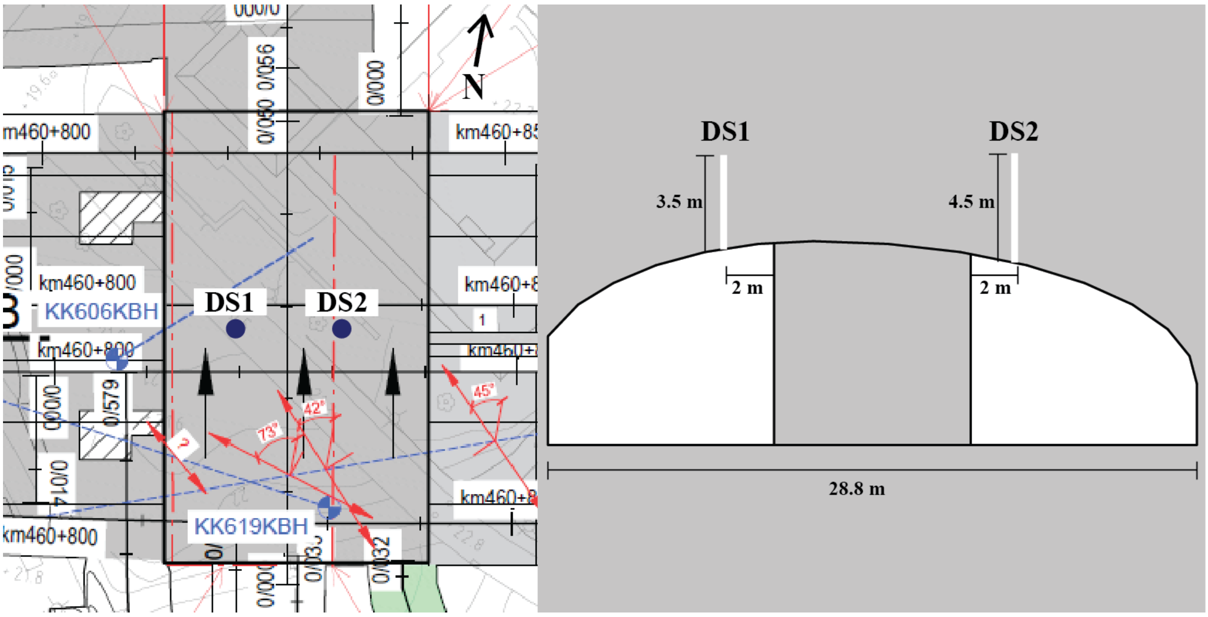

Figure 6.6: Overview and a principal sketch of doorstopper measurements at the vertical holes from the tunnel roofs. The figures are not in scale.

6.3.4 Extensometer monitoring

Multipoint borehole extensometers (MPBX) are placed in three locations at the East pilot, as depicted in Figure 6.7. The contractors have carried out the installation of the extensometers. The MPBXs are referred to as EXT 4.02, EXT 4.03 and EXT 4.04 in the access cavern. These three MPBXs have a length of 15 m and were installed vertically from the tunnel roof in March 2021. The most recent measurement readings of the mentioned extensometers took place in November 2022. The MPBXs have anchors at 7, 10, 12, 14 and 15 metres (Trafikverket, 2022c).

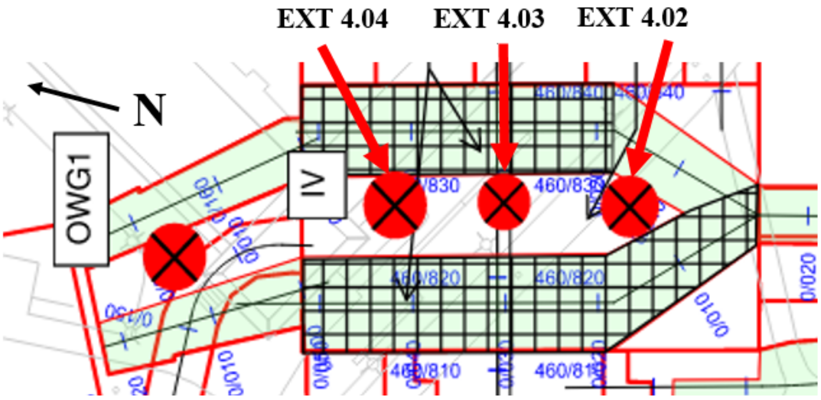

Figure 6.7: Overview of locations of extensometers in Mellanplan. From: Trafikverket (2022c).

Figure 6.7 depicts that EXT 4.03 is closer to the location where the doorstopper measurements were conducted. Therefore, the focus will lie on the result from this extensometer, which will be presented in Sub-chapter 6.7. The extensometer, EXT 4.03, is placed at profile 0/030.

6.3.5 Limitations

The previously executed work from various institutions has been relevant to the thesis study. Nonetheless, there are several limitations within the application of information retrieved from field investigations. The most significant limitations are listed below:

- **Restrictions regarding detailed information**

  The author was not directly involved in the mentioned investigations conducted prior to the thesis work. Therefore, there has been restrictions on achieving detailed information from each investigation. The author has depended solely on the provided knowledge, e.g., result reports and manual registration of material parameters and rock mass properties from the geological mapping. Although results are provided, there was still an absence of detailed methodology, calculations and presentation of a comprehensive evaluation process involving the outcomes of the executed field work.

- **Geological mapping**

  The appendices based on the geological mapping are digitalised and translated versions created by the author. The author could not verify the registered rock mass, material parameters, and joint properties during the project visitations due to the shotcrete-covered tunnel surfaces. This limited the author's ability to evaluate the quality of the existing data.

- **Joint conditions from photogrammetry**

  Photogrammetry is valuable for the estimation of GSI. However, the images from photogrammetry were challenging to utilise for determining joint conditions, such as filling and alteration.

- **Stress measurement calculations**

  The calculations applied to determine the stresses from the measurements were restricted for the author. Thus, it is assumed that the results from stress measurements follow the standard calculations related to the equipment utilised.

6.4 Regional geology

According to the Geological Survey of Sweden, SGU (2020b), the bedrock of Sweden consists of three principal components: 1) Precambrian crystalline rocks, 2) remains of a younger sedimentary rock cover from the Phanerozoic period and 3) Caledonides. The Precambrian rocks are part of an area called the Fennoscandian Shield. Vast areas of Sweden's bedrock contain Paleoproterozoic rocks, Sveconorwegian orogen and Caledonide orogen. Frequently appearing rocks in Sweden are gneiss, granite, granodiorite, sandstone and marble. The Swedish landscape has been shaped by numerous periods of glaciation and deglaciation (SGU, 2020a).

Gothenburg is located in Southwest Sweden, where the bedrock primarily consists of metamorphic rocks formed during Sveconorwegian orogeny. The common rock types in Gothenburg are tonalite-granodiorite, granite-granodiorite, granite, gabbrodiorite, paragneiss and augen gneiss (SGU, 2022). The tectonics in the area is dominated by slip-strike faults and thrust faults (BeFo, 2022). Large-scale weakness zones, and previous rock stress measurement sites, are presented in Figure 6.8. The bedrock map by SGU shows that the majority of the weakness zones have a strike in the northwest-southeast direction.

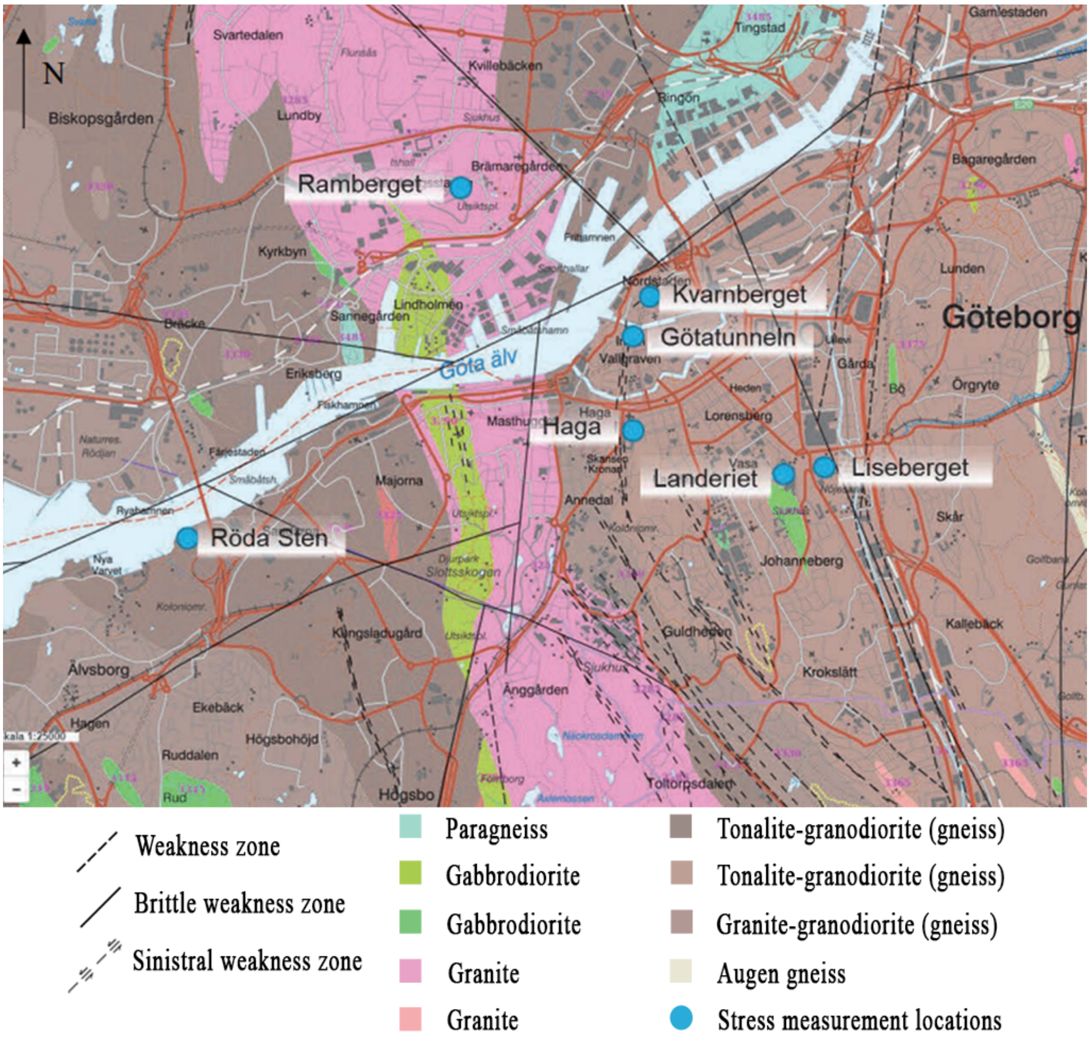

Figure 6.8: *Bedrock map of Gothenburg with weakness zones and locations of former stress measurement sites. Modified after: SGU (2022) and BeFo (2022).*

The soil depth in the central area of Gothenburg varies between 0 to 100 metres. Figure 6.9 presents the variation in the topography of the central part of the city. There are few areas with peaks and slopes in the city. The top of Liseberget hill lies 40 masl., while Johanneberg and Överåsparken have a height up to 80 masl. Most of the central area has a relatively flat topography with a thick soil cover.

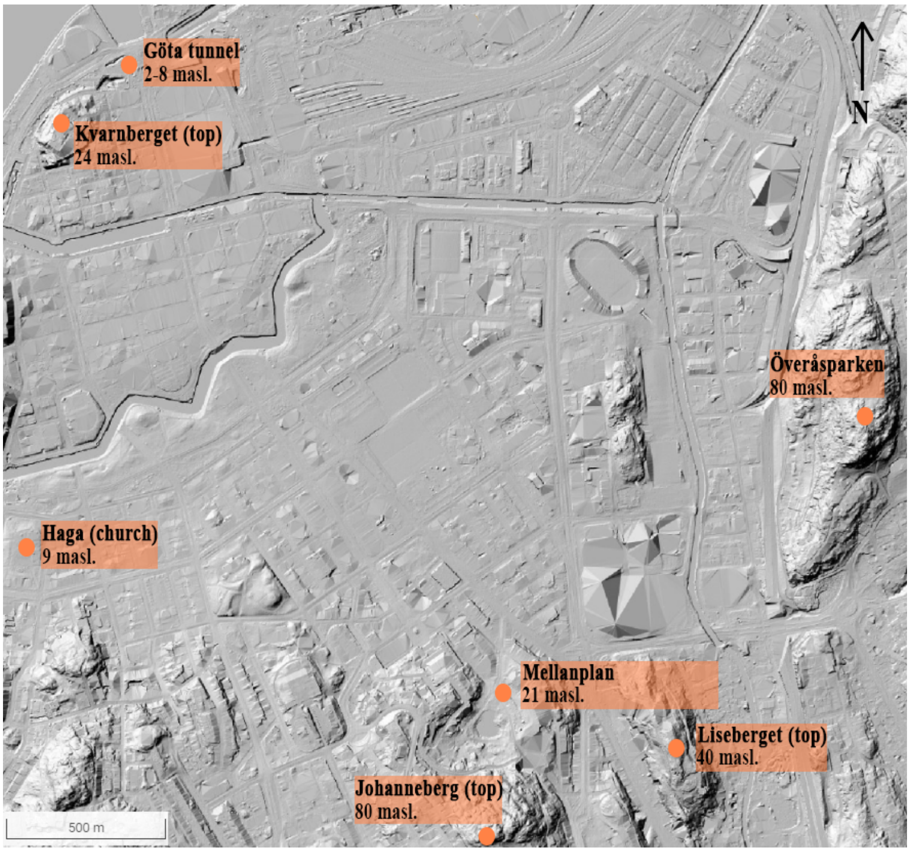

Figure 6.9: *Topography of Gothenburg central area. The orange circles show various locations in Gothenburg and their corresponding height given in metres above sea level (masl.). Modified after: (Lantmäteriet, 2022).*

6.5 Geological conditions in Mellanplan

6.5.1 Rock mass and overburden

There are five predominant rock types in the West Link project area. There are two types of gneiss (gneiss-type 1 and gneiss-type 2), metabasite, pegmatite and a mixture of gneiss-type 1 and metabasite. Gneiss-type 1 has a granodiorite and tonalite composition, while gneiss-type 2 has a granite and granodiorite composition. Metabasite is a fine-grained and very weakly foliated amphibolite (Trafikverket, 2016a). Based on the tunnel mapping of the pilots, the main rock types in Mellanplan are granodiorite gneiss and metabasite. The details from tunnel mapping are given in Appendix A.

Granodiorite gneiss is registered along the entire West pilot and is described as red-grey and grey-red coloured with medium to coarse grains. The description from the tunnel mapping indicates the rock type as gneiss-type 1. Granodiorite gneiss is also observed along the East pilot. However, sections of metabasite appear in a stretch of 32 m alongside gneiss in the pilot tunnel. The gneiss in pilot tunnels is characterised as schistose rocks. Meanwhile, metabasites are described as blocky rocks. Gneiss constitutes 71% of the observed rocks in the pilot tunnels, while the mix of gneiss and metabasite represents 29%.

Rock cover above the cavern crown in Mellanplan varies between 7 m to 15 m. The distance between the top point of the crown and the mean rock surface level is estimated to be 11 m. The average soil thickness above the rock surface is 5.2 m (Boncheva and Olsson, 2022). The soil consists mainly of clay material above Mellanplan (Trafikverket, 2016c). The elevations of the top heading floor, the roof top, and the mean surface level of rock and soil are illustrated in Figure 6.10

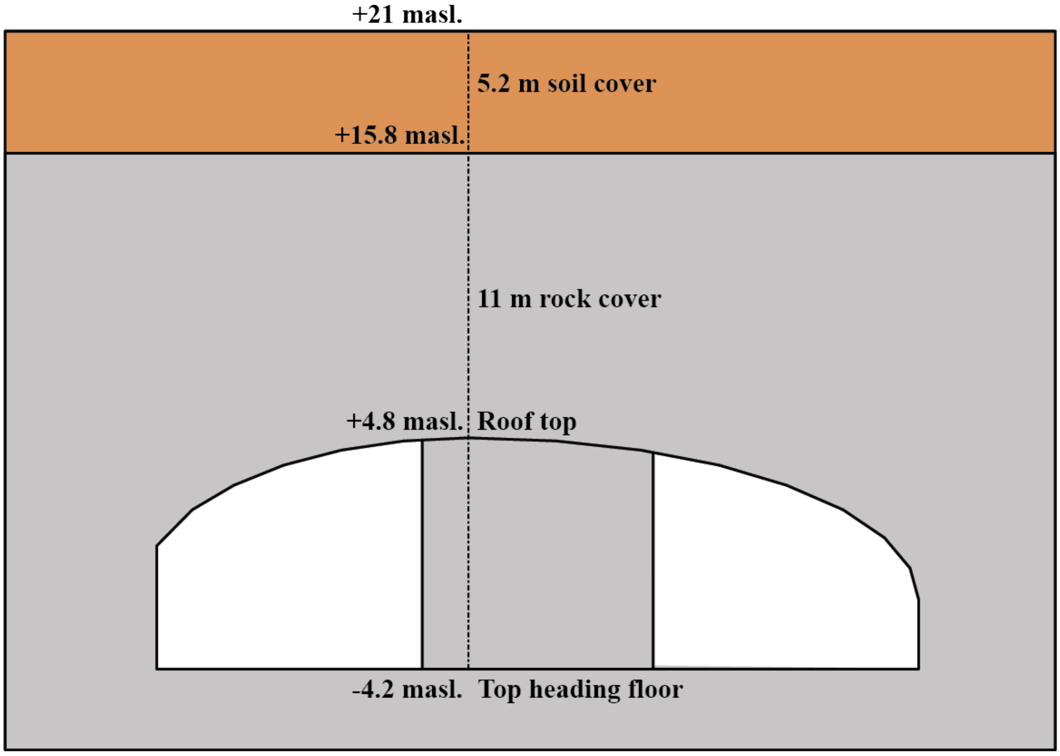

Figure 6.10: *Elevations at top heading floor, roof top, mean rock surface level and mean soil surface level. The grey area depicts rock mass and the brown area depicts soil.*

6.5.2 Discontinuities

Figure 6.11 is based on joint mapping data provided by Trafikverket Appendix B. The stereonet includes joint data from both eastern and western pilots. There are two major joint sets in Mellanplan, foliation joints and cross joints. Foliation joints have an average strike/dip value of N149E/63°SW. Cross joints fall on the opposite direction of foliation joints with an average strike/dip value of N43W/30°NE. Pole vectors outside major joint sets in Figure 6.11 represent random joints.

Foliation joints are dominating joints along the tunnels in the top heading. The mappings of geological structures of both pilots demonstrate the appearance of foliation joints throughout the entire length of tunnel roofs (Appendix C and D). These discontinuities are also visible on the side walls.

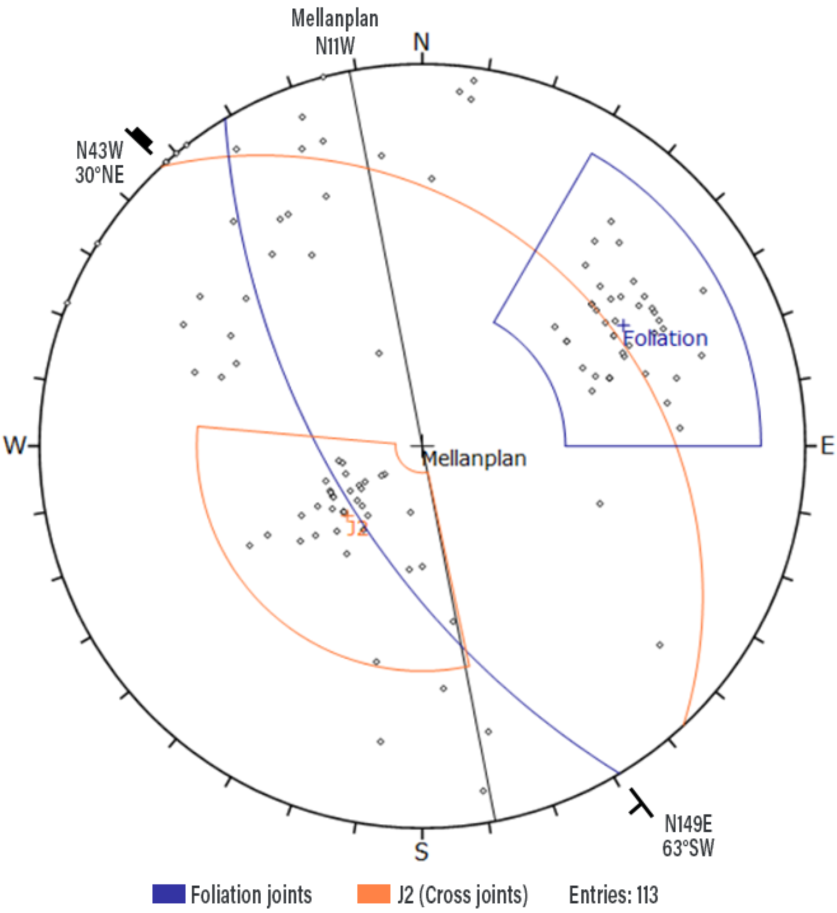

Figure 6.11: *Major joint sets in pilot tunnels in Mellanplan. Generated in Dips (Rocscience, 2022a).*

Statistical evaluation of joint data provides the following joint characteristics presented in Table 6.1. It should be emphasised that all joints are described as dry regarding water inflow, and the roughness in the table below is based on RMR terminology. Although the appearance of cross joints is comparatively less than foliation joints, these discontinuities can have a significant impact on stability due to persistence, joint spacing, and separation. Similar to foliation joints, cross joints also appear in pilot roofs and side walls.

Table 6.1: *Typical joint characteristics of major joint sets. Evaluation of data based on Appendix B.*

Joint characteristics	Description	
	Foliation joints	**Cross joints**
Joint spacing	0.2-0.6 m	0.6-2 m
Length (Persistence)	10-20 m	10-20 m
Separation	0.1-0.25 mm	28% with 0.25-0.5 mm, 22% with >5 mm and 19% with 0.5-2.5 mm
Roughness	52% smooth and 47% slightly rough-rough	45% slightly rough, 24% rough and 30% smooth
Alteration	Variation between unaltered and slightly altered joint walls, with both non-softening and softening mineral coatings	Variation between altered joint walls with softening mineral coatings, and clay mineral fillings with both thickness <5 mm and >5 mm.
Infilling	Variation between mica, clay, calcite, chlorite and sandy particles	Clay is dominant

Table 6.2 presents the JCS and JRC values of gneiss in Mellanplan, identified by Tyréns. The density of the rock type is estimated as 2700 kg/m^3 during the determination of JCS values.

Table 6.2: *JCS and JRC values of rock joints at top heading pilots in Mellanplan.*

Dip/Dip direction	**Joint Rebound Number Mean Rn**	**RN to RL**	**JCS [MPa]**	**JRC$_{100}$ Vertical**	**Joint type**
45/240	46	38	80	4-6	Foliation
82/100	38	30	52	2-4	Random
30/86	54	45	110	9-10	Cross
60/102	61	51	150	9-10	Random
55/220	57	48	148	9-10	Foliation
64/248	52	43	105	10-12	Foliation
80/120	63	53	110	7-8	Random

According to design principles presented in Sub-chapter 2.1, the orientation of the access cavern is not favourable with directions of major joint sets presented in Figure 6.11. The orientation of Mellanplan has close parallelism with the strike of both major joint sets. As previously presented in Figure 6.11 major joint sets have similar strike, however fall in opposite directions. Such joint conditions can develop wedges. Block falls from the roof are registered at the West pilot's end, indicating wedges formation due to joints and low confinement. Nonetheless, the block falls may also result from blasting work during excavation.

Although the orientation of the access cavern may not be favourable considering joints, it should be emphasised that the cavern is only a part of a large and complex railway infrastructure. Moreover, the location of Mellanplan is determined by factors other than joint directions, e.g., railway alignment, connection to track tunnels and station tunnel.

6.5.3 Rock mass quality

Q-system

Rock mass quality and classification in West Link Project is built on Q-system, where Q$_{bas}$ is applied (Trafikverket, 2016b). Unlike traditional Q-system, Q$_{bas}$ does not include joint water reduction factor (J$_w$) and stress reduction factor (SRF). Q$_{bas}$ is equivalent to the Tunneling Quality Index presented in Equation 4.4. Therefore, Q$_{bas}$ is determined by Equation 6.2.

$$Q_{bas} = \frac{RQD}{J_n} \times \frac{J_r}{J_a} \tag{6.2}$$

West Link Project justifies the use of the Q-system due to its well-developed method for descriptions of joint characteristics in crystalline rocks. Furthermore, the Q-system is well known in Sweden and has been applied in many large tunnel projects, e.g., Göta tunnel, Northern Link and Stockholm Bypass (Förbifart Stockholm). Sweden has good knowledge and experience in using Q-system for underground projects (Trafikverket, 2016b).

In the West Link Project, the rock mass is divided into five different classifications based on Q_{bas}. The classifications are presented in Table 6.3.

Table 6.3: *Rock mass classification for West Link Project (Trafikverket, 2016b).*

Rock mass classification	Q_{bas}	**Rock mass quality**
I	$Q_{bas} > 10$	Good
II	$4 < Q_{bas} \leq 10$	Acceptable
III	$1 < Q_{bas} \leq 4$	Poor
IV	$0.1 < Q_{bas} \leq 1$	Very poor
V	$Q_{bas} \leq 0.1$	Extremely poor

Assessment of tunnel mapping data gives following distribution of Q_{bas} and statistics for West pilot in Mellanplan (Figure 6.12). According to Q_{bas} classifications, 82% of rock mass is classified as acceptable to good rock mass. The remaining rock mass is characterised as poor.

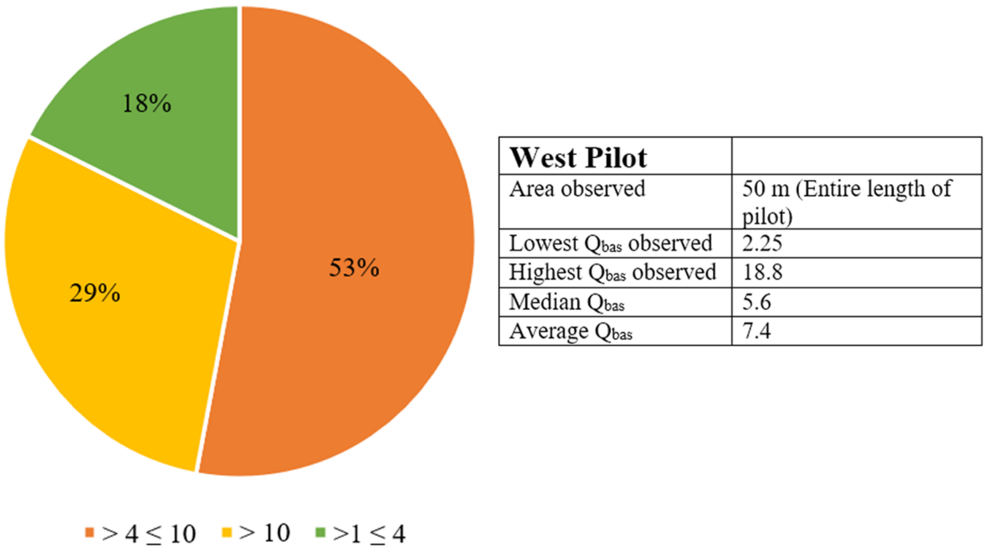

West Pilot	
Area observed	50 m (Entire length of pilot)
Lowest Q_{bas} observed	2.25
Highest Q_{bas} observed	18.8
Median Q_{bas}	5.6
Average Q_{bas}	7.4

Figure 6.12: *Distribution of Q_{bas} and statistics for West pilot. Assessment based on data provided by Trafikverket (Appendix A).*

Likewise, assessment of tunnel mapping provides the following distribution of Q_{bas} and statistics for East pilot (Figure 6.13). In total, 88% of rock mass is classified as acceptable to good. Whereas, 12% is characterised as poor rock mass. The distributions of Q_{bas} show similar rock mass quality in both pilots.

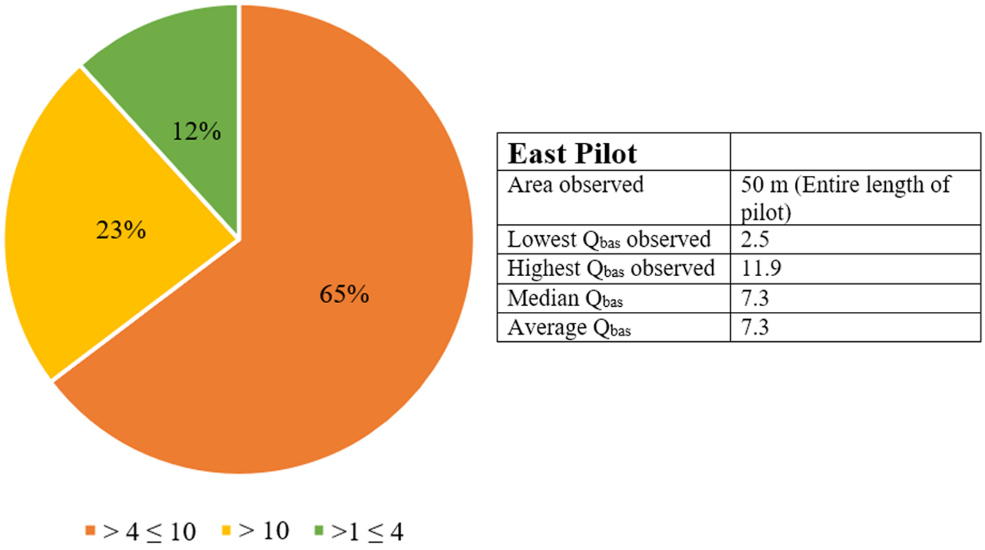

East Pilot	
Area observed	50 m (Entire length of pilot)
Lowest Q_{bas} observed	2.5
Highest Q_{bas} observed	11.9
Median Q_{bas}	7.3
Average Q_{bas}	7.3

Figure 6.13: *Distribution of Q_{bas} and statistics for East pilot. Assessment based on data provided by Trafikverket (Appendix A).*

RMR-system

Although Q_{bas} is applied for rock mass quality and classification in West Link, parameters related to RMR_{bas} are also registered during the joint mapping of the pilots. Unlike the RMR-system, RMR_{bas} does not consider the influence of water inflow and joint orientations. Thus, a completely dry state (RMR rating = 15) and favourable orientations of discontinuities (RMR rating = 0) are estimated while calculating RMR_{bas} values. According to (Trafikverket, 2016c), the interlink between RMR_{bas} and Q_{bas} is given by Equation 6.3 and Equation 6.4.

$$RMR = RMR_{bas} - 5 \tag{6.3}$$

$$Q_{bas} = e^{(RMR-44)/9} \tag{6.4}$$

Joint data provided by Trafikverket include parameters with close relation to RMR_{bas}, such as estimated UCS value, RQD, joint spacing, joint length, width of joints, filling material, J_r, J_a and weathering conditions. In order to calculate RMR_{bas}, some of these parameters have been evaluated and interpreted to fit the RMR parameters. For example, RMR-system omits the joint roughness number (J_r) and joint alteration number (J_a). Nevertheless, they can provide an estimation of RMR parameters *roughness* and *infilling*. Moreover, observed filling materials from mapping are also taken into account for infilling rating estimation.

Table 6.4 depicts the average and median RMR$_{bas}$ achieved from joint data, and its corresponding Q$_{bas}$ obtained from Equation 6.4. These Q-values are higher than those presented in Figures 6.12 and 6.13. Based on this assessment, the rock mass is classified as good, since the Q$_{bas}$ > 10.

Table 6.4: *Calculated RMR$_{bas}$ values and corresponding Q_{bas} values in pilot tunnels. Assessment based on data provided by Trafikverket (Appendix B).*

Classification	**RMR$_{bas}$**		**Q$_{bas}$**	
Pilot	**Average**	**Median**	**Average**	**Median**
West Pilot	73	74	14	16
East Pilot	73	75	14	18

GSI

GSI values of the pilot tunnels are evaluated on the basis of joint mapping, photogrammetry and an equation correlating GSI to Q$_{bas}$. According to Equation 4.5, Q$_{bas}$ can be a function of GSI, as shown below. By applying the average and median Q-values from Figures 6.12 and 6.13 in the equation below, approximately GSI = 60 is achieved.

$$GSI = 9 \times Log_e(Q_{bas}) + 44$$

According to joints observed in both pilots, Table 6.5 shows the percentages of the dominating joint spacings. A combination of joint spacing and a GSI chart can be utilised to describe rock mass blocks.

Table 6.5: *Joint spacing in pilots and GSI block description based on spacing of joints.*

Joint spacing	**Percentage observed**	**GSI - Block description**
>2	22%	Massive
0.6 - 2	35%	Blocky - Massive
0.2 - 0.6	37%	Very blocky - Blocky
Rest	6%	Varies dependent on spacing

From the tunnel mappings, the wall conditions of the joints can be interpreted as fair to good in Figure 6.14. A combination of the joint spacings presented in the table above and a GSI chart suggests that the rock blocks in the pilots vary from very blocky to massive rock mass. Therefore relative to the GSI chart, the GSI value for rock mass in the pilot tunnels of Mellanplan lies between 55 and 70, as demonstrated in Figure 6.14.

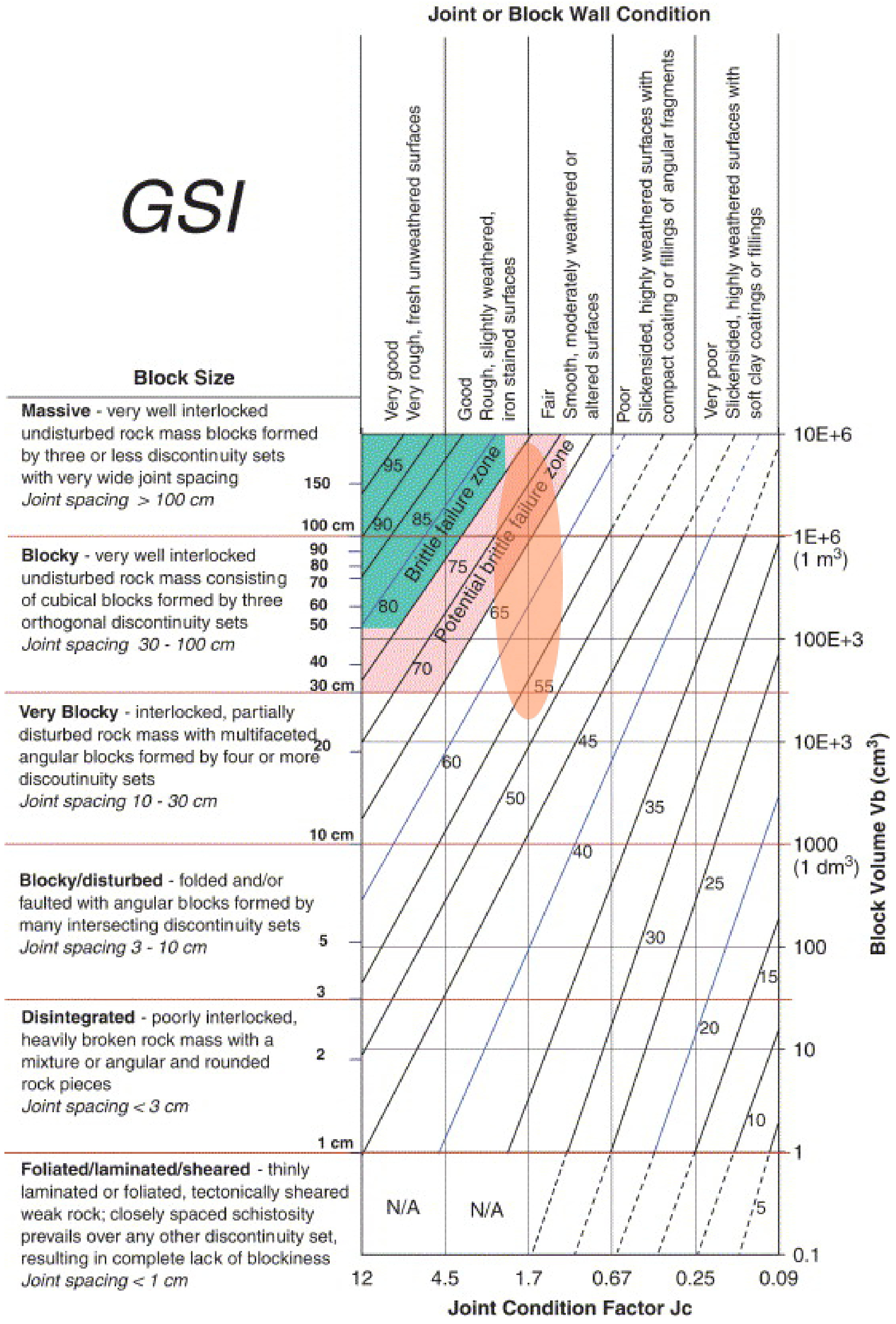

Figure 6.14: *GSI interval (circled) dependent on joint spacing and wall conditions from joint data. GSI Chart from: Cai et al. (2007).*

Figure 6.15 is a photogrammetry picture of pilot tunnels in Mellanplan. The photogrammetry depicts blocky to massive rock mass with good rock surface conditions. Two discontinuity sets frequently well interlock the blocks. Foliation joints depict small joint spacing, resulting in more blocky rock mass than a massive one. The surfaces of the rock walls are observed to be slightly weathered with few iron stained areas. Hence, relative to the visual analysis of the photogrammetry and GSI chart, the estimation of GSI values varies between 60 to 75.

Figure 6.15: *Photogrammetry of pilot tunnels in Mellanplan. Figures are presented towards the east. Photogrammetry images developed by Tyréns are provided by: Olsson (2022d).*

6.5.4 Mechanical properties

Trafikverket (2016a) recommends values given in Table 6.6 as the mechanical properties of an intact rock in West Link. The mechanical properties have been determined by laboratory tests. The rock samples for the tests were from both the West Link Project and Göta Tunnel Project. The values have taken account of the five rock mass classifications described for the West Link.

Table 6.6: *Recommended mechanical properties of intact rock in West Link (Trafikverket, 2016a).*

Parameter		**Value**
		For rock mass classifications I-IV
Uniaxial compressive strength σ_c [MPa]	Minimum	100
	Typical	140
	Maximum	190
Hoek-Brown parameter m_i	Minimum	5
	Typical	13
	Maximum	20
Young's modulus E_i [GPa]	Minimum	55
	Typical	70
	Maximum	80
Poisson's Ratio ν	Minimum	0.15
	Typical	0.25
	Maximum	0.30

In addition, the mechanical properties of rock joints, normal stiffness and shear stiffness in Mellanplan are 50 GPa/m and 25 GPa/m, respectively. These values are applicable for both foliation joints and cross joints (Trafikverket, 2016b).

6.6 Rock stresses

6.6.1 Scandinavian stress database

Figure 6.16 depicts orientations of major horizontal stresses, σ_H, in Scandinavia. The directions of these stresses are derived from a compilation of stress measurements in various depths. The major horizontal stresses in the Fennoscandian Shield typically have orientations in NW-SE directions. According to Wold Stress Map, this trend correlates with the horizontal stress conditions in the Gothenburg region (Heidbach et al., 2018). The maximum horizontal stress orientations in Gothenburg, presented in Figure 6.16, are based on stress determination from focal mechanisms. The World Stress Map also shows that the Gothenburg region is influenced by slip-strike faults (green mark) and thrust faults (blue mark). It should be noted that not all fault regimes and stress orientations from the database are presented in the figure below.

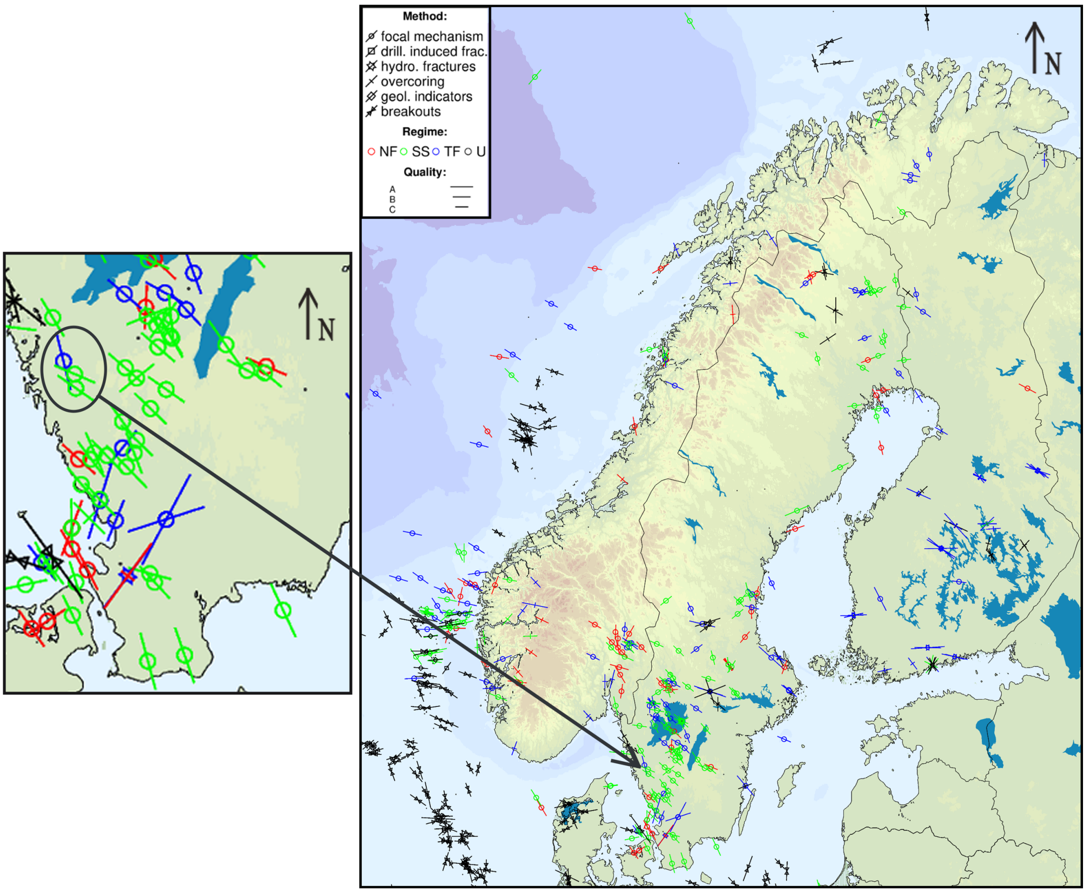

Figure 6.16: *Horizontal stresses in Fennoscandian Shield and Gothenburg (circled). Various fault types are presented in the legend, where NF=Normal fault, SS=Slip-strike, TF=Thrust fault and U=Unknown. From: World Stress Map Database (Heidbach et al., 2018).*

The latitude and longitude of Gothenburg city are 57.708 and 11.974, respectively. From the World Stress Map database, the following stress orientations of major horizontal stress (α_H) are collected based on the latitude and longitude of the locations in and nearby the Gothenburg region.

Table 6.7: *Orientations of major horizontal stress (α_H), in Gothenburg regions and locations nearby. From: Heidbach et al. (2018).*

ID	Latitude	Longitude	α_H	Fault type
wsm00095	57.300	13.250	N134E	Strike-Slip
wsm00135	57.820	12.340	N113E	Strike-Slip
wsm00136	57.870	13.080	N131E	Strike-Slip
wsm00137	57.200	13.210	N159E	Strike-Slip
wsm00143	57.180	12.810	N136E	Strike-Slip
wsm00149	57.200	12.630	N157E	Strike-Slip
wsm00155	57.920	12.180	N166E	Thrust
wsm00161	57.450	13.040	N145E	Strike-Slip
wsm00171	57.710	12.360	N125E	Strike-Slip

For the Fennoscandian shield Martin et al. (2003) compiled horizontal stress data from Swedish and Finnish stress database. The database contains 46 various boreholes with approximately 400 measurements performed in gneiss, granite and diorite. Figure 6.17 illustrates the compiled horizontal stresses against depth. Martin et al. (2003) suggested that the minimum horizontal stress in Scandinavia is less than vertical stress, $\sigma_H > \sigma_v > \sigma_h$. However, this statement is based on stress measurements at great depths. The in-situ stress conditions at shallow depths are more complex. The figures below show widespread in results, particularly at shallow depths.

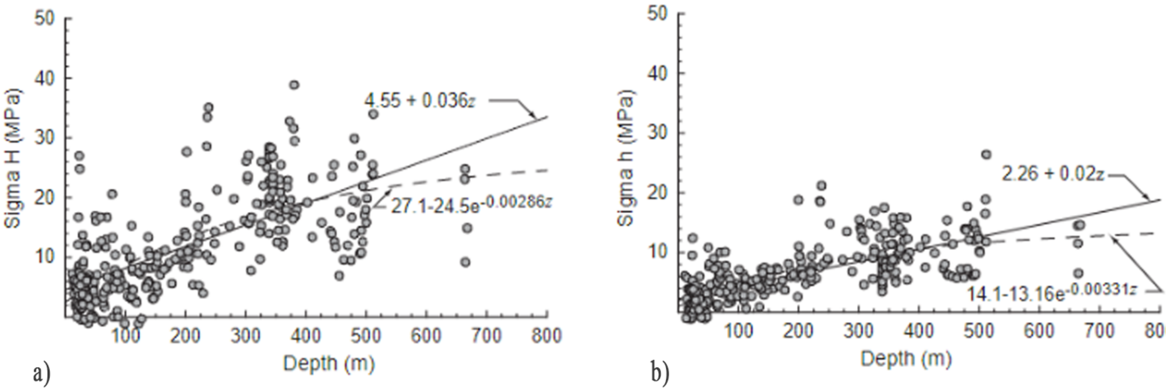

Figure 6.17: *In-situ horizontal stress data from Sweden and Finland. a) Maximum horizontal stress (σ_H) and b) Minimum horizontal stress (σ_h). From: Martin et al. (2003).*

6.6.2 In-situ stress measurements in Gothenburg

In general, few rock stress measurements have been conducted in Gothenburg. Rock stress measurements are relatively costly and technically complex. Therefore, previously conducted stress measurements and documentation are important for future underground projects. The documented stress measurements in Gothenburg have been conducted in Röda Sten, Ramberget, Göta tunnel, Kvarnberget, Haga, Landeriet and Liseberget, as previously shown with bedrock map in Figure 6.8. Landeriet and Liseberget are locations near Mellanplan, where in-situ stress measurements have been performed in relation to the West Link Project.

The results from stress measurements at Landeriert (KK4207KBH) are depicted in Figure 6.18. The points in the graph present the measured in-situ minor and maximum horizontal stresses. Best-fit lines are derived from the measurements.

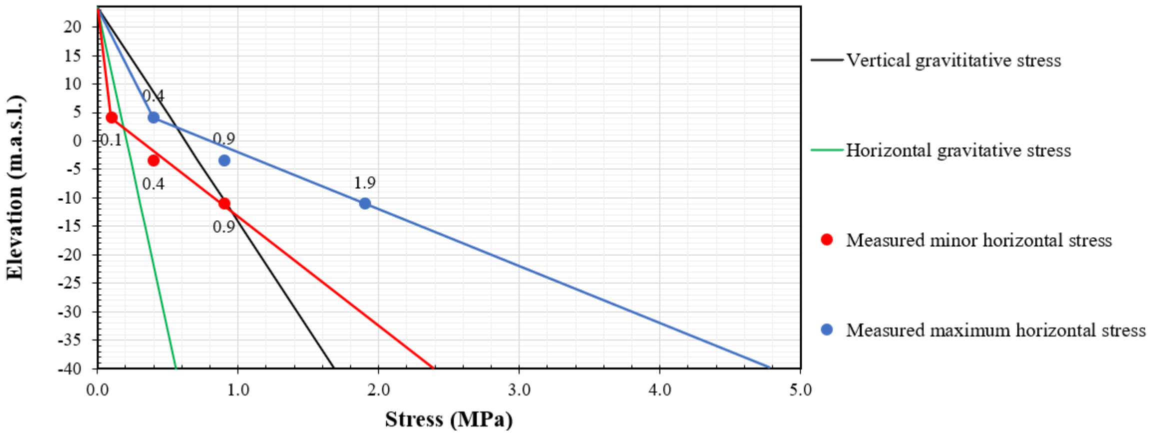

Figure 6.18: *In-situ horizontal stress measurements conducted by FracSinus RSM AB at Landeriet, borehole KK4207KBH. Modified after: Olsson (2020).*

Figure 6.19 presents the results from stress measurements at Liseberget (KK4222KBH). The measured horizontal stresses in this location differ from measurements at Landeriet. It should be recalled that Liseberget is close to a regional weakness zone as depicted previously in Figure 6.8.

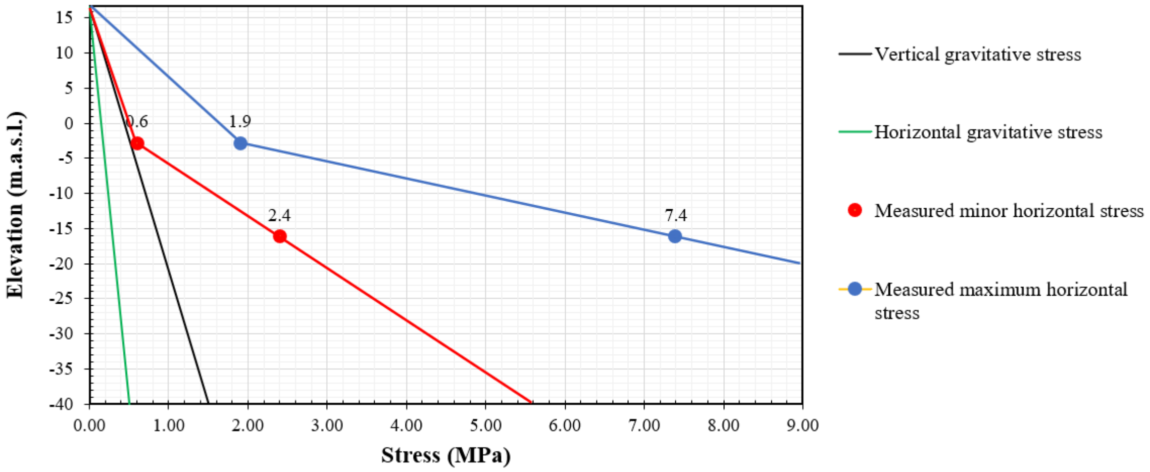

Figure 6.19: *In-situ horizontal stress measurements conducted by FracSinus RSM AB at Liseberget, borehole KK4222KBH. Modified after: Olsson (2020).*

At both overcoring locations, the orientation of σ_H is estimated perpendicular to close to perpendicular to Mellanplan, approximately at N80E ± N10E. While σ_h is parallel, as depicted in

Figure 6.20. According to Olsson (2022c), the results from the 3D overcoring measurements were complex due to widespread of data. The values presented in Figures 6.18 and 6.19 have been reported as the final stress results after processing and evaluating the data from the overcoring measurements.

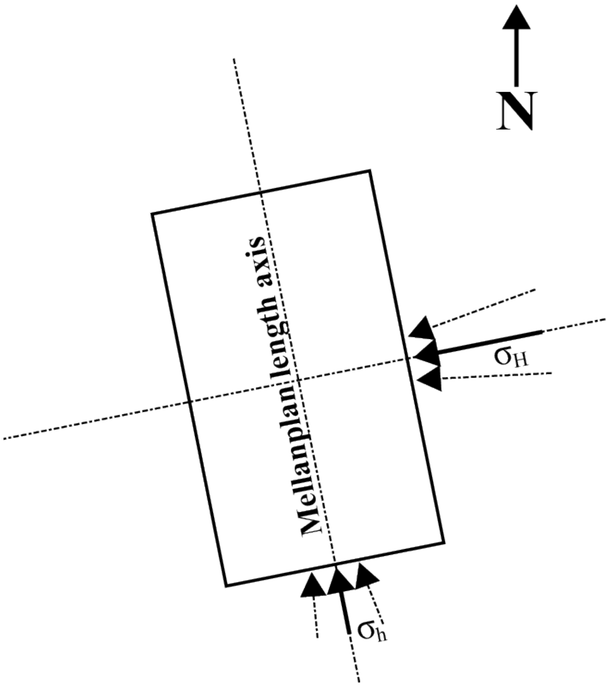

Figure 6.20: *Estimated stress orientations at Mellanplan. Based on: Olsson (2022c).*

Rock Engineering Research Foundation in Sweden (BeFo) has interpreted the in-situ stress state in Gothenburg based on the previously performed stress measurements. BeFo (2022) suggests the following stress state for Gothenburg. The stress orientation of the major horizontal stress is presented under α_H in Table 6.8.

Table 6.8: *In-situ stress state in Gothenburg, estimated by BeFo (2022). (α_H) is the orientation of major horizontal stress.*

	σ_H [MPa]	σ_h [MPa]	σ_v [MPa]	α_H [°]
Minimum	0.077 z	0.007 z	0.021 z	N80E
Best estimated	0.104 z	0.016 z	$\rho g z$	N103E
Maximum	0.171 z	0.037 z	0.032 z	N115E

6.6.3 Secondary stress measurements in Mellanplan

The secondary stress measurements conducted by SINTEF Community involved vertical boreholes. Thus, horizontal stresses perpendicular to the borehole can be obtained by the 2D doorstopper method. The doorstopper measurements were performed from the roof, and upwards. Therefore, the hole depth begins at the roof of the pilot tunnels and increases above the roof. The strains registered by the doorstopper are presented as ϵ_0, ϵ_{90}, ϵ_{45} and ϵ_{135} by SINTEF. The orientations of the various strains are illustrated in Figure 6.21. As reported by SINTEF (2022a), the two-dimensional stress state from the doorstopper is calculated under the assumption of linear elasticity and isotropic rock mass conditions.

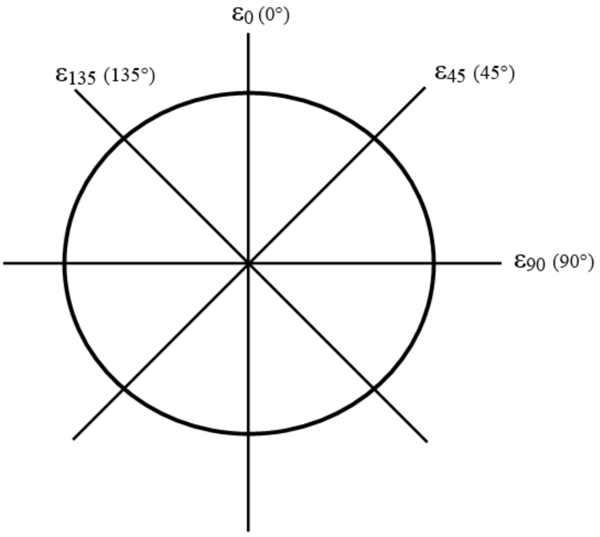

Figure 6.21: *Principal sketch of orientations of the registered strains from the four strain gauges. Based on: SINTEF (2022a).*

Table 6.9 presents the results from West pilot (DSI) provided by SINTEF (2022a). Seven measurements at the depth between 0.6-3.5 m have been utilised to calculate secondary horizontal stresses. The orientations of the major horizontal stresses (α_H) are presented as angles from the north. While the minor horizontal stresses (σ_h) are perpendicular to the corresponding major horizontal stresses (σ_H). The rock mass at the measurement location consists of granodiorite gneiss. Based on the horizontal stresses calculated by SINTEF in the table below, Figure 6.22 presents the stresses in a graph.

Table 6.9: *Calculated horizontal stresses from recorded strain values and corresponding E-modulus from biaxial tests (West pilot, DS1).*

Hole depth [m]	**E-modulus [GPa]**	ϵ_0 $[\mu S]$	ϵ_{90} $[\mu S]$	ϵ_{45} $[\mu S]$	ϵ_{135} $[\mu S]$	$\epsilon_0 + \epsilon_{90}$- $\epsilon_{45} + \epsilon_{135}$	σ_H **[MPa]**	σ_h **[MPa]**	α_H **[°]**
0.6	65.7	134	-28	99	13	-6	8.6	-2.6	N152E
1.0	56.2	233	15	69	222	-43	13.1	-0.2	N3E
1.5	42.5	101	144	309	0	-64	10.7	-0.8	N117E
2.0	75.4	8	-6	-4	12	-6	0.8	-0.6	N9E
2.5	67.7	81	-33	102	-30	-24	6.6	-3.4	N142E
3.0	75.3	-10	1	-15	7	-1	0.5	-1.1	N44E
3.5	66.8	135	12	166	-15	-4	11.0	-1.4	N138E

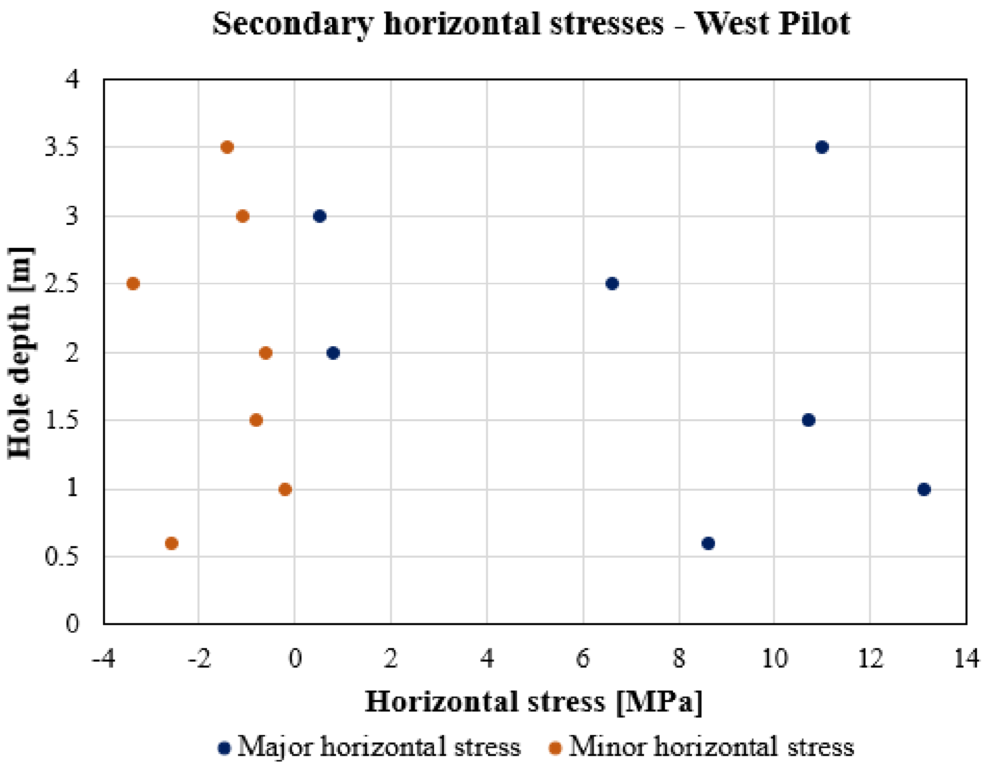

Figure 6.22: *Visual presentation of major and minor horizontal secondary stresses above West Pilot.*

Table 6.10 introduces the secondary stress results from East pilot (DS2). Six successful doorstopper measurements were performed at the hole depth between 1.3-4.1 m. The orientations of the maximum horizontal stresses (α_H) are also provided as angles from the north. The rock mass at DS2 consists of metabasite. Visual presentation of the horizontal stresses calculated from the measurement at East pilot is shown in Figure 6.23.

Table 6.10: *Calculated horizontal stresses from recorded strain values and corresponding E-modulus from biaxial tests (East pilot, DS2).*

Hole depth [m]	**E-modulus [GPa]**	ϵ_0 $[\mu S]$	ϵ_{90} $[\mu S]$	ϵ_{45} $[\mu S]$	ϵ_{135} $[\mu S]$	$\epsilon_0 + \epsilon_{90}$- $\epsilon_{45} + \epsilon_{135}$	σ_H **[MPa]**	σ_h **[MPa]**	α_H [°]
1.3	76.7	-1	-10	5	-13	-3	0.2	-1.1	N142E
2.5	86.2	32	-2	-10	46	-6	3.6	-1.0	N22E
2.8	83.0	18	6	37	-7	-6	2.6	-0.4	N135E
3.2	104.2	-8	-12	7	-21	-6	0.2	-2.3	N132°E
3.6	85.9	20	-6	7	6	1	1.5	-0.3	N172E
4.1	70.6	53	-10	16	33	-6	3.7	0.4	N0E

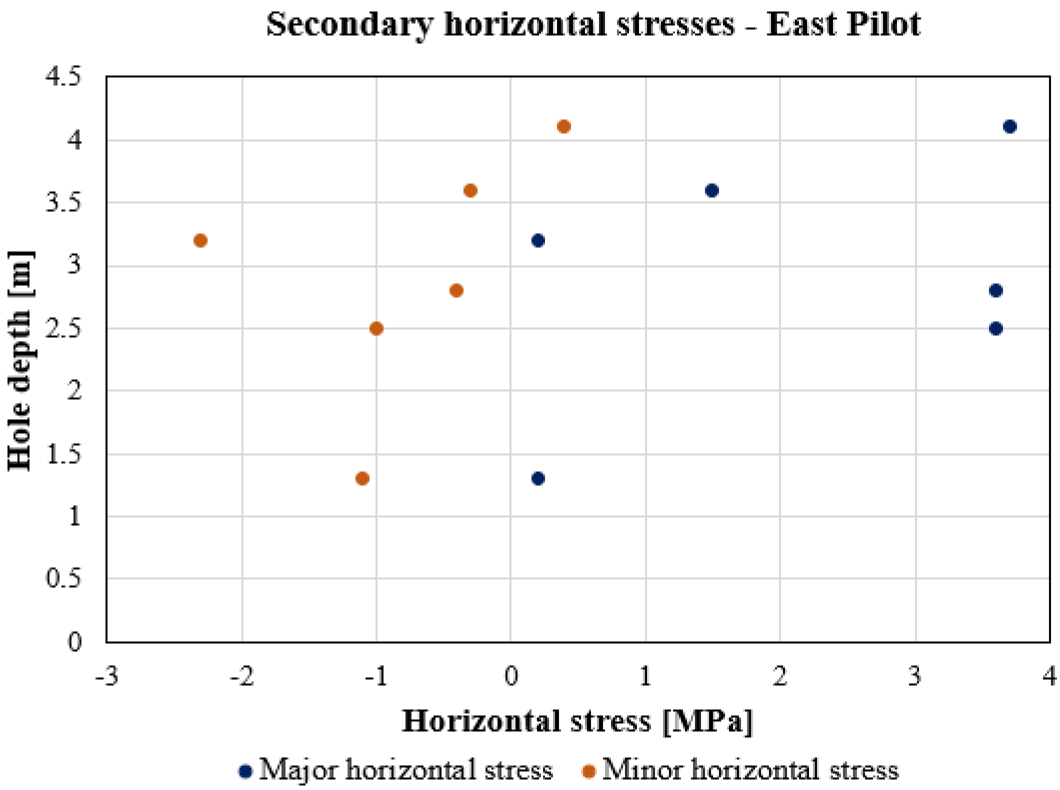

Figure 6.23: *Visual presentation of major and minor horizontal secondary stresses above East Pilot.*

SINTEF applied recorded strains from the doorstopper and E-modulus values from biaxial tests to obtain the horizontal stress values. Furthermore, SINTEF used the Poisson's value obtained in the laboratory to calculate the secondary stresses (SINTEF, 2022b).

6.7 Rock deformation

Vertical deformation is monitored in Mellanplan due to the low overburden. Figure 6.24 displays the results from extensometer monitoring in Mellanplan (EXT 4.02, EXT 4.03 and EXT 4.04) and a section called Olof Wijks (OWG1). The figure below depicts solely vertical deformation at the tunnel roof. EXT 4.03 is near the area of the doorstopper measurement. This extensometer is located approximately in the middle of the length axis of the East pilot and is likely to be less affected by the tunnel face and end. Therefore, the deformation at this extensometer location is of interest. The graph shows the latest vertical displacements recorded on the 7th of November, 2022. The vertical displacement on this date, at EXT 4.03, has been recorded as -2.85 mm, indicating movement of the roof downwards. According to Trafikverket (2022c), the possibility of deformation values being exaggerated should be taken into account.

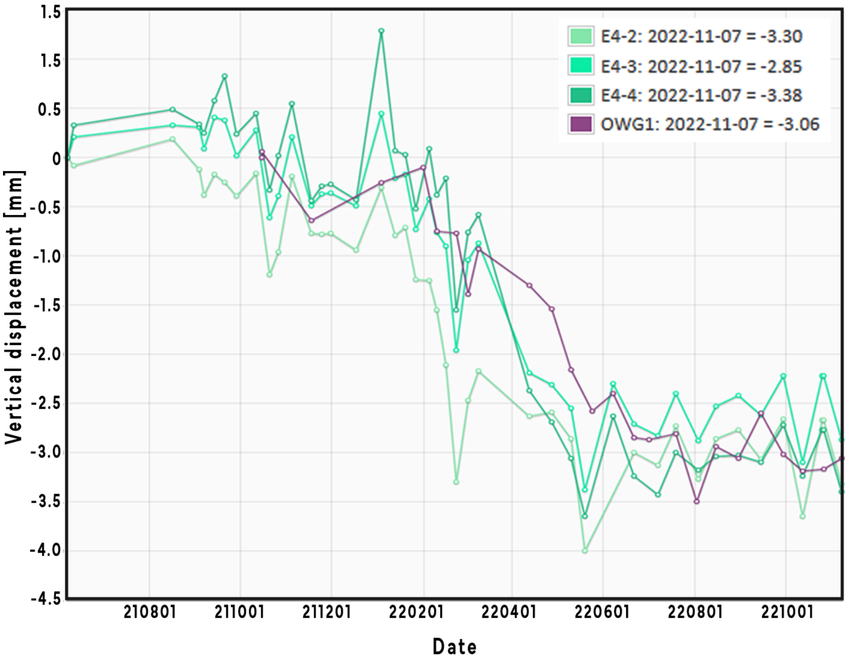

Figure 6.24: *Plot of vertical displacements in Mellanplan and Olof Wijks, from 01.08.2021 to 07.11.22. From: Trafikverket (2022c).*

6.8 Designed rock support

As reported by Trafikverket (2016c), a combination of small overburden and large span is not favourable for forming a natural pressure arch. Therefore, a formation of an artificial pressure arch has been taken into consideration in the support design for the access cavern in Korsvägen. A bolt pattern has been designed in regard to an arch development above Mellanplan.

Figure 6.25 illustrates pilot tunnels divided into various sections based on differing support designs. Sections 1B (West pilot) and 2C (East pilot) are of interest for the study in this thesis, as the doorstopper measurements have been conducted in these areas. In addition, the deformation monitoring at EXT 4.03 have been performed in section 2C. The bolts in the pillar wall are fibreglass bolts, whereas the tunnel wall and roof are applied with PC-bolts. Furthermore, the shotcrete type is fibre-reinforced shotcrete.

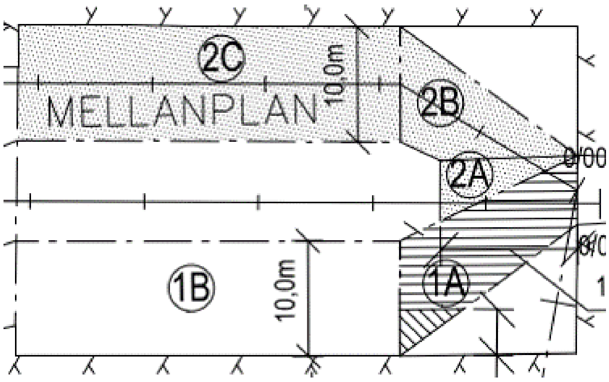

Figure 6.25: *pilot tunnels divided into various sections based on rock support design. From: Trafikverket (2022b).*

Table 6.11: *Rock support design for sections 1A and 1B.*

Location	**1B**			**2C**		
	Shotcrete [mm]	Bolt length [m]	Bolt spacing [m]	Shotcrete [mm]	Bolt length [m]	Bolt spacing [m]
Roof	50	5	1.7	50	6	1.35
Pillar wall	50	3	2	50	4	2
Tunnel wall	50	3	2	50	6	1.35

7 Laboratory investigations

7.1 Rock specimens

The Swedish Transport Administration, Trafikverket, has storage of the remaining rock samples from core drillings conducted during the investigation phase of the West Link Project. With the help of Eric Hegardt from Trafikverket, the author travelled to the project site on the 6th of October 2022 and collected intact rock samples. The rock cores were brought to Rock Mechanics Laboratory in NTNU to perform laboratory tests. The selected rocks were from a drill core named KK606KBH. Figure 7.1 depicts the location of the drill core KK606KBH in Mellanplan. KK606KBH passed mostly through the northwest section of the access cavern with an inclination of 58° towards the northeast.

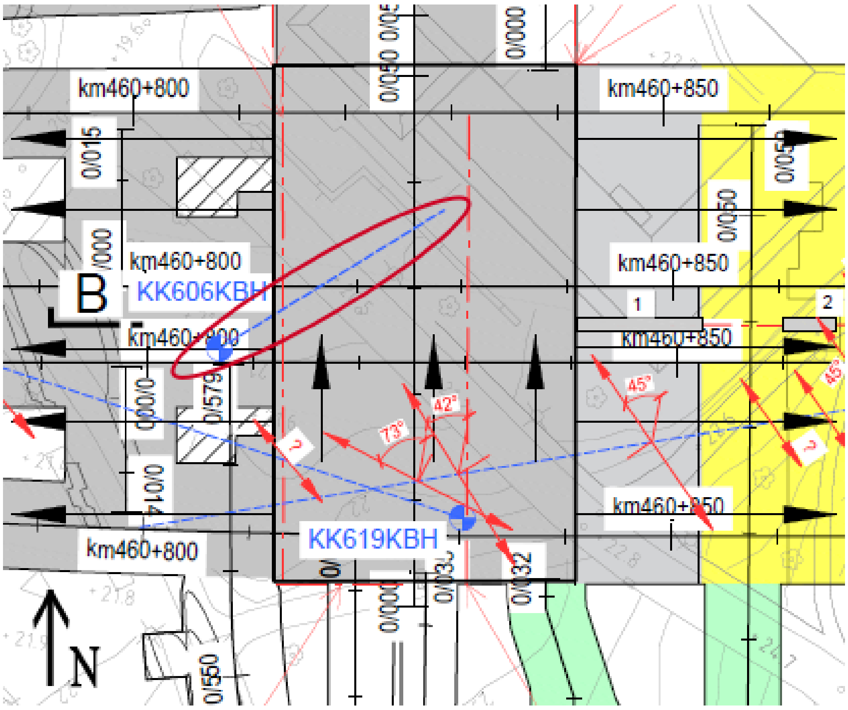

Figure 7.1: Drill core KK606KBH circled with red in Mellanplan. The black box outline shows the area of the access cavern. From: Trafikverket (2018).

The selected rock samples for laboratory tests were from a bore length between 18.7 m to 22.8 m. The rock cores were considered reliable since they were cored before any excavation work started at Mellanplan and its surroundings. The samples were not affected by blasting and had unweathered rock surfaces.

Gunnar Vistnes and Jon Runar Drotninghaug from the Rock Mechanics Laboratory at NTNU prepared the rock specimens and guided the author during laboratory tests. The rock specimens were characterised as granodiorite gneiss with weak foliation. According to the project description, they are known as gneiss-type 1. The rock cores for laboratory tests are shown in Figure 7.2.

Figure 7.2: *Selected rock specimens from drill core KK606KBH.*

The samples for laboratory tests show heterogeneity and overall a good representation of intact rocks in the rock medium. However, specimens from solely one drill core (KK606KBH) and the absence of metabasite samples can be considered limitations.

7.2 Density and sound velocity

The density and the sound velocity of the rock samples can be determined through non-destructive methods. Thus, the rock cores prepared for UCS tests were beforehand utilised for the determination of density and sound velocity. The density of granodiorite gneiss is obtained by applying Equation 7.1, where ρ is density, m is mass of the rock sample, g represents gravitation acceleration, and V is the specimen volume.

$$\rho = \frac{mg}{V} \tag{7.1}$$

For the sound velocity tests, ISRM (1978b) standard was followed. The test procedure involved the following steps:

- Length of a rock core was measured with a caliper.
- The end planes of the cores were applied with a thin film of glycerin before placing them between the transducers (receiver and transmitter) in the apparatus.
- The receiver and the transmitter were positioned opposite to each other, and a pulse generator was used to send a pulse through the rock specimen.
- The velocity of P-wave was calculated as a ratio of the distance between transducers (length of the specimen) and the measured travel time by the equipment.

Table 7.1 shows the obtained values for the density and sound velocity of the rock specimens. The median and mean density values are typical density values for metamorphic rocks, as mentioned in Sub-chapter 3.2. Furthermore, the values for sound velocity lie within a typical range of P-wave velocities for gneiss. The values determined for rock specimen number 2 are excluded, as the UCS results from this sample are not presented later in the chapter.

Table 7.1: *Calculated density and sound velocity for granodiorite gneiss specimens. Specimen number 2 is excluded.*

Rock specimen	Density [kg/m^3]	Sound velocity [m/s]
1	2726	5579
3	2678	5329
4	2646	5553
5	2652	5427
6	2675	5463
7	2682	5489
8	2702	5751
Median	2678	5489
Mean	2680	5513

7.3 Uniaxial compressive strength test

7.3.1 Laboratory procedure and results

Uniaxial compressive strength tests were conducted to classify and measure the strength of the intact rock in Mellanplan at the West Link. In addition, the tests were also performed to determine Young's modulus and Poisson's ratio. The Rock Mechanics Laboratory at NTNU follows the standard for the UCS test suggested by ISRM (1979). The principle of the test involves the use of an apparatus where a rock specimen is subjected to constant load until failure occurs. A simple description of the procedure that was conducted is listed below:

- Measured the average diameter and length of a rock specimen. An average diameter value was obtained by taking a mean of six measurements with a caliper.
- Angle of foliation was determined before the specimen was placed in the apparatus.
- Strain gauges were attached to the rock core. Following this step, the rock core was subjected to a constant load until failure.
- During a test, stress-strain curves were produced, and their values were measured by the equipment.
- The values of UCS, E-modulus and Poisson's ratio were determined from stress-strain curves.

For detailed procedure steps and calculation methods to obtain uniaxial compressive strength, E-modulus and Poisson's ratio, the reader is referred to the ISRM (1979) standard. The rock samples are recommended by ISRM to be tested within 30 days after being cored out, in order to preserve the moisture conditions until the time of the test. However, this suggestion could not be followed during the laboratory tests since the rock specimens were from the investigation phase of the West Link Project, which took place many years ago before the excavation of Mellanplan.

An average length and diameter of a rock specimen for were 119 mm and 45 mm, respectively. The length of the specimen is around 2.65 times the diameter. According to ISRM suggestions, the test cores should have a diameter 2.5-3 times the length of the specimen, with a preferable diameter of approximately 54 mm. The UCS tests fulfil the ISRM recommendations, except for natural moisture conditions and specimen diameter. The results from UCS tests are given in Table 7.2. Specimen number 2 is excluded because the equipment produced a stress-strain curve with anomalies, thus the results were considered invalid (Drotninghaug, 2022).

Table 7.2: *Uniaxial compressive strength, E-modulus and Poisson's ratio of tested rock specimens.*

Rock specimen	Foliation angle [°]	UCS [MPa]	E-modulus [GPa]	Poisson's ratio
1	55	121	69.58	0.24
2	-	-	-	-
3	75	162	72.20	0.24
4	90	202	79.34	0.25
5	90	207	75.47	0.27
6	60	144	80.89	0.25
7	65	138	71.71	0.29
8	65	131	72.52	0.25
Median		144	72.52	0.25
Mean		158	74.53	0.26

Figure 7.3 presents the state of rock cores before and after failure. Some of the cores showed fracture along foliation, while others had either a spalling failure at core sides or axial splitting. In Figure 7.3, it is challenging to observe fracture in specimen numbers 3, 5 and 6. This is due to the fractured parts of the specimens not being completely loosened after the failure. In addition, specimens 3 and 6 have spalling failure at the core sidewalls.

Figure 7.3: *UCS tested rock specimens. a) Specimens before failure. b) Specimens after failure.*

According to ISRM (1978a), the uniaxial compressive strength values of the rock specimens presented in Table 7.2 can be classified as *very high strength* intact rock.

The granodiorite rock specimens consist of foliation planes and thus can behave as an anisotropic material. As discussed earlier in Sub-chapter 3.4, the uniaxial compressive strength of an intact rock can be affected by foliation angle. Figure 7.4 depicts the influence of foliation angle on the compressive strength of granodiorite gneiss cores that were tested. Since the foliation angles vary from 55° to 90°, the trendline in the figure below is extrapolated.

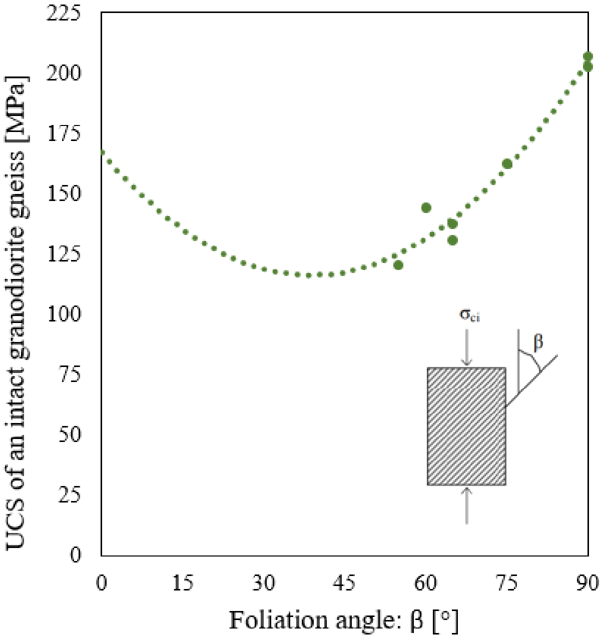

Figure 7.4: *Influence of foliation angle on the compressive strength of granodiorite gneiss. The dashed curve is the best fit line for the scattering obtained values.*

7.3.2 Results from SINTEF

The cores from the doorstopper measurements in both East and West pilots in Mellanplan were used by SINTEF to determine mechanical properties such as compressive strength, E-modulus and Poisson's ratio at their laboratory (SINTEF, 2022a). Table 7.3 presents the results obtained by SINTEF for both granodiorite gneiss and metabasite.

Table 7.3: *Uniaxial compressive strength, E-modulus and Poisson's ratio determined by SINTEF.*

Granodiorite gneiss				**Metabasite**			
Rock specimen	**UCS [MPa]**	**E-modulus [GPa]**	**Poisson's ratio**	**Rock specimen**	**UCS [MPa]**	**E-modulus [GPa]**	**Poisson's ratio**
1	40	58.2	0.079	1	123	96.9	0.215
2	60	72.1	0.136	2	115	94.9	0.206
3	35	60.6	0.155	3	35	76.5	0.269
4	82	75	0.186	4	79	92.6	0.202
5	63	70.7	0.182	5	105	80	0.217
6	106	77.9	0.120	6	124	94.2	0.395
7	51	72.6	0.179	-	-	-	-
Median	60	72.1	0.155	Median	110	93.4	0.216
Mean	62	69.6	0.148	Mean	97	89.18	0.251

Results from SINTEF vary from the results obtained from UCS tests conducted for the thesis.

Following a discussion with Olsson (2022b), the variation in results can be explained by reasoning that the drill cores from SINTEF might be affected by blasting. The rock specimens tested by SINTEF were cored after the excavation of the pilots in Mellanplan, whereas the rock specimens used by the author were from the investigation phase of the West Link Project. The micro-cracks created after the blasting may have an effect on the mechanical properties of rock specimens.

Based on the results from SINTEF, the compressive strength of granodiorite gneiss and metabasite specimens varies between rock classifications *medium strength* to *very high strength* (ISRM, 1978a).

7.4 Brazil test

Brazil tests were carried out to measure the uniaxial tensile strength of rock specimens in an indirect method. The test method is based on the suggestions by ISRM (1978c). A brief description of the procedure followed is listed below:

- The test specimens were circular cylinders. The diameter of a specimen was 45 mm, while the thickness was approximately half of the diameter ($t = 0.5D$).
- The test specimens were wrapped around its periphery with a thin masking tape.
- Each rock specimen was placed between two steel loading jaws on the apparatus and was applied with gradually increasing load from the two loading points until tensile fracture occurred.
- Loads at tensile fracture were recorded by the apparatus and used to calculate the tensile strength of the specimen.

The tensile strength of a rock specimen, σ_t is calculated by utilising Equation 7.2, where P is the load at tensile failure, D is the specimen diameter and t is the thickness of the specimen.

$$\sigma_t = \frac{2}{\pi}\frac{P}{Dt} \tag{7.2}$$

The Brazil tests were carried out on 14 specimens (Appendix E), where the average result achieved was $\sigma_t \approx 17\ MPa$.

7.5 Point-load test

Point load tests were conducted to predict point load strength and strength anisotropy of an intact rock in Mellanplan. The procedure and calculations followed suggestions by ISRM (1985). The procedure applied during the laboratory work is briefly described below:

- Rock cores with a diameter of 45 mm were selected for point load tests. Thus, cut blocks and irregular lumps were not used.
- A rock core was placed between two cone-shaped platens of hardened steel on the apparatus and was subjected to gradually increasing load until failure.
- Both diametral and axial tests were conducted. Diametral tests were conducted with loading parallel to foliation planes. While axial tests were carried out with loading perpendicular to the weakness planes.
- Loads until failure registered by apparatus were used to calculate the point load strength index and strength anisotropy index.

The point load index, I_s is calculated by Equation 7.3, where P is the load recorded at the failure of the specimen, and D_e is the "equivalent core diameter".

$$I_s = \frac{P}{D_e^2} \tag{7.3}$$

where D_e^2 is defined as:

$D_e^2 = D^2$ for diametral tests

$D_e^2 = 4A/\pi$ for axial, block and lump tests

and $A = WD$ minimum cross-sectional area

Figure 7.5 illustrates load directions and the equivalent core diameter for diametral and axial tests.

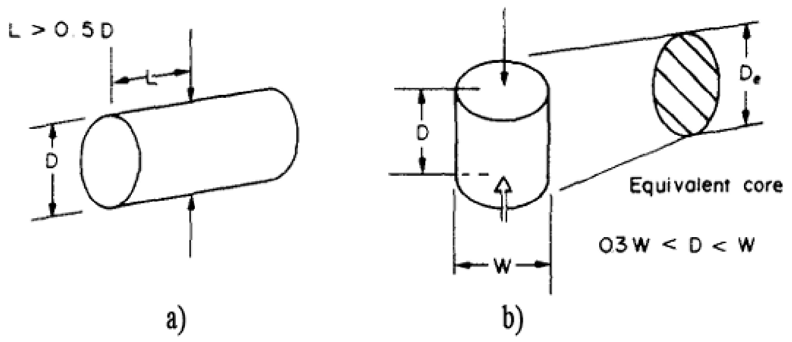

Figure 7.5: a) Diametral test b) Axial test. From: ISRM (1985).

The index I_s varies with the equivalent core diameter. Therefore, correction is applied to the values calculated from Equation 7.3 to obtain consistent test results from the rock specimens. The point load index is corrected for diameter, D = 50 mm. The size-corrected point load strength index, $I_{s(50)}$ is defined by Equation 7.4.

$$I_{s(50)} = F \times I_s \tag{7.4}$$

where the correction factor, F is expressed as:

$$F = \left(\frac{D_e}{50}\right)^{0.45} \tag{7.5}$$

The tested rock cores had a diameter of 45 mm and various lengths. In total, 24 point load tests were carried out. Based on ISRM (1985) requirements, two of the tests were invalid as the fracture plane did not cross through both loading points. Successful diametral tests were conducted on 12 rock specimens, while 10 underwent the axial tests (Appendix E). The results from the diametral and axial tests are often given as the mean value of $I_{s(50)}$. The mean value of the size-corrected point load strength index is calculated by deleting the two highest and lowest values from 10 or more valid tests, followed by calculating the average of the remaining values. Table 7.4 shows the obtained mean values from diametral and axial tests. The table below also presents the strength anisotropy index, $I_{a(50)}$. Since diametral tests were conducted on specimens with foliation planes parallel to loading and axial tests with foliation planes perpendicular, the strength anisotropy can be defined by the ratio of axial to diametral point load strength indices.

Table 7.4: *Mean values of point load strength indices and strength anisotropy index.*

Mean $I_{s(50)}$, diametral	**Mean $I_{s(50)}$, axial**	**Anisotropy index $I_{a(50)}$**
5.6	9.6	1.7

The mean values of point load strength indices proved that the granodiorite gneiss has greater strength in the direction normal to the foliation plane than in the direction parallel. Rock strength in the latter direction is influenced by the weakness planes. Moreover, based on anisotropy classification by Tsidzi (1990), the anisotropy strength index indicates that the sampled gneiss can be classified as *fairly-moderately anisotropic* and *weakly-moderately foliated* rock mass.

7.6 Tilt test

Tilt tests were performed to estimate basic friction angle (ϕ_b). The basic friction angle is essential for estimating the shear strength of discontinuities. The principle behind the basic friction component of shear strength is associated to the angle of response observed for solid materials on inclined surfaces. The Rock Mechanics laboratory at NTNU follows the updated ISRM (2018) suggestion for determining the friction angle. The updated recommendation is a non-destructive test method. Thus, the rock specimens selected for the UCS tests were used for tilt tests beforehand. Below is a brief description of the testing procedure applied for the tilt tests. For a detailed testing procedure, the reader is recommended to study the suggestion presented by ISRM.

- Six rock cores were selected for tilt tests. The specimens were divided into two test groups, with three cores each.

- Three rock cores were stacked and placed on the tilting apparatus. Two cores were placed on the horizontal platform of the equipment, while the third specimen was placed on top of the other pieces. All three cores had surface contact with each other.
- The horizontal platform of the apparatus was gradually tilted until a sliding movement occurred.
- The tilt angle (β) registered by the apparatus as the sliding occurred was recorded.
- Five repetitions on each contact surface were carried out.

As five repetitions were conducted on each contact surface, 30 tilt tests were performed in total for the two test groups. Figure 7.6a shows the placement of the rock cores on the utilised tilt apparatus. Whereas, Figure 7.6b depicts the method to achieve the tilt angle.

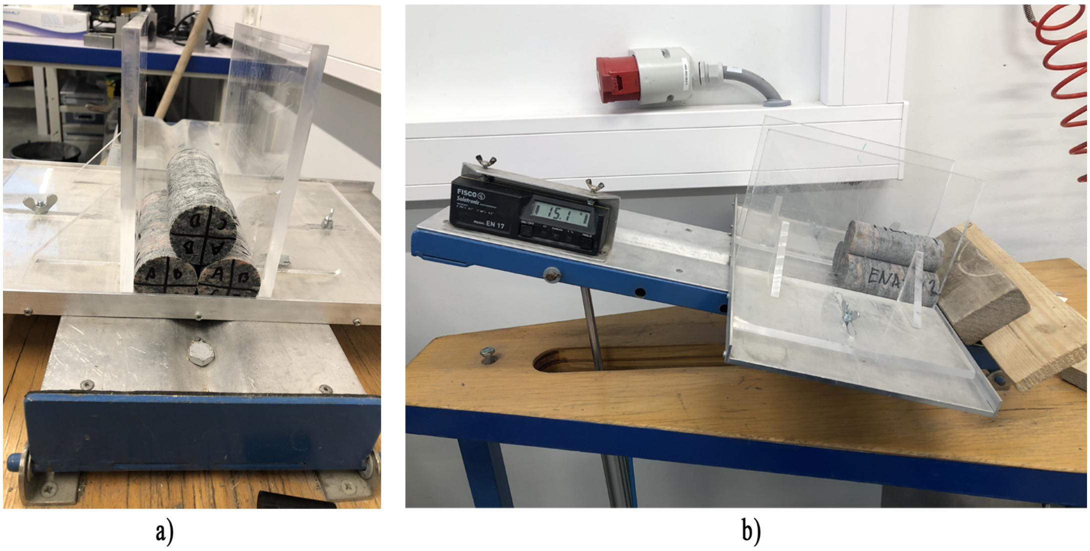

Figure 7.6: *a) Three-core contacts on the tilt apparatus b) Measuring av tilt angle (β) in the laboratory. The tilt starts with horizontal platform.*

ISRM (2018) recommends using the median to obtain a final result rather than an average value. This calculation method is preferred to avoid errors related to the occurrence of outliers. For three-core contacts, the median value for basic friction angle (ϕ_b) is calculated using Equation 7.6.

$$\phi_b = median\left[tan^{-1}\left(\frac{\sqrt{3}}{2}tan\beta_{i=1,\ldots,30}\right)\right] \tag{7.6}$$

From the tilt tests and Equation 7.6, the value of the basic friction angle (ϕ_b) for the six rock specimens is estimated to be 27.7°. In the case of unweathered joints, the residual friction angle is considered (ϕ_r) equivalent to the basic friction angle. On the other hand, for weathered joints, Equation 3.12 is applied to determine ϕ_r.

From Table 6.2, the foliation joint with the lowest JCS value, 80 MPa, is considered a weathered joint surface. While the foliation joint with JCS = 148 MPa is considered unweathered since theoretically, unweathered rock surfaces have a JCS value similar to the UCS value. The rebound numbers of L-type Schmidt hammer (RL) corresponding to these JCS values are applied in Equation 3.12 to obtain ϕ_r for weathered joints. Thus, following ϕ_r values are estimated:

Unweathered joints:

$$\phi_r = \phi_b = 27.7^\circ$$

Weathered joints:

$$\phi_r = (27.7 - 20) + 20\left(\frac{38}{48}\right) = 23.5^\circ$$

These residual friction angles are also assumed to be applicable for cross joints since a single cross joint has been registered in the background material provided by Tyréns in Table 6.2.

8 Stress assessment

8.1 Formation of final rock stress model

Figure 8.1 presents the steps to achieve the final rock stress model (FRSM) suggested by ISRM (2012). The figure below highlights the existing, new, and integrated data that have been feasible to obtain a stress model for this study.

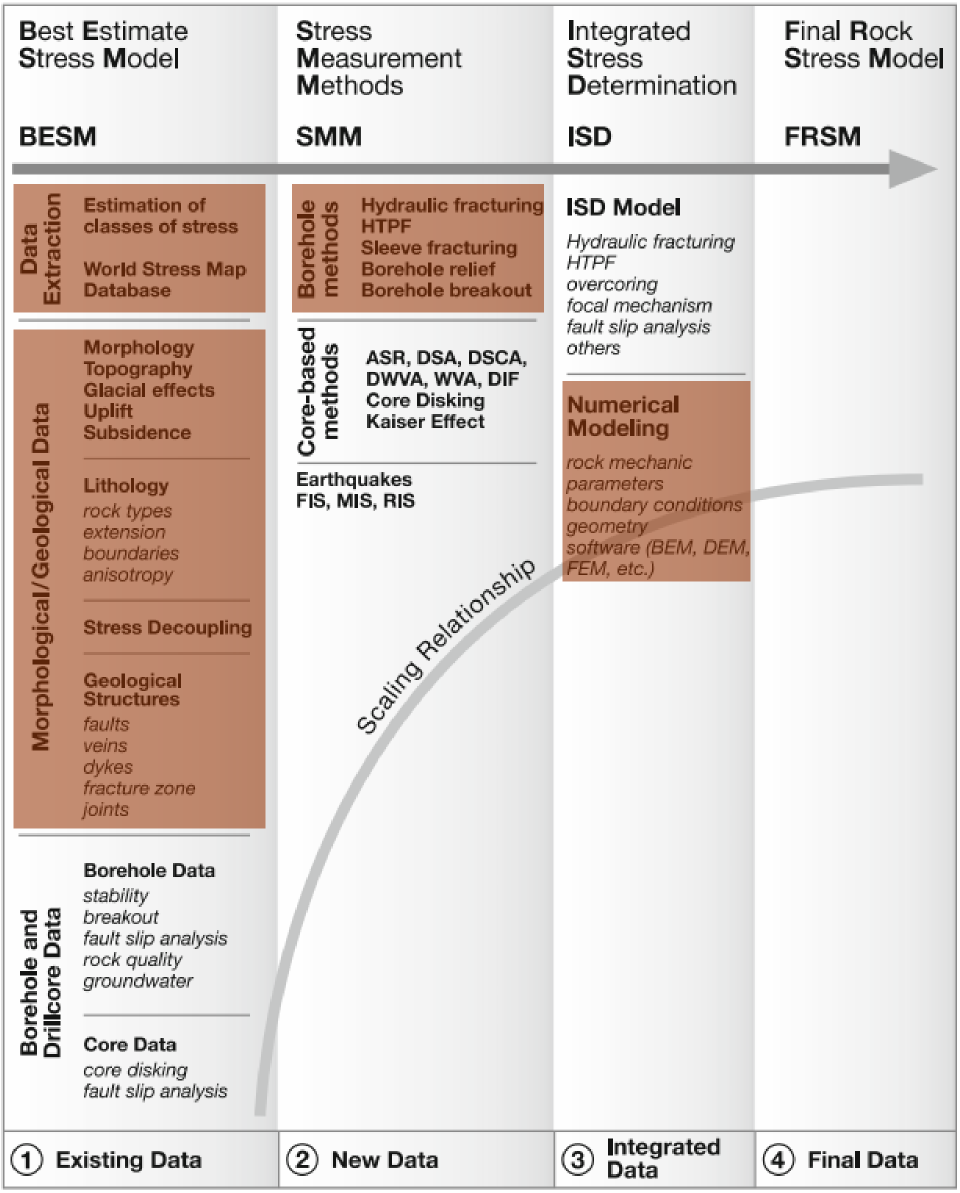

Figure 8.1: Establishment of the final stress model (FRSM) by combining best estimate model, new stress data and integrated stress determination. Red highlights present data utilised for the thesis work. From: ISRM (2012).

8.1.1 Best estimate stress model

The BESM is developed by collecting and analysing the existing data on morphology, topography, geology, borehole and drill core. ISRM (2012) recommends the development of BESM before conducting stress measurements. The function of BESM is to guide engineering geologists and geologists to select appropriate stress measurement techniques and assist in measurement planning. The scope of the master thesis does not involve the author's planning and selection of stress measurements in Mellanplan. Although stress measurements in Mellanplan and locations nearby were conducted before the thesis work, the data required for BESM are valuable for stress assessment. The World Stress Map and geological data are presented beforehand in Chapter 6. These data provide information to determine stress classes and how various factors influence stress conditions.

Based on the existing data, the in-situ stress state in Mellanplan is assumed to consist of gravitational stresses, tectonic stresses and residual stresses. It is common to predict that gravitational stresses exist due to the rock overburden above the access cavern. Moreover, the bedrock in Gothenburg has been subjected to tectonic activities resulting in the development of both regional and local faults. Therefore, it is reasonable to estimate the influence of tectonic stresses on the in-situ stress condition at Mellanplan.

The geology and stress conditions in Sweden have been affected by various periods of glaciation and ice melting. Due to incomplete isostatic recovery from deglaciation, the stress conditions in Sweden, thus Gothenburg, include residual stresses (locked-in stresses). Therefore, high horizontal stresses are expected to occur, considering that tectonic and residual stresses are a part of the stress state in Gothenburg. Consequently, high K-values may be obtained from the stress field in Mellanplan.

Considering the low overburden above the access cavern in Korsvägen, the stresses can be more sensitive to factors such as topography, anisotropy and geological structures. Destressed rock blocks and zones can create anomalies in in-situ horizontal stress estimations. The topography in central Gothenburg does not include high mountain tops and valleys. Therefore, the impact of topography on the virgin stress state in Mellanplan can be considered relatively minimum. As reported by BeFo (2022), the topography has no influence on the stress state at shallow depths in central Gothenburg, except for an area called Ramberget.

8.1.2 Stress measurement method

In the West Link Project, a 2D doorstopper was selected as a measurement method in Mellanplan. The stress measurements were conducted after the excavation of pilot tunnels, thus cannot be considered virgin stress measurement procedure. Nevertheless, the reported secondary stresses can be utilised to back-calculate the in-situ stress state.

It should be stressed that the scope of this thesis involves the application of 2D doorstopper results for back-calculation. Hence, the results from 3D overcoring will not be utilised for back-calculation and will solely be discussed to compare with final numerical stress results.

8.1.3 Integrated stress determination

The Integrated Stress Determination model involves a combination of various stress measurement techniques to determine the in-situ stress conditions. The ISD model is more beneficial than the conventional single measurement method as it increases the reliability in in-situ stress determination. The ISD model also includes employing numerical analyses to predict the in-situ stress field. The results from conducted stress measurements should be used to validate the results from numerical modelling. In case of deviation between measurements and numerical analyses, the models can be calibrated. In addition, numerical models can also be applied to obtain an understanding regarding variability of in-situ stresses and measurement uncertainties (ISRM, 2012).

At Mellanplan, only 2D doorstopper measurements have been conducted. Thus the ISD model is achieved by combining the doorstopper results with numerical analysis. The stresses from doorstopper measurements are evaluated before utilising them to generate the best-fit in-situ stress model through 3D stress analyses and back-calculations.

8.2 Evaluation of doorstopper results

The horizontal stresses derived from the 2D doorstopper method show widespread in the results. Figures 6.22 and 6.23 illustrate scattering data of horizontal stresses above both pilot roofs. Furthermore, the minor horizontal stresses are reported as negative stress components by SINTEF (2022a). Since the doorstopper measurements calculate the secondary or tangential stresses in Mellanplan and not the virgin stresses, the equipment may have measured tensile stresses in Mellanplan. Tensile stress is a negative stress magnitude that occurs when the minimum tangential stress is less than the tensile strength of the rock. Tensile stresses can also arise when existing discontinuities open.

The negative stress components have also been discussed with the research engineer, Trond Erik Larsen, at SINTEF Community. According to Larsen (2022), one of the significant challenges while conducting 2D doorstopper measurements is the incapability of assessing the rock mass conditions surrounding the borehole. Cracks formed during blasting or unknown open joints nearby the borehole can affect the stress measurements and thus obtain stresses as negative components. Larsen also stated that the negative stress components could also result from a combination of low strain values and high E-modulus. Low strain and high E-modulus make the back-calculation of stresses sensitive and may increase the calculation uncertainty. Therefore, tensile stresses are not necessarily the only explanation for negative stress components. Given the low values of minor horizontal stresses, both Larsen (2022) and Olsson (2022c) recommend assuming them as gravity-induced horizontal stresses.

The effect of anisotropy at the West pilot can be the cause of the significant variation between major horizontal stresses (0.5 MPa - 13.1 MPa) at a relatively short borehole depth. The doorstopper measurement at the West pilot was performed in granodiorite gneiss. The laboratory work presented in Chapter 7 shows that gneiss in Mellanplan is anisotropic, as the foliation angle affects the uniaxial compressive strength (Figure 7.4). In addition, the Anisotropy Index ($I_{a(50)}$) classified the gneiss as a fairly to moderately anisotropic rock. The analysis of 2D doorstopper measurements is based on linear elasticity and assumes isotropic rock conditions. Therefore, it is reasonable to consider that the calculated stresses at the West pilot may be affected by some inaccuracy.

The stress measurement at the East pilot was carried out in metabasite. The rock mass containing metabasite has been reported as blocky rocks during mapping. Since metabasite in Mellanplan is not schistose and, according to Trafikverket (2016a) is a very weakly foliated rock mass, it is appropriate to estimate that the metabasite is quasi-isotropic to fairly anisotropic rock. The variation between major horizontal stresses in the East pilot is significantly less than in the West pilot (Figures 6.22 and 6.23). This can be an indication of metabasite having more isotropic conditions than gneiss.

Tables 6.9 and 6.10 reveal that the strain differences ($\epsilon_0 + \epsilon_{90} - \epsilon_{45} + \epsilon_{135}$) are generally less in East pilot than in West pilot. As previously mentioned in Section 5.3.2, a low difference in the orthogonal strains indicates good quality measurement. For the purpose of this study and the uncertainties related to anisotropic conditions and strain differences, it is decided to focus solely on the stress results from the East pilot (Olsson and Dammyr, 2022). Metabasite is a blocky rock, very weakly foliated, and the low strain differences from the measurement indicate good results. Therefore, the assumption of metabasite approaching more isotropic conditions than gneiss is appropriate. The doorstopper measurements from the East pilot are more reliable for the back-calculation of the primary stress state.

8.3 Stresses relative to Mellanplan

The horizontal stresses presented in Section 6.6.3 have magnitudes and orientations with respect to the north direction. The directions of major horizontal stresses are given as angles from the north, with minor horizontal stresses oriented perpendicular to σ_H. For the back-calculation of in-situ stresses from the 3D numerical model, *RS3*, the secondary stresses have to be resolved with respect to the orientation of Mellanplan. In the *RS3* models, the normal stress along Z axis (σ_{ZZ}) represents stresses due to the vertical overburden (z) of the rock mass. The 3D numerical models present induced horizontal stresses along the X and Y axes (σ_{XX} and σ_{YY}), where the length axis of the top heading is in the direction of the Y axis.

In order to compare σ_{XX} and σ_{YY} obtained from *RS3* models with the measured secondary stresses, the latter is resolved to stresses in the X and Y directions of Mellanplan. Consider that measured σ_H makes an angle θ with the Y axis (length axis of Mellanplan) as illustrated in Figure 8.2, where the orientation of σ_h is perpendicular to σ_H. The horizontal stresses along the X and Y directions of Mellanplan, σ_{XX} and σ_{YY} are calculated by using σ_H and σ_h in Equations 8.1 and 8.2, suggested by Basnet and Panthi (2019). These equations take into account the effect of horizontal shear stresses τ_{YX} and τ_{XY}, presented in Figure 8.2. It should be recalled that the orientation of Mellanplan is N11W. The equations below are derived for a linearly elastic model, where the material is anticipated to exhibit linear stress-strain behaviour.

$$\sigma_{XX} = \sigma_H cos^2\theta + \sigma_h sin^2\theta \tag{8.1}$$

$$\sigma_{YY} = \sigma_H sin^2\theta + \sigma_h cos^2\theta \tag{8.2}$$

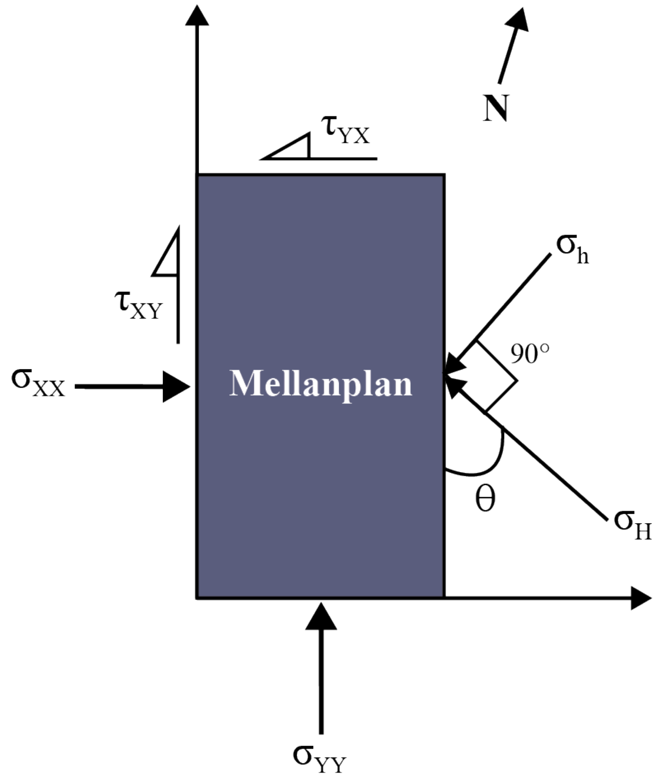

Figure 8.2: *Resolved horizontal stresses, σ_{XX} and σ_{YY} in X and Y directions of Mellanplan.*

Table 8.1 introduces the calculated σ_{XX} and σ_{YY} at the East pilot, by applying Equations 8.1 and 8.2. For clarification, the resolved secondary stresses from the doorstopper will have the stress notifications: $\sigma_{XX(D)}$ and $\sigma_{YY(D)}$. Due to uncertainties regarding the negative stress components, they will be neglected while estimating the in-situ stress conditions in Mellanplan. It should be noted that the negative stress components are ignored rather than assuming them to have a magnitude of 0 MPa.

Table 8.1: *Resolved secondary stresses $\sigma_{XX(D)}$ and $\sigma_{YY(D)}$ from the doorstopper at the East pilot. The angle between Mellanplan and σ_H is positive in the counter-clockwise direction.*

Hole depth [m]	σ_h **[MPa]**	σ_H **[MPa]**	α_H **[°]**	**Angle between Mellanplan and σ_H [°]**	$\sigma_{XX(D)}$ **[MPa]**	$\sigma_{YY(D)}$ **[MPa]**
1.3	-1.1	0.2	N142E	27	-0.8	-0.1
2.5	-1	3.6	N22E	147	0.4	2.2
2.8	-0.4	3.6	N136E	33	0.8	2.4
3.2	-2.3	0.2	N132E	37	-1.4	-0.7
3.6	-0.3	1.5	N172E	-3	-0.3	1.5
4.1	0.4	3.7	N0E	169	0.5	3.6
				Mean value of positive components	0.6	2.4
				Std. deviation of positive components	0.2	0.9

The mean rock cover at the stress measurement location of the East pilot is approximately 12 m. While, the borehole depth with stress measurements above the East pilot end at 4.1 m. Figure 8.3 presents the calculated values of $\sigma_{XX(D)}$ and $\sigma_{YY(D)}$ against hole depth at East Pilot as a scatter plot. The spread of stress data shown in the scatter plot below is as anticipated for stress conditions at shallow depths. The effect of weathering and geological structures on stresses is more likely to occur near surface grounds due to the open joints. Such complexity at shallow depths leads to scattering results, where the stress measurement does not provide a certain trend in data. It is challenging to obtain similar scattering results in numerical modelling. According to Trinh (2022), it is recommended to compare the results from numerical modelling with a range of doorstopper stress data. Instead of selecting random stress values at a scatter plot, an average interval for the entire borehole length should be used to validate the results from numerical stress analyses.

In conclusion, the average intervals for $\sigma_{XX(D)}$ and $\sigma_{YY(D)}$ are determined by the mean values and standard deviations of the positive stress components as shown in Figure 8.3. The mean values and standard deviations include the entire borehole length. The mean value of positive $\sigma_{XX(D)}$ is 0.6 MPa with a standard deviation of 0.2 MPa. While the mean value of positive $\sigma_{YY(D)}$ components is 2.4 MPa with a standard deviation of 0.9 MPa.

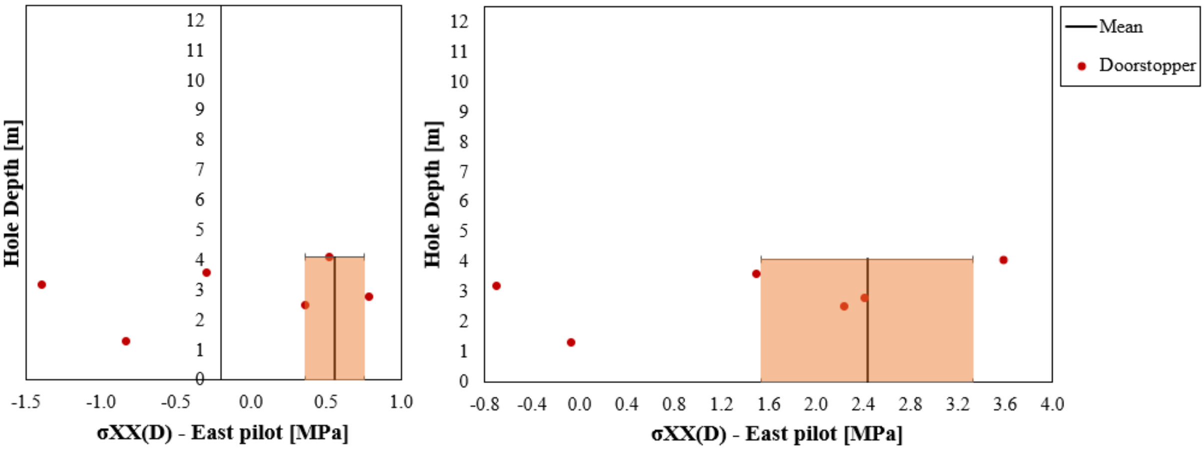

Figure 8.3: Resolved horizontal stresses, $\sigma_{XX(D)}$ and $\sigma_{YY(D)}$ at East pilot. The vertical line in each plot depicts the mean value of the positive components, while the marked area is the standard deviation.

9 Numerical modelling

The main objective of the numerical analyses conducted is to back-calculate the in-situ stress state at the entire top heading area of Mellanplan. The results from back-calculation are further applied to evaluate and compare displacements obtained from numerical models with the monitored deformation. The executed field work and laboratory test results provide insight into the selection of input parameters in the numerical models. Additional knowledge from the background materials provided by Trafikverket and SINTEF are also valuable for the parameter selection.

The numerical analyses are performed in *RS3* and *RS2*. *RS3* is applied to back-calculate in-situ stress, while *RS2* is utilised to assess the deformation. 3D parametric stress analysis is conducted and compared with the doorstopper results to estimate the virgin stresses in the area. In addition, 2D analyses of supported rock mass with two different joint conditions are carried out. The latter is to evaluate whether the deformation of the tunnel crown from numerical calculations corresponds to the monitored deformation.

Simplifications, assumptions and approximations have been made during numerical modelling to reduce their complexity. Still, the results achieved are considered to be representative of the ground conditions. In numerical modelling, there are often limitations regarding the modelled rock mass being entirely accurate with the actual rock mass conditions. Therefore, an understanding of uncertainties is essential for the interpretation of the results. Selections regarding model setup and input parameters are discussed in the following sections.

9.1 Applied software

RS3 is a 3D numerical analysis software, while *RS2* is 2D. Both numerical software are based on the continuum approach (Rocscience, 2022d; Rocscience, 2022c). The rock mass is modelled as a continuous medium which poses limitations regarding the representation of discontinuities. The finite element method (FEM) is applied in both *RS3* and *RS2*. As stated by Jing (2003), three steps are required to complete a FEM analysis: 1) domain discretisation, 2) local approximation and 3) assemblage and solution of the global matrix equation. Domain discretisation consists of dividing a domain into a finite number of continuous integral elements defined by a fixed number of nodes. When setting up a model in *RS3* and *RS2*, geometry, boundary conditions of the domain, mesh, input parameters and the initial ground state are required to be defined.

The reason behind selecting *RS3* and *RS2* for the thesis work is due to their availability at NTNU, and they are relatively user-friendly numerical modelling programs. FEM analyses are widely used in rock engineering to study stress and stability issues regarding the design and rock support (Broch et al., 2016). Such analyses are generally applied to extrapolate experience, to include conditions that have not been encountered or to enhance the knowledge of various mechanisms. There are various benefits of utilising FEM for rock engineering purposes. This numerical method has the capacity to run multiple materials in a single model, and it can take into account boundary conditions and complex geometries. An additional advantage of FEM is its ability to allow material failure and deformation (Nikolic et al., 2016). Nonetheless, there are limitations within FEM since it is based on the continuum method. Hence, it has limitations regarding its efficient usage of failure analysis, cracking and damaged-induced discontinuities. Unlike DEM, FEM programs do not include the detachment of individual blocks (Hammah et al., 2008).

9.2 Selection of input parameters

The knowledge on the rock mass quality in Mellanplan provides valuable insight into the selection of input parameters. As presented in Section 6.5.3, the rock mass quality varies based on the applied classification system. Since the West Link Project predominantly utilises Q$_{bas}$, the rock mass quality defined by the RMR-system has been neglected while assessing the input parameters.

The rock mass quality based on Q$_{bas}$ varies along the pilots in Mellanplan. The complexity in the numerical models increases when the medium is divided into sections with various rock mass qualities. Therefore, a single Q$_{bas}$ value that can best represent the whole rock mass is considered for the numerical modelling. The average and median values of Q$_{bas}$ in the West pilot are 7.4 and 5.6, respectively. Whereas in the East pilot both average and median Q$_{bas}$ is 7.3. Due to the fluctuating variation on Q$_{bas}$ along the tunnels, the median value has been chosen instead of the average value. A Q$_{bas}$ value between 5.6 and 7.3 is acceptable to represent the simplified rock mass model. Hence, Q$_{bas}$ = 6 is selected as the rock mass quality to describe the rock mass in Mellanplan.

The results from numerical analyses depend on the accuracy of the input parameters for rock mass and rock support. In the following sections, considerations regarding the selection of input parameters are discussed. The input parameters utilised in the numerical models are based on rock mass quality, laboratory test results, previously executed field investigations and literature on the topic.

9.2.1 Failure Criterion

The failure criterion utilised in the numerical models is the Generalized Hoek-Brown failure criterion (Hoek et al., 2002). In Section 3.5.2 applicability of the failure criterion and joint sets are discussed. Although there are two major joint sets in Mellanplan, the Generalized Hoek-Brown is selected due to low overburden. In West Link Project, when numerical calculations have been performed in terms of the Mohr-Coulomb failure criterion, its equivalent parameters have been achieved by fitting an average linear relationship to the non-linear Hoek-Brown envelope (Olsson, 2022a). Due to the shallow seated Mellanplan, a low value of σ_{3max} is expected, which will not provide an adequate relationship between the criterion envelopes. The West Link Project generally applies σ_{3max} = 3 MPa for rock tunnels (Trafikverket, 2016c). A combination of σ_{3max} with relevant input parameters for Generalized Hoek-Brown presented in the sections below, provides the stress plot shown in Figure 9.1. The envelopes of the failure criteria overlap each other, where the best-fitted Mohr-Coulomb is challenging to identify. Thus, it is more secure to apply the Hoek-Brown failure criterion.

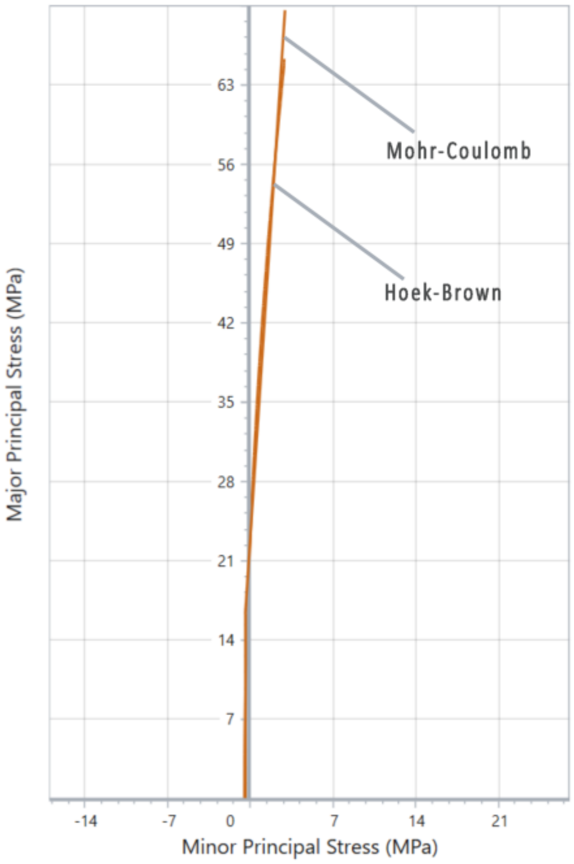

Figure 9.1: *Overlap between Hoek-Brown criterion and Mohr-Coulomb criterion in Mellanplan when* σ_{3max} *= 3* MPa*. Generated in RSData (Rocscience, 2022e).*

9.2.2 Unit weight

The rock types mapped in the pilot tunnels at Mellanplan are granodiorite gneiss and metabasite. Granodiorite gniess is the dominating rock type. Metabasite observed in the East pilot does not appear alone, and intertwines with the gneiss. Therefore, the rock mass is described with the density of granodiorite gneiss obtained from the laboratory work. The laboratory results (Table 7.1) show the average density value as 2680 kg/m^3, approximately equivalent to the median value. This gives a unit weight of 0.0268 MN/m^3, which is applied in the numerical models.

9.2.3 Poisson's ratio

The laboratory results shown in Table 7.2 present the median and mean value of Poisson's ratio as 0.25 and 0.26, respectively. Although the Poisson's ratio for gneiss provided by SINTEF (Table 7.3) has lower values, Trafikverket recommends the typical value of ν as 0.25 for Q_{bas}=6 (Trafikverket, 2016c). In conclusion, Poisson's value of 0.25 has been used in the numerical analyses.

9.2.4 Young's modulus and deformation modulus

RS3 models

Table 6.6 shows the typical value of Young's modulus (E_i) as 70 GPa, recommended at the West Link Project. The laboratory results present E_i = 72.52 GPa as a median, and E_i = 74.53 GPa as a mean value for granodiorite gneiss. These values are close to the suggested typical value. Therefore, in this case, E_i = 70 GPa is selected as input.

Since Young's modulus is applicable for intact rock, the modulus of deformation has to be determined for the rock mass. In this study, the rock mass deformation modulus equation suggested by Hoek and Diederichs (2006) has been applied (Table 3.5), which gives E_{rm} value of 44 GPa.

RS2 models

In *RS3* models, joints are included indirectly through GSI. However, in *RS2* models, the discontinuities are modelled directly and defined by joint properties. The rock blocks between the joints can behave as intact rocks. Nevertheless, the existence of micro discontinuities in these rock blocks should be considered. According to Olsson (2022a), at the West Link Project, it is recommended to use deformation modulus for rock mass with Q$_{bas}$ > 10 to describe these rock blocks. Trafikverket (2016b) suggests that the typical value for E_{rm} when Q$_{bas}$ > 10 is 50 GPa. Thus, E_i = 80 GPa is selected as an input to achieve E_{rm} = 50 GPa, using the deformation modulus equation suggested by Hoek and Diederichs (2006). These rock blocks are supposed to depict a similar behaviour as an intact brittle rock.

9.2.5 UCS

The typical value for UCS suggested by Trafikverket is 140 MPa, as shown in Table 6.6. The laboratory results show the median and mean for UCS as 144 MPa and 158 MPa, respectively. After discussing with the supervisor, the selected UCS value of 145 MPa is used (Olsson, 2022b). The model input for UCS is slightly higher than the recommended typical value from Trafikverket. This selection is made due to the higher mean value for UCS achieved from the laboratory results.

When the Generalized Hoek-Brown failure criterion is selected in the applied Rocscience programs, the rock mass strength (σ_{cm}) is automatically calculated based on the empirical formula suggested by Hoek et al. (2002), presented in Table 3.4. This results in σ_{cm} = 20.6 MPa.

9.2.6 GSI

The input on GSI is based on geological mapping, Equation 4.5 and photogrammetry, as discussed in Section 6.5.3. Table 9.1 presents the GSI values estimated for the rock mass in Mellanplan. A GSI value of 65 is selected since it is an approximate average of the GSI values presented in the table below.

Table 9.1: *GSI values derived from various evaluation methods in Section 6.5.3.*

Evaluation method	**GSI**
Geological mapping	55-70
Equation 4.5	60
Photogrammetry	60-75

9.2.7 Hoek-Brown constant, m$_i$

The typical and maximum values for m_i, recommended by Trafikverket are 13 and 20 (Table 6.6). However, the numerical software *RS3* and *RS2* suggest the Hoek-Brown constant as 28 for gneiss. The maximum m_i value suggested by Trafikverket is considered low for gneiss (Olsson, 2022b). Hence, m_i = 28 is selected as input.

9.2.8 Disturbance factor, D

The disturbance factor, D, is considered equivalent to zero. This value for the disturbance factor is applicable for controlled blasting. Since the tunnels in the top heading are shallow-seated, it is logical to assume that the pilots are excavated with careful blasting to avoid local damage in the surrounding rock mass.

9.2.9 Joint properties

As a result of model complexity and obtaining reasonable computation time, *RS3* models do not include joints directly. On the other hand, *RS2* showed good compatibility to be computed with a joint network. Nonetheless, simplifications of the joint network in 2D models are still required to avoid unnecessary computation difficulties. Table 9.2 presents the joint properties applied in the *RS2* models. The two major joints, foliation and cross joints, are utilised in the 2D numerical analyses. The input parameters for joints also vary depending on the weathering condition.

Q_{bas} = 6 is classified as acceptable rock mass quality. However, the rock mass classification describes that slightly weathered joints can appear when Q_{bas} has a value between 4 to 10. Furthermore, altered joints with calcite, chlorite or clay are expected to occur when Q_{bas} = 6 (Trafikverket, 2016b). The evaluation of joint characteristics presented in Table 6.1 indicates variation between unaltered and slightly altered joints. Tunnel mapping of the East pilot (Appendix B) demonstrates slightly weathered rock mass throughout the entire pilot, except for profile 0/023 to profile 0/026 which is registered as highly weathered. Similarly, the tunnel mapping of the West pilot demonstrates mostly unweathered and slightly weathered rock mass throughout the tunnel. The only exception is registered from tunnel profile 0/040 to 0/045, where the rock mass is moderately weathered. Due to the variation regarding the weathering of rock surfaces, both weathered and unweathered conditions are utilised for joints in 2D modelling.

Table 9.2: *Joint properties in RS2 models.*

Material property	Unit	Joint type		Source
		Foliation joints	**Cross joints**	
Failure/Slip criterion	-	Barton-Bandis		
Inclination	Degree	34°SW	17°NE	Appendix F
Spacing	Metre	0.6	2	Table 6.1
Length	Metre	Infinite	15	Table 6.1
JCS	MPa	Unweathered: 145 Weathered: 80	110	Table 6.2
JRC	-	Unweathered: 9 Weathered: 4	9	Table 6.2
ϕ_r	Degree	Unweathered: 27.7 Weathered: 23.5		Laboratory results
Normal stiffness	GPa/m	50		Trafikverket (2016b)
Shear stiffness	GPa/m	25		Trafikverket (2016b)

For foliation joints in weathered conditions, JCS = 80 MPa from Table 6.2 is applied. Its corresponding JRC value of 4 is also considered input for weathered foliation joints. Theoretically, JCS is equal to UCS when the joints are considered unweathered. Therefore, JCS = 145 MPa is applied for unweathered foliation joints. In Table 6.2, foliation joint with JCS value close to 145 MPa is associated with JRC equivalent to 9-10. For model input, JRC = 9 is chosen for unaltered foliation joints. For cross joints, a single Schmidt hammer result is provided in Table 6.2. Therefore, JCS and JRC values are selected to be identical for both weathered and unweathered cross joints. The residual friction angles for weathered and unweathered joints are obtained from laboratory tilt tests and Equation 3.12.

Joint inclinations in 2D models are apparent dips, which are determined by utilising an apparent dip nomogram. The complexity in *RS2* models is reduced by defining the joint spacings with the greater distances shown in Table 6.1. Furthermore, the length of cross joints is limited to 15 m, although they have similar persistence as foliation joints.

9.2.10 Rock stresses

The back-calculation of in-situ stresses in this thesis work is conducted by parametric analysis of stresses. The stress parameters such as K-values (horizontal to vertical stress ratio), stress orientations and locked-in stresses are the main input that can induce changes in the stress field. The horizontal in-situ stresses are the variable input, whereas vertical in-situ stress is a constant parameter. The vertical stress (σ_v) is considered equivalent to the vertical gravitational stress since it is a common estimation in Scandinavia. Note that the stress input in *RS3* defines in-situ stresses, while the numerical results after the excavation present secondary stresses.

In this study, the secondary stresses from *RS3* models are compared with the stresses from the doorstopper measurements. *RS3* presents the induced horizontal stresses as σ_{XX} and σ_{YY} in X and Y axes of Mellanplan. Therefore, with the purpose of comparing the numerical results with the measured stresses, doorstopper measurement results have been resolved to $\sigma_{XX(D)}$

and $\sigma_{YY(D)}$ in Sub-chapter 8.3. Figure 9.2 illustrates the directions of σ_{XX} and σ_{YY} for both resolved stresses from the doorstopper and the stress components shown by the results in *RS3*.

Initially, the input for major horizontal in-situ stress, σ_H is varied between N80E and N150E (Figure 9.2) based on the stress orientations from overcoring, in-situ stress estimation by BeFo and the World stress map. The orientations of σ_H parallel or close parallel to Mellanplan (N160E-180E) are ignored as input in this study, considering they indicate a complete rotation of the stresses compared to stress directions derived from overcoring estimation. The overcoring measurement locations are nearby the access cavern. Even though the possibility of a complete stress rotation is plausible, it is considered unlikely and is therefore not investigated further (Olsson and Dammyr, 2022).

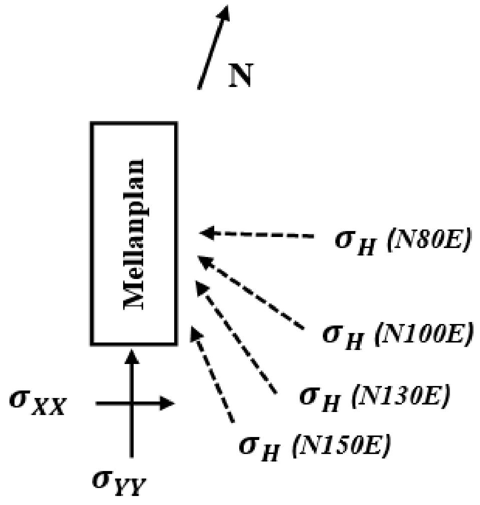

Figure 9.2: *Orientations of secondary stresses in RS3 (σ_{XX} and σ_{YY}) and model input for major horizontal in-situ stress (σ_H) with varying directions.*

The input for the orientation of minor horizontal stress, σ_h, in *RS3* is automatically set perpendicular to σ_H. From the main results, in-situ stresses at the top heading of the access cavern are determined. The in-situ stresses obtained from the 3D analyses are further applied as stress input in 2D analyses.

9.2.11 Loading

The soil cover in numerical models is decided to be modelled as a uniform load. According to Trafikverket (2016c), the soil density in Korsvägen is 1800 kg/m^3. This gives a uniform load of 0.094 MPa.

9.2.12 Rock support

Rock support is not included in *RS3* models, as it does not influence the rock stress condition in the rock mass after the opening of the pilot tunnels. However, rock support is applied for 2D analyses, since the function of rock support is to reinforce, hold and retain the rock mass. The 2D analyses are performed to evaluate the deformation of the pilot tunnels after the excavation. The input parameters for the rock support are presented in Table 9.3 and in Table 9.4. The bolt lengths, spacings and shotcrete thickness vary as they follow the rock support design shown in Table 6.11. The rest of the rock support properties are based on the recommendations by Trafikverket.

Table 9.3: *Bolt properties applied in RS2 models.*

Bolt property	Unit	Data	Source
Bolt type	-	Fully bonded	-
Bolt diameter	Millimetre	25	Trafikverket (2016b)
Bolt Modulus	MPa	200 000	Trafikverket (2016b)
Tensile Capacity	MN	0.246	Trafikverket (2016b)
Out-of-plane spacing	Metre	1.5	Trafikverket (2022b)
In-plane spacing	Metre	1.35, 1.7 and 2	Table 6.11
Bolt length	Metre	3, 4, 5 and 6	Table 6.11

Table 9.4: *Liner properties applied in RS2 models.*

Liner property	Unit	Data	Source
Material type	-	Plastic	Trafikverket (2016b)
Liner type	-	Standard Beam	-
Young’s modulus	MPa	16 000	Trafikverket (2016b)
Poisson’s ratio	-	0.25	Trafikverket (2016b)
Compressive peak strength	MPa	30.5	Trafikverket (2016b)
Compressive residual strength	MPa	0	Trafikverket (2016b)
Tensile peak strength	MPa	4	Trafikverket (2016b)
Tensile residual strength	MPa	3	Trafikverket (2016b)
Thickness	Millimetre	50	Table 6.11

9.2.13 Discussion on input parameters

The rock mass in the numerical models is not divided into sections with various geological parameters. In reality, the geological parameters can vary over small distances. This has also been noted while studying the tunnel mappings of the pilots at Mellanplan. Therefore, the selected input parameters for numerical models are intended to give an overall good representation of the entire rock mass in the domain. The uncertainties related to the input data and the natural geological variation may affect, to a certain degree, the representation and the validity of the results.

The input parameters for UCS, Young’s modulus and Poisson’s ratio are based on the laboratory testing at the NTNU laboratory and the recommendations made by Trafikverket. The laboratory results on rock cores from Mellanplan, provided by SINTEF (2022a) are not used to determine the input for the mechanical properties of the intact rock. The main reason behind this is due to the significant difference between the UCS values. According to the laboratory results from SINTEF, the average UCS value for granodiorite gneiss and metabasite is 62 MPa and 97 MPa, respectively (Table 7.3). The UCS values suggested by SINTEF are much lower than the selected UCS input of 145 MPa. The explanation for this deviation is addressed in Subchapter 7.3. Additionally, Figure 9.3 depicts the UCS database for Norwegian rocks compiled by SINTEF. The bedrock in Norway is also a part of the Fennoscandian Shield, and therefore this database can be applied for rocks in Sweden as well. It should also be recalled that metabasite is a type of amphibolite. The figure below displays the median uniaxial compressive strength values for gneiss and amphibolite are above 100 MPa. Moreover, the upper quartile for gneiss lies around 150 MPa, while for amphibolite it is approximately 140 MPa. Following the comparison with this UCS database, the selected input for the uniaxial compressive strength in the models can be justified.

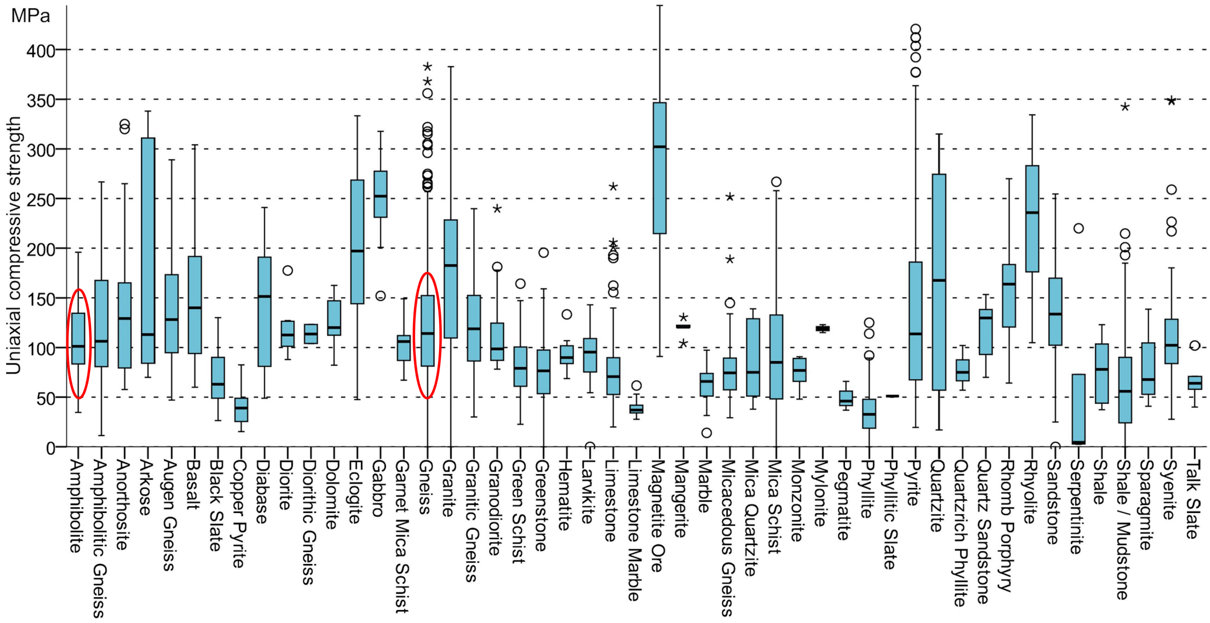

Figure 9.3: *SINTEF database on UCS for various rock types. Gneiss and amphibolite are circled. From SINTEF, reproduced by: Høien et al. (2019).*

SINTEF's laboratory results presented in Table 7.3 show that the average Young's modulus for granodiorite gneiss is similar to the selected input value. However, the mean E_i for metabasite is given as 89 GPa. The Young's modulus suggested by SINTEF surpasses Trafikverket's recommendation of E_i. Therefore, it is not considered for model input. However, the Poisson's ratio for metabasite, obtained by SINTEF is similar to the ν selected as input for the model.

The Hoek-Brown constant, m_i, utilised in the numerical models is not determined from laboratory tests. As stated earlier, the suggested m_i value by Trafikverket is assumed to be relatively low for gneiss. Therefore, the standard m_i value for intact gneiss, suggested by the Rocscience programs, is used. The standard value for gneiss is given with an uncertainty variation of ± 5. Furthermore, the disturbance factor in the models is set to zero, indicating that the rock mass surrounding the tunnels is not subjected to blast damage. In reality, the rock mass is likely affected to some degree by the blasting.

Overall, metabasite is less represented in the numerical models than granodiorite gneiss. This is mainly due to gneiss comprising the majority of the rock type registered in the tunnel mappings. Around 70% of the rock type consists of gneiss, according to the tunnel mapping data. The rest of the rock type is described as a mixture of granodiorite gneiss and metabasite appearing alongside each other. Most of the rock type at Mellanplan is observed to be gneiss, and thus the numerical models are best represented by it. Moreover, the absence of metabasite samples for laboratory investigations has also limited the opportunity to evaluate the rock properties of metabasite and compare them with the results determined by SINTEF.

Note that the residual rock parameters are not included as input for the numerical models. The 3D models are defined with continuous elastic material as they are only applied for stress analyses. Deformation is not evaluated in the *RS3* models, and thus do not require plastic analysis in the continuum model. Furthermore, the deformation analyses in *RS2* involve directly defined joints. The closely spaced joints are defined with a slip criterion and exhibit plastic behaviour, while the rock blocks between the joints are assumed to be similar to intact brittle rocks and thus behave elastically. Thus, the residual parameters to define the rock blocks between joints are not necessarily required in such model setups.

Simplifications and assumptions are often necessary in numerical modelling in order to manage computation successfully. The chosen input parameters are considered to represent the entire rock mass at the top heading in Mellanplan. Therefore, the results from the models should be studied as indications rather than an exact solution, as the variation in geological properties in nature may depict different in-situ rock stress and rock mass behaviour.

9.3 Stress analyses in 3D models

9.3.1 Model setup

The only section of the access cavern under construction is the top heading. Therefore, the excavation geometry in *RS3* models consists solely of the top heading. The cross-section of the excavation geometry is based on the theoretical blasting profile. A 2D CAD drawing of the pilot tunnels with the rock pillar, provided by Trafikverket (2022d), is imported into *RS3* and extruded to obtain a 3D volume. The profile of pilot tunnels and the rock pillar in the top heading follows the dimensions presented in Figure 6.3.

The geometry and geological conditions in the model setup have been subjected to some simplifications. Figure 9.4a illustrates the actual excavation geometry while Figure 9.4b depicts the shape of excavated pilot tunnels in 3D models. In the *RS3* models, the rock pillar at the first 10 metres of the top heading is removed, as well as the pilot tunnels.

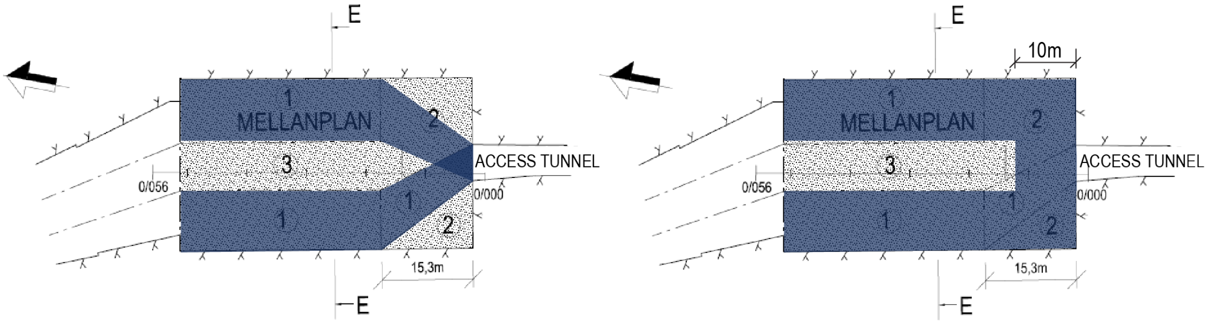

a) b)

Figure 9.4: *Plan view of Mellanplan from above. a) Blue overlay illustrates the actual excavation shape. b) Blue overlay shows the excavation shape in RS3 models. Figures modified after: Trafikverket (2022d).*

The total length of Mellanplan in the 3D models is 50 m. The 3D models consist of two stages, the initial stage and the excavation stage. Figure 9.5 presents the model setup used in 3D modelling, where the red volume depicts the volumes removed in the excavation stage. Joint planes are not generated directly in the *RS3* models. This simplification is made due to the complex generation of mesh when the discontinuities are included, and to obtain a reasonable computation time for stress analyses.

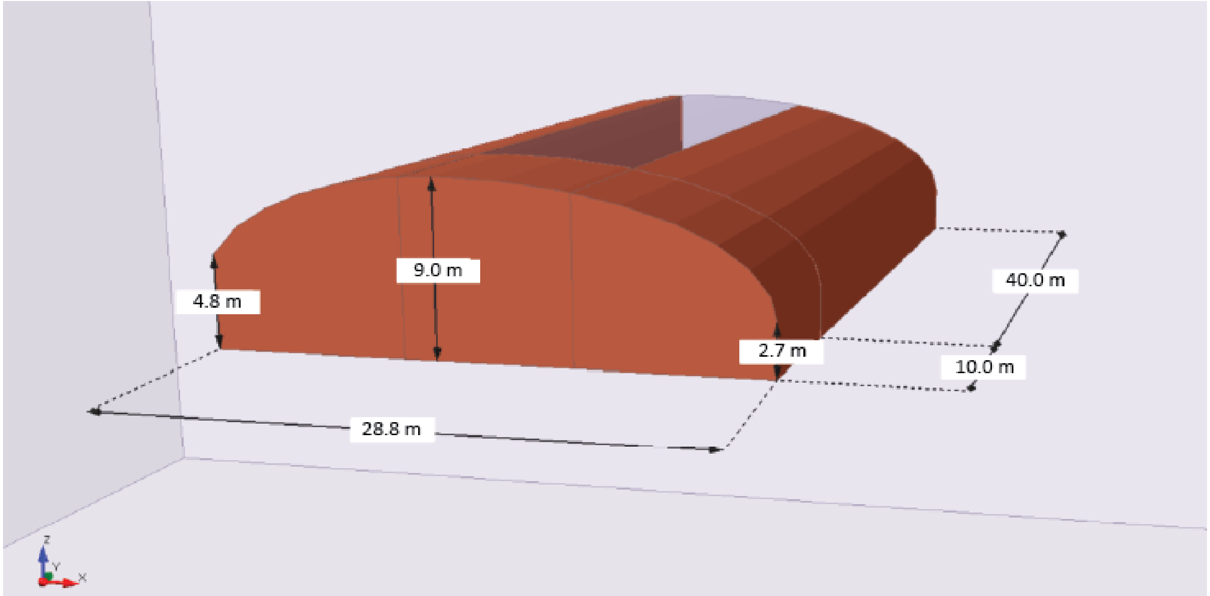

Figure 9.5: *Snippet of the model setup in RS3. The red volumes are removed during the excavation stage.*

The 3D models are linear elastic models where the rock mass is considered isotropic and homogeneous material on a large scale. This choice fits well since the calculated stresses from doorstopper measurements are based on linear elasticity and assume isotropic and homogeneous rock mass conditions. The model setup consists of a finer mesh near the excavation zone to increase the accuracy of rock mass behaviour around the tunnel periphery (Figure 9.6). The mesh setup involves graded mesh with 4-noded tetrahedra element type. The external boundary of an *RS3* model is chosen to prevent any influence from the boundary onto the excavation. The boundary conditions are defined with surface restrain, where the ground surface is free of restraints, and nodes are free to move in the Z-axis.

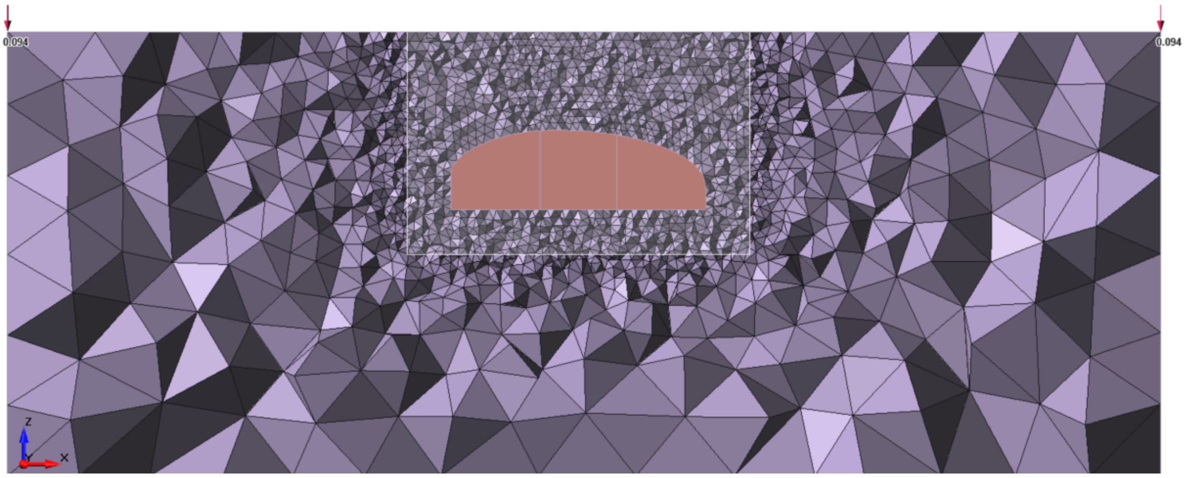

Figure 9.6: *Mesh setup in XZ plane in 3D modelling. The arrows at the ground surface illustrate a uniform load of soil.*

9.3.2 Stress notation and presentation

The 3D numerical analyses include various stresses and their presentations. Table 9.5 presents the notations for different stresses and parameters related to them. This overview includes descriptions to avoid misunderstanding of the various stresses discussed in this chapter.

Table 9.5: *Notations for stresses and parameters related to them.*

Notation	Description
σ_H	Major horizontal in-situ stress (Input stress in numerical models)
σ_h	Minor horizontal in-situ stress (Input stress in numerical models)
σ_v	Gravitational vertical in-situ stress (Input stress in numerical models)
σ_{XX}	Secondary stress perpendicular to Mellanplan in the numerical models
σ_{YY}	Secondary stress parallel to Mellanplan in the numerical models
$\sigma_{XX(D)}$	Secondary stress perpendicular to Mellanplan derived from doorstopper
$\sigma_{YY(D)}$	Secondary stress parallel to Mellanplan derived from doorstopper
σ_{LH}	Locked-in stress for major horizontal in-situ stress (Input parameter in numerical models)
σ_{Lh}	Locked-in stress for minor horizontal in-situ stress (Input parameter in numerical models)
α_H	Orientation of σ_H, with an angle from the north (Input parameter in numerical models)
K_H	Ratio between σ_H and σ_v (Input parameter in numerical models)
K_h	Ratio between σ_h and σ_v (Input parameter in numerical models)

The induced stresses from the numerical models and resolved stresses from the doorstopper are presented and compared with various graphs in Sections 9.3.4 and 9.3.5. Figure 9.7 displays an example of a graph and demonstrates the difference between the various stress plots.

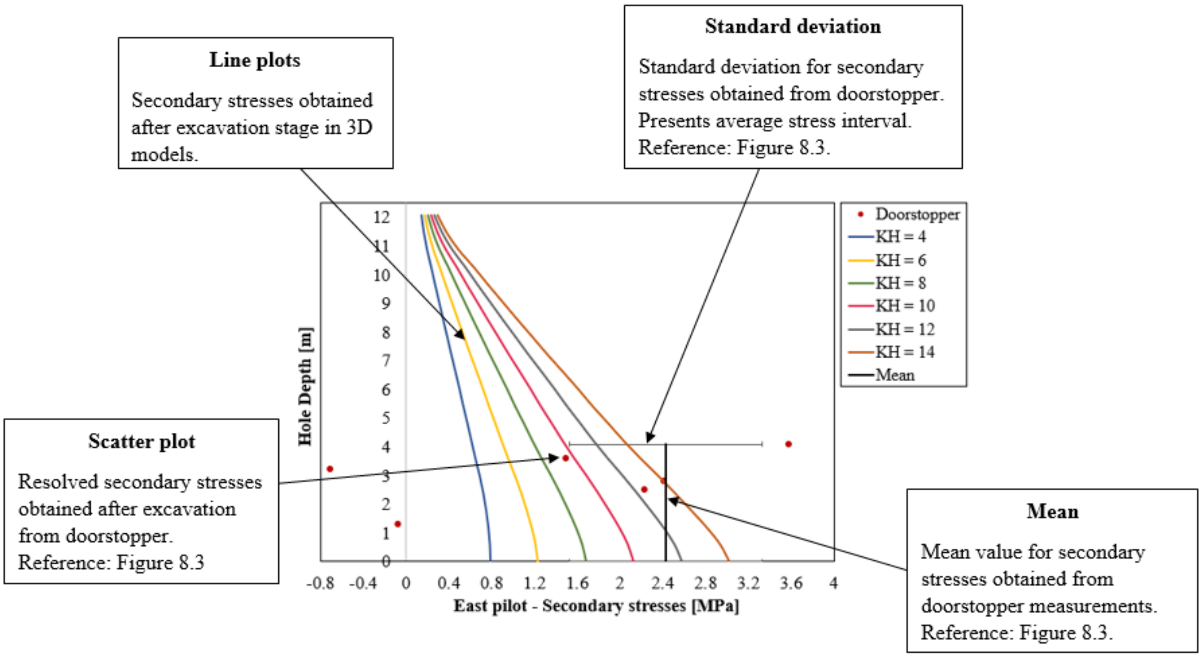
Line plots

Secondary stresses obtained after excavation stage in 3D models.

Standard deviation

Standard deviation for secondary stresses obtained from doorstopper. Presents average stress interval. Reference: Figure 8.3.

Scatter plot

Resolved secondary stresses obtained after excavation from doorstopper. Reference: Figure 8.3

Mean

Mean value for secondary stresses obtained from doorstopper measurements. Reference: Figure 8.3.

__Figure 9.7:__ Description of various stress plots utilised for stress analyses.

9.3.3 Model section for stress analyses

The stress results from *RS3* are obtained from a specific section at the top heading. Figure 9.8 displays σ_{YY} from one of the performed 3D analyses. The doorstopper measurement at the East pilot was conducted 28 m inwards from the south of Mellanplan. Therefore, the query line for stress analyses in the *RS3* models has been placed at the same location, as shown in Figure 9.8b.

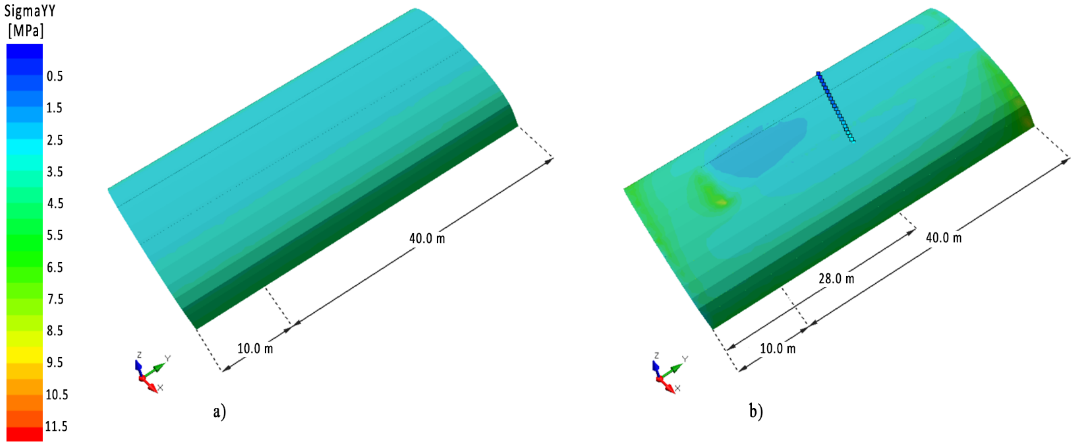

__Figure 9.8:__ a) Initial stage and b) Excavation stage with query line on the roof. The figures display σ_{YY} on the tunnel contour when input parameters are K_H = 10, K_h= 0.33 and α_H = N150E.

The secondary stresses from 3D models are obtained from the query line at the excavation stage. Figure 9.9 demonstrates a snippet of a 2D section from one of the *RS3* models. The query line is placed 2 m from the rock pillar to imitate the doorstopper placement at the East pilot. The query line starts from the roof at the East pilot and ends at the ground surface, with a length of approximately 12 m. The σ_{XX} and σ_{YY} results from the query line are plotted and compared with the stresses from doorstopper measurements.

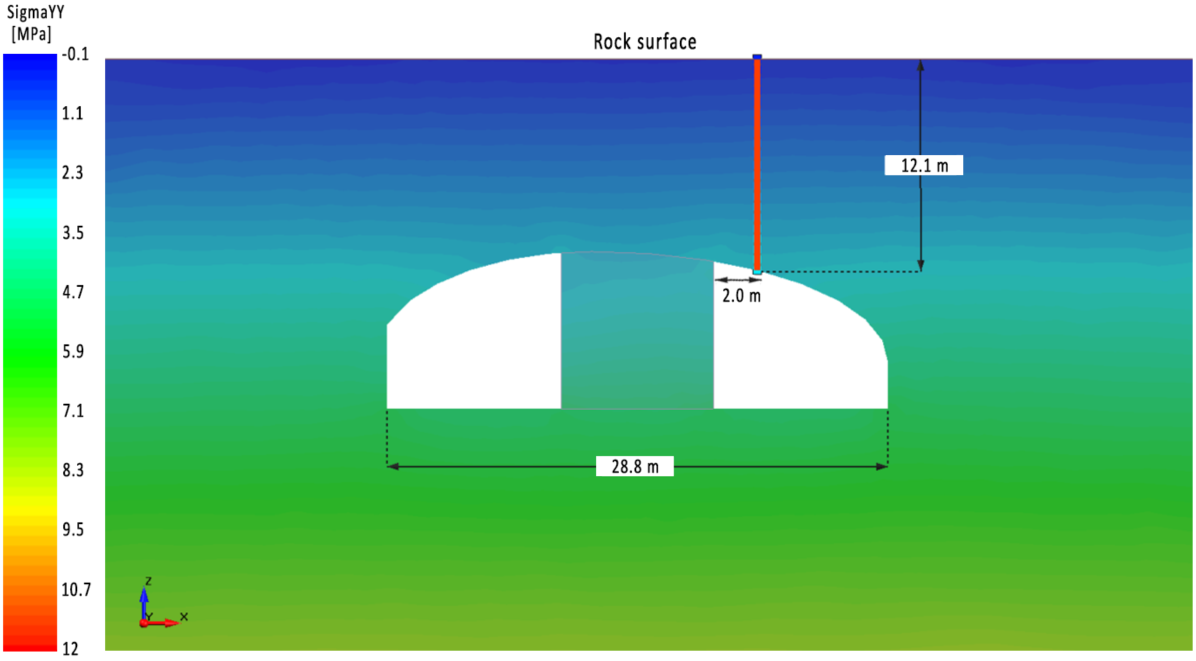

Figure 9.9: *Secondary (induced) stresses are obtained from the query line above the East pilot. The figure displays an example of σ_{YY} results from one of the 3D models, where input parameters are K_H = 10, K_h= 0.33 and α_H = N150E.*

9.3.4 Workflow

For stress analyses, many numerical trials have been conducted in *RS3* with various stress magnitudes and orientations as input. The rock properties and vertical stress (σ_v) are kept as constant parameters. With the purpose of determining representative back-calculated in-situ stresses at Mellanplan, the stress data from 3D overcoring and stress estimation data provided by BeFo, are initially used. Following these methods, a trial and error approach with different K-values and stress orientations is carried out. The main objective is to compare the secondary stresses achieved from numerical modelling with the stresses obtained from doorstopper measurements. Therefore, the numerical results that show the best fit with the mean stress value and lie within the standard deviation, presented in Figure 8.3, are considered the best estimate of stresses for the in-situ rock stress model.

Figure 9.10 below presents a workflow chart, illustrating the processes that lead to the final method for the back-calculation of in-situ stresses. The stress orientations for σ_H are given as angles from the north (α_H). The horizontal to vertical stress ratios (K-values) are considered stress ratios that exhibit a linear increase in stresses with depth.

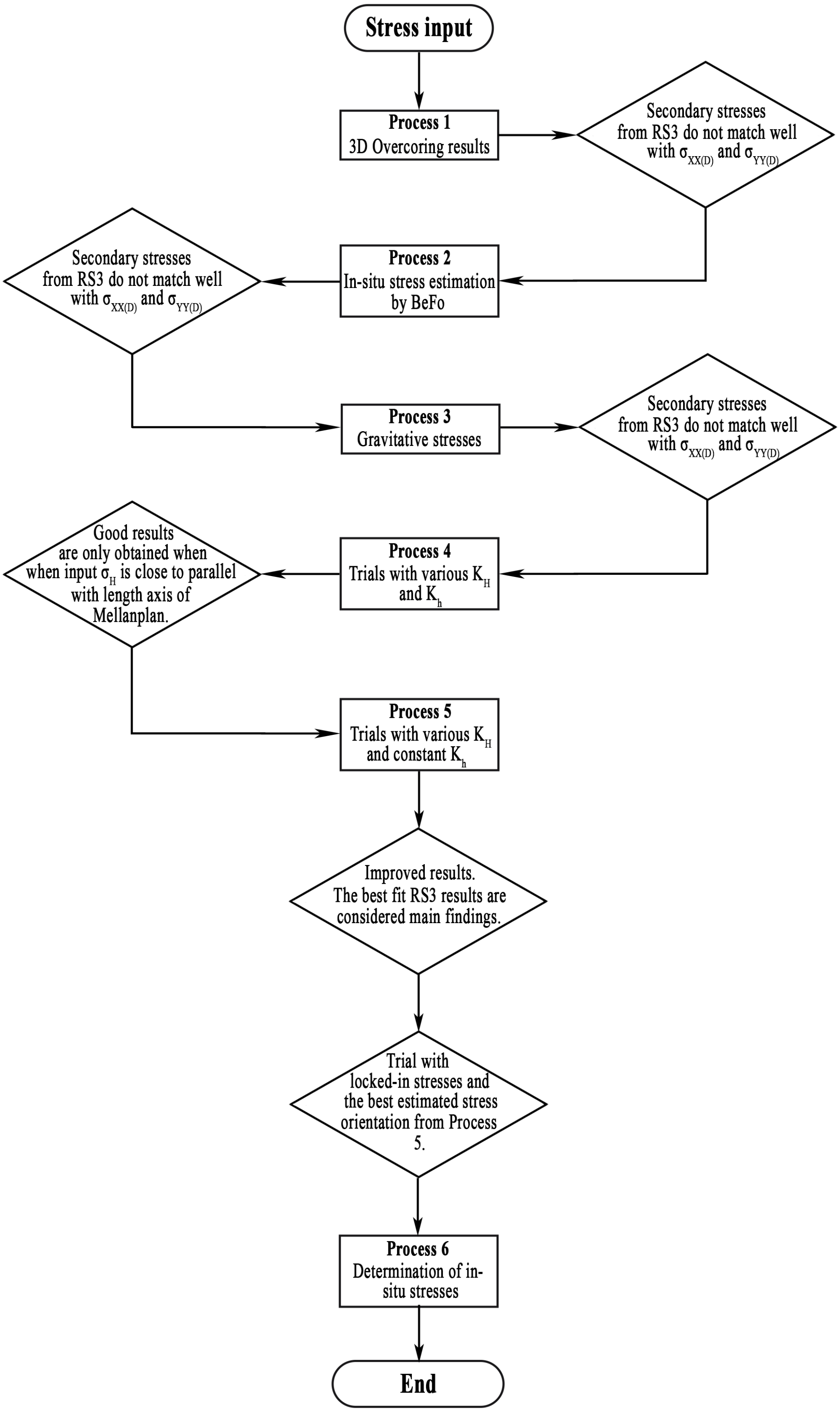

Figure 9.10: *Workflow chart presenting the processes leading to the final method applied to estimate the in-situ rock stresses at Mellanplan.*

Examples regarding the processes presented in Figure 9.10 are listed below.

- **Process 1**

K-values are determined from overcoring measurements at both Landeriet and Liseberget. The input orientation of σ_H in the example below is perpendicular to Mellanplan as estimated from overcoring results. K_H and K_h values are derived from the best-fit lines, presented in Figures 6.18 and 6.19. However, the best-fit lines until the first measurement points are taken into account, as they are located at shallow depths. Table 9.6 presents the K-values and stress orientations applied as input for *RS3* models. The overcoring location, Landeriet, lies closer to Mellanplan.

Table 9.6: *Input parameters derived from overcoring measurements.*

Overcoring location	K_H	K_h	α_H [°]
Landeriet	0.79	0.20	N80E
Liseberget	3.73	1.18	N80E

Figure 9.11 shows that model input from the table above results in secondary stresses that do not lie within the average intervals of doorstopper stresses.

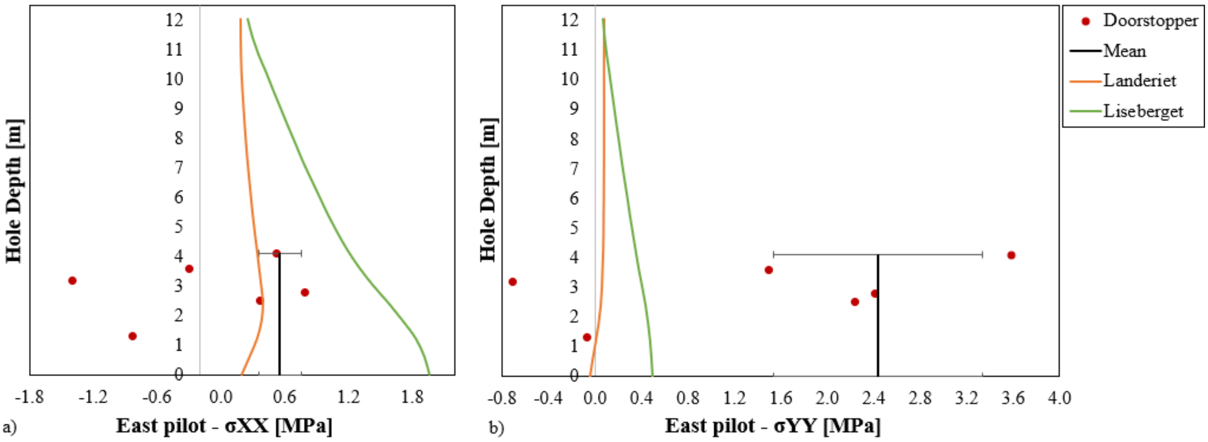

Figure 9.11: *Input stresses from Landeriet and Liseberget, result in secondary stresses that do not lie within average stress intervals at Mellanplan.*

- **Process 2**

Table 9.7 presents the K_H and K_h values determined from the minimum, best estimated and maximum horizontal stresses in Gothenburg suggested by BeFo. The stress orientations presented in Table 6.8 are applied as input.

Table 9.7: *Input parameters obtained from BeFo estimation on in-situ stress state in Gothenburg.*

BeFo estimation	K_H	K_h	α_H [°]
Minimum	2.87	0.26	N80E
Best estimated	3.88	0.6	N103E
Maximum	6.38	1.38	N126E

Figure 9.12 illustrates that the numerically calculated induced stresses do not correlate well with $\sigma_{XX(D)}$ and $\sigma_{YY(D)}$.

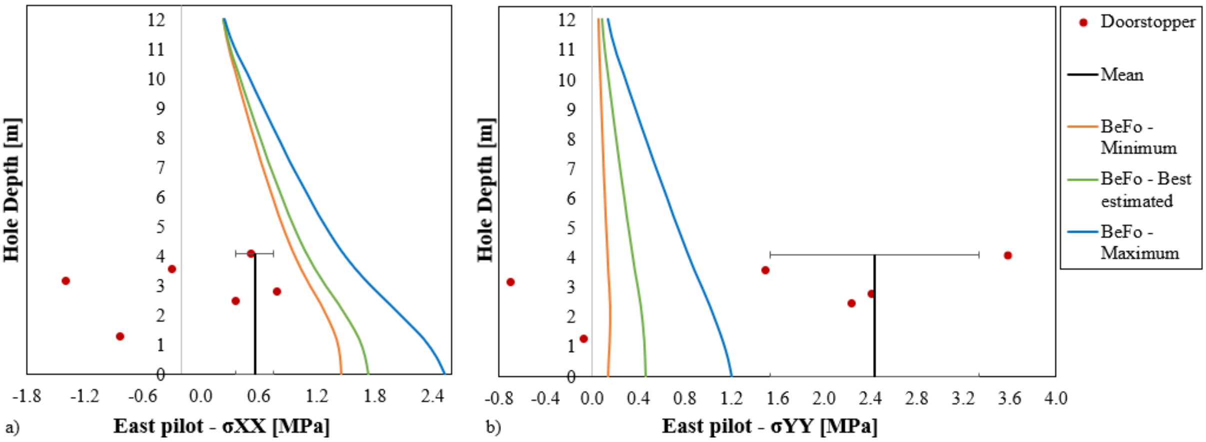

Figure 9.12: *Stress input from BeFo result in secondary stresses that do not lie within average stress intervals at Mellanplan.*

- **Process 3**

For gravitational stresses, the stress ratios $K_H = K_h$ are 0.33. The induced stresses, σ_{XX} and σ_{YY}, do not show any variation with different stress orientations. In addition, the secondary stresses do not match the doorstopper stresses, as shown in Figure 9.13.

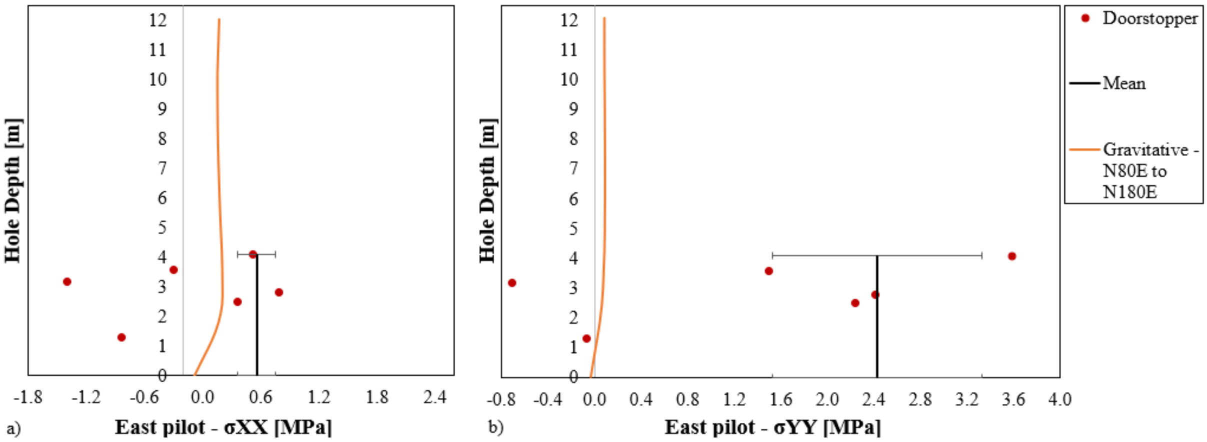

Figure 9.13: *Gravitational stress input results in identical secondary stresses for various stress orientations. The secondary stresses from RS3 do not lie within the average stress intervals.*

- **Process 4**

Trials with various K_H and K_h involved K-values higher than 0.33, as well as $K_H > K_h$. The numerical trials in this process also included variations in stress orientations, from N80E to N180E. Secondary stresses from *RS3* displayed good fit with both $\sigma_{XX(D)}$ and $\sigma_{YY(D)}$, given that input for σ_H is close to parallel with the length axis of Mellanplan (N160E-N180E). In this instance, K_H is approximately 6-7 times greater than K_h. Figure 9.14 shows an example from Process 4, where $K_H = 9$ and $K_h = 1.5$. The stress input with orientations N160E-N180E demonstrates minimum misfit between *RS3* results and secondary stresses from the doorstopper. Nevertheless, it has been stated earlier that virgin stress orientations at N160E-N180E are not likely to occur at Mellanplan. Therefore, these results are not further investigated for the back-calculation of in-situ stresses.

Regarding the remaining stress orientations, although some numerical results for σ_{YY} lie within the average interval, σ_{XX} do not show the same behaviour. Both secondary stresses from a numerical model need to appear within the average interval area to be considered an acceptable result.

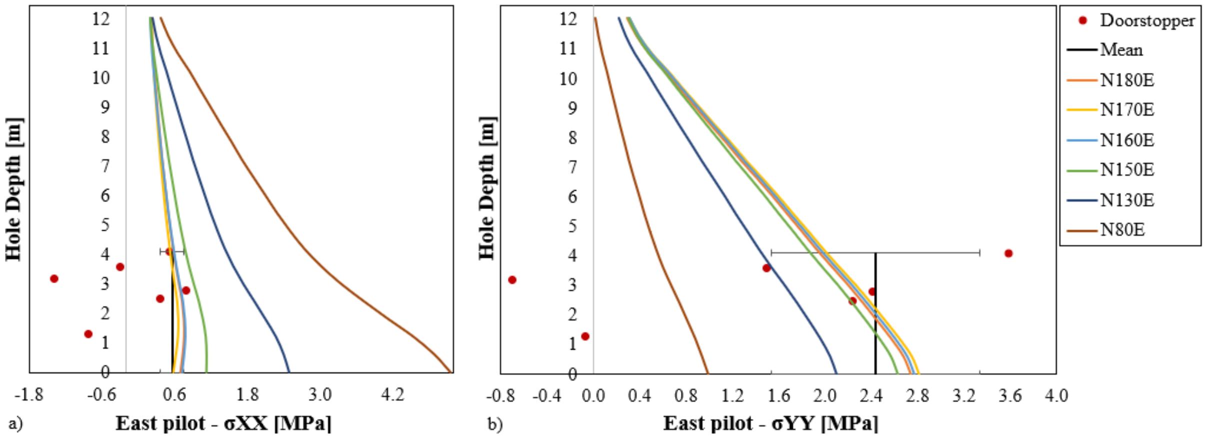

Figure 9.14: *One of the trials with various K-values.* K_H *= 9,* K_h *= 1.5 and various tress orientations.*

- **Process 5**

Considering the assumption that σ_H in direction N160E-N180E is unlikely, these stress orientations are not included as input variables in Process 5. This process of numerical trials involved K_h as a constant parameter, with a value of 0.33 that considers σ_h only as a gravity induced horizontal stress. Whereas, K_H values vary. The results from this process are considered representative and are the main findings of the parametric stress analysis. The results are presented in Section 9.3.5.

The stress orientation that displays the best correlation between secondary stresses from *RS3* and the doorstopper is further applied to determine the locked-in stresses. The results from locked-in stresses are analysed to evaluate whether they match well with the average stress interval obtained from the doorstopper. The main findings regarding locked-in stresses are also presented in the following section.

- **Process 6**

Based on the results from Process 5, in-situ stress state at the top heading of Mellanplan is determined.

9.3.5 Conclusive stress results

Process 5 is considered a representative method to determine the in-situ stress state at Mellanplan, where the minor horizontal stress, σ_h, is assumed to be only gravity-induced stress. While the major horizontal stress, σ_H, varies with different K_H values as input. Due to the time and constraint, only the K_H values of 4, 6, 8, 10, 12 and 14 have been selected as variable input parameters. Furthermore, this section solely presents the results for α_H = N130E, N140E and N150E since these directions provide numerical results that correlate well with resolved stresses from doorstopper measurements.

Major horizontal stress - N130E

Figure 9.15 presents results from the numerical models alongside scattered $\sigma_{XX(D)}$ and $\sigma_{YY(D)}$. Table 9.8 below shows the input parameters utilised. K_H = 4 as input shows the best fit with the stress interval for $\sigma_{XX(D)}$. On the other hand, K_H = 12 and K_H = 14 as input demonstrate best fit in relation to $\sigma_{YY(D)}$. Since the best fits for both average stress intervals are not achieved by the identical K_H values, 3D models with a different α_H need to be conducted.

Table 9.8: *Input parameters for RS3 models providing results in Figure 9.15*

K_H	K_h	α_H [°]
4, 6, 8, 10, 12, 14	0.33	N130E

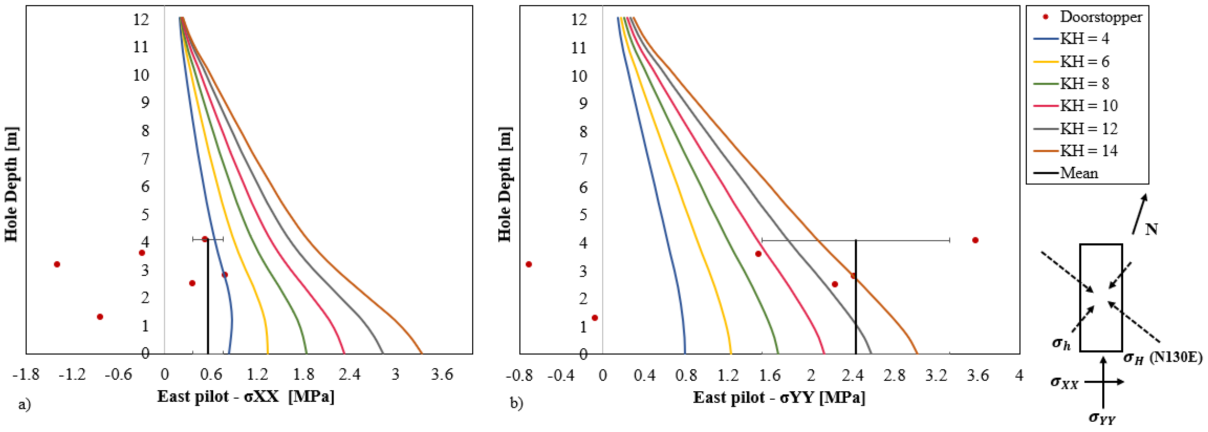

Figure 9.15: *Secondary stresses from 3D models compared with scattered doorstopper stresses, when σ_H has an orientation of N130E.*

Major horizontal stress - N140E

Figure 9.16 presents results from 3D analyses alongside scattered secondary stresses from the doorstopper. Table 9.9 below shows the input parameters applied in this set of numerical trials. Both K_H = 4 and 6 appear within the average stress interval in Figure 9.16a. However, these K-values do not depict the same behaviour regarding $\sigma_{YY(D)}$ interval area. In Figure 9.16b, K_H values of 10 and 12 display the best fit with the doorstopper results. A good correlation between *RS3* results and doorstopper stresses is not attained by the same K_H values when α_H = N140E. Thus, 3D analyses with alternative stress orientation are required.

Table 9.9: Input parameters for RS3 models providing results in Figure 9.16

K_H	K_h	α_H [°]
4, 6, 8, 10, 12, 14	0.33	N140E

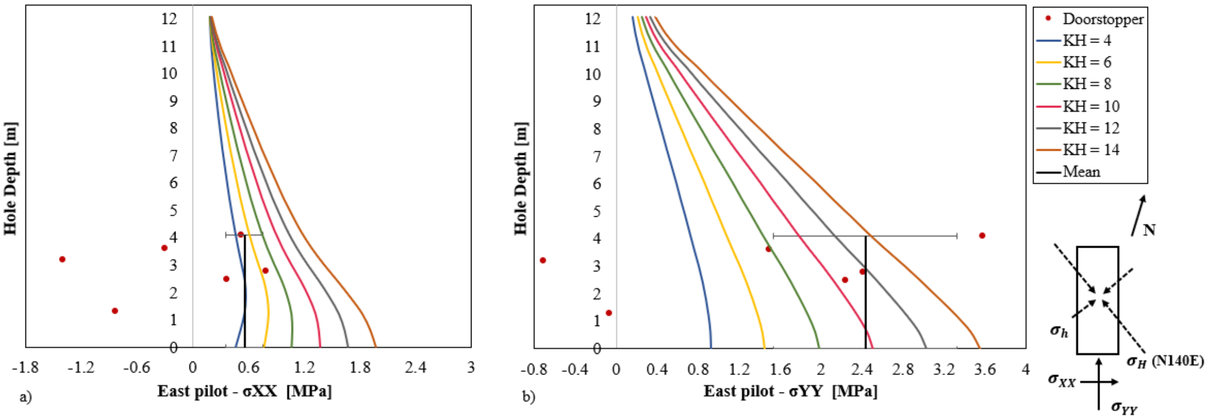

Figure 9.16: *Secondary stresses from 3D models compared with scattered doorstopper stresses, when* σ_H *has an orientation of N140E.*

Major horizontal stress - N150E

Figure 9.17 presents secondary stresses from the models compared with scattered doorstopper stresses when σ_H has an orientation of N150E. Table 9.10 shows the input parameters used for the stress analyses for this direction. As the figure below indicates, the results achieved with a K_H value of 10 correlate best with the average stress interval for both $\sigma_{XX(D)}$ and $\sigma_{YY(D)}$. Throughout the doorstopper hole depth, up to 4.1 m, the induced stresses resulting from K_H = 10 lie within the standard deviations and are close to the mean stress value in correlation with measured stresses at East pilot.

It is emphasised here that K_H values of 8 and 12 also provide secondary stresses within the average stress intervals throughout the entire borehole length. However, the best fit in Figure 9.17 occurs when the input is K_H = 10. Therefore, a combination of K_H = 10 and K_h = 0.33 with major horizontal stress oriented in N150E is selected to be utilised to determine the in-situ stress state at the top heading location of Mellanplan.

Table 9.10: Input parameters for RS3 models providing results in Figure 9.17

K_H	K_h	α_H [°]
4, 6, 8, 10, 12, 14	0.33	N150E

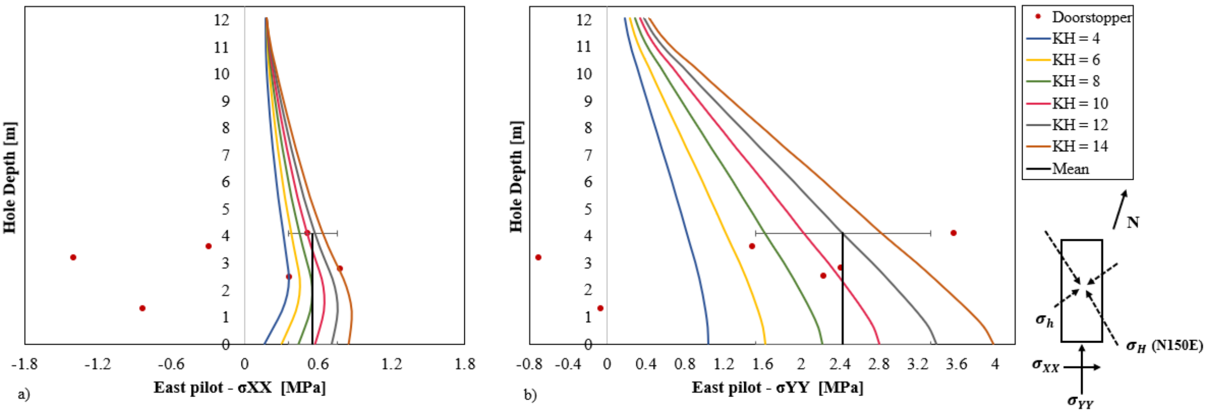

Figure 9.17: *Secondary stresses from 3D models compared with scattered doorstopper stresses, when* σ_H *has an orientation of N150E.*

Locked-in stresses

Given that major horizontal stress with the orientation of N150E provided good results, numerical models with this orientation incorporating locked-in stresses as input is also carried out. These analyses are made to evaluate whether the in-situ stresses at the shallow depth of Mellanplan can be affected by locked-in stresses or not. In *RS3* locked-in components are fixed components added to the horizontal stresses defined by stress ratio and vertical stress (Rocscience, 2022b). Thus, these stresses can be defined by the following Equations 9.1 and 9.2, where locked-in stresses are given as σ_{LH} and σ_{Lh}. Such fixed stresses can be the contribution of both glacial uplift and tectonic stresses.

$$\sigma_H = \frac{\nu}{1-\nu}\sigma_v + \sigma_{LH} \tag{9.1}$$

$$\sigma_h = \frac{\nu}{1-\nu} + \sigma_{Lh} \tag{9.2}$$

Table 9.11 presents the input parameters used for the stress analysis with locked-in stresses, considering K_H and $k_h = \nu/(1-\nu)$. The minor horizontal stress, σ_h is assumed to be gravitational stress only. On the other hand, the major horizontal stress, σ_H, is influenced by both gravitational stress and a fixed horizontal stress component. Locked-in stresses presented in the table below, result in secondary stresses that appear within the average intervals of $\sigma_{XX(D)}$ and $\sigma_{YY(D)}$. In Figure 9.18, the best fit is displayed when σ_{LH} equals 2.5 MPa. Unlike the secondary stresses presented above, the 3D models with locked-in stresses do not move towards 0 MPa when approaching the rock ground surface. This indicates high horizontal stresses near the ground surface. The stress measurement by doorstopper at East pilot is only conducted up to 4.1 m above the roof, and thus stress conditions near the surface level are unknown. Due to the uncertainty associated with high horizontal stresses near the surface bedrock, locked-in stresses are not further utilised to determine the in-situ stress state.

Table 9.11: *Input parameters for RS3 models with locked-in stresses.*

K_H	K_h	σ_{LH}	σ_{Lh}	α_H [°]
0.33	0.33	2, 2.5, 3	0	N150E

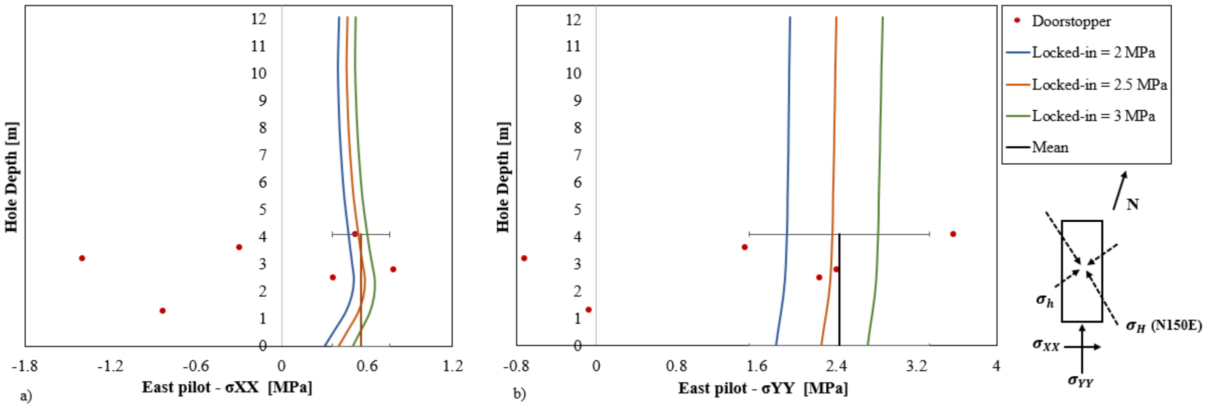

Figure 9.18: *Secondary stresses from 3D models compared with scattered doorstopper stresses, where σ_H has an orientation of N150E, and locked-in stresses are applied.*

9.3.6 In-situ stress state

The results from 3D models showed that the best fits between numerical and doorstopper stresses are achieved when the major horizontal stress has an orientation of N150E. Table 9.12 presents a range of input stress parameters that showed optimal results when secondary stresses from numerical analyses are compared with the doorstopper stresses. Estimation of in-situ stresses should be provided in a range of minimum, best and maximum estimated values. Therefore, these input values are further applied to back-calculate the range of the in-situ stress state at the top heading of the access cavern in Korsvägen.

Table 9.12: *Input parameters from 3D analysis that showed optimal results.*

	K_H	K_h	α_H [°]
Minimum	8	0.33	N150E
Best estimated	10	0.33	N150E
Maximum	12	0.33	N150E

Considering the vertical stress in Mellanplan is assumed to be gravitational, in-situ horizontal stresses, σ_H and σ_h, can be back-calculated by multiplying the K-values with σ_v. Vertical gravitational stress depends on depth, and thus the horizontal in-situ also increases with depth. Based on the back-calculation, Table 9.13 and Figure 9.19 present the in-situ stresses at a shallow depth in Mellanplan. The rock stresses σ_h and σ_v are presented as gravity induced stresses, while σ_H is greater than the gravitational stress. The minimum and maximum estimation for σ_H is depicted as a stress range for the major horizontal stress in Figure 9.19.

Table 9.13: *Final estimation of in-situ stresses at a shallow depth in Mellanplan.*

	σ_H [MPa]	σ_h [MPa]	σ_v [MPa]	α_H [°]
Minimum	0.214 z	0.009 z	ρgz	N150E
Best estimated	0.268 z	0.009 z	ρgz	N150E
Maximum	0.322 z	0.009 z	ρgz	N150E

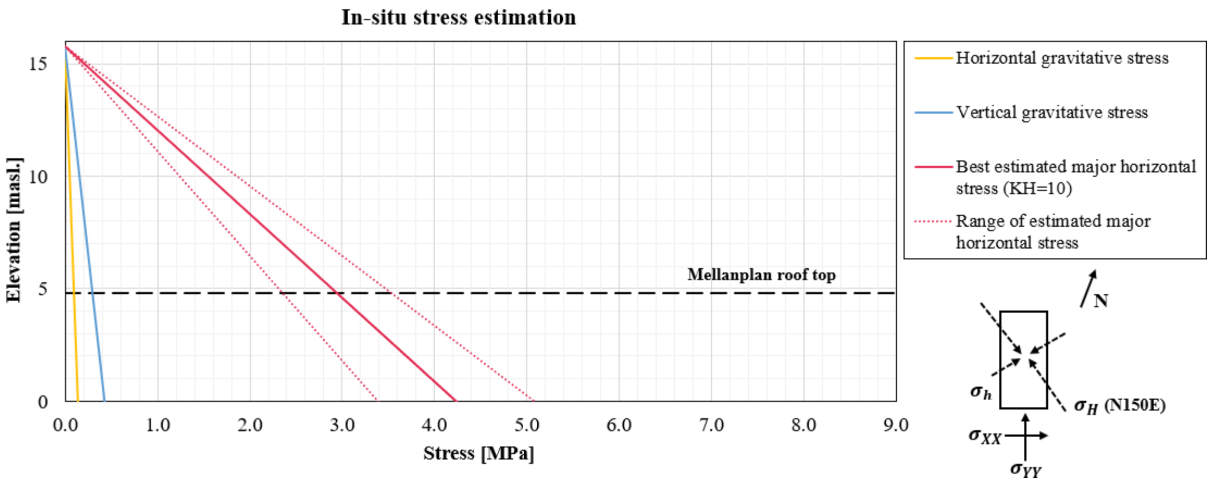

Figure 9.19: *Final rock stress model with estimated in-situ stresses at a shallow depth in Mellanplan. The stress domain applies for elevation from -5 masl. to 15.8 masl. at Mellanplan.*

Although doorstopper measurement at the East pilot was conducted above the tunnel roof, the rock stresses presented in Figure 9.19 are extrapolated until the elevation at 0 masl. The back-calculated virgin stresses are assumed to be viable from an elevation of 0 masl. to 15.8 masl. The stress measurements conducted by SINTEF are not applicable to determine the stress conditions below the top heading. It must also be emphasised that 15.8 masl. represents the rock surface.

9.4 Displacement analyses in 2D models

9.4.1 Model setup

The geometry in *RS2* consists of a 2D cross-section of the top heading in Mellanplan. Likewise, *RS3* models, the cross-section of the top heading is based on the theoretical blasting profile. The 2D CAD drawing of the pilot tunnels and the rock pillar provided by Trafikverket (2022d), is imported into *RS2*. The shape of the top heading in *RS2* also follows the dimensions presented in Figure 6.3.

Unlike 3D models, 2D models are generated and computed with defined joints. Figure 9.20 shows an excerpt of the model setup in *RS2*. A joint network consisting of two joints, foliation and cross joints, is generated in the entire domain. Note that the model excerpt below is presented without displaying mesh to achieve a less noisy image of the joints. The mesh setup in *RS2* models is graded with 6 noded triangles as an element type. Due to the application of XFEM in 2D analyses, the joints in the domain do not conform the mesh. Moreover, the external boundary and boundary conditions in *RS2* models have the same setup as in *RS3* models. The rock surface is free of restraints, the boundary walls have rollers, and the bottom part of the boundary is fixed.

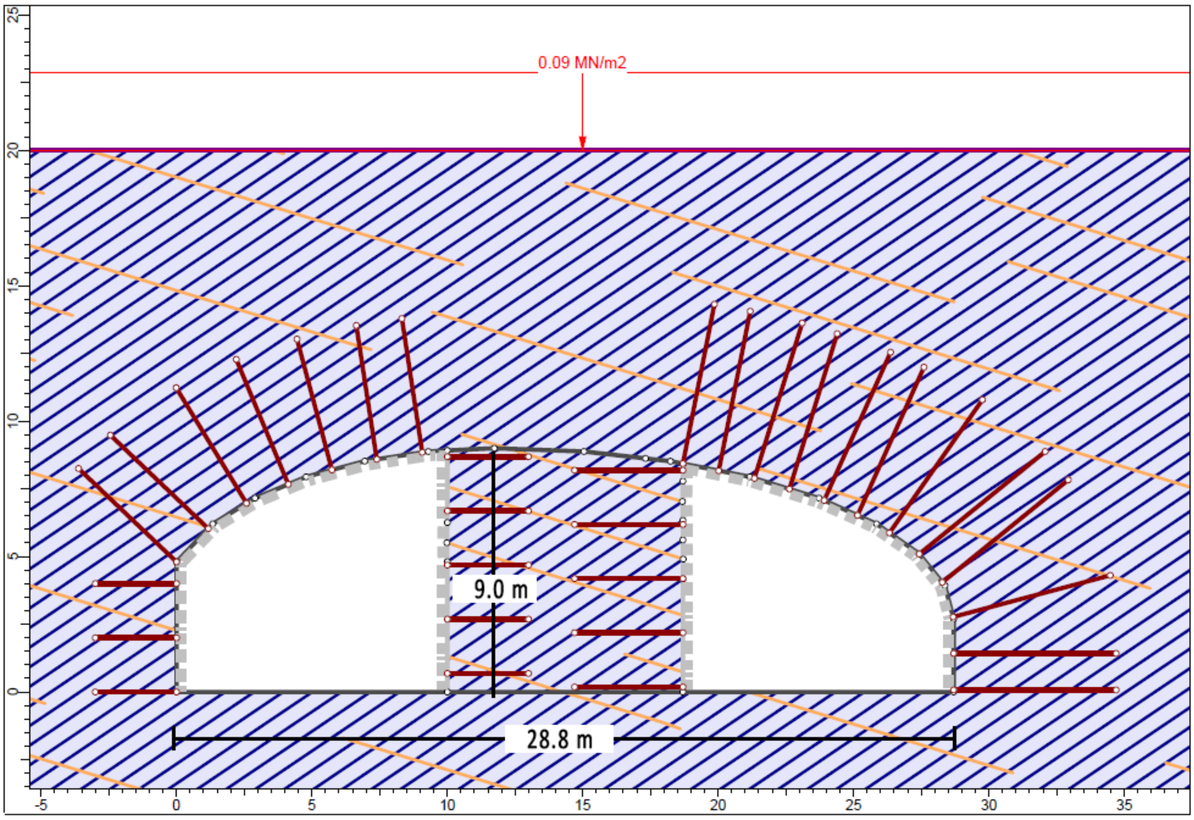

Figure 9.20: *Excerpt of the model setup in RS2. The blue lines are foliation joints, while the orange lines are cross joints.*

Two stages are computed in a 2D numerical analysis. The first stage is the initial stage, and the second stage involves the excavation, including the assignment of rock support. As stated previously, the rock pillar in the top heading is thus far not excavated at the West Link Project. The aim of the 2D analyses is to compare the measured vertical displacement with the displacement results from numerical modelling. Therefore, the rock pillar is not excavated in the *RS2* models either.

9.4.2 Jointed 2D models

In the specialisation project work prior to this thesis study, it was discovered that *RS2* models presented good results for displacement analysis when joint networks were included (Panthi, 2022). *RS2* models with directly modelled joint networks gave more reliable displacement values than a continuous model defined as a plastic material. On that account, the *RS2* models are also created with defined joints in this work. The rock blocks between the joints behave as an elastic material, while the joints behave plastically and allow the plastic slip to occur due to the slip criterion (Rocscience, 2022c).

The strength factor is often applied to determine whether the rock mass in a *RS2* model requires to be defined as elastic or plastic material. In the case of elastic rock mass, when the strength factor is less than a unity (< 1) around the tunnel boundary after excavation, the material should be defined as a plastic medium. When the rock mass in the model domain behaves like a plastic material, the strength factor is always greater than or equal to unity. To evaluate the strength factor after excavation, the *RS2* models are first created without rock support. Figures 9.21 and 9.22 display that the models generated for this study show a strength factor greater than unity after the excavation of pilot tunnels. Despite the rock blocks between joints being defined as an elastic material the rock mass in *RS2* behaves like an elasto-plastic medium if joint networks are generated.

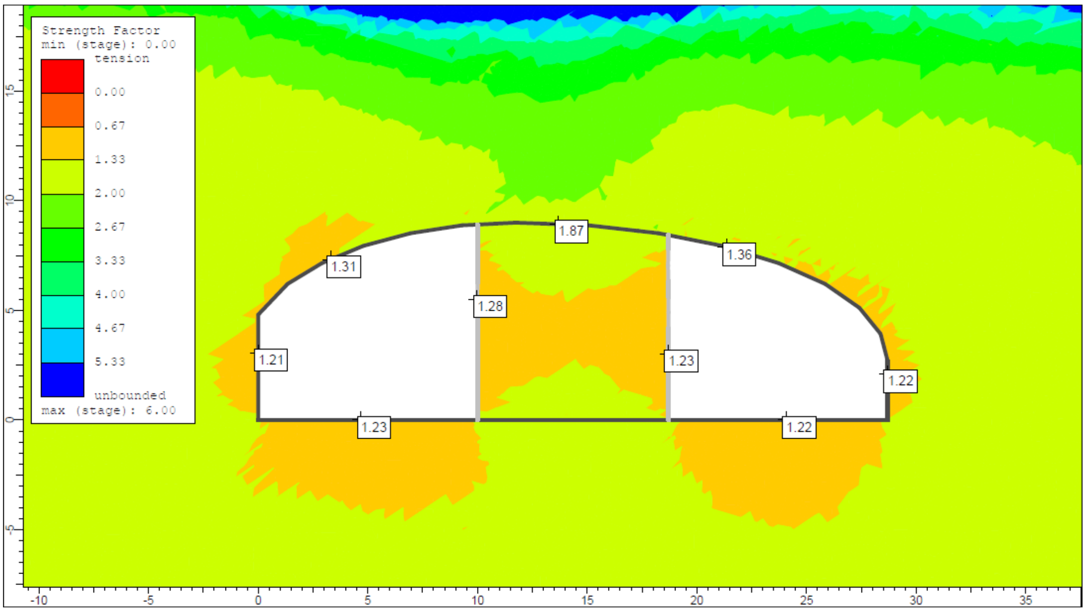

Figure 9.21: *Strength factor for model with unweathered joint network.*

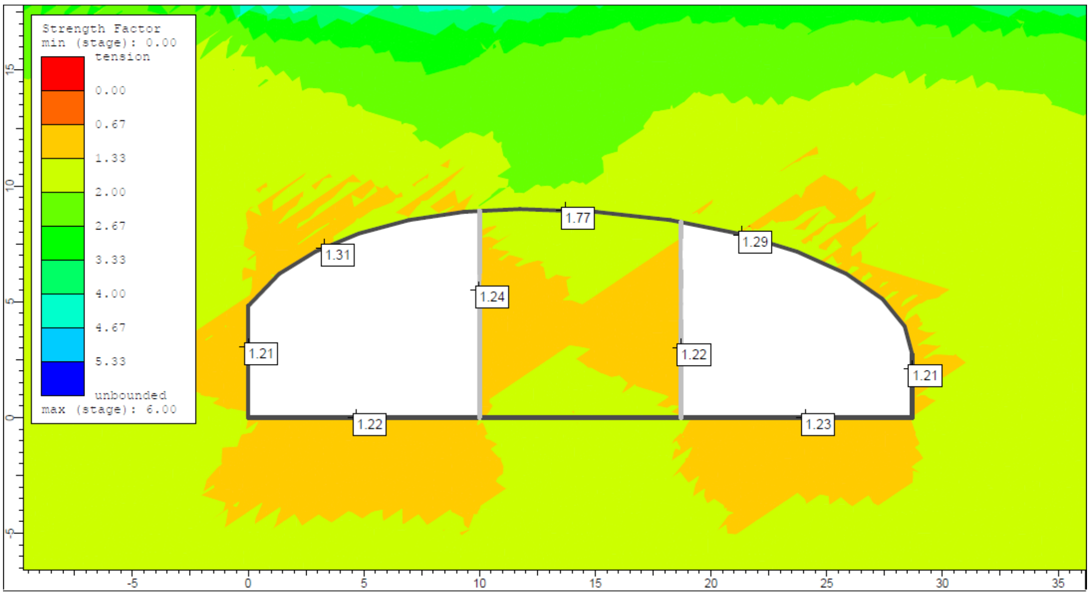

Figure 9.22: *Strength factor for model with weathered joint network.*

Among the objectives of this study is to apply the back-calculated in-situ stresses derived from 3D analyses to a 2D numerical model to assess the vertical displacements on the tunnel roofs. For 2D models, only the best estimated in-situ stress state is utilised as input for displacement analyses. The minimum and maximum estimated rock stresses are not included. Prior to displacement analyses, the secondary stresses, σ_{XX} from 2D models are compared with the σ_{XX} results from the 3D model. Figure 9.23 demonstrates that the results from 2D models are close to the σ_{XX} results from 3D model. However, as the figure below indicates, the 2D model with unweathered joints has σ_{XX} closer to the one from the 3D model. Due to the similarity in the stress results, the jointed rock mass in 2D models resembles the continuous rock mass in *RS3*.

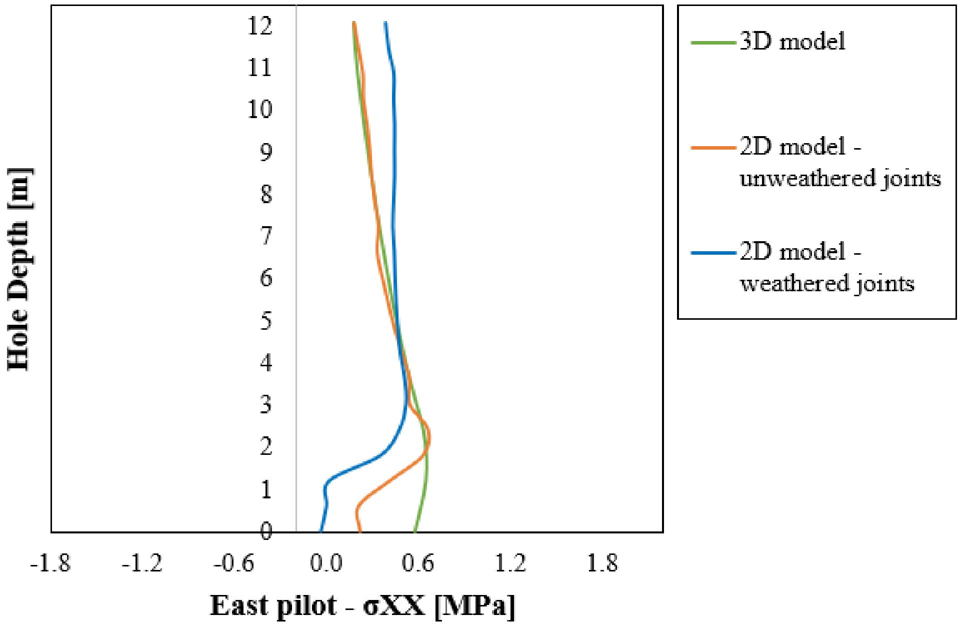

Figure 9.23: *Comparison between secondary stresses, σ_{XX}, obtained in 3D and 2D models.*

9.4.3 Vertical displacement on supported pilots

Figure 9.24 shows vertical displacements at the top heading, when the 2D model is computed with unweathered joint conditions. The displacement of interest is the vertical displacements at the crown. The entire crown of the top heading is subjected to vertical deformation downwards, as presented in Figure 9.26. The deformation magnitude varies from 1.1 mm to 1.4 mm along the crown, when the joint network is generated under unweathered conditions. The maximum displacement at the roof of both pilot tunnels is 1.35 $mm \approx 1.4\ mm$.

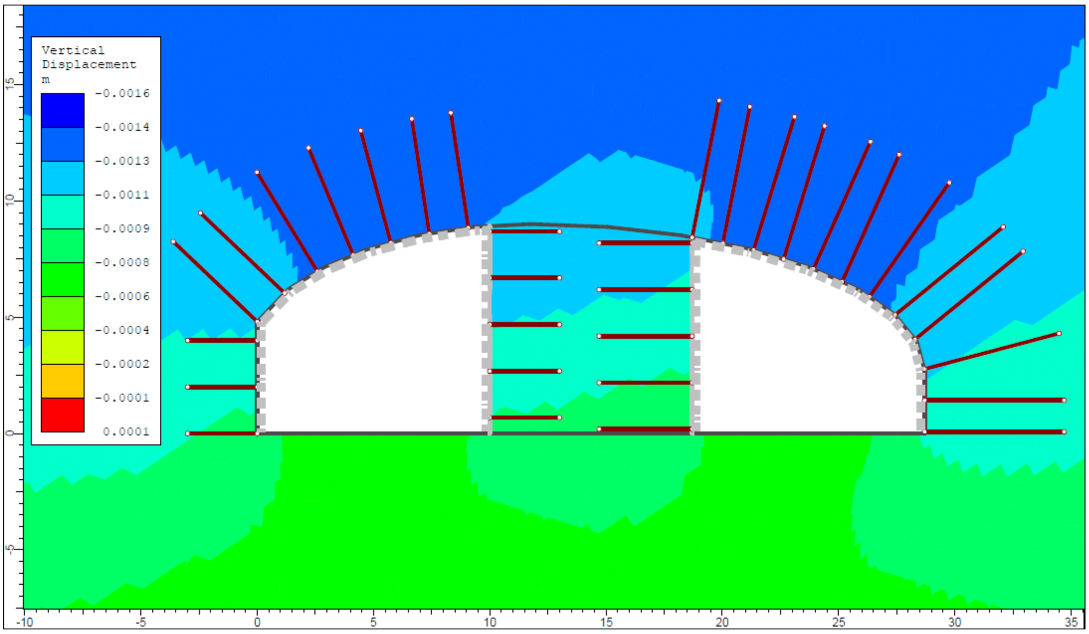

Figure 9.24: *Vertical displacements with unweathered joints.*

Figure 9.25 presents vertical displacement at the top heading when the 2D model is generated with weathered joint conditions. Similar to the model with unweathered joint network, the entire crown of the top heading exhibits downwards deformation. As presented in Figure 9.26, the vertical displacement varies from 1.1 mm to 1.7 mm along the whole crown, when the joint network is defined with input parameters for weathered joints. The results from this deformation analysis indicate that the maximum vertical deformation at the roof of the East pilot is 1.6 mm, while at the roof of the West pilot is 1.7 mm.

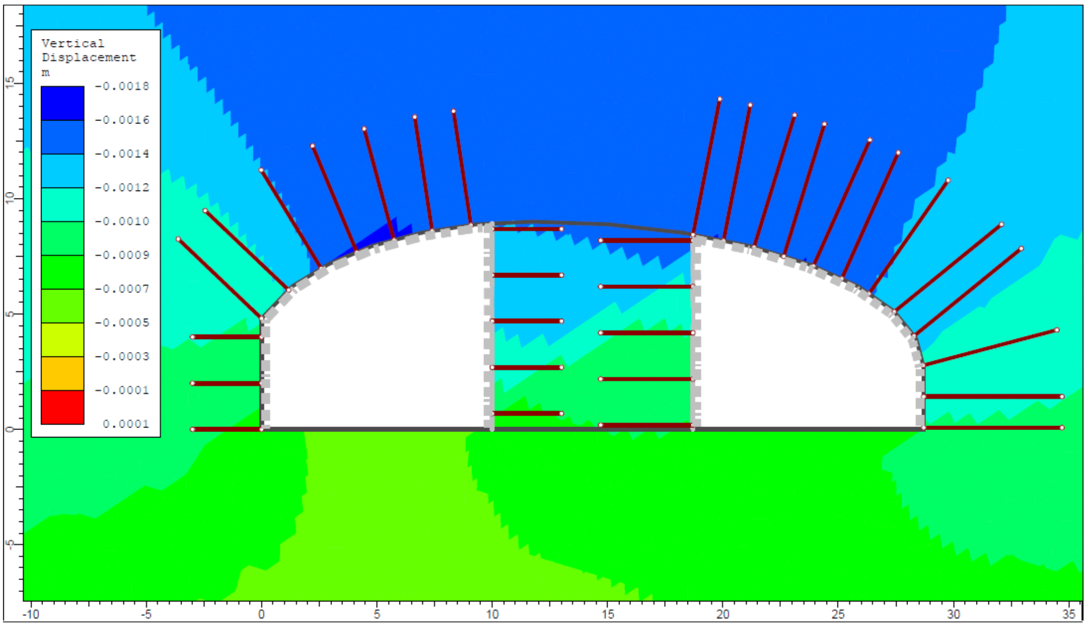

Figure 9.25: *Vertical displacements with weathered joints.*

Figure 9.26 displays vertical displacements for both unweathered and weathered joint networks in the models. Both numerical results demonstrate higher displacement at the roof of the excavated pilots, than at the designed crown profile of the rock pillar. Nonetheless, the joint network with weathered conditions displays greater deformation at the pilot roofs. As presented in Sub-chapter 6.7, the measured vertical displacement of interest at East Pilot is 2.85 mm. In comparison, the maximum displacements at both pilot tunnels, obtained from 2D numerical analyses, are lower than the measured one.

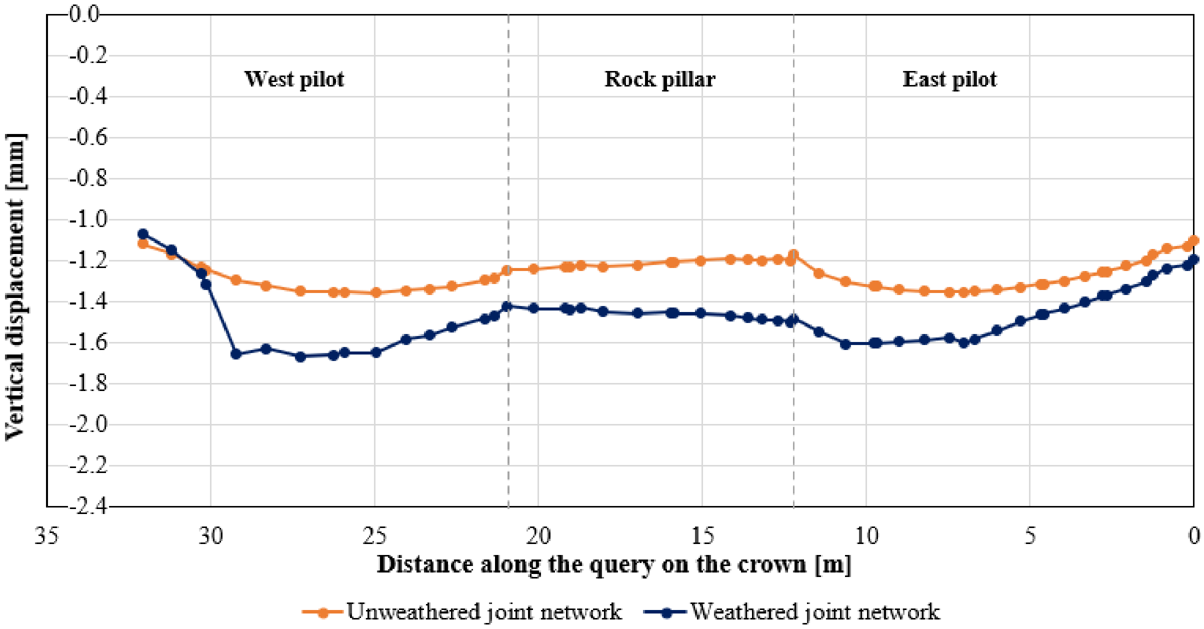

Figure 9.26: *Vertical displacements along the top heading crown, when 2D models are generated with unweathered and weathered joint network. The dashed lines depict the rock pillar section.*

10 Discussion

In this chapter, the results from 3D stress analyses are discussed, with a focus on the back-calculated in-situ stresses. Further, the applicability of 3D numerical modelling for stress assessment is discussed. Finally, the discussions are made on the results from deformation analyses using 2D numerical modelling.

10.1 Results from stress analyses

10.1.1 Estimated in-situ stress state

The final estimation of the in-situ stress state at a shallow depth in Mellanplan shows that major horizontal stress is greater than the vertical and minor horizontal stress, $\sigma_H > \sigma_v > \sigma_h$. Such stress condition correlates with the suggested stress state by Martin et al. (2003), as presented in Sub-chapter 6.6. Nonetheless, this proposal also includes stress measurements at greater depths. The in-situ stresses at shallow depths can show complexity.

The assessment of the best estimate stress model (BESM) suggested that the stress field in Mellanplan is likely to be influenced by tectonic and residual stresses, in addition to gravitational stresses. The predicted in-situ stress condition in Figure 9.19 demonstrates that σ_H is significantly higher than σ_h and σ_v. This indicates that the tectonic stress contributes considerably to the major horizontal stress component, σ_H. The data from World Stress Map presents major horizontal stresses oriented in the northwest-southeast direction in Gothenburg, where the region consists of strike-slip and thrust faults. The study on regional geology revealed that the majority of the faults in Gothenburg have strike in the northwest-southeast direction. This shows a good correlation between the tectonic activity and the orientation of σ_H at Mellanplan since it is predicted as α_H = N150E. The estimated stress state is in accordance with the paleo-stresses derived from the strike-slip faulting. However, it should be underlined that the orientations of the principal stresses from the origin of the tectonic regimes may change due to later tectonic events, glaciations and deglaciations and respective uplifts. Thus, there is also a probability that the mechanism of a thrust fault contributes to the stress condition at Mellanplan. However, the present stresses may have been modified from the paleo-stresses. Figure 10.1 presents these two possible outcomes.

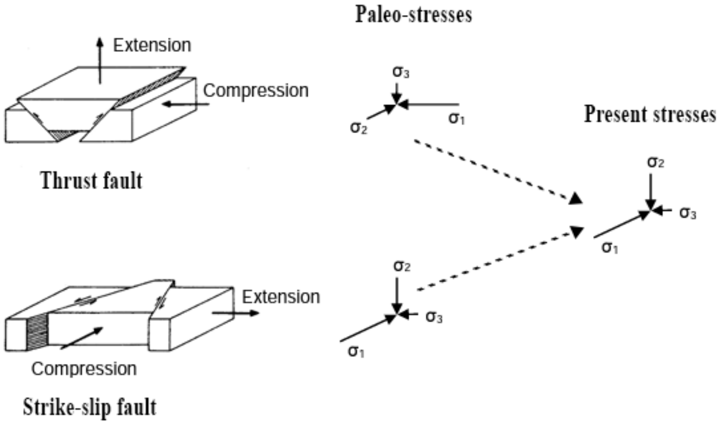

Figure 10.1: Present stresses at Mellanplan, with two possible origins of paleo-stresses and fault regimes. Modified after: Anderson (1951)

The ratio between the major horizontal stress and the vertical stress should be larger at the shallow depth above the top heading than at a greater depth. This is due to the fact that the tectonic stress at a shallow depth generally represents a larger part of the total stress field than the gravity-induced stress. Moreover, the residual stress developed from the deglaciation periods may also affect the stress ratio at shallow depths. In this case, the residual stress can also contribute more to the major horizontal stress than the other stress components.

The estimated minor horizontal stress at Mellanplan is assumed as gravitational stress. Nonetheless, the low values of σ_h may also be a result of the stress sensitivity at shallow depths. The joint mapping of the East pilot indicates that the doorstopper measurement is located at a slightly weathered area. While the profiles close to the measurement site at the East pilot (profiles 0/023-0/026) are described as highly weathered (Appendix B). Weathering and geological structures can cause destressed rock blocks and zones, resulting in anomalies by reducing the already low minor horizontal stress. Regardless of the assumption of careful blasting, there is still a risk of blast damage, decreasing the ability of a rock mass to sustain stresses.

The knowledge of in-situ stresses is important to evaluate the stability of underground openings. The tunnel mappings of the Mellanplan pilots have registered a few block falls from the roofs. This form of instability issue is a structurally controlled failure, which can appear in low confining-stress conditions at shallow depths. The predicted σ_h and σ_v above the top heading are defined as gravitational stresses. Due to the low overburden of rock mass, these gravity induced stresses are relatively low. Despite the major horizontal stress with higher magnitude, the low minor horizontal and vertical stress components can lead to loss of confinement in the rock mass. The low stress magnitudes combined with unfavourable joint orientations can be associated with gravity driven fallout of rock wedges and blocks from the roof. Therefore, the observed block falls from the pilot tunnels indicate the existence of low stresses at the top heading of Mellanplan. Figure 10.2a illustrates a sketch of a block fall from a tunnel roof, where σ_H is parallel to the strike of foliation, and σ_v and $\sigma_h << \sigma_H$. Similar block falls can also occur during the removal of the rock pillar in the future, and thus the combination of low stresses and joint conditions must be assessed. The scope of this study does not include block stability assessment, and therefore it is given as one of the recommendations for further studies.

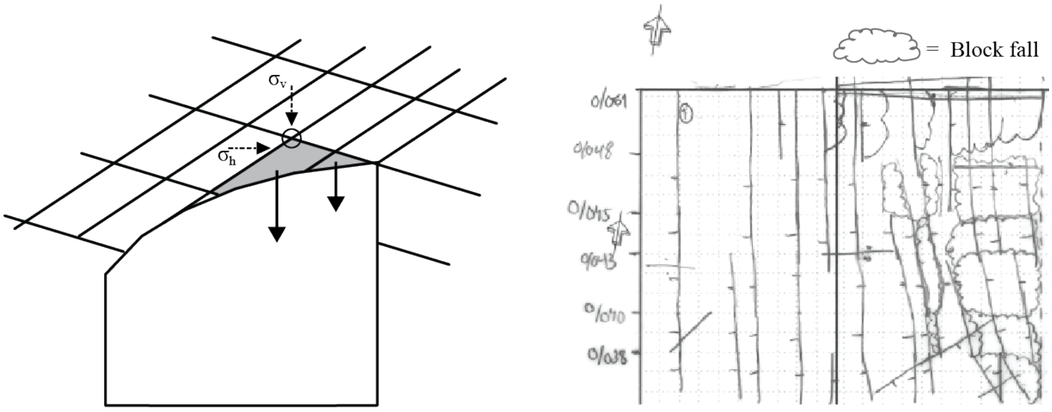

a) Gravity driven block falls from a pilot roof

b) Section with block falls from West pilot roof

Figure 10.2: *a) Principal sketch of block fall from West pilot roof. The joint spacings are not in scale.* σ_v *and* $\sigma_h << \sigma_H$*. b) Snippet from structural mapping of West pilot displaying block falls from roof. See Appendix C and D for details.*

The development of the final rock stress model (FRSM) comprises different steps. The study focused on achieving a rock stress model through 3D numerical analyses and validating the induced stress results with doorstopper measurements of secondary stresses. The determination of the in-situ stress field at Mellanplan involved various processes and trials with different stress inputs. As input variables, stresses from 3D overcoring at Landeriet and Liseberget demonstrated that induced stresses from numerical models deviate from the measured doorstopper stresses (Figure 9.11). A similar deviation occurs when previously estimated in-situ stresses by BeFo are applied as input stresses (Figure 9.12). This shows the complexity of determining the in-situ stress field at a shallow depth.

Despite the distinction between numerical results and doorstopper measurements, the stress orientation of σ_H derived from overcoring played an important role in deciding the input for stress directions. In this study, α_H from N160E to N180E are disregarded, as they demonstrate a complete rotation of σ_H from previously estimated stress orientations by overcoring. This decision can be justified as there are no other in-situ stress measurements at or nearby Mellanplan that can verify such rotation of σ_H. In addition, the stress orientations suggested by BeFo correlate well with the stress directions derived from overcoring. Figure 10.3 demonstrates the rotation of stresses compared with estimated orientations from overcoring.

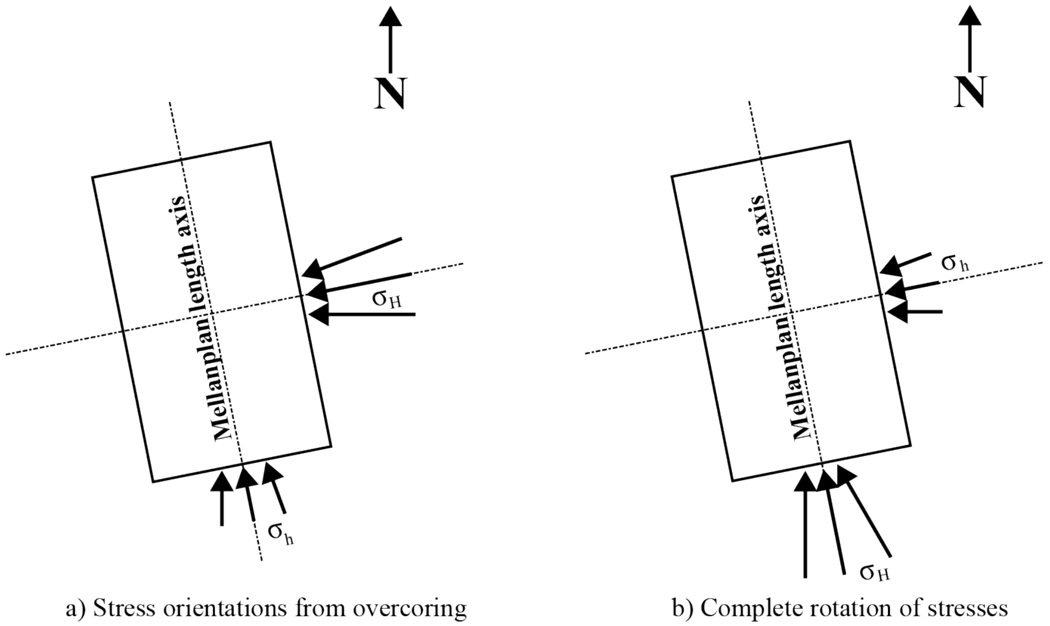

a) Stress orientations from overcoring

b) Complete rotation of stresses

Figure 10.3: *a) Estimated stress orientations from 3D overcoring. b) Neglected stress orientations.*

The obtained direction of the major horizontal stress (α_H = N150E) in this study differs from the estimated orientations by overcoring and BeFo. Geological structures may have attenuated the stress orientations slightly. As mentioned previously, there is a correlation between the strike of the faults and the orientation of σ_H. Furthermore, open joints can also influence stress distribution, which can be the cause of the rotation of stresses.

Doorstopper measurements performed at tunnel roofs after excavation provide good indications of induced stress magnitudes. However, some limitations were experienced with the applicability of the results from doorstopper measurements. Following the evaluation of doorstopper measurements, the author chose to investigate further on the results from the East pilot only. Moreover, negative stress components achieved from the doorstopper and shallow hole depths for stress measurements are also considered sources of limitations. Consequently, the stress data available for verification of numerical results was reduced. In case more doorstopper measurements with longer boreholes were available at Mellanplan, the final rock stress model would have been improved. Furthermore, magnitudes of horizontal stresses up to the rock ground surface could have been attained. This would improve the data gap experienced during stress analyses, especially regarding locked-in stresses.

The integrated stress determination (ISD) for the thesis work involved combining the doorstopper results with numerical analyses. Further improvement of the final rock stress model can be accomplished, provided different stress measurement method is utilised at Mellanplan in the future, e.g, overcoring or hydraulic fracturing tests. The results from two different measurement methods can increase the reliability in rock stress determination.

10.1.2 Applicability of 3D numerical modelling

The virgin rock stresses at Mellanplan are derived on the basis of the secondary stress analyses performed in a 3D numerical program, *RS3*. The model generated in the applied numerical program involves various assumptions and simplifications addressed in the previous chapter. The secondary stress results from these models will not be able to reflect the exact true nature of the induced stresses at the shallow depth of Mellanplan. Unlike the doorstopper measurements, the numerical models for stress analyses did not display scattering secondary stresses as results. The main source for this distinction can be the use of FEM software, where the rock mass is defined as an isotropic material. In reality, the rock mass in Mellanplan possesses some degree of anisotropy. Additionally, the absence of directly modelled joints and the exclusion of excavated access tunnel connected to the top heading can also affect the stress results obtained from the numerical modelling.

The accuracy of the numerical modelling increases with the accuracy of the input parameters. As discussed in the previous chapter, there are assumptions connected to the selected input parameters. The author is aware that there may be some uncertainty regarding the input parameters. Parametric analyses are often valuable in reducing such uncertainties. The thesis work has focused on the parametric analyses of rock stresses. In order to improve the numerical model, parametric analyses on geological variables, such as GSI and Poisson's ratio, may further increase the reliability. Furthermore, sensitivity analysis with alternative methods to determine rock mass strength (σ_{cm}) and deformation modulus (E_{rm}) may have been beneficial.

Despite the simplifications and assumptions connected to the numerical models, the author believes that the numerical results from stress analyses are not that far from reality. Considering the limited and widespread results of secondary stresses from doorstopper measurements, it is challenging to back-calculate in-situ stresses that exhibit a certain trend with depth. However, the estimated primary stress field provides valuable indications of the magnitudes and orientations of the rock stresses, which are discussed in the section above.

10.2 Results from deformation analyses

10.2.1 Vertical displacements

The main objective of deformation analyses in this thesis is to compare the displacements derived from numerical modelling with the measured vertical deformation at Mellanplan. The stress input in these analyses is the best estimated in-situ stresses determined from the back-calculation. The 2D model generated with weathered joint conditions displayed maximum vertical displacements of 1.6 mm and 1.7 mm from the pilot roofs. These deformation values are closer to the measured one of 2.85 mm. On the other hand, the model with unweathered conditions displayed a maximum displacement of 1.4 mm, which is half the deformation measured by the extensometer. Although both measured deformation and displacements obtained from numerical models are relatively low, the deformation analyses show that the displacement increases with weathering joint conditions. In addition, the numerical results demonstrate deformation downwards from the tunnel roofs, which corresponds with the monitored deformation.

The representation of joints is believed to be the primary reason for the deviation between numerical results and measured displacement. Although there are two major joint sets at Mellanplan, several random joints are registered during joint mapping. These random joints are not included in the 2D models. In reality, these discontinuities can influence the deformation of tunnel roofs. Another predicted source of error in numerically calculated displacements is the joint spacing. The typical spacing of foliation joints is 0.2-0.6 m, while cross joints vary between 0.6-2 m. For model simplicity, the models are generated with the larger values describing the joint spacings, i.e., 0.6 m for foliation joints and 2 m for cross joints.

10.2.2 Applicability of 2D numerical modelling

In *RS2*, only 2-dimensional cross-sectional excavation geometry can be generated. The program considers the cross-section of the top heading to be infinite in the out-of-plane direction. This implies that the face-effect is neglected in these models. The deformation behaviour near tunnel ends can be affected by the excavated faces or the end walls. Therefore, the extensometer of interest in this study is located around the middle of the pilot length. It is believed that 2D models for deformation analyses are applicable in this situation.

The generated 2D models also include assumptions and simplifications, which can affect the displacement results deviating from the true nature of vertical deformation at Mellanplan. Despite the modelling of joints in *RS2*, the rock blocks in between the joint network are defined as elastic material. The author is aware that in case rock blocks are defined as plastic material, the vertical deformation results can differ. In addition, residual parameters could as well indirectly include the effect of random joints. However, it was necessary to define the rock blocks as elastic material to reduce the jointed model complexity.

Similar to 3D analyses, the accuracy of the numerical results increases with the accuracy of the input parameters. As addressed in Section 10.1.2, various parametric analyses can be conducted to reduce input uncertainties.

11 Conclusion and recommendations

11.1 Conclusion

The access cavern in Korsvägen, Mellanplan, has low overburden and a large cavern span. High horizontal stresses are often advantageous for underground caverns with large spans at shallow depths. The knowledge of rock stress conditions is important for further stability assessments related to Mellanplan in the West Link project. The thesis demonstrates that the back-calculation of in-situ stresses can be achieved by combining results from stress measurements with 3D numerical analyses. To generate numerical models for stress analyses, it is important to identify geological conditions that can influence the stress field. Moreover, the stresses derived from stress measurements should be assessed before verifying the numerical results.

Although the main objective of the thesis work is the back-calculation of in-situ stresses at Mellanplan, the estimated rock stresses are further applied for deformation analyses performed in a 2D numerical program. The only aim of the deformation analyses is to compare the measured vertical displacement with the numerically calculated results. The results from the analyses have led to the following conclusions:

1. The final rock stress model (FRSM) achieved in this thesis demonstrates the stress field at Mellanplan as $\sigma_H > \sigma_v > \sigma_h$. This stress state is only viable at a shallow depth, from 0 masl. to 15.8 masl.
2. Based on the best estimated stress model (BESM) and the results from numerical analyses, it is suggested that tectonic stress contributes considerably to the major horizontal stress. Furthermore, residual stress may also have a greater influence on the major horizontal stress component.
3. Due to the low overburden, the relatively low magnitude of minor horizontal stress is assumed as gravity-induced stress. However, weathering and geological structures may have reduced the already low magnitude of σ_h.
4. The indications of low stress magnitudes, σ_h and σ_v, are validated by the observed block falls from pilot roofs at Mellanplan.
5. The estimated orientation of σ_H differs from the predicted stress directions by overcoring measurements and BeFo. This provides an indication of the influence of geological structures that can lead to some degree of stress rotation.
6. The displacement results from deformation analyses deviate from the measured vertical deformation on the roof of a pilot tunnel. The primary source of error, in this case, is believed to be the representation of the joints generated in the model. Application of larger joint spacing distances and neglection on the influence of random joints can be the cause for this deviation.
7. Both *RS3* and *RS2* are useful tools for 3D stress analyses and 2D deformation analyses, respectively. Nonetheless, the numerical results may not depict the exact nature of secondary stresses and rock mass behaviour due to assumptions and simplifications related to the generated models. In general, the reduction of model complexity is necessary during numerical analyses. Despite the simplifications, the results derived from numerical analyses are important as they enhance knowledge of various rock mechanisms.

11.2 Recommendations

The following recommendations are selected for further studies, related to the work conducted in this thesis:

1. Perform laboratory tests on metabasite rock samples from Mellanplan.
2. To improve the numerical models, conduct parametric analyses on other model input parameters than rock stress.
3. For further improvement of the final rock stress model (FRSM), more stress measurements should be performed at Mellanplan. It is recommended to use a different measurement technique to develop an integrated stress determination (IDS) model. The alternative measurement methods are 3D overcoring and HTPF (Hydraulic test on pre-existing fractures). In the case of 3D overcoring, the stresses should be calculated based on the solutions for anisotropic rocks. HTPF is considered a better method as geological structures or high stresses do not cause any obstacles to obtaining reliable results. However, HTPF is more time-consuming. Thus the decision on the alternative method for future studies depends on time and cost-efficiency.
4. In the future, when additional stress measurements are conducted at shallow depths after the excavations at the West Link, the borehole depth should reach the ground surface. This reduces the uncertainty regarding the horizontal stresses closer to the ground and increases the measured stress data. This is valuable for assessing the locked-in stresses.
5. Perform block stability assessment at the top heading of Mellanplan by applying the back-calculated in-situ stresses as input. This can be useful for the stability analysis related to rock pillar excavation. For block stability assessment it is recommended to utilise a distinct element method (DEM) software.
6. Perform displacement analyses of the top heading at Mellanplan by utilising a 3D numerical program, e.g., *RS3*.

12 References

Amadei, B. and Stephansson, O. (1997) *Rock Stress and Its Measurement*. 1st ed. Springer Dordrecht.

Anderson, E. M. (1951) *The Dynamics of Faulting and Dike Formation with Applications in Britain*. 2nd ed. Edinburgh: Oliver and Boyd.

Barton, N. (1976) The Shear Strength of Rock and Rock Joints. *International Journal of Rock Mechanics and Mining Sciences & Geomechanics Abstracts*, 13.9, pp. 255–279.

Barton, N. (1995) The Influence of Joint Properties in Modelling Jointed Rock Masses. *8th congress of ISRM*. Vol. 3. Tokyo, Japan, pp. 1023–1032.

Barton, N. (2002) Some New Q-value Correlations to Assist in Site Characterisation and Tunnel Design. *International Journal of Rock Mechanics and Mining Sciences*, 39.2, pp. 185–216.

Barton, N. and Bandis, S. (1990) Review of Predictive Capabilities of JRC-JCS Model in Engineering Practice. *International Symposium on Rock Joints*. Balkema, Rotterdam, pp. 603–610.

Barton, N. and Choubey, V. (1977) The Shear Strength of Rock Joints in Theory and Practice. *Rock Mechanics and Rock Engineering*, 10.1, pp. 1–54.

Barton, N. and Hansteen, H. (1978) Large Underground Openings at Shallow Depth: Comparison of Deformation Magnitudes from Jointed Models and Linear Elastic F.E. Analyses. *Fjellsprengningsdagen - Bergmekanikkdagen*. Oslo, Norway: Norwegian Tunneling Society, pp. 20.1–20.30.

Barton, N. R., Lien, R., and Lunde, J. (1974) Engineering Classification of Rock Masses for the Design of Tunnel Support. *Rock Mechanics and Rock Engineering*, 6.4, pp. 189–236.

Basnet, C. B. and Panthi, K. K. (2019) Evaluation on the Minimum Principal Stress State and Potential Hydraulic Jacking from the Shotcrete Lined Pressure Tunnel: A Case from Nepal. *Rock Mechanics and Rock Engineering*, 52, pp. 2377–2399.

BeFo (2022) Evaluation and Interpretation of Initial Rock Stresses for Stockholm and Gothenburg. Tech. rep. BeFo - Rock Engineering Research Foundation.

Bieniawski, Z. T. (1976) Rock Mass Classification in Rock Engineering. *Exploration for rock engineering, proc of the symp*. Cape Town, pp. 97–106.

Bieniawski, Z. T. (1978) Determining Rock Mass Deformability: Experience from Case Histories. *International Journal of Rock Mechanics and Mining Sciences & Geomechanics Abstracts*, 15.5, pp. 237–247.

Bieniawski, Z. T. (1989) *Engineering rock mass classifications*. New York: Wiley.

Bieniawski, Z. T. (1993) “Classification of Rock Masses for Engineering: The RMR System and Future Trends”. *Rock Testing and Site Characterization*. Ed. by J. A. Hudson. Oxford: Pergamon, pp. 553–573.

Bieniawski, Z. T. and Van Heerdan, W. L. (1975) The Significance of In-situ Tests on Large Rock Specimens. *International Journal of Rock Mechanics and Mining Sciences & Geomechanics Abstracts*, 12.4, pp. 101–113.

Boncheva, L. and Olsson, R. (2022) *Mail correspondence - Overburden in Mellanplan*.

Brady, B. H. G. and Brown, E. T. (2006) *Rock Mechanics*. 3rd ed. Springer Dordrecht.

Broch, E., Grasbakken, E., Engelstad, Ø., and Gjæringen, G. (2016) Norwegian Rock Caverns. *Norwegian Tunneing Society*, 25.

Brown, E. T. and Hoek, E. (1978) Trends in Relationships between Measured Rock In-Situ Stress and Depth. *International Journal of Rock Mechanics and Mining Sciences & Geomechanics Abstracts*, 15.4, pp. 211–215.

Cai, M., Kaiser, P. K., Tasaka, Y., and Minami, M. (2007) Determination of Residual Strength Parameters of Jointed Rock Masses Using the GSI system. *International Journal of Rock Mechanics and Mining Sciences*, 44.2, pp. 247–265.

Corthesy, R., Gill, D. E., and Nguyen, D. (1990) The Modified Doorstopper Cell Stress Measuring Technique. *Proceedings of the Conference on Stresses in Underground Structures*. Ottawa, pp. 23–32.

Deere, D. U. and Miller, R. P. (1966) Engineering Classification and Index Properties for Intact Rock. Tech. rep. Illinois: University of Illinois, Department of Civil Engineering.

Drotninghaug, J. R. (2022) *Discussion during Laboratory tests*.

Eberhardt, E. (2012) The Hoek-Brown Failure Criterion. *Rock Mechanics and Rock Engineering*, 45, pp. 981–988.

Fairhurst, C. (1986) In-situ Stress Determination - An Appraisal of Its Significance in Rock Mechanics. *Symposium on Rock stress and Rock Stress Measurements*. Stockholm, pp. 3–17.

Goodman, R. E. (1989) *Introduction to rock mechanics*. 2nd. New York: Wiley.

Hammah, R. E., Yacoub, T., Corkum, B., and Curran, J. H. (2008) The Practical Modelling of Discontinuous Rock Masses with Finite Element Analysis. *The 42nd US Rock Mechanics Symposium*. San Fransico.

Heidbach, O. et al. (2018) The World Stress Map Database Release 2016: Crustal Stress Pattern Across Scales. *Tectonophysics*, 744, pp. 484–498.

Hoek, E. and Brown, E. T. (1980) *Underground Excavations in Rock*. London: The Institution of Mining and Metallurgy.

Hoek, E. and Brown, E. T. (1997) Practical Estimates of Rock Mass Strength. *International Journal of Rock Mechanics and Mining Sciences*, 34.8, pp. 1165–1186.

Hoek, E., Carranza-Torres, C., and Corkum, B. (2002) Hoek–Brown Failure Criterion – 2002 Edition. *Proc. NARMS-TAC Conference*. Toronto.

Hoek, E. and Diederichs, M. S. (2006) Empirical Estimation of Rock Mass Modulus. *International Journal of Rock Mechanics and Mining Sciences*, 43.2, pp. 203–215.

Hoek, E., Kaiser, P. K., and Bawden, W. F. (1995) *Support of Underground Excavation in Hard Rock*. Rotterdam: A.A. Balkema.

Hoek, E. (1994) Strength of Rock and Rock masses. *ISRM News Journal*, 2.2, pp. 4–16.

Hoek, E. (2007) *Practical Rock Engineering*. Chap. 13 - Design of Large Underground Caverns. URL: https://www.rocscience.com/learning/hoeks-corner.

Høien, A. H., Nilsen, B., and Olsson, R. (2019) Main Aspects of Deformation and Rock Support in Norwegian Road Tunnels. *Tunnelling and Underground Space Technology*, 86, pp. 262–278.

Hudson, J. A. and Harrison, J. P. (1997) *Engineering Rock Mechanics - An introduction to the Principles*. Pergamon Press.

ISRM (1975) Report of the commission on terminology. Tech. rep. Lisbon.

ISRM (1978a) International Society for Rock Mechanics Commission on Standardization of Laboratory and Field Tests: Suggested Methods for the Quantitative Description of Discontinuities in Rock Masses. *International Journal of Rock Mechanics and Mining Sciences & Geomechanics Abstracts*, 15.6, pp. 319–368.

ISRM (1978b) Suggested Methods for Determining Sound Velocity. *International Journal of Rock Mechanics and Mining Sciences & Geomechanics Abstracts*, 15.2, pp. 53–58.

ISRM (1978c) Suggested Methods for Determining Tensile Strength of Rock Materials. *International Journal of Rock Mechanics and Mining Sciences & Geomechanics Abstracts*, 15, pp. 99–103.

ISRM (1979) Suggested Methods for Determining the Uniaxial Compressive Strength and Deformability of Rock Materials. *International Journal of Rock Mechanics and Mining Sciences & Geomechanics Abstracts*, 16.2, pp. 137–140.

ISRM (1981) Commission on the Classification of Rocks and Rock Masses - Basic geotechnical description of rock masses. *International Journal of Rock Mechanics and Mining Sciences & Geomechanics Abstracts*, 18.1, pp. 85–110.

ISRM (1985) Suggested Method for Determining Point Load Strength. *International Journal of Rock Mechanics and Mining Sciences & Geomechanics Abstracts*, 22.2, pp. 51–60.

ISRM (2003) ISRM Suggested Methods for Rock Stress Estimation Part 1: Strategy for Rock Stress Estimation. *International Journal of Rock Mechanics and Mining Sciences*, 40, pp. 991–998.

ISRM (2009) ISRM Suggested Method for Determination of the Schmidt Hammer Rebound Hardness: Revised Version. *International Journal of Rock Mechanics and Mining Sciences*, 46.3, pp. 627–634.

ISRM (2012) ISRM Suggested Methods for Rock Stress Estimation—Part 5: Establishing a Model for the In Situ Stress at a Given Site. *Rock Mechanics and Rock Engineering*, 45, pp. 955–969.

ISRM (2018) ISRM Suggested Method for Determining the Basic Friction Angle of Planar Rock Surfaces by Means of Tilt Tests. *Rock Mechanics and Rock Engineering*, 51, pp. 3853–3859.

Jing, L. (2003) A Review of Techniques, Advances and Outstanding Issues in Numerical Modelling for Rock Mechanics and Rock Engineering. *International Journal of Rock Mechanics and Mining Sciences*, 40.3, pp. 283–354.

Kaiser, P., Tannant, D., and McCreath, D. (1996) “Canadian Rock Burst Support Handbook”. Sudbury, Ontario: Geomechnaics Research Center, p. 385.

Lantmäteriet (2022) *Min karta*. URL: https://minkarta.lantmateriet.se/. (Accessed 14 November 2022).

Larsen, T. E. (2022) *Discussion on 2D doorstopper measurements conducted by SINTEF at Mellanplan*.

Li, C. C. (2006) Correlation of In-situ Stresses to Geological Structures in Two Underground Mines. *Proceedings of the Int. Conf. on In-situ Rock Stress*. Trondheim, Norway, pp. 151–158.

Li, C. C. (2021) *Rock Mechanics - Basic course*. Norwegian University of Science and Technology.

Li, C. C. (2017) Principles of Ground Support Design. *ISRM 3rd Nordic Rock Mechanics Symposium*. Helsinki, Finland, pp. 8–18.

Ljunggren, C., Chang, Y., Janson, T., and Christiansson, R. (2003) An Overview of Rock Stress Measurement Methods. *International Journal of Rock Mechanics and Mining Sciences*, 40.7-8, pp. 975–989.

Marinos, V., Marinos, P., and Hoek, E. (2005) The Geological Strength Index: Applications and Limitations. *Bulletin of Engineering Geology and the Environment*, 64, pp. 55–65.

Martin, C., Kaiser, P., and Christiansson, R. (2003) Stress, Instability and Design of Underground Excavations. *International Journal of Rock Mechanics and Mining Sciences*, 40, pp. 1027–1047.

Myrvang, A. (2001) *Rock Mechianics*. Trondheim: Norwegian University of Science and Technology.

NGI (2022) *Handbook - Using the Q-system*. 2022nd ed. Oslo.

Nikolic, M., Roje-Bonacci, T., and Ibrahimbegovic, A. (2016) Overview of the Numerical Methods for the Modelling of Rock Mechanics Problems. *Technical Gazette*, 23, pp. 627–637.

Nilsen, B. (2016) *Ingeniørgeologi-Berg Grunnkurskompendium*. Norwegian University of Science and Technology.

Nilsen, B. and Palmström, A. (2000) *Engineering Geology and Rock Engineering - Handbook No. 2*. Norwegian Rock Mechanics Group.

Nilsen, B. and Thidemann, A. (1993) “Rock Engineering”. Vol. 9. Hydropower Development. Norwegian Institute of Technology Division of Hydraulic Engineering.

Olsson, R. (2020) In-situ stress presentation Gothenburg. Tech. rep. NGI.

Olsson, R. (2022a) *Discussion on geological conditions*.

Olsson, R. (2022b) *Discussion on laboratory results*.

Olsson, R. (2022c) *Discussion on stress measurements*.

Olsson, R. (2022d) *Mail correspondence*.

Olsson, R. and Dammyr, Ø. (2022) *Discussion on stress measurements and anisotropy*.

Palmstrøm, A. (1995) RMi - A Rock Mass Characterization System for Rock Engineering Purposes. PhD thesis. University of Oslo.

Palmström, A. (2009) Combining the RMR, Q, and RMi Classification Systems. eprint: https://rockmass.net/files/combining_RMR-Q-RMi.pdf.

Palmström, A. and Broch, E. (2006) Use and Misuse of Rock Mass Classification Systems with Particular Reference to the Q-system. *Tunnelling and Underground Space Technology*, 21.6, pp. 575–593.

Panthi, K. (2006) Analysis of Engineering Geological Uncertainties Related to Tunnelling in Himalayan Rock Mass Conditions. PhD thesis. Norwegian University of Science and Technology.

Panthi, K. K. (2017) Review on The Prevailing Methods for the Prediction of Potential Rock Burst/Rock Spalling in Tunnels. *Fjellsprengningsdagen - Bergmekanikkdagen 2017*. Oslo: Norsk Forening for Fjellsprengningsteknikk and Norsk Bergmekanikkgruppe, pp. 29.1–29.8.

Panthi, K. (2022) Rock Pillar Stability in Tunnels. Research rep. Trondheim: Norwegian University of Science and Technology.

Patton, F. D. (1966) Multiple Modes of Shear Failure In Rock. *1st ISRM Congress*. Lisbon, Portugal.

Reynolds, J. M. (2011) *An Introduction to Applied and Environmental Geophysics*. 2nd. Wiley-Blackwell.

Rocscience (2022a) *Dips*. URL: https://www.rocscience.com/software/dips. (Accessed 21. October, 2022).

Rocscience (2022b) *Gravity Field Stress - Locked In Stress*. URL: https://www.rocscience.com/help/rs3/documentation/loading/field-stress/gravity-field-stress. (Accessed 10. November, 2022).

Rocscience (2022c) *RS2 User Guide*. URL: https://www.rocscience.com/help/rs2/overview. (Accessed 28. September, 2022).

Rocscience (2022d) *RS3 User Guide*. URL: https://www.rocscience.com/help/rs3/overview. (Accessed 28. September, 2022).

Rocscience (2022e) *RSData*. URL: https://www.rocscience.com/software/rsdata. (Accessed 26. October, 2022).

Rocscience (2022f) *XFEM Theory*. URL: https://www.rocscience.com/help/rs2/verification-theory/theory-manuals/xfem. (Accessed 29. September, 2022).

Selmer-Olsen, R. and Broch, E. (1977) General Design Procedure for Underground Openings in Norway. *Proc.Int. Symp. ROCKSTORE*. 77. Stockholm, pp. 11–18.

SGU (2020a) *Geology of Sweden*. Geological Survey of Sweden. URL: https://www.sgu.se/en/geology-of-sweden/. (Accessed 10. November, 2022).

SGU (2020b) *The Bedrock of Sweden*. Geological Survey of Sweden. URL: https://www.sgu.se/en/geology-of-sweden/rocks/the-bedrock-of-sweden/. (Accessed 19 September 2022).

SGU (2022) *Berggrund 1:50 000 - 1:250 000*. URL: https://apps.sgu.se/kartvisare/kartvisare-berg-50-250-tusen.html. (Accessed 10. November, 2022).

SINTEF (2022a) 2-dimentional Rock Stress Measurements by Doorstopper. Vestlinken, Mellanplan DS1 and DS2. Tech. rep. 2022:00452, Version: 1.

SINTEF (2022b) *Mail correspondence with Trond Erik Larsen*.

Stille, H. and Palmström, A. (2003) Classification as a Tool in Rock Engineering. *Tunnelling and Underground Space Technology*, 18.4, pp. 331–345.

Töyrä, J. (2004) Stability of Shallow Seated Constructions in Hard Rock - A Pilot Study. Research rep. Luleå University of Technology.

Trafikverket (2014) Bergspänningssituationen i Göteborgsområdet -Sammanställning av Befintlig Information. Tech. rep. TRV2012/15258, Version: A.

Trafikverket (2016a) Ingenjörsgeologisk Prognos. Tech. rep. E00-17-025-0000-0100, Version: B.

Trafikverket (2016b) Redogörelse för Förutsättningar och Metoder Fördimensionering av Bergkonstruktioner. Tech. rep. E00-17-025-0000-0006, Version: B.

Trafikverket (2016c) Tekniskt PM Bergteknik Bilaga 2, Station Korsvägen. Tech. rep. E05-17-013-0700-1001, Version: B.

Trafikverket (2018) *Västlänken - Station Korsvägen West - Overall Construction and Risk and Safety Plan.* Drawing nr: 6417.200.003. AutoCAD.

Trafikverket (2021) *The West Link Project (Västlänken)*. URL: https://bransch.trafikverket.se/en/startpage/projects/Railway-construction-projects/The-West-Link-ProjectVastlanken/. (Accessed 19 September 2022).

Trafikverket (2022a) *Deletapp Korsvägen*. URL: https://www.trafikverket.se/vara-projekt/projekt-i-vastra-gotalands-lan/vastlanken/deletapp-korsvagen/. (Accessed 19 September 2022).

Trafikverket (2022b) Geological Mapping and Rock Support Mellanplan 2022-10-25. Tech. rep.

Trafikverket (2022c) Produktionsrapport för E05 Tunnel V.45 - Projekt Västlänken. Tech. rep.

Trafikverket (2022d) *Västlänken - Station Korsvägen - Galleri Mellanplan*. Drawing nr: E05-17-300-0700-150. AutoCAD.

Trafikverket (2022e) *Västlänkens digitala karta*. URL: https://gis.trafikverket.se/portal/apps/opsdashboard/index.html#/3ad0c0fdb17f42e4abf180122d0cb1bb. (Accessed 19 September 2022).

Trafikverket (2022f) *Västra Götaland - Västlänken*. URL: https://www.trafikverket.se/vara-projekt/projekt-i-vastra-gotalands-lan/vastlanken/. (Accessed 19 September 2022).

Trinh, N. (2022) *Discussion on stress measurements near ground surface and numerical modelling*.

Trinh, N. Q., Holmøy, K. H., Larsen, T., and Myrvang, A. (2016) Continued Rock Stress and Displacement Measurements Combined With Numerical Modeling as an Active, Realistic Rock Engineering Tool. *7th ISRM International Symposium on In-Situ Rock Stress*. Tampere, Finland, pp. 181–193.

Tsidzi, K. E. N. (1990) The Influence of Foliation on Point Load Strength Anisotropy of Foliated Rocks. *Engineering Geology*, 29.1, pp. 49–58.

Tyréns and Olsson, R. (Sept. 2022) *Mail correspondance - Schmidthammer test*.

Worotnick, G. and Walton, R. J. (1976) Triaxial Hollow Inclusion Gauges for Determination of Rock Stress In situ. *Symposium on Investigation of Stress in Rock : Advances in Stress Measurement*. Sydney, pp. 1–8.

Yaméogo, S. T., Corthésy, R., and Leite, M. H. (2013) Influence of Local Heterogeneity on Doorstopper Stress Measurements. *International Journal of Rock Mechanics and Mining Sciences*, 60, pp. 288–300.

Zoback et al., M. L. (1989) Global Patterns of Tectonic Stress. *Nature*, 341, pp. 291–298.

Appendix A

Q_{bas} West Pilot

Table A1: *Registered Q_{bas} from the tunnel mapping at the West Pilot.*

Profile	Area	RQD	Jn	Jr	Ja	Jw	SRF	Q_{bas}
0/002-0/008	Roof	80(-90)	6	1.5	4	1	1	5
0/008-0/012	Roof and walls	90	6	1.5	8-12	1	1	2.25
0/012-0/018	Roof and walls	90	6	1.5	8-12	1	1	2.8
0/018-0/021	Roof	(80-)90	6	(1.5)-3	(4-12)10	1	1	4.5
0/021-0/023	Roof	(90-)100	4(-6)	(1.5)-3	(3-)8	1	1	9.4
0/023-0/025	Roof and walls	90	4(-6)	2	(4-)8	1	1	5.6
0/025-0/028	Roof and walls	90(-100)	4(-6)	2	(4-)8	1	1	7.5
0/028-0/030	Roof	90(-100)	4(-6)	(1.5-3)2	(4-)8	1	1	11.3
0/030-0/033	Roof and walls	95	(3-)4	(1.5-3)2	4	1	1	11.9
0/033-0/035	Roof and walls	90(-100)	4	(2-)3	4	1	1	18.8
0/035-0/038	Roof and walls	90(-100)	4	(1.5-3)2	4	1	1	12.5
0/038-0/040	Roof and walls	90(-100)	4	2(-3)	4	1	1	11.3
0/040-0/043	Roof and walls	(50-90)70	4(-6)	(1.5)-2	(6-)8	1	1	3.3
0/043-0/045	Roof and walls	(80-100)90	4(-6)	(1.5)-2	(6-)8	1	1	4.2
0/045-0/048	Roof and walls	80(-90)	4(-6)	(2-)3	(6-)8	1	1	4.4
0/048-0/051	Roof and walls	80(-90)	4	(2-)3	(6-)8	1	1	5.6
0/051-0/052	Roof and walls	90	4	(1.5-3)2	(6-)8	1	1	5.6

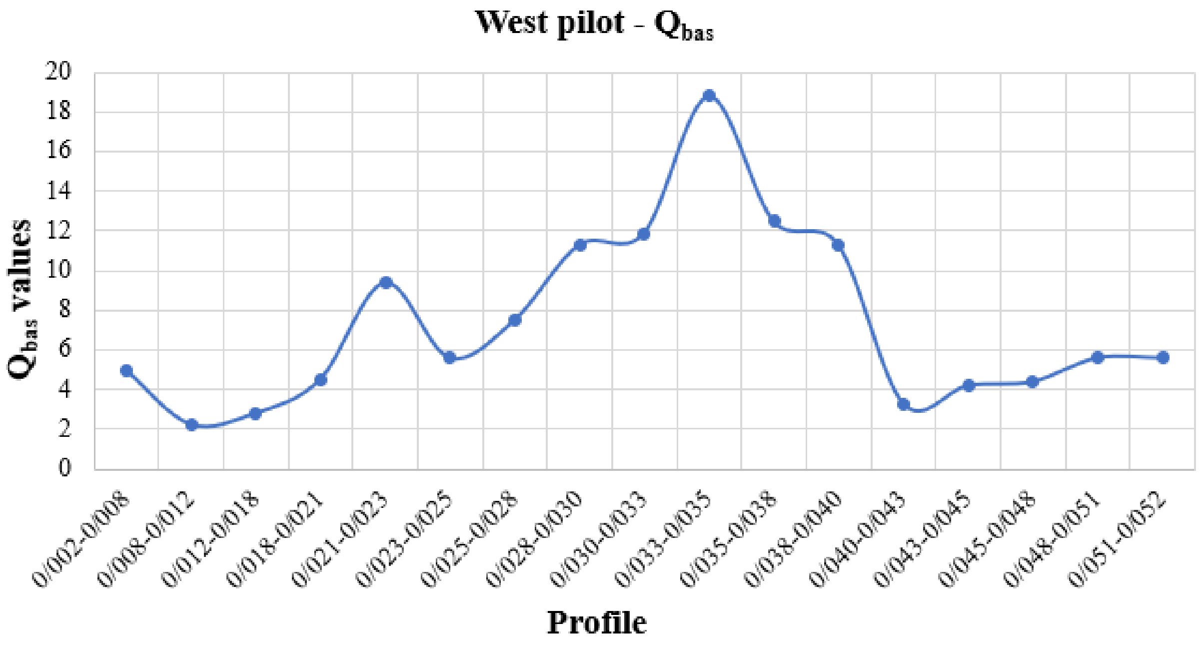

Figure A1: *Variations in Q_{bas} along the profiles at the West Pilot.*

***Table A2:** Registered rock types and descriptions from the West Pilot.*

Profile	Rock type	Grain size	Description
0/002-0/008	Granodiorite gneiss	Coarse	Red-grey coloured gneiss. Foliation joints are planar and rough, while the steep joints have calcite/phyllosilicate infilling. Cross joints appear in walls but not on the roof with the same frequency. No visible clay, but Ja is still estimated to be 4 in Q_{bas} due to the occurrence of clay in a nearby area.
0/008-0/012	Granodiorite gneiss	Coarse	Clear foliation. Mica-rich rock mass. Clay fillings of around 1 cm in the opposite cross joint. Steep foliation joints of 80 degrees. Phyllosilicate fillings in vertical joints. No block falls.
0/012-0/018	Granodiorite gneiss	Medium-coarse	Red-grey colored granodiorite gneiss. Clear foliation. Less bock falls in walls. Clay fillings in opposite cross joints (0.5-1 cm). Dry section.
0/018-0/021	Granodiorite gneiss	Medium	Red-grey coloured gneiss. Foliation is dominating, which gives schistose rocks. Clay is observed in the cross joints and is relatively thick and in some joints. Swelling clay behaviour is predicted.
0/021-0/023	Granodiorite gneiss	-	Red-grey colored gneiss. Foliation is dominating. Wavy structures with foliation joints creating schistose rock mass. Clay infilling in the cross joints.
0/023-0/025	Granodiorite gneiss	Medium-coarse	Grey-red colored gneiss. Clear foliations, that are undulating. Biotite and mica in the whole rock mass. Quite steep foliations. Generally thin infilling, except for cross joints with clay (5 mm-10 mm).
0/025-0/028	Granodiorite gneiss	Medium	Grey-red colored gneiss. Phyllosilicate infilling is typical in the vertical joints and clay (with phyllosilicate) in the opposite cross joints. Less block fall in walls. Around 2-10 mm clay infilling.
0/028-0/030	Granodiorite gneiss	Coarse	Grey-red gneiss with schistose structure. Foliations are tight and mostly without infilling. Clay fillings in cross joints are mostly planar and slightly rough. Clay fillings are less than 1 cm. Steep joints are filled with crushed rock and are undulating.
0/030-0/033	Granodiorite gneiss	Coarse	Grey-red colored gneiss. Foliation is dominating joint. Foliation joints are tight and have little alteration. Some have planar to undulating structure. Clay filling in cross joints are thinner than previously observed with 1-2 mm.
0/033-0/035	Granodiorite gneiss	Medium-coarse	Red-grey gneiss, undulating and rough. Calcite filling is around 2 mm in the cross joints.
0/035-0/038	Granodiorite gneiss	Medium-coarse	Red-grey gneiss. Foliation is less undulating. Less block falls from roof. Thin band of metabasite on the roof. Clay filling in the cross joint.
0/038-0/040	Granodiorite gneiss	Coarse	Red-grey gneiss. Foliation is generally undulating, and wavy. Less block falls from roof. Phyllosilicate filling in cross joints, around 4 mm filling.
0/040-0/043	Granodiorite gneiss	Medium-coarse	Red-grey gneiss. Foliation varies between undulating and wavy. Relative big block falls from the roof (1 m deep and 2.5 m deep). Issues during charging of tunnel face due to block falls.
0/043-0/045	Granodiorite gneiss	Medium-coarse	Red-grey gneiss. Foliation varies between undulating and wavy. Less block falls from the roof but an area with 1 m deep block fall. Clay filling in cross joints.
0/045-0/048	Granodiorite gneiss	Coarse	Grey-red coloured gneiss. Wavy and undulating foliation, with schistose structures in some places. Clay filling in cross joints. Block falls from the roof. Joints are irregular and smooth, and rough.
0/048-0/051	Granodiorite gneiss	Coarse	Grey-red gneiss. Foliation is very wavy, but sometimes smooth. Cross joints have thick clay filling.
0/051-0/052	Granodiorite gneiss	Medium-coarse	Red-grey gneiss. Foliation varies between undulating and wavy. Less block fall. Clay filling in cross joints.

Q_{bas} East Pilot

Table A3: *Registered Q_{bas} from the tunnel mapping at the East Pilot.*

Profile	Area	RQD	Jn	Jr	Ja	Jw	SRF	Q_{bas}
0/002-0/005	Roof and walls	80(-90)	9	2	(4-)6	1	1	2.96
0/005-0/010	Roof and walls	(85-)90	6	2	(2-)3	1	1	10
0/010-0/012	Roof and walls	90	6	2	(2-)4	1	1	7.5
0/012-0/015	Roof and walls	95(-100)	6	(2-)3	(3-)4	1	1	11.9
0/015-0/018	Roof and walls	90	6	1(-2)	6-8	1	1	2.5
0/018-0/022	Roof and walls	(50-90)75	6	(1.5-)2	4	1	1	6.3
0/019-0/023	Roof and walls	(50-90)75	6	2	4	1	1	6.3
0/023-0/026	Roof and walls	80	6	(1.5-)2	4	1	1	5
0/026-0/030	Roof and walls	90(-100)	6	1.5	4	1	1	5.6
0/030-0/033	Roof and walls	80	4(-6)	(1-3)2	(4-)8	1	1	5
0/033-0/036	Roof and walls	90	4	1.5	8	1	1	4.2
0/036-0/038	Roof and walls	90	4	2	4	1	1	11.3
0/038-0/041	Roof and walls	90	4	2(-3)	(2-8)4	1	1	11.3
0/041-0/045	Roof and walls	90(-100)	6	2(-3)	4(-6)	1	1	7.5
0/045-0/047	Roof and right wall	90(-100)	4(-6)	2(-3)	(4-)8	1	1	7.3
0/047-0/050	Roof and walls	90(-100)	(4-)6	2(-3)	(4-)9	1	1	7.5
0/050-0/052	Roof and walls	90(-100)	(4-)6	2(-3)	(1-)4	1	1	11.3

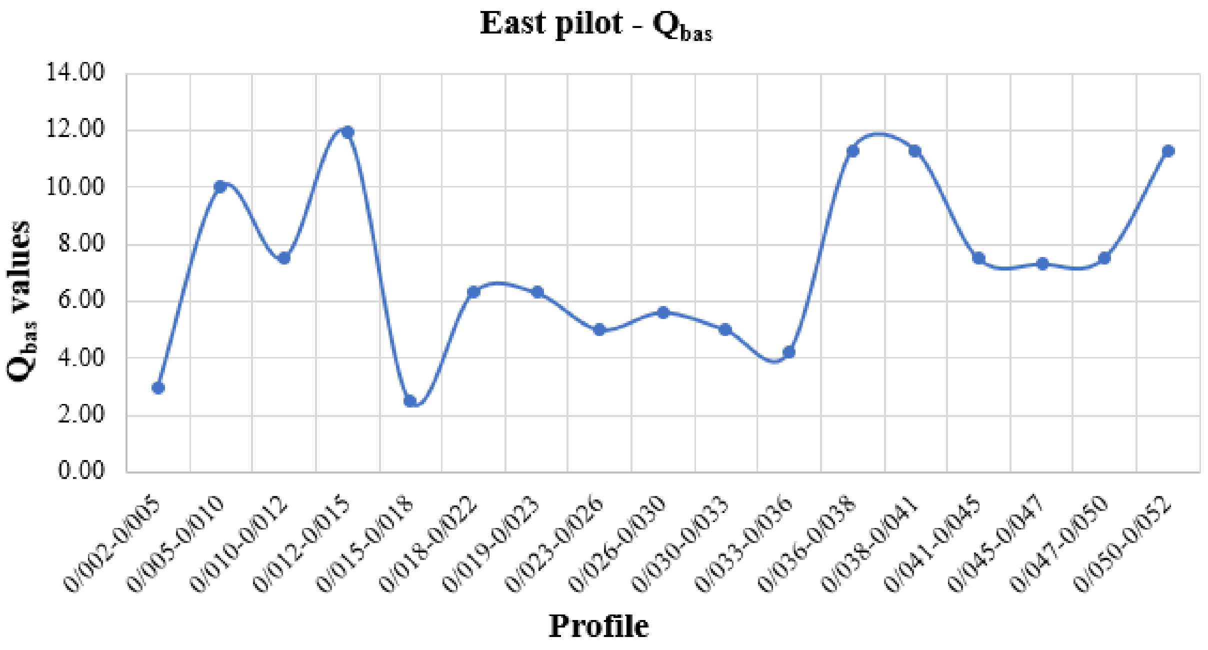

Figure A2: *Variations in Q_{bas} along the profiles at the East Pilot.*

Table A4: *Registered rock types and descriptions from the East Pilot.*

Profile	Rock type	Grain size	Description
0/002-0/005	Granodiorite gneiss	Medium-coarse	Red-grey colored gneiss. Clear foliations. Clay filling in cross joints around 2 mm thick.
0/005-0/010	Granodiorite gneiss	-	Gneiss with irregular foliations. Foliation joints are dominating. Some schistosity in some areas. Clay fillings in opposite cross joints. Phyllosilicate in vertical cross joints.
0/010-0/012	Granodiorite gneiss	Medium-coarse	Red-grey colored gneiss. Clear foliations and cracks along the foliation plan. Thin clay filling in foliations and cross joints.
0/012-0/015	Granodiorite gneiss and metabasite.	Medium	Gneiss in roof and left wall, and metabasite in right wall. Thin clay infilling in cross joints. Phyllosilicate in vertical joints.
0/015-0/018	Granodiorite gneiss and metabasite.	Medium	Gneiss and metabasite (amphibolite body) are dominating. Metabasite is blocky, while gneiss is schistose. Clay appears in cross joints and vertical joints. One block fall with 2.3 m depth in roof and one block fall of 1 m depth in the right wall.
0/018-0/022	Granodiorite gneiss and metabasite.	Medium-coarse	Red-grey colored gneiss in left roof and walls, while metabasite in right roof. Metabasite in roof has a width of 4 m. Blocky metabasite and schistose gneiss.
0/019-0/023	Granodiorite gneiss and metabasite.	Medium-coarse	Metabasite in roof has a width of 3-4 m. Metabasite is blocky while gneiss is schistose in the left side of the roof. Clay filling in cross joints.
0/023-0/026	Granodiorite gneiss and metabasite.	-	Metabasite is a part of a chlorite alteration. Chlorite filling in most of the joints. Bigger block falls in roof along metabasite. Joints are generally smooth and undulating.
0/026-0/030	Granodiorite gneiss and metabasite.	-	Diabae band with clear foliation, and gneiss with clear foliation. Joints along foliations and 2 opposite cross joints with thin clay filling. Diabase band is blocky. Less block falls from the roof.
0/030-0/033	Granodiorite gneiss and metabasite.	Medium	Red-grey gneiss and metabasite. Foliation is steep, and chlorite is in contact with metabasite. Clay filled joints are 3 mm thick. Thinner clay and chlorite appear in cross joints.
0/033-0/036	Granodiorite gneiss and metabasite.	Medium	Gneiss and metabasite in walls and roof. Thick clay filling in cross joints and chlorite in vertical joints.
0/036-0/038	Granodiorite gneiss and metabasite.	Medium-coarse	Red-grey gneiss and metabasite in left roof and pillar wall. Block fall in pillar wall. Clay filling in the opposite cross joint. Clay filling in some foliation joints.
0/038-0/041	Granodiorite gneiss and metabasite.	Medium-coarse	Red-grey gneiss with 0.5 m metabasite band in left roof. Pillar wall has also metabasite. Foliation is rough and undulating. Clay is mixed with phyllosilicate, and has a thickness of 2-5 mm.
0/041-0/045	Granodiorite gneiss	Coarse	Grey-red colored gneiss. Metabasite does not appear. Gneiss has strong foliations. Cross joints have thin clay filling in some areas.
0/045-0/047	Granodiorite gneiss	Coarse	Red-grey colored gneiss. Clay fillings along foliation joints. Thinner clay filling in cross joints.
0/047-0/050	Granodiorite gneiss	Medium-coarse	Red-grey colored gneiss. Less block fall in roof and walls. Clay filling in cross joints have thickness of 4-5 cm.
0/050-0/052	Granodiorite gneiss	Coarse	Red-grey colored gneiss. Nearly schistose rock mass along foliation joints. Irregular joints in all joint sets. Chlorite, phyllosilicate and calcite in cross joints. Smooth and undulating joints.

Appendix B

Joints and RMR$_{bas}$ West Pilot

The table is divided into three parts due to the large data set. RMR$_{bas}$ *and* Q_{bas} *are calculated from the joint data registered. Note that parameters for roughness and infilling are based on registered* J_r *and* J_a *values, as well as descriptions given from tunnel mapping. The highlighted blue cells show ratings for the RMR parameters.*

Table B1: *Part 1 - Calculated RMRbas and Qbas from joint mapping in West Pilot*

Profile	Joint frequency	Joint	Dip direction	Dip	UCS [MPa]	RQD	Spacing [m]	Length [m]	Separation [mm]	Roughness	Jr	Infilling	Weathering	Ja	Water inflow	RMRbas	Qbas
0/002-0/008	12	Foliation	288	52	100-250	80(-90)	0.2-0.6	> 10	-	Slightly rough	1.5	Mica	Slightly	4	Dry		
					12	17	10	1	5	3		2	5		15	70	10
0/002-0/008	2	J2	70	30	100-250	80(-90)	0.2-0.6	> 10	-	Slightly rough	1.5	-	Slightly	-	Dry		
					12	17	10	1	5	3		6	5		15	74	16
0/002-0/008	4	Random	188	85	100-250	80(-90)	0.6-2	> 10	-	Slightly rough	1.5	Chlorite	Slightly	4	Dry		
					12	17	15	1	5	3		2	5		15	75	18
0/008-0/012	20	Foliation	230	60	100-250	90	0.2-0.6	> 10	0.1-0.5	Slightly rough	1.5	-	Slightly	1	Dry		
					12	17	10	1	4	3		6	5		15	73	14
0/008-0/012	3	J2	50	30	100-250	90	> 2	> 10	> 5	Slightly rough	1.5	Clay	Slightly	8-12	Dry		
					12	17	20	1	0	3		0	5		15	73	14
0/008-0/012	3	Random	350	50	100-250	90	> 2	> 10	0.1-0.5	Smooth	2	Clay, Calcite	Slightly	3-4	Dry		
					12	17	20	1	4	1		2	5		15	77	22
0/008-0/012	2	Random	150	60	100-250	90	> 2	> 10	0.25-2.5	Slightly rough	1.5	Phyllosilicate	Slightly	4	Dry		
					12	17	20	1	3	3		2	5		15	78	25
0/008-0/012	1	Foliation	241	80	100-250	90	0.06-0.02	> 10	0.1-0.25	Slightly rough	1.5	Clay	Slightly	4	Dry		
					12	17	5	1	4	3		2	5		15	64	5
0/012-0/018	15	Foliation	224	66-80	100-250	90	0.2-0.6	10-20	0.1-0.5	Slightly rough	1.5	Calcite	Slightly	1-2	Dry		
					12	17	10	1	4	3		4	5		15	71	12
0/012-0/018	6	J2	50	30	100-250	90	> 2	10-20	> 5	Slightly rough	1.5-3	Clay	Slightly	8-12	Dry		
					12	17	20	1	0	3		0	5		15	73	14
0/012-0/018	3	Random	124	70	100-250	90	> 2	10-20	0.25-0.5	Smooth	2	Chlorite	Slightly	3	Dry		
					12	17	20	1	4	1		4	5		15	79	28
0/018-0/021	30	Foliation	237	62	100-250	(80-)90	0.2-0.6	10-20	0.1-0.25	Slightly rough	1.5-3	-	Unweathered	2	Dry		
					12	17	10	1	4	3		6	6		15	74	16
0/018-0/021	4	J2	55	32	100-250	(80-)90	0.6-2	10-20	0.5-2.5	Rough	3	Clay	Unweathered	8-12	Dry		
					12	17	15	1	2	5		0	6		15	73	14
0/018-0/021	6	Random	188	88	100-250	(80-)90	0.6-2	3-10	0.25-0.5	Smooth	2	Chlorite	Unweathered	3-4	Dry		
					12	17	15	2	4	1		2	6		15	74	16
0/018-0/021	4	Random	114	56	100-250	(80-)90	0.6-2	3-10	0.25-2.5	Rough	3	Chlorite, Calcite Clay	Unweathered	4	Dry		
					12	17	15	2	3	5		2	6		15	77	22
0/021-0/023	8	Foliation (left side)	244	50	100-250	(90-)100	0.2-0.6	10-20	0.1-0.25	Slightly rough	1.5	Sandy particles	Unweathered	2	Dry		
					12	20	10	1	4	3		4	6		15	75	18
0/021-0/023	13	Foliation (right side)	260	66	100-250	(90-)100	0.06-0.2	10-20	0.1-0.25	Rough	3	Mica	Unweathered	2	Dry		
					12	20	8	1	4	5		2	6		15	73	14
0/021-0/023	5	J2	49	30	100-250	(90-)100	0.2-0.6	10-20	0.5-2.5	Rough	2-3	Clay	Unweathered	(6-)8	Dry		
					12	20	10	1	2	4		0	6		15	70	10
0/021-0/023	5	Random	186	86	100-250	(90-)100	0.6-2	1-3	0.1-0.25	Smooth	1.5-2	Calcite	Unweathered	3	Dry		
					12	20	15	4	4	1		4	6		15	81	35

Table B2: *Part 2 - Calculated RMRbas and Qbas from joint mapping in West Pilot*

0/023-0/025	20	Foliation	240	60	100-250	90	0.2-0.6	10-20	0.1-0.5	Smooth	2	Biotite	Slightly	2	Dry		
					12	17	10	1	4	1		4	5		15	69	9
0/023-0/025	10	J2	60	30-40	100-250	90	0.6-2	> 20	0.5- > 5	Smooth	2	Clay	Slightly	4-8	Dry		
					12	17	15	0	0	1		0	5		15	65	6
0/023-0/025	6	Random	130	62	100-250	90	0.2-0.6	3-10	0.5-2.5	Rough	3	Chlorite	Slightly	3-4	Dry		
					12	17	10	2	2	5		2	5		15	70	10
0/025-0/028	25	Foliation	240	60	100-250	90(-100)	0.2-0.6	10-20	0.1-0.25	Smooth	2	-	Slightly	2	Dry		
					12	20	10	1	4	1		6	5		15	74	16
0/025-0/028	5	J2	50	25	100-250	90(-100)	0.6-2	> 20	0.5- > 5	Smooth	2	Clay	Slightly	4-6	Dry		
					12	20	15	0	0	1		0	5		15	68	8
0/025-0/028	3	Random	142	65	100-250	90(-100)	0.6-2	3-10	0.5-2.5	Smooth	2	Phyllosilicate	Slightly	4	Dry		
					12	20	15	2	2	1		2	5		15	74	16
0/028-0/030	18	Foliation	252	63	100-250	90(-100)	0.2-0.6	3-10	0.1-0.25	Smooth	2	-	Unweathered	1	Dry		
					12	20	10	2	4	1		6	6		15	76	20
0/028-0/030	5	J2	58	25	100-250	90(-100)	0.2-0.6	10-20	0.25-2.5	Slightly rough	1.5	Clay	Unweathered	4-8	Dry		
					12	20	10	1	3	3		0	6		15	70	10
0/028-0/030	4	Random	148	70	100-250	90(-100)	0.6-2	10-20	0.25-0.5	Rough	3	Bl	Slightly	4	Dry		
					12	20	15	1	4	5		2	5		15	79	28
0/030-0/033	16	Foliation	246	60	100-250	95	0.2-0.6	10-20	0.1-0.25	Smooth	1.5-2	Sandy particles	Slightly	1-2	Dry		
					12	20	10	1	4	1		4	5		15	72	13
0/030-0/033	6	J2	53	14	100-250	95	0.2-0.6	10-20	0.5-2.5	Slightly rough	1.5	Clay	Slightly	4	Dry		
					12	20	10	1	2	3		2	5		15	70	10
0/030-0/033	2	Random	117	70	100-250	95	0.6-2	10-20	0.25-0.5	Rough	3	Clay	Slightly	4	Dry		
					12	20	15	1	4	5		2	5		15	79	28
0/030-0/033	4	Random	159	70	100-250	95	0.6-2	10-20	0.25-0.5	Smooth	2	Calcite	Slightly	3-4	Dry		
					12	20	15	1	4	1		2	5		15	75	18
0/033-0/035	15	Foliation	266	68	100-250	90(-100)	0.2-0.6	10-20	0.1-0.25	Rough	2-3	-	Slightly	1-2	Dry		
					12	20	10	1	4	4		6	5		15	77	22
0/033-0/035	2	J2	38	26	100-250	90(-100)	0.6-2	3-10	0.25-2.5	Rough	3	Clay	Slightly	4-6	Dry		
					12	20	15	2	3	5		2	5		15	79	28
0/033-0/035	2	Random	347	75	100-250	90(-100)	0.6-2	3-10	0.5-2-5	Slightly rough	1.5-3	Calcite	Slightly	3	Dry		
					12	20	15	2	2	3		2	5		15	76	20
0/033-0/035	2	Random	155	30	100-250	90(-100)	0.6-2	3-10	0.25-0.5	Rough	3	Calcite	Slightly	2-3	Dry		
					12	20	15	2	4	5		4	5		15	82	39
0/035-0/038	15	Foliation	244	68	100-250	90(-100)	0.2-0.6	10-20	0.1-0.25	Slightly rough	1.5-3	-	Slightly	1-2	Dry		
					12	20	10	1	4	3		6	5		15	76	20
0/035-0/038	4	J2	54	15	100-250	90(-100)	> 2	10-20	0.5- > 5	Rough	3	Clay	Slightly	4	Dry		
					12	20	20	1	0	5		2	5		15	80	31
0/035-0/038	2	Random	12	60	100-250	90(-100)	> 2	10-20	0.5-2.5	Slightly rough	1.5	Calcite	Slightly	3	Dry		
					12	20	20	1	2	3		4	5		15	82	39

Table B3: *Part 3 - Calculated RMRbas and Qbas from joint mapping in West Pilot*

0/038-0/040	15	Foliation	237	68	100-250	90(-100)	0.2-0.6	10-20	0.1-0.25	Smooth	2	-	Slightly	1-2	Dry		
					12	20	10	1	4	1		6	5		15	74	16
0/038-0/040	6	J2	61	30	100-250	90(-100)	0.6-2	10-20	> 5	Rough	2-3	Clay	Slightly	4	Dry		
					12	20	15	1	0	4		2	5		15	74	16
0/040-0/043	15	Foliation	252	75	100-250	(50-90)70	0.2-0.6	10-20	0.1-0.25	Smooth	2	-	Moderately	1-2	Dry		
					12	13	10	1	4	1		6	3		15	65	6
0/040-0/043	6	J2	35	30	100-250	(50-90)70	0.06-0.2	10-20	0.1-0.25	Slightly rough	1.5-3	Clay	Moderately	6-8	Dry		
					12	13	8	1	4	3		0	3		15	59	3
0/040-0/043	3	Random	310	78	100-250	(50-90)70	0.6-2	1-3	0.1-0.25	Slightly rough	1.5	Calcite	Moderately	2	Dry		
					12	13	15	4	4	3		2	3		15	71	12
0/043-0/045	12	Foliation	250	55	100-250	(80-100)90	0.2-0.6	10-20	0.1-0.25	Smooth	2	-	Moderately	1-2	Dry		
					12	17	10	1	4	1		6	3		15	69	9
0/043-0/045	6	J2	45	25	100-250	(80-100)90	0.06-0.6	10-20	> 5	Slightly rough	1.5	Clay	Moderately	6-8	Dry		
					12	17	9	1	0	3		0	3		15	60	3
0/045-0/048	12	Foliation	248	52	100-250	80(-90)	0.2-0.6	10-20	0.1-0.25	Smooth	2	Mica	Slightly	1-2	Dry		
					12	17	10	1	4	1		4	5		15	69	9
0/045-0/048	8	J2	58	22	100-250	80(-90)	0.2-0.6	10-20	0.5-2.5	Rough	2-3	Clay	Slightly	3	Dry		
					12	17	10	1	2	4		0	5		15	66	7
0/045-0/048	1	Random	160	85	100-250	80(-90)	> 2	3-10	0.1-0.25	Slightly rough	1.5	Calcite	Slightly	3	Dry		
					12	17	15	2	4	3		4	5		15	77	22
0/048-0/051	14	Foliation	245	60	100-250	80(-90)	0.2-0.6	10-20	0.1-0.25	Smooth	2	Mica	Slightly	1-2	Dry		
					12	17	10	1	4	1		4	5		15	69	9
0/048-0/051	8	J2	35	38	100-250	80(-90)	0.6-2	> 20	0.5-> 5	Slightly rough	1.5-3	Clay	Slightly	6-8	Dry		
					12	17	15	0	0	3		0	5		15	67	7
0/051-0/052	12	Foliation	255	69	100-250	90	0.2-0.6	10-20	0.1-0.25	Rough	2-3	Mica	Slightly	2	Dry		
					12	17	10	1	4	4		4	5		15	72	13
0/051-0/052	6	J2	55	22	100-250	90	0.6-2	10-20	0.5-> 5	Slightly rough	1.5-3	Clay	Slightly	6-8	Dry		
					12	17	15	1	0	3		0	5		15	68	8
0/051-0/052	2	Random	158	80	100-250	90	0.6-2	1-3	0.1-0.25	Slightly rough	1.5	-	Slightly	1-2	Dry		
					12	17	15	4	4	3		6	5		15	81	35

Joints and RMR$_{bas}$ East Pilot

The table is divided into three parts due to the large data set. RMR$_{bas}$ and Q$_{bas}$ are calculated from the joint data registered. Note that parameters for roughness and infilling are based on registered J_r and J_a values, as well as descriptions given from tunnel mapping. The highlighted blue cells show ratings for the RMR parameters.

Table B4: *Part 1 - Calculated RMRbas and Qbas from joint mapping in East Pilot*

Profile	Joint frequency	Joint	Dip direction	Dip	UCS [MPa]	RQD	Spacing [m]	Length [m]	Separation [mm]	Roughness	Jr	Infilling	Weatherning	Ja	Water inflow	RMRbas	Qbas
0/002-0/005	10	Foliation	244	62	100-250	80(-90)	0.06-0.6	> 20	0.1-0.25	Smooth	2	-	Slightly	1	Dry		
					12	17	9	0	4	1		6	5		15	69	9
0/002-0/005	5	J2	64	30	100-250	80(-90)	0.6-2	10-20	0.5-2.5	Slightly rough	1.5-3	Clay	Slightly	4-8	Dry		
					12	17	15	1	2	3		2	5		15	72	13
0/002-0/005	4	Random	138	90	100-250	80(-90)	0.6-2	3-10	0.1-0.5	Rough	2-3	Calcite	Slightly	2	Dry		
					12	17	15	2	4	4		4	5		15	78	25
0/002-0/005	3	Random	108	64	100-250	80(-90)	0.6-2	10-20	0.25-0.5	Rough	3	Calcite	Slightly	2	Dry		
					12	17	15	1	4	5		4	5		15	78	25
0/005-0/010	15	Foliation	250	55	100-250	(85-)90	0.2-0.6	10-20	0.1-0.5	Rough	3	Calcite	Slightly	1-2	Dry		
					12	17	10	1	4	5		4	5		15	73	14
0/005-0/010	2	J2	80	25	100-250	(85-)90	> 2	3-10	0.25-0.5	Smooth	2	Clay	Slightly	3	Dry		
					12	17	20	2	4	1		2	5		15	78	25
0/005-0/010	4	Random	165	90	100-250	(85-)90	> 2	3-10	0.25-2.5	Smooth	2	Calcite	Slightly	2-3	Dry		
					12	17	20	2	3	1			5		15	75	18
0/005-0/010	3	Random	355	65	100-250	(85-)90	0.6-2	3-10	0.1-0-25	Smooth	2	-	Slightly	1-2	Dry		
					12	17	15	2	4	1		6	5		15	77	22
0/010-0/012	15	Foliation	228	50	100-250	90	0.2-0.6	10-20	0.25-0.5	Smooth	2	Calcite, Clay	Slightly	2-4	Dry		
					12	17	10	1	4	1		4	5		15	69	9
0/010-0/012	6	J2	70	24	100-250	90	0.6-2	3-10	0.25-0.5	Slightly rough	1.5-3	Clay	Slightly	2-4	Dry		
					12	17	15	2	4	3		4	5		15	77	22
0/010-0/012	3	Random	122	90	100-250	90	0.6-2	3-10	0.25-0.5	Slightly rough	1.5	Phyllosilicate	Slightly	2-3	Dry		
					12	17	15	2	4	3		4	5		15	77	22
0/010-0/012	2	Random	172	75	100-250	90	> 2	3-10	0.25-0.5	Rough	3	Calcite	Slightly	2	Dry		
					12	17	20	2	4	5		4	5		15	84	49
0/012-0/015	15	Foliation	250	55	100-250	95(-100)	0.2-0.6	> 20	0.1-0.25	Rough	3	Calcite, Biotite	Slightly	1	Dry		
					12	20	10	0	4	5		4	5		15	75	18
0/012-0/015	4	J2	60	55	100-250	95(-100)	> 2	> 20	0.5-2.5	Smooth	2	Calcite, Clay	Slightly	4	Dry		
					12	20	20	0	2	1		2	5		15	77	22
0/012-0/015	6	Random	140	75	100-250	95(-100)	0.6-2	10-20	0.25-0.5	Smooth	2	Calcite	Slightly	3	Dry		
					12	20	15	1	4	1		4	5		15	77	22
0/012-0/015	6	Random	150	70	100-250	95(-100)	0.6-2	10-20	0.25-0.5	Smooth	2	Calcite	Slightly	2	Dry		
					12	20	15	1	4	1		4	5		15	77	22
0/015-0/018	15	Foliation	220	75	100-250	90	0.2-0.6	> 20	0.25-2.5	Smooth	1	Calcite	Slightly	4	Dry		
					12	17	10	0	3	1		2	5		15	65	6
0/015-0/018	7	J2	60	30	100-250	90	0.6-2	> 20	> 5	Smooth	2	Calcite, Clay	Slightly	6-8	Dry		
					12	17	15	0	0	1		0	5		15	65	6
0/015-0/018	4	Random	140	90	100-250	90	> 2	3-10	0.1-0.5	Smooth	2	Calcite, Clay	Slightly	4-6	Dry		
					12	17	20	2	4	1		4	5		15	80	31

Table B5: *Part 2 - Calculated RMRbas and Qbas from joint mapping in East Pilot*

0/018-0/022	20	Foliation	242	70	100-250	(50-90)75	0.06-0.6	10-20	0.25-0.5	Smooth	2	Calcite	Slightly	2	Dry		
					12	13	9	1	4	1		4	5		15	64	5
0/018-0/022	6	J2	78	24	100-250	(50-90)75	0.2-0.6	10-20	0.25-2.5	Slightly rough	1.5-3	Clay	Slightly	4	Dry		
					12	13	10	1	3	3		2	5		15	64	5
0/018-0/022	3	Random	142	90	100-250	(50-90)75	0.6-2	3-10	0.1-0.25	Smooth	2	Calcite	Slightly	2	Dry		
					12	13	15	2	4	1		4	5		15	71	12
0/019-0/023	25	Foliation	232	70	100-250	(50-90)75	0.06-0.6	10-20	0.25-0.5	Smooth	2	Calcite	Slightly	2	Dry		
					12	13	9	1	4	1		4	5		15	64	5
0/019-0/023	6	J2	58	20	100-250	(50-90)75	0.2-0.6	10-20	0.25-2.5	Slightly rough	1.5-3	Clay	Slightly	4	Dry		
					12	13	10	1	3	3		2	5		15	64	5
0/019-0/023	4	Random	112	90	100-250	(50-90)75	> 2	3-10	0.1-0.25	Smooth	2	Calcite	Slightly	2	Dry		
					12	13	20	2	4	1		4	5		15	76	20
0/023-0/026	17	Foliation	244	70	100-250	80	0.2-0.6	10-20	0.25-2.5	Slightly rough	1.5	Chlorite	Highly	4	Dry		
					12	17	10	1	3	3		2	1		15	64	5
0/023-0/026	6	J2	45	35	100-250	80	0.6-2	3-10	0.25-0.5	Smooth	2	Chlorite	Highly	4	Dry		
					12	17	15	2	4	1		2	1		15	69	9
0/023-0/026	1	Random	109	58	100-250	80	> 2	3-10	0.25-0.5	Slightly rough	1.5	Chlorite	Highly	4	Dry		
					12	17	20	2	4	3		2	1		15	76	20
0/026-0/030	20	Foliation	240	70	100-250	90(-100)	0.2-0.6	> 20	0.25-0.5	Slightly rough	1.5	Biotite	Slightly	4	Dry		
					12	20	10	0	4	3		2	5		15	71	12
0/026-0/030	1	J2	60	40	100-250	90(-100)	0.6-2	> 20	> 5	Slightly rough	2-3	Clay	Slightly	4-8	Dry		
					12	20	15	0	0	3		0	4		15	69	9
0/026-0/030	1	Random	360	35	100-250	90(-100)	0.6-2	> 20	> 5	Slightly rough	2-3	Clay	Slightly	4-8	Dry		
					12	20	15	0	0	3		0	4		15	69	9
0/030-0/033	10	Foliation	232	64	100-250	80	0.2-0.6	10-20	0.1-0.25	Smooth	2	Calcite, Chlorite	Slightly	4	Dry		
					12	17	10	1	4	1		2	5		15	67	7
0/030-0/033	1	Foliation	222	65	100-250	80	> 2	10-20	0.5 - > 5	Slightly rough	1-3	Clay	Slightly	8-12	Dry		
					12	17	20	1	0	3		2	5		15	75	18
0/030-0/033	5	J2	50	40	100-250	80	0.2-0.6	3-10	0.25-0.5	Rough	3	Clay, Chlorite	Slightly	6-8	Dry		
					12	17	10	2	4	5		2	5		15	72	13
0/030-0/033	1	Random	8	76	100-250	80	> 2	3-10	0.25-0.5	Smooth	2	Chlorite	Slightly	3	Dry		
					12	17	20	2	4	1		4	5		15	80	31
0/033-0/036	14	Foliation	220	70	100-250	90	0.2-0.6	> 20	> 5	Smooth	2	Clay, Calcite	Slightly	8	Dry		
					12	17	10	0	0	1		2	5		15	62	4
0/033-0/036	5	J2	50	30	100-250	90	0.6-2	> 20	> 5	Smooth	2	Clay, Chlorite	Slightly	8	Dry		
					12	17	15	0	0	1		0	5		15	65	6
0/033-0/036	1	Random	350	85	100-250	90	> 2	> 20	0.5-2.5	Slightly rough	1.5	Chlorite, Clay	Slightly	4	Dry		
					12	17	20	0	2	3		2	5		15	76	20

Table B6: *Part 3 - Calculated RMRbas and Qbas from joint mapping in East Pilot*

0/036-0/038	15	Foliation	234	50	100-250	90	0.2-0.6	> 20	0.1-0.25	Slightly rough	2-3	-	Slightly	1	Dry		
					12	17	10	0	4	3		6	5		15	72	13
0/036-0/038	2	Foliation	234	50	100-250	90	> 2	10-20	0.5- > 5	Smooth	1	Clay	Slightly	6	Dry		
					12	17	20	1	0	1		2	5		15	73	14
0/036-0/038	8	J2	10	20	100-250	90	0.6-2	10-20	0.25-0.5	Smooth	2	Clay	Slightly	4	Dry		
					12	17	15	1	4	1		2	5		15	72	13
0/038-0/041	20	Foliation	252	50	100-250	90	0.2-0.6	> 20	0.1-0.25	Slightly rough	2-3	Calcite	Slightly	2	Dry		
					12	17	10	0	4	3		4	5		15	70	10
0/038-0/041	1	Foliation	228	64	100-250	90	0.2-0.6	10-20	> 5	Smooth	1	Clay, Chlorite	Slightly	8-12	Dry		
					12	17	10	1	0	1		1	5		15	62	4
0/038-0/041	3	Random	120	60	100-250	90	> 2	10-20	0.1-0.25	Rough	3	-	Slightly	1	Dry		
					12	17	20	1	4	5		6	5		15	85	55
0/041-0/045	22	Foliation	239	70	100-250	90(-100)	0.2-0.6	10-20	0.1-0.25	Rough	3	-	Slightly	1	Dry		
					12	20	10	1	4	5		6	5		15	78	25
0/041-0/045	1	Foliation	236	70	100-250	90(-100)	> 2	10-20	0.5-2.5	Smooth	2	Clay, Calcite	Slightly	6	Dry		
					12	20	20	1	2	1		2	5		15	78	25
0/041-0/045	3	J2	6	36	100-250	90(-100)	0.6-2	3-10	0.25-0.5	Smooth	2	Clay	Slightly	4	Dry		
					12	20	15	2	4	1		2	5		15	76	20
0/041-0/045	2	Random	148	85	100-250	90(-100)	0.6-2	3-10	0.1-0.25	Slightly rough	1.5	Calcite	Slightly	2-3	Dry		
					12	20	15	2	4	3		4	5		15	80	31
0/045-0/047	1	Foliation	230	60	100-250	90(-100)	> 2	10-20	> 5	Smooth	2	Clay	Slightly	8	Dry		
					12	20	20	1	0	1		2	5		15	76	20
0/045-0/047	12	Foliation	233	66	100-250	90(-100)	0.2-0.6	10-20	0.1-0.25	Rough	3	Mica, Calcite	Slightly	2	Dry		
					12	20	10	1	4	5		4	5		15	76	20
0/045-0/047	5	J2	60	50	100-250	90(-100)	0.6-2	10-20	0.25-0.5	Rough	3	Clay	Slightly	4	Dry		
					12	20	15	1	4	5		2	5		15	79	28
0/045-0/047	2	Random	138	90	100-250	90(-100)	> 2	3-10	0.1-0.25	Smooth	2	Calcite	Slightly	2	Dry		
					12	20	20	2	4	1		4	5		15	83	44
0/047-0/050	20	Foliation	230	60	100-250	90(-100)	0.2-0.6	10-20	0.25-2.5	Smooth	2	Clay	Slightly	4-8	Dry		
					12	20	10	1	4	1		2	5		15	70	10
0/047-0/050	6	J2	52	44	100-250	90(-100)	0.6-2	10-20	0.25-0.5	Slightly rough	2-3	Clay	Slightly	4	Dry		
					12	20	15	1	4	3		2	5		15	77	22
0/047-0/050	4	Random	162	80	100-250	90(-100)	0.2-0.6	10-20	0.1-0.5	Slightly rough	2-3	Calcite	Slightly	2	Dry		
					12	20	10	1	4	3		4	5		15	74	16
0/050-0/052	12	Foliation	232	60	100-250	90(-100)	0.2-0.6	10-20	0.1-0.25	Rough	3	-	Slightly	1	Dry		
					12	20	10	1	4	5		6	5		15	78	25
0/050-0/052	1	Foliation	236	60	100-250	90(-100)	> 2	10-20	0.5- > 5	Smooth	2	Clay	Slightly	6	Dry		
					12	20	20	1	0	1		2	5		15	76	20
0/050-0/052	4	J2	63	30	100-250	90(-100)	0.6-2	10-20	0.25-0.5	Smooth	2	Clay, Chlorite	Slightly	4	Dry		
					12	20	15	1	4	1		2	5		15	75	18
0/050-0/052	1	Random	182	70	100-250	90(-100)	> 2	3-10	0.1-0.25	Smooth	2	-	Slightly	1	Dry		
					12	20	20	2	4	1		6	5		15	85	55

Appendix C

Structural mapping - West Pilot

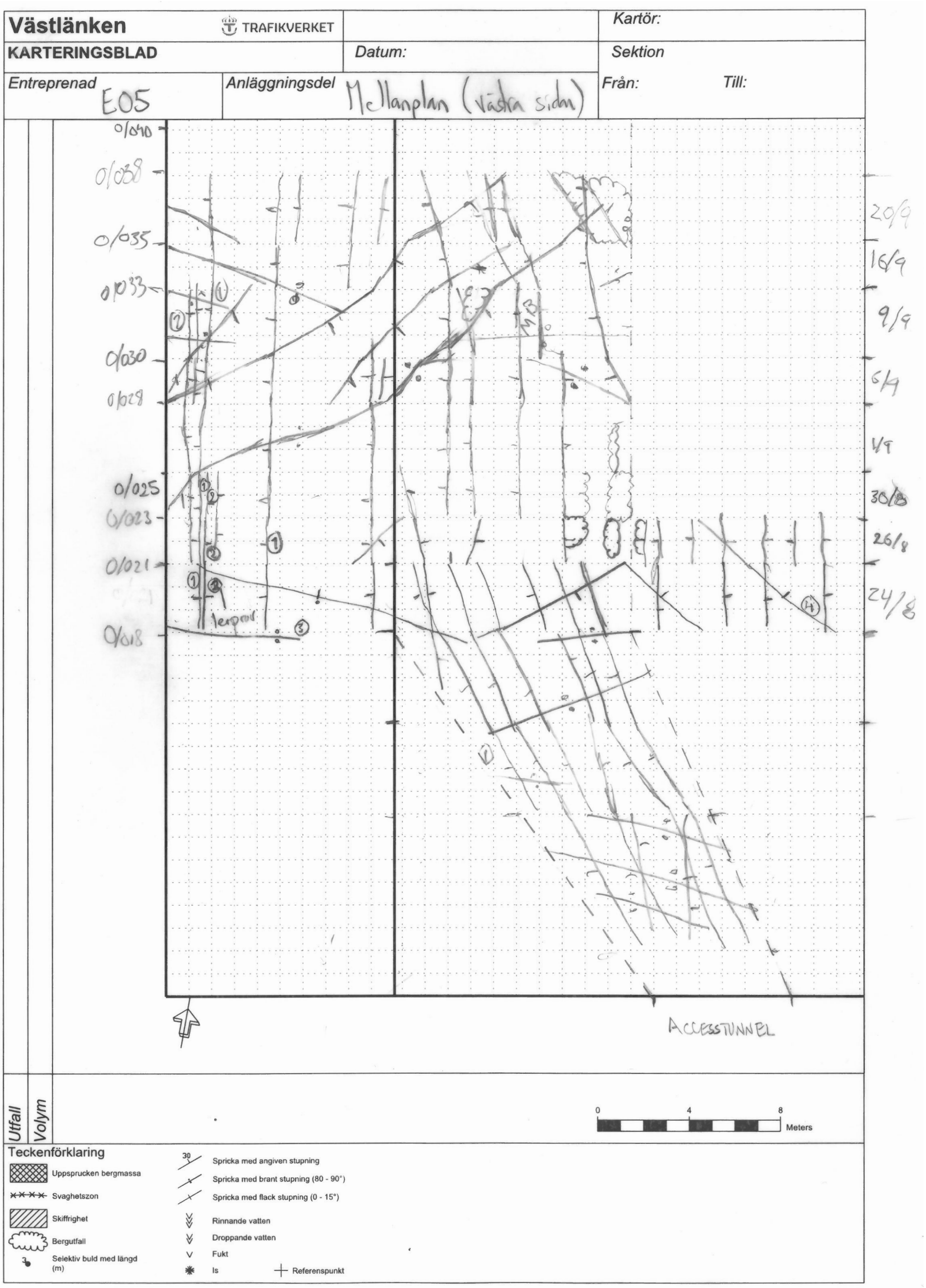

Västlänken TRAFIKVERKET		Kartör:
KARTERINGSBLAD	Datum:	Sektion
Entreprenad E05	Anläggningsdel Mellanplan (västra sidan)	Från: Till:

Figure C1: *Structural mapping at West Pilot from profile 0/002 to profile 0/038.*

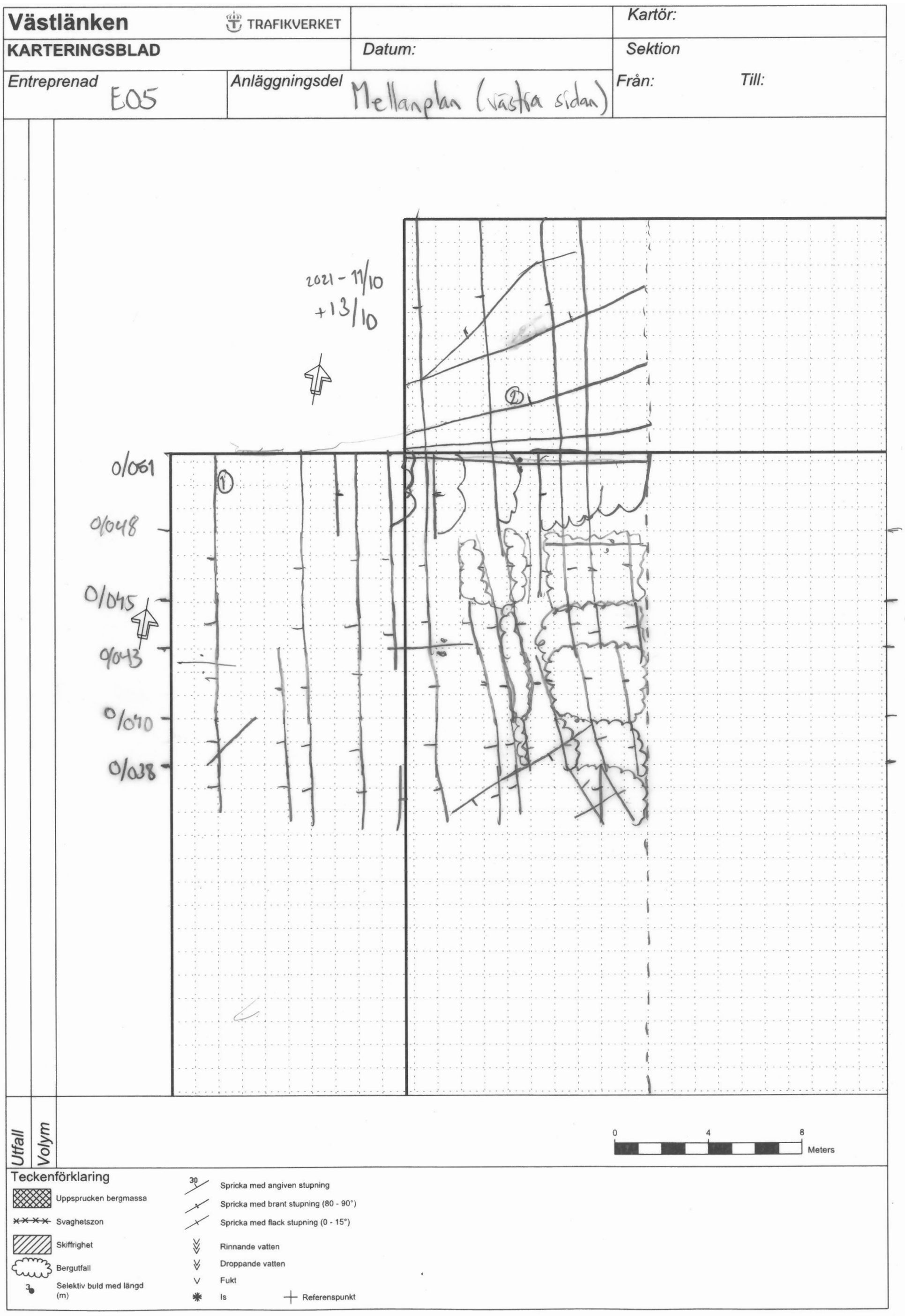

Västlänken TRAFIKVERKET

Kartör:

KARTERINGSBLAD

Datum:

Sektion

Entreprenad E05

Anläggningsdel Mellanplan (västra sidan)

Från:

Till:

Utfall

Volym

Figure C2: *Structural mapping at West Pilot from profile 0/038 to profile 0/052.*

Appendix D

Structural mapping - East Pilot

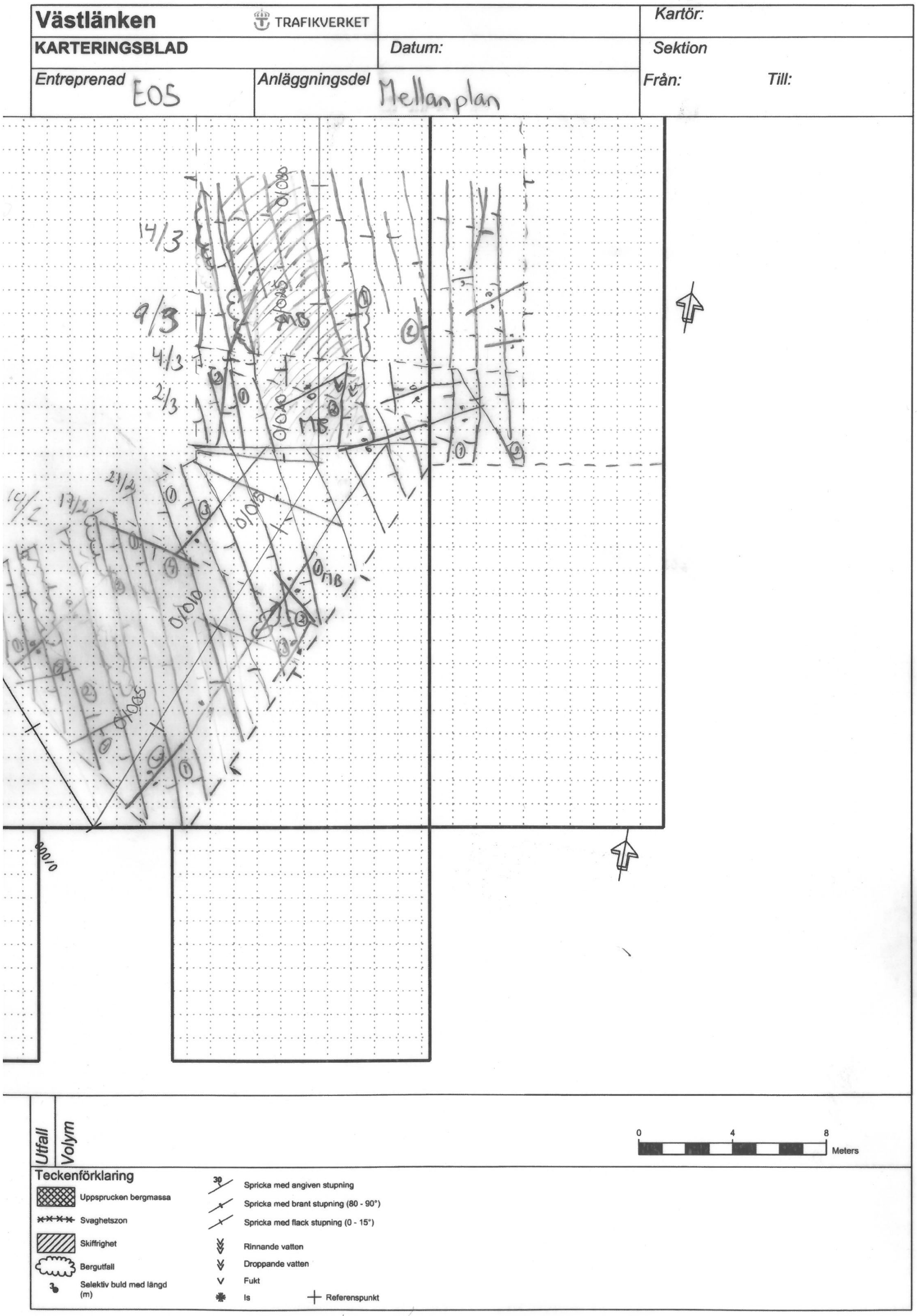

Västlänken TRAFIKVERKET		Kartör:
KARTERINGSBLAD	Datum:	Sektion
Entreprenad EOS	Anläggningsdel Mellanplan	Från: Till:

Utfall

Volym

Teckenförklaring

- ▩ Uppsprucken bergmassa
- ✕✕✕✕ Svaghetszon
- ▨ Skiffrighet
- Bergutfall
- Selektiv buld med längd (m)
- Spricka med angiven stupning
- Spricka med brant stupning (80 - 90°)
- Spricka med flack stupning (0 - 15°)
- Rinnande vatten
- Droppande vatten
- V Fukt
- Is
- + Referenspunkt

Figure D1: Structural mapping at East Pilot from profile 0/002 to profile 0/030.

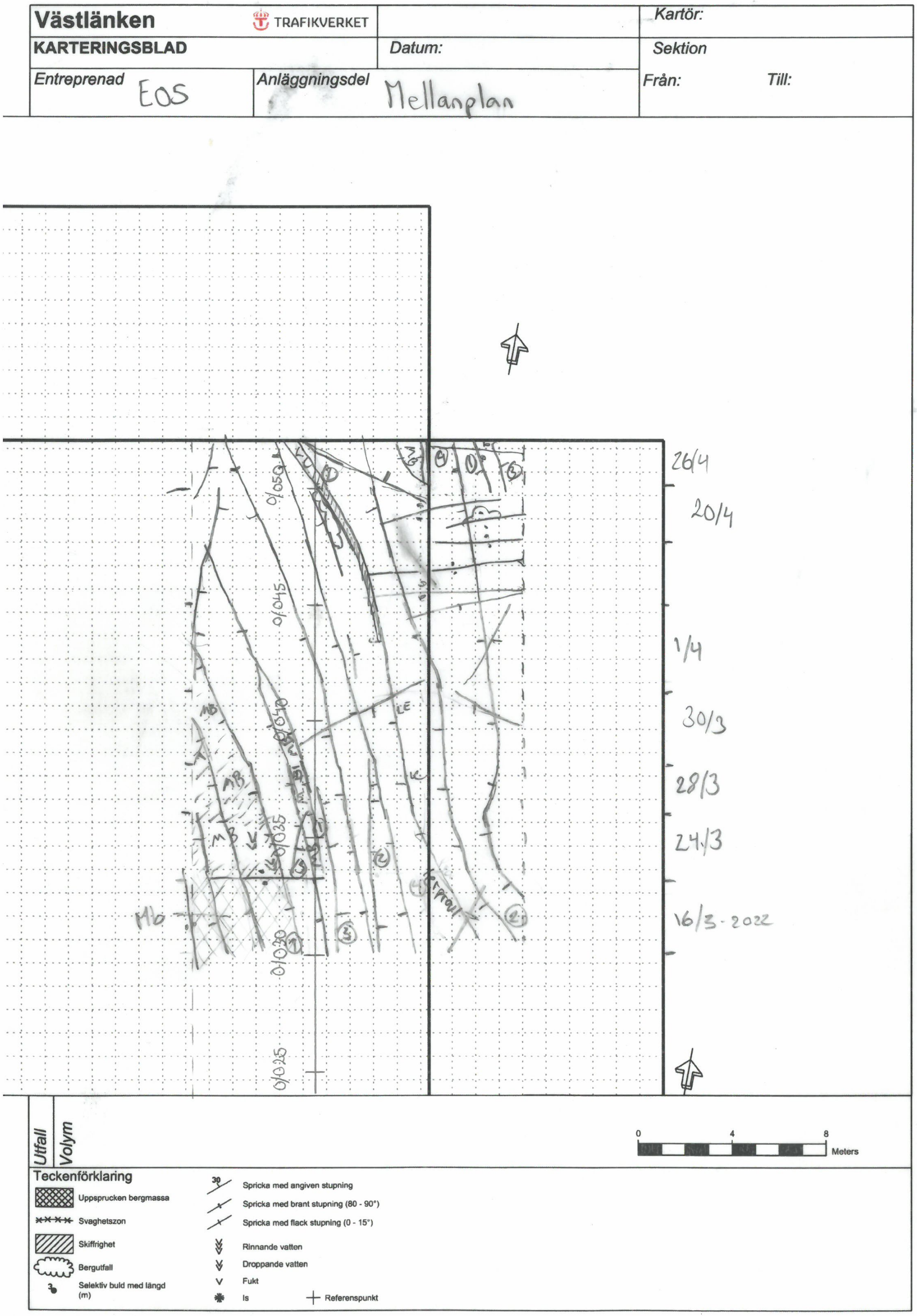

Västlänken	TRAFIKVERKET		Kartör:
KARTERINGSBLAD		Datum:	Sektion
Entreprenad EOS	Anläggningsdel Mellanplan		Från: Till:

Utfall

Volym

Teckenförklaring

- ▩ Uppsprucken bergmassa
- ✕✕✕ Svaghetszon
- ▨ Skiffrighet
- Bergutfall
- Selektiv buld med längd (m)
- Spricka med angiven stupning
- Spricka med brant stupning (80 - 90°)
- Spricka med flack stupning (0 - 15°)
- Rinnande vatten
- Droppande vatten
- Fukt
- Is
- Referenspunkt

Figure D2: Structural mapping at East Pilot from profile 0/030 to profile 0/052.

Appendix E

Laboratory results

Density and sound velocity

Table E1: *Density and sound velocity of the rock specimens.*

Specimen nr.	Diameter [mm]	Length [mm]	Weight [g]	Volume [mm^3]	Density [g/mm^3]	Travel time [μs]	Sound velocity [m/s]
1	45.13	118.83	518.2	190098.5	0.002726	21.3	5579
2	45.06	119.68	513.88	190836.6	0.002693	21.4	5593
3	45.08	118.83	507.78	189635.5	0.002678	22.3	5329
4	45.05	118.83	501.18	189411.2	0.002646	21.4	5553
5	45.03	118.85	502.02	189274.9	0.002652	21.9	5427
6	45.05	119.63	509.36	190432.5	0.002675	21.9	5463
7	45.04	119.67	511.41	190665.4	0.002682	21.8	5489
8	45.05	119.63	515.38	190771	0.002702	20.8	5751

Uniaxial compressive strength test

Table E2: *UCS, E-modulus and Poisson's ratio of rock specimens.*

Specimen nr.	Rock type	Diameter [mm]	Length [mm]	Foliation [°]	UCS [MPa]	E-modulus [GPa]	Poisson's ratio
1	Gneiss - Type 1	45.13	118.83	55	121	69.58	0.24
2	Gneiss - Type 1	45.06	119.68	55	77	91.36	0.37
3	Gneiss - Type 1	45.08	118.83	75	162	72.20	0.24
4	Gneiss - Type 1	45.05	118.83	90	202	79.34	0.25
5	Gneiss - Type 1	45.03	118.85	90	207	75.47	0.27
6	Gneiss - Type 1	45.05	119.63	60	144	80.89	0.25
7	Gneiss - Type 1	45.04	119.67	65	138	71.71	0.29
8	Gneiss - Type 1	45.05	119.63	65	131	72.52	0.25

Table E3: *Rock failure type during UCS test.*

Specimen nr.	Failure type
1	Fracture along foliation
2	Anomalies detected and the test is not approved
3	Spalling failure
4	Axial splitting
5	Spalling failure
6	Fracture along foliation
7	Fracture along foliation
8	Axial splitting

Brazil test

Table E4: *Brazil test on granodiorite gneiss specimens.*

Specimen nr.	**Diameter**	**Thickness**	**Force**	**Tensile strength**	**Comments**
	[mm]	**[mm]**	**[kN]**	**[MPa]**	
BTS 1	45.07	22.56	29.79	18.652	
BTS 2	45.12	22.09	27.81	17.763	
BTS 3	45.04	22.65	26.1	16.287	
BTS 4	45.06	22.23	19.02	12.088	Existing discontinuity before test
BTS 5	45.07	22.03	31.21	20.011	
BTS 6	45.09	22.48	25.09	15.758	
BTS 7	45.03	22.37	29.64	18.732	
BTS 8	45.06	22.55	27.93	17.499	
BTS 9	45.09	22.61	29.92	18.684	
BTS 10	45.1	21.91	26.86	17.305	
BTS 11	45.05	22.28	22.68	14.385	Existing discontinuity before test
BTS 12	45.09	23.15	24.46	14.918	
BTS 13	45.1	22.53	27.12	16.992	
BTS 14	45.09	22.61	29.43	18.378	

Point load test

Table E5: *Diametral point load test with loading parallel to foliation planes. Rock specimens are granodiorite gneiss (Gneiss - Type 1).*

Specimen nr.	**D**	**Failure load**	**Correction failure load**	**De^2**	**De**	**Is**	**F**	**Is$_{50}$**	**Comment**
	[mm]	**[kN]**	**[N]**	**[mm^2]**	**[mm]**	**[MPa]**	**-**	**[MPa]**	
PL1	45.04	14.56	14050.4	2028.602	45.04	6.926	0.954	6.608	High value
PL2	45.04	12.92	12467.8	2028.602	45.04	6.146	0.954	5.864	
PL3	45.04	14.44	13934.6	2028.602	45.04	6.869	0.954	6.554	High value
PL4	45.04	7.54	7276.1	2028.602	45.04	3.587	0.954	3.422	Test not approved
PL5	45.04	13.18	12718.7	2028.602	45.04	6.270	0.954	5.982	
PL6	45.04	11.22	10827.3	2028.602	45.04	5.337	0.954	5.092	
PL7	45.04	11.22	10827.3	2028.602	45.04	5.337	0.954	5.092	
PL8	45.04	14.08	13587.2	2028.602	45.04	6.698	0.954	6.390	
PL9	45.04	13.46	12988.9	2028.602	45.04	6.403	0.954	6.109	
PL10	45.04	9.56	9225.4	2028.602	45.04	4.548	0.954	4.339	Min value
PL11	45.04	10.14	9785.1	2028.602	45.04	4.824	0.954	4.602	
PL12	45.04	6.64	6407.6	2028.602	45.04	3.159	0.954	3.014	Min value
PL13	45.04	12.42	11985.3	2028.602	45.04	5.908	0.954	5.637	
PL14	45.04	8.76	8453.4	2028.602	45.04	4.167	0.954	3.976	Test not approved

Table E6: *Axial point load test with loading perpendicular to foliation planes. Rock specimens are granodiorite gneiss (Gneiss - Type 1).*

Specimen nr.	**W**	**D**	**Failure load**	**Correction failure load**	**De^2**	**De**	**Is**	**F**	**Is$_{50}$**	**Comments**
	[mm]	**[mm]**	**[kN]**	**[N]**	**[mm^2]**	**[mm]**	**[MPa]**		**[MPa]**	
PL1	45.04	27.01	21.84	21075.6	1548.935	39.357	13.607	0.898	12.217	High value
PL2	45.04	32.84	21.76	20998.4	1883.266	43.397	11.150	0.938	10.461	
PL3	45.04	29.08	17.72	17099.8	1667.642	40.837	10.254	0.913	9.361	
PL4	45.04	30.04	23	22195	1722.695	41.505	12.884	0.920	11.848	High value
PL5	45.04	35.86	25.26	24375.9	2056.453	45.348	11.853	0.957	11.344	
PL6	45.04	36.54	10.96	10576.4	2095.449	45.776	5.047	0.961	4.851	Min value
PL7	45.04	20.66	15.44	14899.6	1184.783	34.421	12.576	0.845	10.631	
PL8	45.04	38.88	20.36	19647.4	2229.640	47.219	8.812	0.975	8.588	
PL9	45.04	22.32	10.44	10074.6	1279.979	35.777	7.871	0.860	6.770	Min value
PL10	45.04	19.18	9.5	9167.5	1099.910	33.165	8.335	0.831	6.929	

Tilt test

Table E7: *Tilt test on granodiorite rock specimens. Two test groups are utilised.*

Test group	**Test nr.**	**Beta**	$\left[tan^{-1}\left(\frac{\sqrt{3}}{2}tan\beta_{i=1,\dots,30}\right)\right]$	**Median**
		[°]		
1	1	31.2	27.67627	27.67627
	2	27.8	24.5416	
	3	31.6	28.0479	
	4	29	25.64313	
	5	30.9	27.39796	
1	6	30.5	27.0274	
	7	33.4	29.72803	
	8	31.4	27.86201	
	9	32.5	28.88636	
	10	30.5	27.0274	
1	11	27.6	24.3585	
	12	32.3	28.69976	
	13	30.6	27.11998	
	14	32	28.42016	
	15	29.2	25.82723	
2	16	32	28.42016	
	17	29.8	26.38037	
	18	31.1	27.58346	
	19	30.2	26.74988	
	20	30.5	27.0274	
2	21	32.2	28.60652	
	22	33.5	29.82175	
	23	29.2	25.82723	
	24	32	28.42016	
	25	29.4	26.01146	
2	26	31.6	28.0479	
	27	32	28.42016	
	28	32	28.42016	
	29	31.2	27.67627	
	30	32.8	29.16655	

Appendix F

Apparent Dip Nomogram

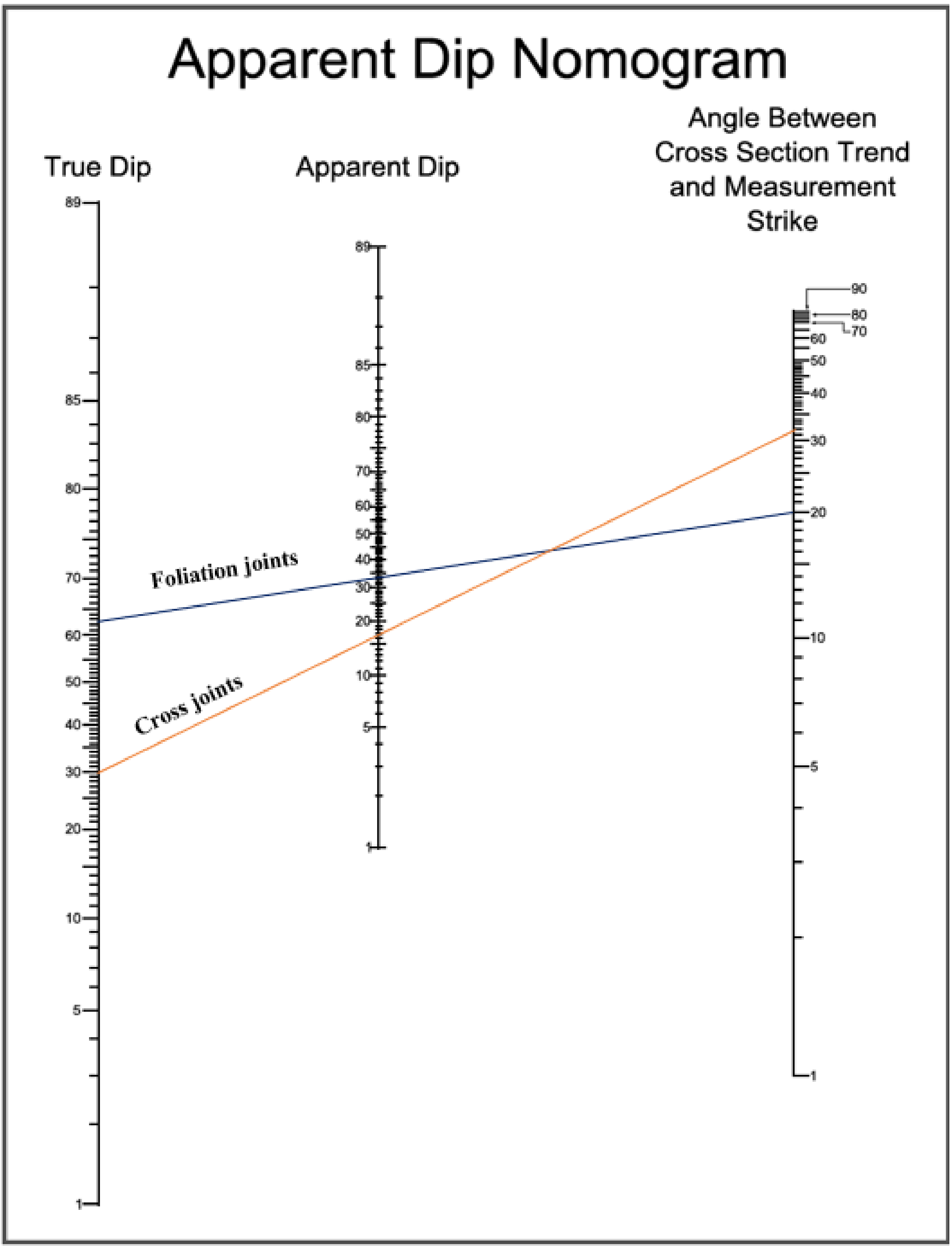

Figure F1: *Apparent dip nomogram to determine the apparent dips for joints.*

NTNU
Norwegian University of
Science and Technology